Proportional Resonant Control of Three-Phase Grid-Connected Inverter During Abnormal Grid Conditions

Ahmed Othman Althobaiti

Electrical Electronic Engineering

School of Engineering

Newcastle University

A thesis submitted for the degree of

Doctor of Philosophy

November, 2017

Abstract

The development of using grid-connected three-phase inverter has augmented the standing of realizing muted distortion along with high-quality current waveform. The standard three-phase grid-connected inverter is the full-bridge voltage source inverter. This inverter is usually controlled by proportional integral (PI) controller in order to ensure sinusoidal current injection to the grid. Although the PI controller is well established and easy to use under normal grid conditions, it leads to system instability under abnormal grid conditions. When abnormal grid conditions are likely to occur, the control system with PI controller can be configured to include two separate PI controllers for the positive and negative sequence components of the grid current. However, this increases control complexity and total harmonic distortion (THD).

More recently, the proportional resonant (PR) controller started to replace PI controller in a different application including grid-connected current control. In this thesis, a comprehensive theoretical and experimental comparison between the PI and PR controllers is presented. The comparison shows that the PR controller offers lower total harmonic distortion (THD) in the current signal spectrum and is simpler to implement as it uses only the positive sequence component of the grid current and consequently only one PR controller is needed. For these reasons, the PR controller is adopted in this thesis.

Despite the PR controller offering enhanced functioning under abnormal grid conditions compared to PI controller, a sudden change in the grid voltage could additionally raise the error between the reference signal and the controlled signal which results in causing significant divergence from its ostensible value. In this case, the performance of the conventional PR controller will not keep up with the increase in the error which weakens controller performance. To overcome this problem, a new design concept for controlling the current of the three-phase grid connected inverter during normal and abnormal conditions is presented in this thesis. The proposed technique replaces the static control parameters by adaptive control parameters based on a look-up table. This adaptive PR, controller has been investigated and demonstrated with different normal and abnormal grid conditions. The proposed control technique is capable of providing low THD in the injected current even during the occurrence of abnormal grid conditions compared with PI and PR controllers. It also achieves lower overshoot and settling time as well as smaller steady-state error.

Additionally, despite the fact that both PI and PR controllers are relatively straightforward to tune, and are sometimes capable of dealing with many time-varying grid conditions. This research also presented an adaptive controller tuned using advanced optimization techniques based on particle swarm optimisation (PSO). PSO is presented to optimize the control parameters of both PI and PR controllers for the three-phase grid-connected inverter**.** There are many advantages of using PSO, such as no additional hardware being required. Thus, it can be extended to other applications and control methods. In addition, the proposed method is a self-tuning method and can thus be suitable for industrial applications where manual tuning is not recommended for time and cost reasons. Simulation and experimental test were carried out to investigate the performance of the proposed techniques. In the simulation, the system was tested under 100 kW model using Matlab/Simulink environment. In addition, the system was also investigated through a practical implementation of the control system using a Digital Signal Processor (DSP) and grid-connected three-phase inverter. This practical system was demonstrated a 300 W scaled-down prototype. As a result, the comparisons between experimental and simulation results show the behaviour and performance of the control to be accurately evaluated.

Acknowledgements

I want to thank God (Allah), the most merciful and the most gracious, who gave me patience, strength and help to achieve this scientific research.

First and foremost, I would like to thank Dr. Matthew Armstrong for his guidance and support, throughout these years and for patiently reading and commenting on this thesis. I also appreciate the input of Dr. Mohammed Elgendy throughout my time at Newcastle University for his trust, guidance and support. Very sincere thanks are due to my friends in the UG lab, technicians and staff.

I have not enough words to thank my ever first teachers in this life, my parents, who have been inspiring me and pushing me forward all the way. Their prayers and blessings were no doubt the true reason behind any success I have realized in my life.

Special thanks to my wife. Thank you for supporting me for everything, and especially I can't thank you enough for encouraging me throughout this experience. To my beloved son Anas and daughter Aleen, I would like to express my thanks for being such good children always cheering me up.

I am grateful to all my family members for their kind support, endurance and encouragements, which have given me the energy to carry on and to motivate myself towards crossing the finish line.

To my dear father and mother

Acronyms

Acronyms	Full Names
AIO	Artificial intelligent optimization
ANN	Artificial neural networks
BJT	The bipolar junction transistor
BPSC	Balance positive sequence control
DD-SRF-PLL	Decoupled double synchronous reference frame phase locked loop
DG	Distribution generator
DSC	Delayed signal cancellation
DSP	Digital signal processor
FFT	Fast Fourier Transform
FL	Fuzzy logic
GA	Genetic algorithms
IARC	Instantaneous active reactive control
IEEE	Institute of Electrical and Electronic Engineering
IGBT	Insulated-gate bipolar transistor
ISE	The integral of squared error
ITAE	The integral time absolute error
MATLAB	Matrix laboratory
MOSFET	The metal-oxide-semiconductor-field-effect-transistor
MPP	Maximum Power Point
MPPT	Maximum Power Point tracking
NSS	Negative sequence signal
PCC	Point of common coupling

Acronyms	**Full Names**
PI	Proportional integral controller
PLL	Phase locked loop
PNSC	Positive and negative sequence control
PR	Proportional Resonance
PSO	Particle Swarm Optimization
PSS	Positive sequence signal
PWM	Pulse width modulation
SOGI	Second order generalized integrator
SPWM	Sinusoidal pulse width modulation
SRF	Synchronous reference frame
STATCOM	Static synchronous compensators
SVM	Space vector pulse width modulation
THD	Total harmonic distortion
Ts	Sampling time (sec)
UPFC	Unity power factor control
UPQC	Unified power quality conditioner
VOC	Voltage oriental control
VSI	Voltage Source Inverter

Symbol

Symbol	Full Names
I_a	Current in phase a
I_b	Current in phase b
I_c	Current in phase c
I_d	Current in reference frame direct current (d)
I_q	Current in reference frame quadratic current (q)
I_α	Current in the stationary reference frame (α alpha transform)
I_β	Current in the stationary reference frame (β beta transform)
k_i	Integral gain of the controller
k_p	Proportional gain of the controller
V_a	Voltage in phase a
V_b	Voltage in phase b
V_c	Voltage in phase c
D	Diode
f	Frequency
L_1	Inverter side inductance
L_2	Grid side inductance
P	Active power

Symbol	Full Names
p.u	Per unit
Q	Reactive power
t	Time
θ	Phase angle

Table of Contents

List of Tables

Table of Figures

Chapter 1.Introduction

1.1 Background and Motivation

The aggressive use of non–renewable resources has caused major issues such as the production of more pollution and greenhouse gas emissions leading to environmental concerns [1]. Furthermore, the upsurge seen in global energy demand from fossil fuel suppliers has resulted in higher oil prices [2]. These issues have encouraged organizations to use renewable sources instead of non-renewable energy sources. In the last few years, distributed power generation (DGs) based on renewable energy has continued to develop across the world due to its benefits for the global environment.

Photovoltaic (PV) energy is a renewable energy that can be identified as a rapidly growing element of renewable energy existing in the market, and according to renewable energy policy network for the 21st century (REN21) to be the biggest supplier of renewable energy [3]. Statistics from the European Photovoltaic Industry Association (EPIA) have shown that in 2014 there was 40 GW installed globally. In Europe, there was 75% increase in installed PV system reaching a capacity of 21.9 GW. U.K leading the way and has installed PV capacity 5.4 GW in 2014 from 0.96 GW in 2010 as shown in Figure 1.1[4]. Overall, global PV capacity had increased to 177 GW by end of 2014 [5].

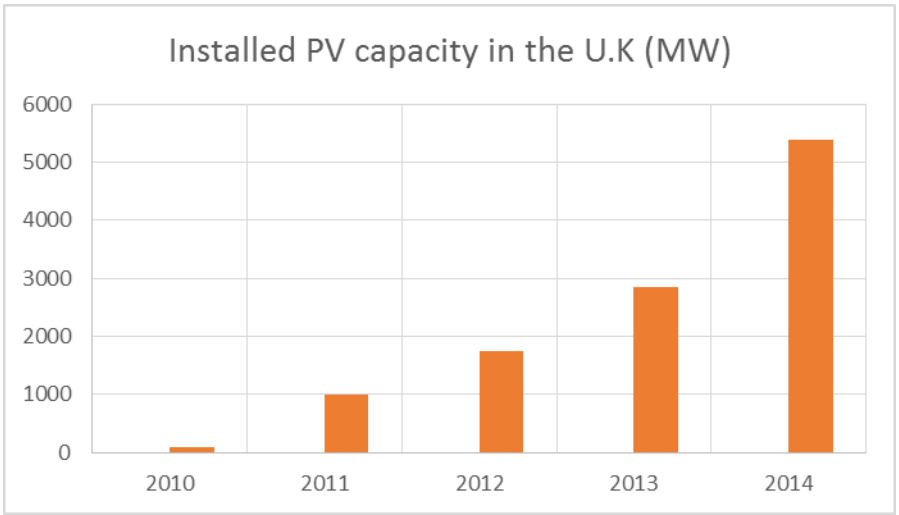

Figure 1.1 PV capacity installed in the U. K

Saudi Arabia is one of the developing countries that is leading producers of PV systems in the Middle East. Figure 1.2 shows the 2 MW grid–connected PV system at the King Abdullah University for Science and Technology (KAUST) [6], and this system can reduce annual carbon emissions in the region by 1700 tons.

Figure 1.2. Photovoltaic PV system at KAUST, Saudi Arabia [7]

The price of PV panels is one of the main issues which discourages consumers from adopting these systems. Therefore, improvements in PV technology are ongoing and, in the days to come, its cost will drop substantially, something identified as attributable to the solar cells effectiveness and the size of the cells. Consequently, per unit capacity has been improved [8]. Hence, the cost of PV panel production continues to decrease, and solar power generation will become comparable to other forms of renewable energy [9].

Distributed generators can generate electricity at or near the customer place where it is used as different to the normal mode of power generation. The utilization of power electronic technology in power system applications has been steadily increasing during recent decades. The continuous improvement of semiconductor device technology and the availability of digital control systems with endlessly increasing performance have reinforced this development. Power electronic converter technology has also been an important enabling factor for recent developments in distributed generation and renewable energy systems, including photovoltaic systems due to several advantages and factors. A smaller size and lighter weight are important factors which have led manufacturers to produce smaller power electronic converter products for businesses customers. In addition, this high conversion efficiency and the capability to

control the power from a source to the utility load play an important role in the growth of power electronic systems. As a result, such systems can be found in many applications of different kinds for energy conversion, uninterruptible power supply (UPS), transportation, switch mode power supply, utility systems, aerospace, telecommunications, factory automation, process control and many other fields.

In recent years, voltage source converters (VSCs) have been increasingly developed supported by this widespread with many benefits in industrial application. VSCs can be used in adjustable speed electric drive systems [10] and UPS applications [11, 12]. VSCs, which are operating as active rectifiers, has recently been seen as increasingly pertinent options to replace diode rectifiers or line-commutated converters. This is owing to the pulse width modulated (PWM) operation, that enables imperfect current distortion and concentrated harmonic filter necessities composed to allow control of the power factor and DC-link voltage [13, 14]. Moreover, VSCs are further used for distributed energy resources like photovoltaic and fuel cell systems, all of which innately deliver a direct current (DC) output and are contingent on power from sunlight and store it via solar cells using either batteries or any other generation electronic converters for incorporation within the AC grid [15, 16]. Solar panels can extract electrical energy to feed distribution farms or utility grids. Typically, PV panels are interfaced with utility grid via a power electronic converter. Pulse width modulation (PWM) techniques are used to control the three-phase power converter. In order to connect the PV module to the utility grid, a three-phase inverter is used.

Nowadays, the three-phase inverters are small in the size and the weigh as well as high efficiency and reliability. Figure 1.3 shows a basic single line of three-phase grid-connected PV inverter.

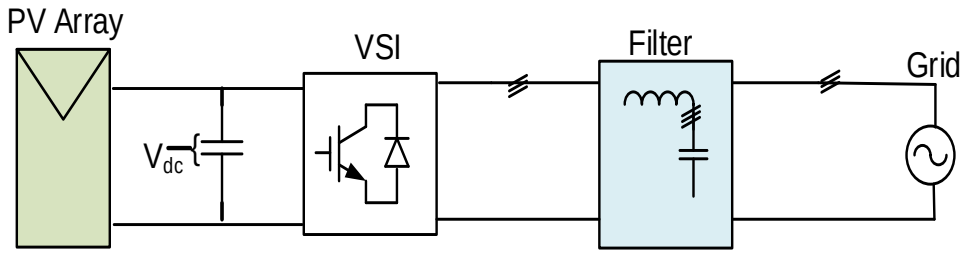

Figure 1.3 Basic single line diagram of three-phase grid-connected PV inverter

On the other hand, in connecting the converters to the utility grid there are international recommendations that must be observed. These recommendations could vary from country to country, and some of the criteria follow [17, 18]:

- DC current level injected.
- Total harmonic distortion (THD).
- The grounding of the system.
- Voltage, current, and frequency.
- Automatic reconnection and synchronization.

1.2 Three-phase Grid-connected Inverter

Generally, a three-phase grid-connected inverter is used to interface the PV panels which generates DC voltage into appropriate AC voltage for the utility grid. The three-phase inverter aims to meet three targets: The first target is to confirm that the PV panels operate at the maximum power point (MPP). The second is to inject the demand sinusoidal current to the utility grid. The third target is the control of the inverter so as to be able to deal with normal operation and detect any abnormal conditions that occur in the grid. In fact, different processing stages are used to connect the PV system to the utility grid. The first method as shown in Figure 1.4 (a) is a single stage or centralized topology where PV panels are connected in series or parallel to achieve certain voltage and current level due to the low input voltage provided from the PV system. In this topology, the inverter holds all tasks such as maximum power point tracking (MPPT) and the desired value of the voltage. A dual-stage topology is shown in Figure 1.4(b). It can be seen from the Figure 1.4(b) that the model is separated into two stages: The first stage is a DC-DC converter and the second is a DC-AC inverter. A DC-DC converter can be used in this application to boost the voltage to the higher desirable values with MPPT to work at the highest efficiency. Due to its simplicity, the most widely used MPPT technique is Perturb and Observe method (P&O) [19]. The inverter in the second stage converts the DC values to three-phase AC and controls the current to the utility grid. Due to the advantages of connecting a number of PV panels in series. The single-stage type is preferred in most industries as it is more efficient and economical in case of homogeneous irradiance conditions [20], [21].

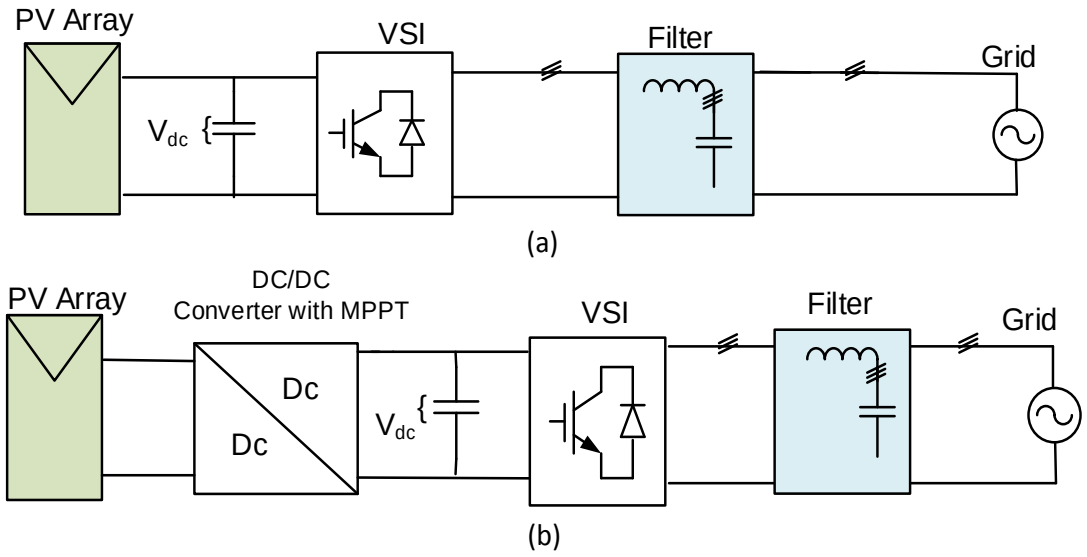

Figure 1.4 Processing stages for single line diagram of the three-phase PV grid connected inverter: (a) single-stage case (b) multi-stage case

Three-phase grid-connected inverter is a very flexible topology that can be designed and implemented for a wide range of applications and voltage levels, spanning the power range from a few hundred watts (W) to hundreds of (MWs). The most common voltage source inverter is a two-level voltage source inverter (VSI) as shown in Figure 1.5. The main difference between the conventional two-level topology and the varieties of multi-level converters involves the pulse width modulation (PWM) technique used to control the operation of the individual switches. Therefore, the main principles of operation, as well as the general structure and functionality of the control systems are usually the same for most of the applications in grid-connected VSCs. The multi-level voltage source inverter (VSI) has many topologies such as neutral point clamped (NPC), flying capacitors (FC) and cascaded full bridge [22]. Among these, the NPC inverter is the most commonly used for high voltage purposes in industrial applications [23]. A modular cascaded H-bridge has been used recently in grid-connected application [24]. By increasing the number of levels of the topology, the output voltage and current will be increased and the total harmonic distortion will be reduced. However, the power losses are one of the challenges due to the large numbers of power switches for low voltage multilevel inverters compared with the two-level VSI [25]. The complexity of the control technique and the separate DC sources are other issues in the multilevel inverter [26]. On the other hand, the multi-level VSI is suitable for high power applications with high voltage and high current while the two-level VSI is suitable for low and medium voltage applications. This thesis considers the use of the two-level VSI which consists of 6 semiconductors transistor switches. In industry, there are many different switching transistors such as insulated-gate

bipolar transistors (IGBTs) which can be used in medium power applications. The other semiconductor switch type is the metal-oxide-semiconductor-field-effect transistor (MOSFET) which can be used in small and medium power applications. In the three-phase inverter, the output of each leg is shifted by 120° degrees, and the most commonly used modulation techniques are sinusoidal pulse width modulation (S-PWM), hysteresis band PWM, third harmonic PWM and space vector modulation (SVM) strategies [26].

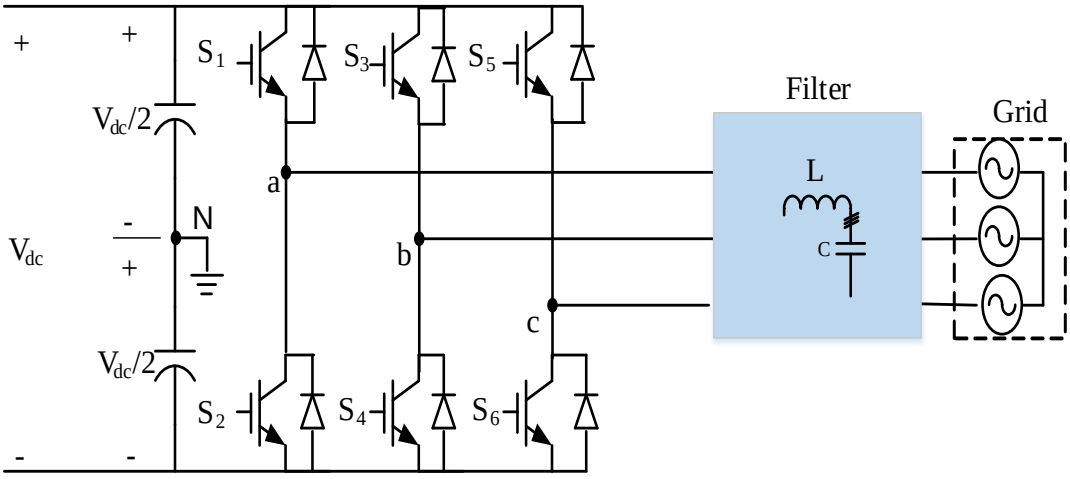

Figure 1.5 Two-level three phase inverter (VSI)

The three-phase grid-connected PV inverter is connected to the grid filter to reduce the harmonics injected into the utility grid.

1.3 Grid Filter Types

Filter design is an essential part of the grid-connected inverter, due to a wide range of harmonics and noise of the switching frequency for the three-phase generated current. The noise and high-frequency harmonics can be attenuated by passive filters. Different types of passive filters have been reported such as L-filter, LC-filter, LCL-filter and LCCL-filter. In designing a low pass filter the cost, weight, power losses and volume should be taken into account. Figure 1.6 shows filter configuration schemes. Traditionally, the L-filter is the first filter to be used due to its ease of control. However, the L-filter cannot be employed with low switching frequency. Therefore, high inductance and/or high switching frequency is required. The LC-filter is a second order filter which offers better attenuation of 40 dB/dec. The capacitor C is selected to satisfy the harmonic requirements.

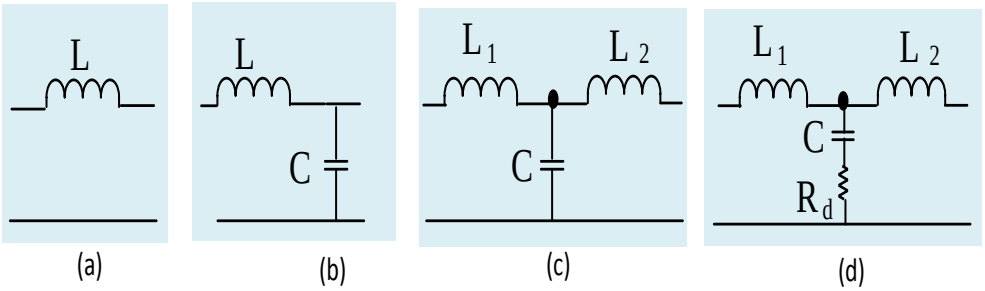

Figure 1.6 Filter configuration schemes: (a) L-filter; (b) LC-filter; (c) LCL-filter; (d) LCL-filter with damping resistor

On the other hand, the LCL filter has several advantages compared with the L-filter and the LC-filter, such as the low THD of the three-phase current output, low cut-off frequency, power density and the reduced cost of components, and also it provides a 60 dB/dec attenuation [27],[28]. The resonance needs to be removed from the switching frequency and should not affect the dynamic response of the current control [29].

In spite of these advantages of the LCL filter, it has a resonance peak at the resonance frequency from the inverter or from the grid. To overcome this, many researchers have proposed passive and active damping. One of these methods is to damp this resonance by adding a resistor within a series with the capacitor, dampening the high frequency in the filter [30],[31]. However, power losses will be a major issue in passive damping [32]. Active damping has also been investigated to eliminate the resonance without increasing the losses [33],[34]. However, this method has to take any change in the grid impedance into account and increased the sensors of the system. This increases the cost and complexity of the technique[32].

1.4 Grid Synchronization Method

Grid synchronization is a very important task in grid-connected applications, stable and accurate current control of the system to the grid being the goal. [35]. Grid synchronization is accountable for phase angle, amplitude, and frequency of the grid voltage. Various grid synchronization methods have been proposed in the literature such as zero crossing method (ZCM), phase locked loop (PLL) and virtual flux (VF).

1.4.1 Zero Crossing Method (ZCM)

The zero-crossing detection (ZCD) technique is the plainest synchronization technique used to obtain the frequency and the phase angle. Figure 1.7 shows the zero-crossing detection scheme. The zero-crossing method is based on counting the grid voltage zero crossing from the estimation of the fundamental frequency. As a result, the grid phase angle is obtained. Zero crossing only can be sensed every half cycle within the fundamental voltage frequency [36-38]. However, it shows poor performances and slows dynamic response when the grid voltage is unstable due to notches or harmonics occurring in the grid [39]. In addition, fast dynamic performance is impossible using this method due to the lag of the phase angle tracking.

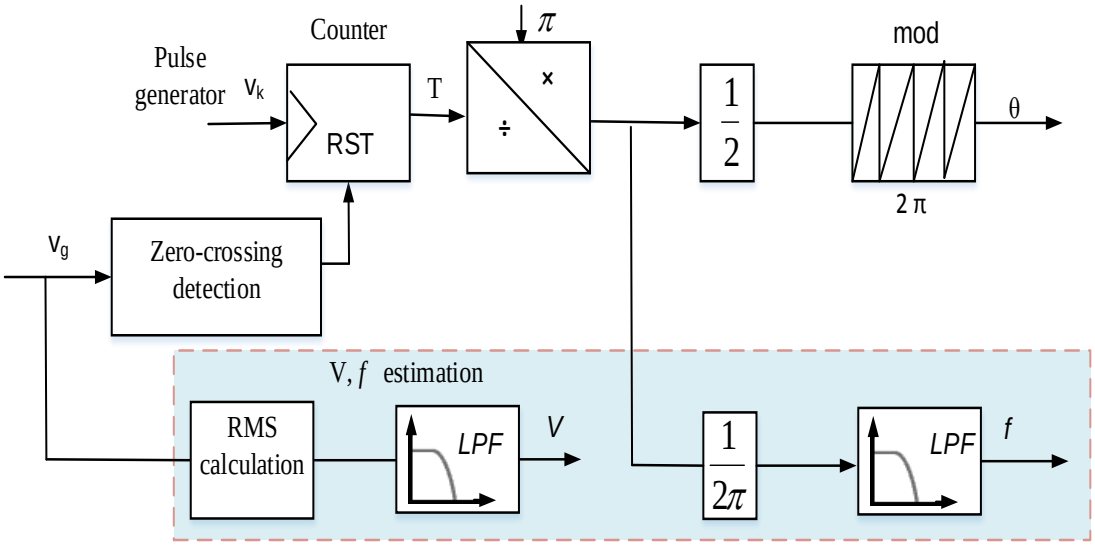

Figure 1.7 Zero crossing detection method

1.4.2 Phase Locked Loop (PLL)

The phase-locked loop (PLL) is one that is commonly used, a widely used grid synchronization method. This is connected to its associated high performance along with effortlessness implementation and ability to synchronize an output signal in addition to the input reference signal, amid respect for phase angle and occurrence [40]. The phase-locked loop was first used in an implementation of synchronization in radio signals by Appleton in 1923 and by Bellescize 1932 [40]. Later on, the PLL became widespread for use in a variety of industrial applications. The basic PLL contains three main parts: a phase detector, loop filter, and voltage controlled oscillator as shown in Figure 1.8.

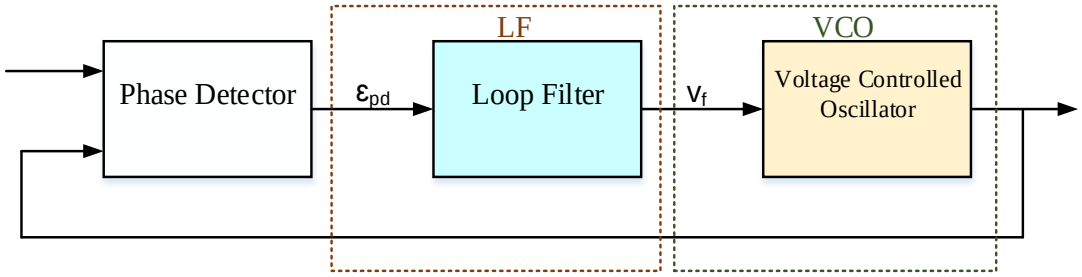

Figure 1.8 Basic PLL scheme

In the case of the three-phase grid-connected inverter, the three-phase synchronous reference frame phase locked loop (SRF-PLL), also called the *dqo-PLL*, is commonly used for synchronization [41]. Figure 1.9 shows the three-phase locked loop scheme in αβ frame. Here, PI controller is used in order to lessen the error amongst the reference and the measured grid voltage. The PLL has the ability to provide information at the point of common coupling (PCC) like grid voltage amplitude, grid frequency, and the phase angle. Additional work was proposed by using adaptive PLL that consist of three control unit includes the phase, frequency, and the voltage controllers [42].

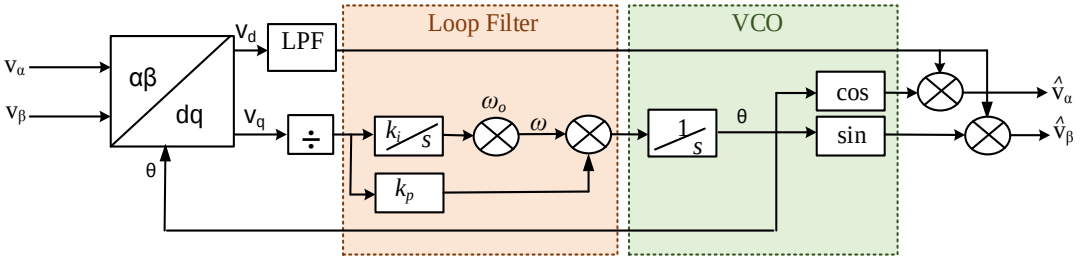

Figure 1.9 The three-phase PLL scheme in SRF

Another synchronization method is based on virtual flux estimation, and the first implementation in grid-connected inverter was accomplished in 1991 by Weinhold [43]. The basic idea is based on replacing the voltage angle of the PLL by the angle of virtual flux. Figure 1.10 shows the basic virtual flux scheme. It is based on the assumption that the grid is induced by a virtual grid flux. To make it simple, the three-phase synchronous reference frame uses two low-pass filters in order to remove the offset in the voltage of the virtual flux. The virtual flux mostly used in direct power control to improve the operation of active and reactive power control [44]. However, due to some limitation under unbalance grid conditions, the virtual flux method cannot outperform the phase locked loop in vector control method [29].

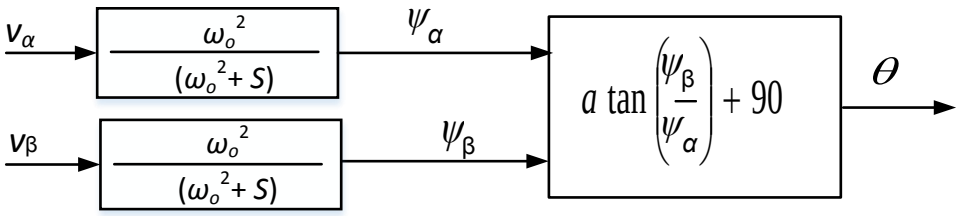

Figure 1.10 Basic virtual flux scheme

1.5 Thesis Objectives

The major aim of the present research is to investigate the performance and characteristics of the three-phase grid-connected inverter under normal and abnormal grid conditions with a view to improving its performance and stability. The main objectives of the study can be summarized as follows:

- To investigate the operational characteristics and control methods used for three-phase grid-connected PV inverters during normal and abnormal supply conditions. This research addresses these issues in such a way that is valid for an increasing variety of applications.
- To investigate different current control techniques for the three-phase grid-connected inverter and to determine their limitations in order to improve the control method. In addition, to study the suitability of the digital phase locked loop (PLL) for grid synchronization with positive and negative voltage components.
- To investigate and demonstrate a proposed technique based on adaptive proportional resonance (PR) controller based on a look-up table to reduce the error between sine reference syntheses and therefore to reduce the distortion of the waveform.
- To design a suitable controller to deal with the abnormal conditions investigated as well as the behaviour of an unbalanced system and to verify the results experimentally.
- To optimize the control method using an advanced intelligent optimization method based on particle swarm optimization (PSO).

1.6 Contributions of the Thesis

This research presented in this thesis the performance of the three-phase grid-connected inverter and takes into account the principles design, analysis and comparison of the current control based on the PR controller in the stationary reference frame and PI controller in synchronous reference frame for injected the current under abnormal conditions under any circumstance such as grid fault, where the grid current varies from normal operating case. Thus, the current control techniques based on the most suitable strategies that could achieve better results during normal and abnormal conditions in the thesis are: positive and negative sequence control *(*PNSC*)* and balance positive sequence control (BPSC).

Under abnormal grid conditions, the controlled signal instigating an unexpected decline in voltage could promote a rise in the error between the reference signal, and the controlled signal. This can be identified as creating large-scale aberration from its nominal value. The implementation of the established PR controller cannot match the rise in error, in turn, this lessens controller performance weakening. To get beyond this concern, this shows an enhancement in present-day control using a novel adaptive PR controller. A novel method for adaptive PR controller for abnormal conditions in the grid using a look-up table. The adaptive PR control techniques have been used in the stationary reference frame to control the current. The proposed control technique is qualified to provide low total harmonic distortion (THD) in the inserted current even during the incidence of abnormal grid conditions. The adaptive control has the ability to reduce the error.

Despite the fact that both PI and PR controllers are relatively straightforward to tune, and are sometimes capable of dealing with many time-varying conditions, most disturbances associated with grid-connected inverter technology, such as (grid voltage dip or changes in network impedance) are significantly more challenging and depends on the designer to obtain the best performance. This research also presented a novel concept of self-tuning of the current controller using particle swarm optimization (PSO). An adaptive controller tuned using PSO is presented to optimize the parameters of both PI and PR controllers for the three-phase grid-connected inverter**.** There are many advantages of using PSO, such as no additional hardware being required. Thus, it can be extended to other applications and control methods. In addition, the proposed method is a self-tuning method and can thus be suitable for industrial applications where manual tuning is not recommended for time and

cost reasons. Both the PI current control in the synchronous reference frame and the PR current control in the stationary reference frame are considered in this study.

1.7 Publication

Publications from this work are listed below.

1. A. Althobaiti, M. Armstrong, and M. Elgendy. "Three-Phase, Grid-Connected Inverter Using Different Control Schemes." *Proceedings of the Eighth Saudi Students Conference in the UK*. 2016. [45].
2. A. Althobaiti, M. Armstrong, and M. A. Elgendy. "Current control of three-phase grid-connected PV inverters using adaptive PR controller." *Renewable Energy Congress (IREC), 2016 7th International*. IEEE, 2016.
3. A. Althobaiti, M. Armstrong and M. A. Elgendy, "Control parameters optimization of a three-phase grid-connected inverter using particle swarm optimisation," *8th IET International Conference on Power Electronics, Machines and Drives (PEMD 2016)*, Glasgow, 2016.
4. Althobaiti, M. Armstrong, M. A. Elgendy and F. Mulolani, "Three-phase grid connected PV inverters using the proportional resonance controller," *2016 IEEE 16th International Conference on Environment and Electrical Engineering (EEEIC)*, Florence, 2016.
5. A. Althobaiti, M. Armstrong and M. A. Elgendy, "Space vector modulation current control of a three-phase PV grid-connected inverter," *2016 Saudi Arabia Smart Grid(SASG)*, Jeddah, 2016, 1-6. 2016.

1.8 Thesis Outline:

The content of this thesis is described below:

- **Chapter 1:** This chapter gives an introduction to the thesis, provides the background of the grid-connected inverter, describes some of the more important points in research on power electronics and emphasises the motivation and importance of the present research work. This chapter also discusses the grid synchronization methods. In addition, the present study's aim and objectives, followed by thesis contributions and the publications resulting from this research are presented.

- **Chapter 2**: A literature review of various types of control methods for grid-connected inverters is provided in this chapter describing the background and various types of control and how their use affects the environment. Also, the challenges faced in the development of these systems are highlighted here.
- **Chapter 3**: This chapter considers the modelling and design of the three-phase grid-connected inverter and grid synchronization in three-phase inverters under abnormal conditions.
- **Chapter 4**: Highlights the steps in the control approaches used for grid-connected inverters in the synchronous rotating reference frame and stationary reference frame
- **Chapter 5**: Simulations and practical results of the PI controller and PR controller are presented. In addition, it presents experimental hardware equipment with an overview of the hardware
- **Chapter 6:** Simulation and practical results of adaptive PR controller are presented in balance and unbalanced grid conditions. The controller has been tested with different grid faults such as line-to-line fault and two line-to-line faults.
- **Chapter 7**: This chapter present advanced optimization control method using Particle Swarm Optimisation (PSO) to find the optimal control parameters of PI and PR controller. Simulation results of the PI controller and PR controller are presented under abnormal grid conditions.
- **Chapter 8**: A summary of the research is provided in this chapter along with the conclusions of the study. Possible future research work is then discusse.

Chapter 2. Literature Review

2.1 Introduction

The rapid increase in the use of distributed power generation systems (DPGS) grounded on renewable energy sources has boosted the implementation of voltage source converters (VSCs) in distribution networks. As a result, the voltage source inverter (VSI) and its control system have become main elements of distributed generation. There has been an intense research effort in the development and analysis of various current control techniques for the three-phase applications during the last couple of decades. In addition, different methods of grid synchronization have been proposed and analysed. Many studies have aimed to improve and develop the control technique used firstly for electrical machine drive systems such doubly fed induction generator (DFIG) also known as wound rotor induction generator. These techniques are also successfully applied in grid-connected inverters and bidirectional AC-DC flywheel converters to interface between the DPGS and the power grid. Moreover, active-reactive voltage source converters have also become an interesting alternative for diode rectifiers or line commuted converters due to pulse width modulation (PWM) technique. This method has the ability to control the power factor and DC-link voltage which ensures a reduction in harmonics of the system [46, 47].

The performance of a three-phase grid-connected inverter depends mainly on the quality of current control to the load or the grid. This factor plays an important role in power electronics in meeting the requirements of standards such as IEEE 519 and 1547 which require a maximum of 5% for the current total harmonic distortion (THD) [48, 49]. In order to comply with the above requirements, the three-phase grid-connected inverter should have very good current control which has a good harmonic rejection.
The thesis focuses on the current controls techniques which depend on the voltage oriental control.

2.2 Methods of Three-phase Current Control

In three-phase grid-connected inverter, current control is a high-status issue, which needs to be dealt with. The main function of current control is to ensure that the reference signal is followed

by the measured signal. The concept of current control has been widely discussed in the literature [50, 51]. A basic three-phase grid-connected inverter with current control is shown in Figure 2.1.

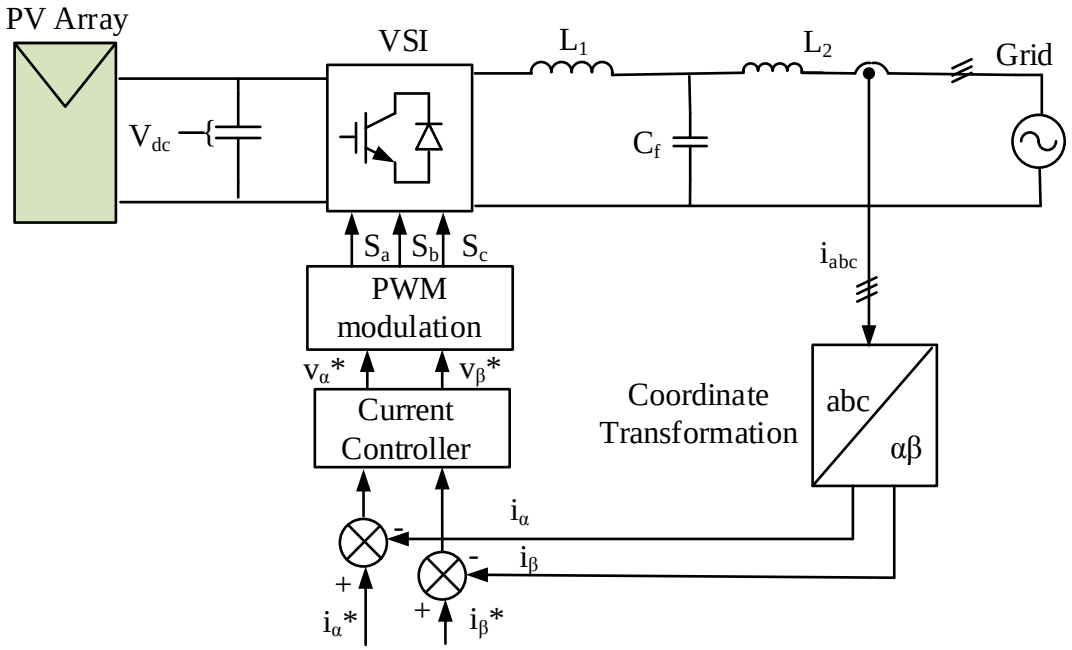

Figure 2.1 Basic single line diagram of the three-phase grid-connected inverter with current control scheme

Many different current control techniques have been utilized in order to achieve the better quality of the current waveform. In the three-phase system, current control can be implemented in various ways such as the natural reference frame *abc*, the synchronous rotating reference frame *dq*, and the stationary reference frame *αβ*.

2.2.1 Proportional Integral (PI) Current Controller in the Synchronous Reference Frame

For the control of the output current, a PI controller would be currently the most popular scheme used. In the three phase-system, the three-phase reference frame *abc* coordinates are transformed into *dq* synchronous coordinates in a rotating reference frame with angular frequency using Park's transformation [52].

A PI controller is a combination of the proportional and integral terms and it can be defined by the subsequent transfer function [53]:

$$G_{pi}(s) = k_p + \frac{k_i}{s} \tag{2.1}$$

where k_p is the proportional gain, k_i is the integral gain of the PI controller.

The two current components in the rotating synchronous reference frame *dq* coordinates appear as DC components. The *d* coordinate represents the direct component while *q* coordinate represents the quadrature component. The PI current controller has a number of plus points, a principal one being that it is relatively straightforward to use within the control system. This makes it more preferable for engineering, and therefore control and filtering can be obtained. However, the PI controller has the following drawbacks such as:

- In a single-phase inverter, the PI controller has a steady state error in the stationary reference frame which cannot be eliminated. This error is between the sinusoidal reference signal and the output measured signal [54, 55].
- PI controller has poor performance due to cross-coupling between *d* and *q* coordinators. As a consequence, the functioning of the PI controller can be enriched by presenting a decoupling term between the d and q coordinators and the voltage feedforward [30, 38, 56]
- The PI controller is poor at eliminating the low order harmonics, and this can cause problems when used in grid-connected applications [39].
- The PI current controller requires more transformation from three to two phases, which therefore requires more space in a low-cost fixed-point DSP [30].
- To overcome these issues, many improvements have been implemented in PI controllers. As a result, the feedforward control method is able to reduce the grid current harmonics caused by grid voltage distortion without changing the dynamic response [39].

2.2.2 Proportional Resonance (PR) Current Controller in Stationary Reference Frame

Given the shortcomings of the PI controller, an alternative solution for a current controller has been presented which is the proportional resonant controller (PR). The PR controller is a combination of a proportional term and a resonant term. The PR controller has been used in the stationary reference frame method [39], [57, 58]. Within the control system; grid current is

conveyed to the stationary reference frame using Clark's transformation from three-phase $i_{a,b,c}$ to $i_{\alpha,\beta}$ coordinators [59]. Hence, PR controller variables are sinusoidal. In addition, a PR controller has several advantages which are as follows:

- It has the capability to eradicate steady-state error by offering extra gain at the particular resonant frequency of the controlled signal [60].
- The PR controller has the capability to implement harmonic compensator (HC) minus the introduction of any deviations in dynamic control; thus, this accomplishes a high-quality current [61].
- The intricacy of current control can be seen to be lower in a statutory reference frame in comparison to the synchronous reference frame *dq* because Park's transformation does not need to be used in the control system.
- Currents in α-β coordinates are not cross-coupled and so do not need to be decoupled [62].
- PR control can be used as a notch filter to compensate the harmonic in the control signal [56].

The transfer function of the PR controller is given by:

$$G_{PR}(\mathrm{s}) = K_p + K_i \frac{s}{(s^2 + {\omega_0}^2)} \tag{2.2}$$

Where, k_p is the proportional gain, k_i is the integral gain of the controller, ω_0 is the resonance frequency.

To sidestep the problem of obtaining infinite gain at the resonant frequency; a non-ideal PR controller can instead be used by including a bandwidth of the controller system. Although this type of control provides very low steady-state tracking error, any such error will affect the current control.

$$G_{PR}(\mathrm{s}) = K_p + K_i \frac{2\omega_c s}{(s^2 + 2\omega_c s + {\omega_0}^2)} \tag{2.3}$$

where, kp is the proportional gain, ki is the integral gain of the controller, ω_0 is the resonance frequency, and ω_c is the cut off frequency.

In grid-connected uses, it is useful to apply Harmonic Compensator (HC) terminologies in parallel with the PR controller to focus upon low order harmonics (5^{th}, 7^{th}); these will be noted as being problematic.

The equation next is important for implementation of the HC:

$$G_{HC}(s) = \sum_{h=5,7} \frac{2\ K_{ih}\ s}{s^2 + (\omega h)^2} \tag{2.4}$$

2.2.3 The *abc* Reference Frame Current Control

The first current control technique proposed for pulse width modulation (PWM) was based on the three-phase reference frame [50], [63]. The principle of the control task is to keep the three-phase measured current aligned with the three-phase reference current based on the state of inverter switches. Therefore, the control depends on the output of the three-phase current of the inverter compared with the phase current reference. One of the most common control techniques using this reference frame is the hysteresis controller (HC) method. Hence, the results of the three-phase errors are used at the same time to feed the PWM through the upper and lower hysteresis bands in the loop. The advantages of this type of control are that it is easy to implement in the three-phase system, and gives faster transit responses. However, the aforementioned control has several drawbacks:

- High switching frequency and high ripples are produced by the hysteresis bandwidth [64].
- There is interference between the phase currents which could lead to increased distortion.
- This controller has no fixed switching frequency, and therefore it has bad harmonic performance and this leads the system to be unstable.
- The *abc* reference frame parameters are independent of each other and therefore it is necessary to generate the duty cycle for the PWM which will make the control technique is more complex [65].
- The *abc* reference frame could be used in synchronous reference frame using a PI controller. However, due to the off-diagonal terms repressing the cross coupling between the phases in the matrix which make the control technique is more challengeable [39].

2.2.4 Other Control Strategy

Many recent methods have not used the vector orientated control approach. Direct power control (DPC) is another control strategy based on active power and reactive power control [66, 67]. The advantages of this control technique are that it is a simple method and there is no need for the internal control loop for the current or the voltage. However, high frequency is needed

to obtain good performance. In addition, switching frequency is variable due to the use of hysteresis comparators, which makes it difficult to design the grid filter [44].
On the other hand, other studies have used predictive control. This technique predicts the error vector of the current waveform at the sampling modulation period [51, 68]. The concept of predictive control has been used for direct power control by minimizing the error for active and reactive power [69]. However, this method has issues in the grid filter which is affected by unwanted frequencies due to the current spectrum distribution [70].

2.3 Power Quality

The three-phase grid-connected inverter is most commonly a factor in injection and absorption of the power to the grid. An example of this would motor drives which concentrate absorbing active power taken from the grid in order to reach the optimum performance of an electrical motor. In normal grid conditions, the three-phase inverter injects all active power to the grid. However, the widespread use of electronic-based loads and nonlinear loads has led to negative effects on the power quality which is an important issue. Therefore, the term power quality can be used to refer to any issues arising from an unusual situation in the system. The power quality is commonly affected negatively when the system is subjected to abnormal conditions in the voltage, current, and frequency when disturbances in the utility grid occur [71].

When operated in grid-connected applications, the three-phase grid-connected inverter can be exposed to the disturbances, transients, and interruptions that propagate through the electric power system. Thus, a large share of such disturbances and transients are likely to introduce temporary unbalanced grid voltage conditions [72, 73]. Moreover, due to a low quality of DGs, there are many causes for unbalanced voltage produced by a nonlinear load. Single phase generators, unbalanced loads and the negative impact of induction motors [74],[75]. Therefore, voltage disturbance in the grid has a negative effect on the grid and can cause a major trip and high cost in general [76]. These abnormal conditions can be caused in the utility grid by short circuit faults like a line to ground fault, voltage sags, voltage swell and injected harmonics. These faults can be produced by abnormal situations in the grid such as direct on-line starting of large motors, transformer energizing and capacitor bank charging. During this abnormality, one or more of phase voltage is reduced or increased beyond than the nominal level at the point of common coupling (PCC).

2.3.1 Voltage Sags

One of the major types of abnormal conditions in the system is voltage sag (also called a voltage dip). The voltage sag occurs as any disturbance of the voltage in the network caused by an abnormality in the grid. In accordance with 'IEEE standards 1159/95', A voltage sag is defined as a reduction in one or more phases of the voltage waveform at the point of common coupling (PCC) [77]. The percentage of the voltage decreases to a value ranging from 10% to 90% of the nominal value for an interval of between 0.5 cycles to 1 minute [78]. The voltage sag can be classified into two categories, namely balanced voltage sags and unbalanced voltage sags. In the balanced voltage sag, all the three-phase voltage are reduced in the magnitude at the same time. In the unbalanced voltage sag, the voltage magnitude in one or two-phase is reduced, making the voltages unbalanced for the duration of the sag [79]. The unbalanced voltage sags can be caused by single phase to ground faults, two-phase to phase to ground fault and unbalanced three-phase to ground faults. As a consequence, the current is increased in order to maintain the injected power as it was under normal conditions. Thus, the current waveform can be found to have double the normal value. This effect leads to disturbance in the network or even damage to the system, or the operating time of the inverter itself, one of the requirements is limiting the current to a safe level to avoid tripping or possible damage to the system [79].

If the system should show voltage sag, a voltage scheme to support the raising of the voltage in all phases as quickly as possible is employed. As a result, if one or two phases in the system are affected, this problem can be overcome by applying a voltage equalizing strategy. Voltage equalization technique succeeds when the difference between voltages is reduced in (*r.m.s*). Furthermore, the positive sequence voltage remains the same while the negative sequence voltage is reduced. This is very important to control the three-phase grid-connected inverter so that it can function properly. In addition, in practice, unbalanced voltage sags have the most significant impact in terms of amplified current harmonics, showing a ripple within output power, thus leading to the reductions in power quality.

2.3.2 Voltage Swell

A voltage swell is an increase in one or more phases of the voltage waveform in (*r.m.s*) for a duration ranging from 0.5 cycles to 1 minute according to the IEEE 1159/95 standard [77]. However, voltage swells are not as familiar as voltage sags and are a less frequent type of abnormal grid conditions. Voltage swells can be caused many conditions such as a single line

to ground faults or when switching in large capacitor banks, or when large loads are switched off [80].

2.4 Methods of Decomposition of Positive and Negative Sequence Components

In the studies described above for power quality, the three-phase grid-connected inverter was tested under normal grid conditions. Notwithstanding how the control introduces good performance during normal operation, some important issues regarding the operation of the three-phase inverter during unbalanced grid conditions have been pointed out. Abnormal grid conditions can be divided into two main sections. The first section demonstrates balanced fault when the drop or rise of all three-phase voltage representing the same amplitude. The second section demonstrates unbalanced fault where the voltage amplitudes are unequal or any changes of phase shift between the phases due to voltage in one or more phase dropping or rising suddenly. Under abnormal grid conditions such as voltage sags or voltage swells, the current injected into the grid loses its sinusoidal and balanced presence.

When unbalanced conditions occur, negative sequence components should appear in the grid as well as the positive sequence, which is creating a more challenging control system. As a result, the power inverter needs to change the amplitude or the phase angle of the injected current in order to ride through the fault during unbalanced voltage conditions. In this case, the negative sequence component is used to overcome the effect of the fault in the injected current. Hence, a method of the decomposing the voltage and current into its positive and negative sequence components is necessary.

A positive voltage sequence is defined as consisting of the balanced three-phase voltage which is equivalent in magnitude and phase, transferred by 120 degrees rotation at the system frequency with a phase sequence of normally *a, b, c*. However, the adverse (negative) sequence set is also well-adjusted with three equal magnitude quantities at 120 degrees phase shift separately with the phase rotation of counter-clockwise or reversed phase sequence *a, c, b* [29]. Figure 2.2 shows the positive and the negative sequence components.

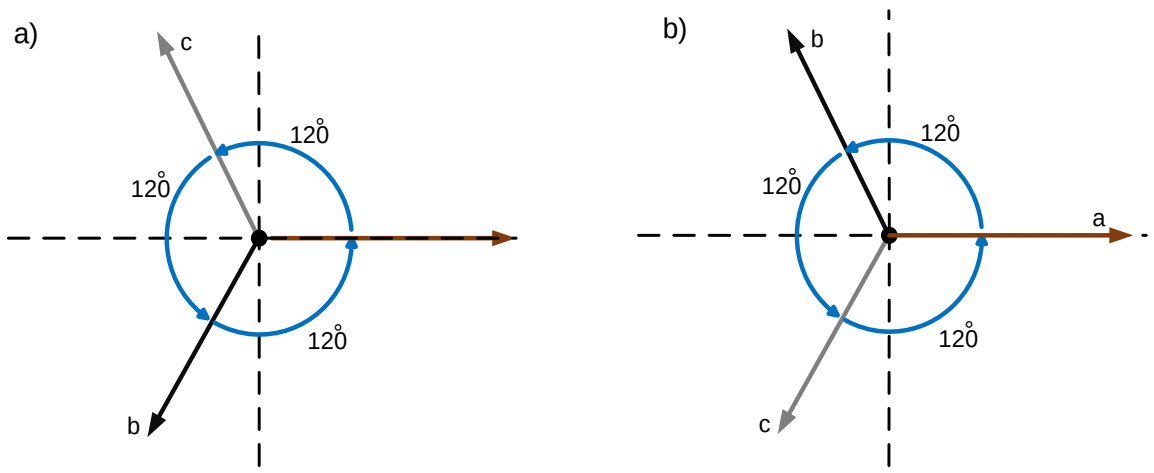

Figure 2.2 a) Positive sequence components, b) Negative sequence components

The detection of the positive and negative voltage sequences is vital for the control of the system in abnormal grid conditions. Many control techniques have been tested in the literature such as control of positive and negative sequence active power [71],[79], positive and negative sequence reactive power,[81],[82] positive and negative active and reactive power [83]. Such techniques are used in order to minimize DC bus voltage oscillations, total harmonic distortion, peak current, and voltage. These techniques can be applied in applications such as interfaced voltage source converters using active-reactive methods to improve the power system. However, the implementation of these approaches allows the injection of unbalanced currents into the grid network. Series active filters inject negative sequence voltage and parallel filters compensate power factor of nonlinear load [84, 85]. An alternative method uses a shunt active filter to inject negative sequence current [86, 87]. A unified power quality conditioner (UPQC) that is a modification of the conventional series-parallel structure has also been presented in [88]. Static synchronous compensators (STATCOM) have also been proposed which adapt positive and negative reactive power have been presented. However, there are some limitations of injected reactive power practically due to economic cost [89],[90],[91].

Several techniques have been used to compensate for the abnormal operation of the grid. The method of the decomposition of symmetrical components is used in order to simplify the analysis of unbalanced three-phase grid-connected inverters in both normal and abnormal conditions. Under unbalanced operation conditions, the dynamic behaviour of the grid synchronization method based on the conventional synchronous reference frame PLL becomes very poor and the technique does not perform well. As a result, there will be oscillations at double the fundamental frequency. Therefore, this approach is then not able to deal with this distortion. Therefore, the oscillations and the distortion in the system will increase. In order to

avoid issues regarding the lack of balance, a few advanced PLLs are applied. In the literature, there are different advanced grid synchronization approaches based on the most common decomposition categories such as synchronous reference frame and stationary reference frame [92], [93], [94].

To deal with these abnormal conditions, an appropriate technique is needed with a specific strategy that requires the designer to calculate the current that should be injected into the grid by the grid-connected inverter. However, the implementation of the above approaches allows the introduction of unbalanced currents within the network. Consequently, specific current control structures that are able to properly regulate the positive-sequence and negative-sequence components, are necessary in order to obtain satisfactory results.

2.4.1 Decouple Double Synchronous Reference Frame PLL

Synchronous reference frame (SRF) techniques based on the phase locked loop (PLL) is usually used in normal grid condition [95],[96]. In this type of method, the three-phase voltage is converted from the *abc* reference frame to the synchronous reference frame *dq*. Nevertheless, this method cannot be used when unbalanced condition occurs in the system or when there is a disturbance in the network due to oscillatory errors arising from the negative sequence voltage, so, the identifiable dynamic behavior will be seen to become progressively worse. In order to alleviate this concern, the double synchronous reference frame phase locked loop (DSRF-PLL) has been used [13],[97].

The DSRF-PLL is depended on two synchronous reference frames one for the positive sequence components and another for the negative voltage sequence components. This method can obtain the amplitude and the phase angle θ under unbalanced grid conditions into two *dq* components. However, this technique gives rise to the oscillation at double the fundamental frequency that is injected by positive and negative sequence current to the grid. In order to cancel out the oscillation term, the decoupled double synchronous reference frame phase locked loop (DD-SRF-PLL) is used [98].

Figure 2.3 shows the decoupled double synchronous reference frame PLL. In this technique, a cross-decoupling term is added to the double synchronous reference frame. While the DD-SRF technique shows good performance, the implementation of it is quite complex and the dynamic response is slow [99]. Overall, this method produces an extra delay in the PLL [100]. Other

methods of a three-phase system based on a voltage zero-crossing detector have been proposed [101]. However, the dynamic response is sensitive to any change in the phase angle due to any fault occurring in the impedance of the grid, which is a serious issue [102].

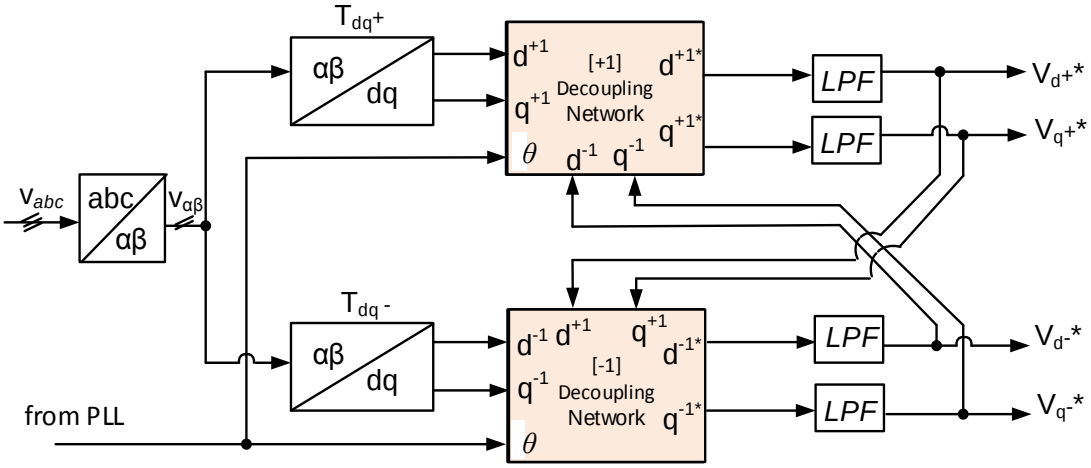

Figure 2.3 The decoupled double synchronous reference frame PLL

2.4.2 Delayed Signal Cancellation

In recent years, the method of delayed signal cancellation (DSC) has been exploited to divide the positive and negative sequence components from the grid voltage in the stationary reference frame [93], [94]. Figure 2.4 shows the delayed signal cancellation scheme. In this method, the *abc* reference frame is converted to the *αβ* stationary reference frame using Clarke's transformation and the negative sequence can be found by subtracting or adding the present real-time signal with the delayed signal for $T/_4$ [103].

The DSC has several advantages, such as being easy to implement and the ability to eliminate underside harmonics from the fundamental component [93],[94]. In addition, it can improve the sequence detection in the transient operation of the system as well as being able to control the time delay of the synchronous frame magnitudes. In this method, the oscillatory error can be eliminated by combined the original *αβ* components with their quarter-cycled delayed $T/_4$. However, the system dynamic still impacts from this method due to the complexity of the control and multiple digital signal processing, which affect the execution time of the algorithm [104],[105].

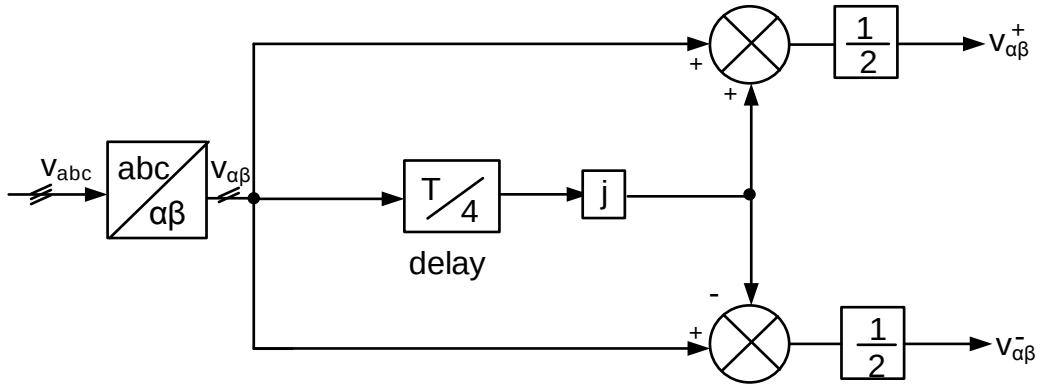

Figure 2.4 Delayed signal cancellation method

Additionally, it is possible to use a delay buffer in order to create a delayed signal for $^{T}/_{4}$, as the principle of deferral signal revocation can be enriched using a method with a low-pass filter based on a second-order generalized integrator. This method has been applied by using two filters to create a 90° phase shift delay at the fundamental frequency of the negative voltage sequence [106],[107], [108]. In [106], A bandpass filter and low-pass filter have been proposed in the stationary reference frame based on a second-order generalized integrator (SOGI).

Despite their successful implementation, however, the cascaded delay of the different filters can be an issue. In [107], the compensation system was proposed by decomposing the voltage into the positive and the negative sequence components and then applied the concept of estimated the virtual flux separately. In this thesis, due to the better solution, the concept of decomposing the positive sequence and negative sequence has been chosen from [107], then two PLL are proposed, one for positive sequence and the other one for negative sequence components.

2.5 Control of Three Phase Inverter under Abnormal Conditions

Under unbalanced conditions, the most important things are that the current controller is capable of providing a high-quality waveform within a shorter transient response. Once an unbalanced condition occurs in the grid, the current controller must inject the desired positive and negative sequence currents to the grid. During the past few years, several interesting methods have been proposed to deal with abnormal conditions using various techniques. The most popular are voltage oriental control (VOC) which is based on the synchronous reference frame and the stationary reference frame. Other control schemes such as the direct power control method, predictive control, and hysteresis current control have also been proposed.

A vector control approach was proposed for the first time for a grid rectifier under abnormal grid conditions to derive positive and negative current sequences in 1996 by Rioual *et al.*[109]. In this work, only a PI current controller was implemented in the synchronous reference frame to control the positive sequence in case of abnormal grid conditions in order to track positive and negative sequence components. Nevertheless, one of the main drawbacks of this type of the control is that the negative sequence voltage during unbalance conditions cannot work properly with this control due to the limitation of the bandwidth. Therefore, in 1999, a combination of two sequence components with the DC link voltage controller in the *dq* synchronous reference frame has been proposed [110]. The proposed method has a dual current control scheme for the positive and negative sequence currents. The technique is able to reduce the steady state error compared with single current control. However, this method is used when operating the grid-connected inverter only in steady-state conditions and it cannot be applied under unbalanced supply conditions due to limitations in the dynamics of the system.

In another subsequent method, one PI controller was used with resonant (*R*) instead of dual current controllers allowing a rectifier to generate a dc output under unbalanced grid conditions at double frequency [111]. However, eliminating a steady state error at twice of the fundamental frequency was one of the main critical issues.

In addition, vector control technique has been used in a distributed generation (DG) inverters under abnormal grid operation conditions [112]. Optimum power quality characteristics were achieved, under unbalanced grid voltages. This research focused on many important aspects, such as DC voltage optimization and maximum power exchange, and also a combination of the different methods called a hybrid strategy was described.

Control of the three-phase grid-connected inverter during unbalanced grid conditions using direct power control based on instantaneous active and reactive power has also been proposed. Other research proposed a new concept for selecting active power quality characteristics based on a fast current controller and a rearrange reference current during unsymmetrical voltage [113]. Similar research has proposed reactive power control based on symmetrical component [114]. Another study finding a higher smoothing active and reactive power characteristics using a method previously for selecting active power quality characteristics [115].

On the other hand, vector control method during unbalanced gird condition needs double reference synchronization frames for the positive and negative sequences transformation modules for voltage and current. However, PI controller has some drawbacks such as:

- Four PI controllers should be implemented for the positive and negative sequences based on the double synchronous reference frame which will increase the complexity and computational load
- In the PI controller, grid synchronization can be achieved with two PLLs using one for the positive sequence components of the voltage and another one of the negative voltage sequence.

As an alternative method to PI current control based on the double synchronous reference frame, proportional-resonant controllers can extend the operation on stationary reference α-β rotating frame to control the current injected by the grid-connected power converter under abnormal grid conditions [116]. In this control scheme, the output currents are converted to the stationary reference frames that results in two AC current signals to be controlled [112, 117]. This type of control is based on frequency adaptive filters. These filters give the same performance for both positive and negative frequencies [62], [118]. In addition, the multiple *d*-*q* rotations become unnecessary.

It can be said that there are many advantages of using PR controller including:

- We do not require additional controllers for the positive and negative sequence currents. Synchronization can be achieved with one PLL using the positive sequence component of the voltage.
- Only one PR controller can regulate positive and negative sequences ($+\omega$ and $-\omega$)
- Only the positive sequence angle needs to be synchronized.

Based on current control approaches, the current injected into the grid by the three-phase inverter should follow different strategies in unbalance grid conditions at the point of common coupling (PCC). In the literature, different control approaches are used to meet the requirement of control under abnormal conditions and to enhance the system's response [79]. The first approach is instantaneous unity power factor control (IUPFC). This method of control is essential to be used if the injected current vector is required to follow the voltage vector. A second approach is average unity power factor control (AUPFC). In this strategy, the harmonics can be reduced, resulting in a lower THD.

A further method is instantaneous active reactive control (IARC). This method is more useful in control active and reactive power based on p-q theory. In this type of method, both active and reactive power is controlled instantaneously since the current vector is aligned with voltage vector as well as any orthogonal components. However, the voltage vector has oscillations at twice the fundamental grid frequency that increases the harmonics into the grid [29].

To overcome these drawbacks another strategy has been proposed, called the positive and negative sequence control (PNSC). This strategy can deal with the current control under unbalanced conditions. Here, both positive and negative sequence current control is applied in the system. This method can be used in the synchronous reference frame using dual PI controllers. However, one of the issues can be that when the reactive power not considered, the oscillation term of q will not appear.

In the balance positive sequence control (BPSC) method a balanced sinusoidal waveform is injected by applying positive sequence control to the grid during unbalanced conditions. There are many advantages of this strategy, such as improving the power quality of the system by allowing the current waveform to be symmetrical during unbalanced conditions. In addition, it is a simple method since only the positive sequence angle needs to be synchronized. This method can be easily applied to stationary reference frame using PR controller while needs double synchronous reference frame using dual PI controllers. This method is the only one can obtain the balanced current among other strategies [29].

2.6 Advanced Intelligent Optimization Methods

Beside conventional control techniques, many intelligent advanced control methods have been successfully applied. One of these control advanced methods is based on a self-commissioning tuning process using advanced optimization algorithms which tune the parameters of the controllers to manage different normal and abnormal conditions and the transitions among them. PI and PR controllers have been widely used for speed and position control in many various applications.

Conventionally, the tuning of these controllers may be accomplished with the most method using a trial-and-error principle. In addition, tuning can also be achieved using many algorithmic methods, including Ziegler-Nichols, root locus, and pole placement techniques. The controller parameters can be tuned in a similar way based on the root locus of the system [119]. The Ziegler-Nichols method is the most well-known, but it might not provide good tuning and tends to produce an overshoot. Moreover, it takes more time to achieve control and

reduces the stability of the system. Not only that, but the operator is required to be very familiar with the characteristics and parameters of the system. In addition, such techniques can take significant time to achieve an optimum solution [120].

For this reason and to enhance the robustness and increase the performance of the traditional parameter-tuning techniques, artificial intelligent optimization (AIO) methods are used, such as artificial neural networks (ANN), fuzzy logic (FL), genetic algorithms (GA) and particle swarm optimization (PSO). Such approaches can be necessary to regulate the parameters of the controller and improve the performance [121, 122]. AIO has been used in many applications such as the drive application, machine design, and fault detection. PSO is one of the most widely used methods in advanced optimization control due to an effective and powerful technique for solving a problem.

Compared to GA and ANN, PSO can operate much more easily and faster to optimize, making it well suited for real-time control applications which experience time-varying disturbances. Moreover, it is a stable optimization method that is relatively easy to implement, because there are few parameters to adjust and it does not impose a significant computational burden to the microcontroller [123, 124]. Unlike GA, PSO has no complicated evolution operatives such as crossover and mutation [125].

PSO algorithm is a stochastic search technique that uses a population or swarm of individual elements which are called particles. Each particle shows independent achievement solution to a problem and adjusts its own flying experience in the boundary space. In order to determine the optimal solution of an objective function, each particle has two main variables which represent a group of parameters to identify the current position $\vec{X}_i(t)$ and current velocity $\vec{V}_i(t)$. The best previous position is shown the best minimum fitness value of any particle in the neighbourhood which is recorded and represented as new $\vec{X} = x_1, x_2, x_3, \dots, x_i$ and this is called Personal Best P_{best}. The index of the best particle among all particles in the population group called Global Best G_{best} and to be encountered by the i^{th} particle is a point in domain space (S).

PSO can be designed based on three main stages:

I. Assessing the fitness value of each particle.
II. Updating local and global best fitness and positions.
III. Every particle can update its own velocity and position.

Several studies have used PSO in different areas. In 1995, PSO was proposed by James Kennedy and Russell C. Eberhart as a stochastic algorithm based on deterministic points of natural selection [126]. They proposed an algorithm which is based on intelligent methods that simulate the social behaviour of the domains posed in animals and plants, such as bird flocking and swarm theory [126]. They observed that every particle is a part of the neighbourhood particles that indicate the best particle. However, the performance still in it is early stages and needs more improvement. Shi and Eberhart added a new parameter called inertia in order to improve the performance of particle swarm optimization [127]. Another study investigated in detail the PSO algorithm [128], and It was proven that each particle of the PSO represents a potential solution to a problem and adjusts its own "flying experience" in a defined boundary space. Later, several applications have used PSO, such as to optimize the geometry of an antenna [129],[130]. Recently, this technique has been successfully applied in power electronics applications [131], [132], including the maximum MPPT of photovoltaic systems [133], micro-grid voltage source inverters [134] and the PI controller grid-connected inverter with LC filter [132].

The PSO algorithm is employed for self-tuning parameters where an optimum solution is determined by using the integral time absolute error (ITAE) as a cost function. The most commonly utilized cost functions are integral-based such as the ITAE, the integral of squared error (ISE) and integral of time multiplied by squared error (ITSE) [135], [136]. In the current research, the ITAE is used:

$$ITEA = \int_0^\infty t|e(t)|dt \tag{2.8}$$

Where *e(t)* is the difference between the reference and actual values. The cost function is minimised using the current control method such as PI and PR controllers throughout the optimisation process. A block diagram of the optimization process is shown in Figure 2.5.

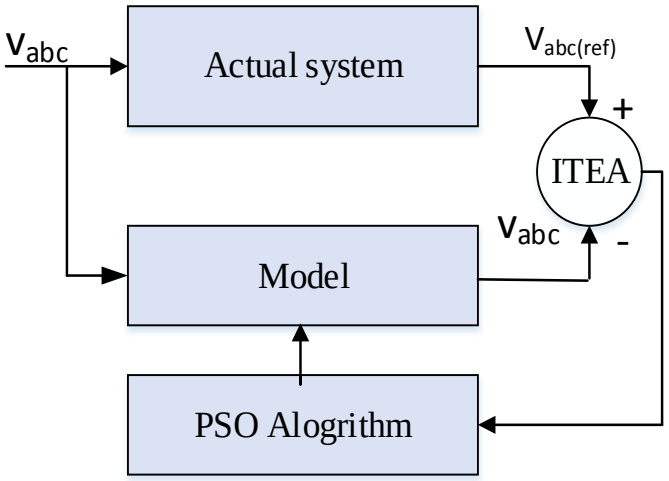

Figure 2.5 General structure of the PSO optimization algorithm

On the other hand, the principle of the advanced optimization method has been used to determine and find the optimal parameters of the grid filter. The undesired values of the chosen by the traditional calculation of LCL filter could cause instability of the system. Therefore, PSO can enhance the dynamic performance of the LCL filter by determining the optimal values of the filter parameters. The optimal value of the capacitor C of the filter will improve the stability and the dynamic response of the filter.

2.7 Chapter Summary

This chapter has presented in the main review of the three-phase grid-connected inverter, common current control techniques, a comparison of these techniques. Moreover, a power quality issues in the grid-connected applications in abnormal conditions such as voltage sags and swell have been discussed, followed by methods of decompensation have been presented in order to deal with unbalanced grid conditions as well as proposed current control technique. In addition, advanced optimization techniques to obtain the optimal values of the control parameters along are also demonstrated.

Chapter 3. Working Principle of a Three-phase Grid-connected Inverter

3.1 Introduction

This chapter presents the working principle of a three-phase grid-connected inverter. Generally, a three-phase grid-connected inverter is used to interface photovoltaic (PV) panels, transforming DC voltage into the appropriate AC voltage for the utility grid. There are two main means of connecting PV panels to the utility grid. The first method is a single-stage or centralized type, whereby the PV panels are connected in series or parallel to achieve certain voltage and current levels due to the low input voltage provided by the PV system. The output of the inverter is then connected via a filter, as shown in Figure 3.1(a). This type of application can be used for sizes over 50–100 kW. In contrast, using the second method, the double-stage conversion system avoids the use of bulky low-frequency transformer components, which can cause low efficiency, as shown in Figure 3.1(b). It can be seen from the figure that the model comprises two stages. The first stage is a DC-DC converter, which can be used in this application to boost the voltage to the higher desired values with maximum power point tracking (MPPT) to work at the highest efficiency point and acceptable level of different kinds of inverters. The second stage converts the DC value to the three-phase AC values via a three-phase inverter.

The single-stage inverter method is usually preferred as it is more efficient economically in cases of homogeneous irradiance conditions [20], [21]. The three-phase output current of the inverter is connected to an LCL filter to reduce the harmonics injected into the utility grid.

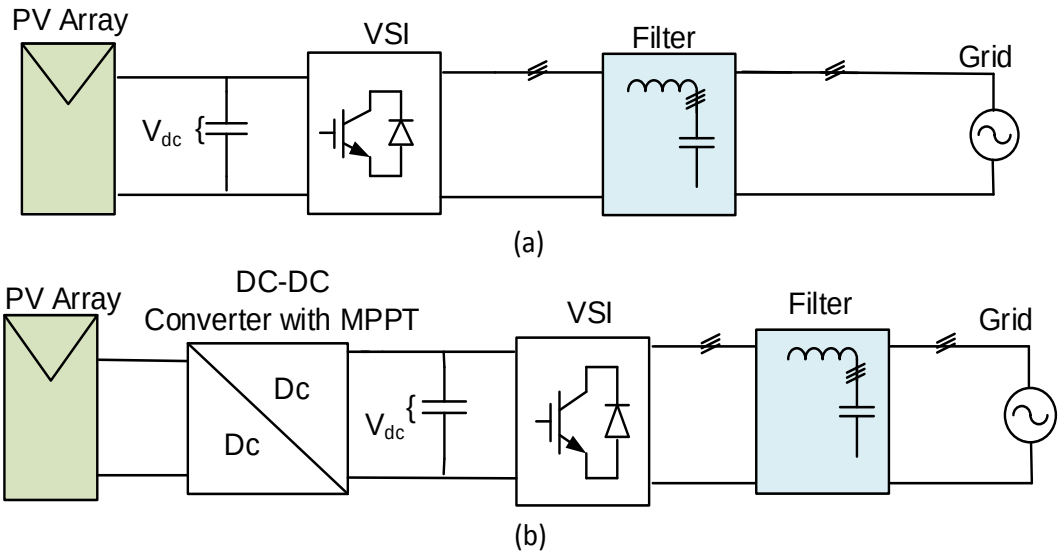

Figure 3.1 Single line diagrams of three-phase grid-connected inverter: (a) single stage, (b) double stage

3.2 PV Module

A PV cell is a source and the core of the power conversion system. The PV cell is employed to convert light energy into electrical energy. Either several cells are connected in series to produce more voltage or several cells are connected in parallel to increase the current. The simple theory of the PV cell came from the simple P-N junction semiconductor. The ideal PV cell circuit model contains an ideal current source in parallel with an ideal diode. Thus, the diode determines the equivalent circuit I-V characteristics of the solar cell as shown in Figure 3.2, where I_{ph} is the PV current source, which is based on the solar irradiance and ambient temperature, and I_j is the shunt current through the diode.

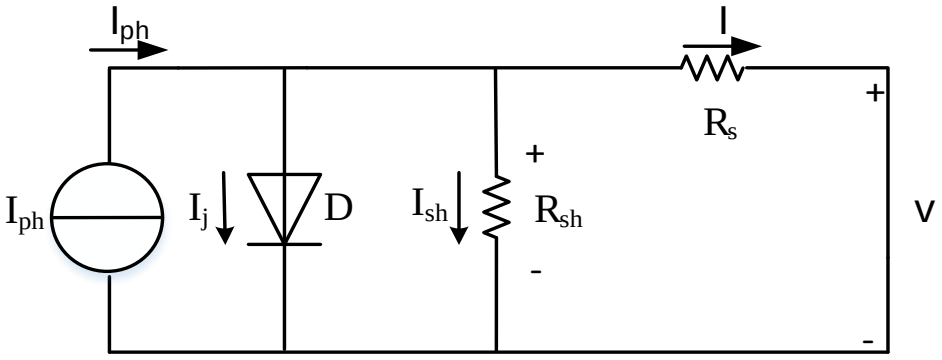

Figure 3.2 Equivalent circuit I-V characteristics of the solar module

According to Kirchhoff's current law, the output current is given by [137]:

$$I = I_{ph} - I_j - \frac{V}{R_{sh}} \tag{3.1}$$

where I_{ph} is the photon current and I_j is the diode current and D is the parallel diode. R_{sh} is the shunt resistance and R_s is the series resistance. The current-voltage relationship of the PV cell is given by the I-V equation:

$$I = I_{ph} - I_o \left\{ \exp\left(\frac{q.V}{AKT}\right) - 1 \right\} - I_{sh} \tag{3.2}$$

where I_o is the reverse saturation current of the diode. I_{sh} is the shunt current, q is the electron charge $q = 1.6 * 10^{-19}\, C$, A is the current fitting factor, K is Boltzmann's constant $A = 1.381 * 10^{-23}\, J/K$and T is the junction temperature (K). R_s is normally very small resistance while R_{sh} is very. To simplify, the equation (3.2) R_{sh} can be neglected and the equation will be:

$$I = I_{ph} - I_o \left\{ \exp\left(\frac{q.V}{AKT}\right) - 1 \right\} \tag{3.3}$$

where I_{ph} is the photon current and I_o is the reverse saturation current of the diode.

In normal operating conditions, the standard test condition for irradiance is $1000\ W/m^2$and for the temperature is $T = 25^{\circ}\mathrm{C}$. Figure 3.3 and Figure 3.4 show the (I-V) and (P-V) characteristics of the PV panels respectively. It can be seen from the figures that the current is directly proportional to the solar irradiance. The characteristics of the PV panels between (I-V) and (P-V) are non-linear. Therefore, an MPPT algorithm is essential. Due to its simplicity, the MPPT technique most widely used is the perturb and observe (P&O) method [19]. The output voltage is the reference DC, either to the DC-AC inverter in the single-stage method or to the DC-DC inverter in the dual-stage method.

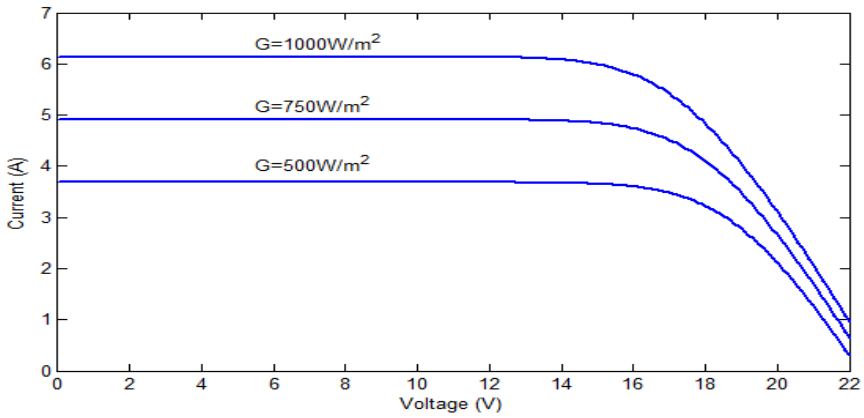

Figure 3.3 I-V characteristic plot of the PV module

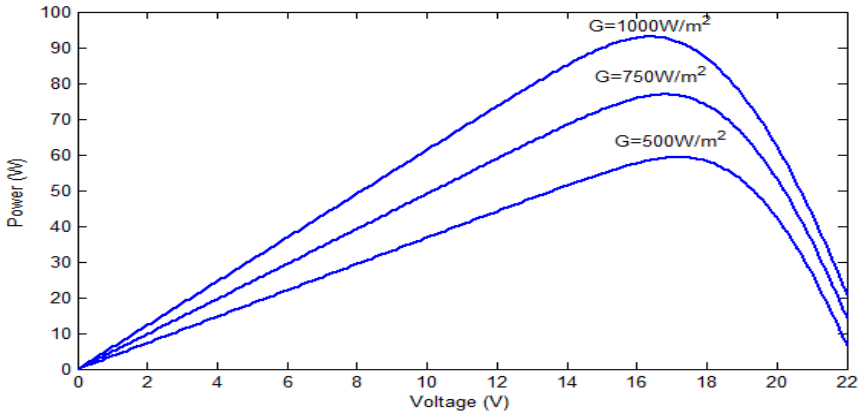

Figure 3.4 P-V characteristic plot of the PV module

3.3 Working Principle of the Three-Phase Inverter

The most important part of the connection between the source PV system and the utility grid is the inverter. The three-phase inverter is classified as a power electronic-based scheme. The main idea of the three-phase inverter is to convert the DC voltage to a three-phase balanced AC voltage. Figure 3.5 shows the three-phase inverter scheme. This consists of six switches (transistors) and six freewheeling diodes (S1, S2, S3, S4, S5, and S6). In industry, there are many different switching transistors, such as the insulated-gate bipolar transistor (IGBT), the metal-oxide-semiconductor-field-effect-transistor (MOSFET) and the bipolar junction transistor (BJT). Each kind of switch has its own characteristics based on operating power level, switching frequency requirements, and acceptable power losses. In the three-phase inverter, every leg has two switches complementary to each other which cannot be switched ON or OFF at the same time [26].

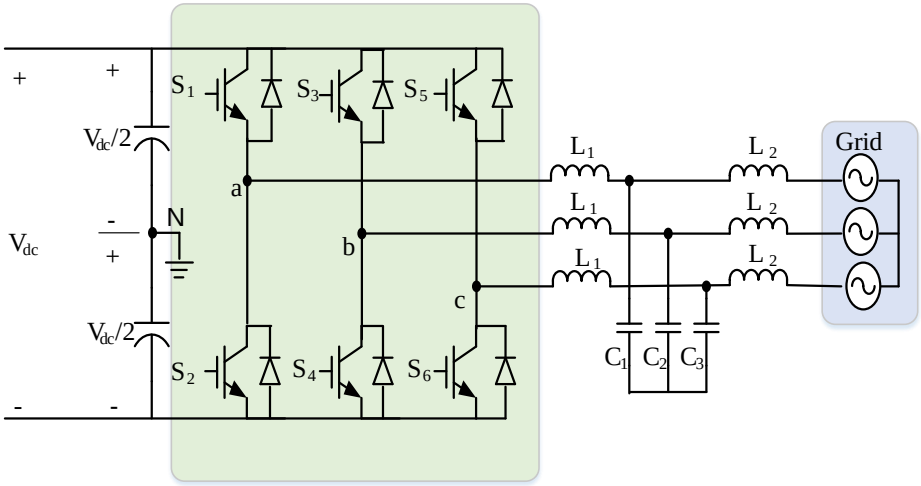

Figure 3.5 The three-phase inverter

The three-phase inverter is operated in switch mode, in which it is necessary to switch ON and OFF at very accurate desired times. This can be accomplished by varying the duty cycles for ON/OFF employing pulse width modulation (PWM) switching techniques [138].

3.4 Pulse Width Modulation (PWM)

The three-phase inverter employs PWM to produce sinusoidal output voltage waveforms. There are different types of PWM switching technique, such as sinusoidal PWM, space vector modulation (SVM), hysteresis band PWM and third harmonic elimination PWM. Of these, the most common are carrier-based sinusoidal PWM and SVM, in which the carrier frequency is fixed. In contrast, in hysteresis band PWM, the switching frequency is variable with output waveform [139].

3.4.1 Sinusoidal Pulse Width Modulation (SPWM)

Sinusoidal PWM or carrier base modulation is one of the simplest PWM switching techniques and can easily be implemented both in analogue and digital model form [138]. The idea of this scheme is that the triangular carrier waveform is compared with a three-phase output reference signal as separate signals and thus gate pulse signals are generated, as shown in Figure 3.6. The operating principle of PWM is that it is limited by the modulation index (mi) [26]. The modulation index can be defined as the ratio of the amplitude of the reference signal to the carrier signal as in (3.4):

$$mi = \frac{V_r}{V_c} \tag{3.4}$$

where V_r is the reference amplitude and V_c is the carrier amplitude.

Note that the maximum modulation index is $mi_{max} = \frac{\sqrt{3}}{2} V_{dc}$. The modulation index will vary when the modulation signal V_r varies between 0 and 1 and the carrier signal remains constant. Over-modulation occurs when the peak of the modulation signal is greater than the peak of the carrier signal [140]. The three-phase sinusoidal waveforms (v_a, v_b, v_c) are displaced in the time domain by 120°:

$$v_a(t) = mi\, V_{dc} \cos(\omega t) \tag{3.5}$$

$$v_b(t) = mi\, V_{dc} \cos(\omega t + \frac{2\pi}{3}) \tag{3.6}$$

$$v_c(t) = mi\, V_{dc} \cos(\omega t - \frac{2\pi}{3}) \tag{3.7}$$

where $v_a(t), v_b(t)$ and $v_c(t)$ are the fundamental signals of the three-phase symmetrical sinusoidal signals and V_{dc} is the D.C voltage. Thus, the sum of the three balanced voltages should be zero:

$$v_a(t) + v_b(t) + v_c(t) = 0 \tag{3.8}$$

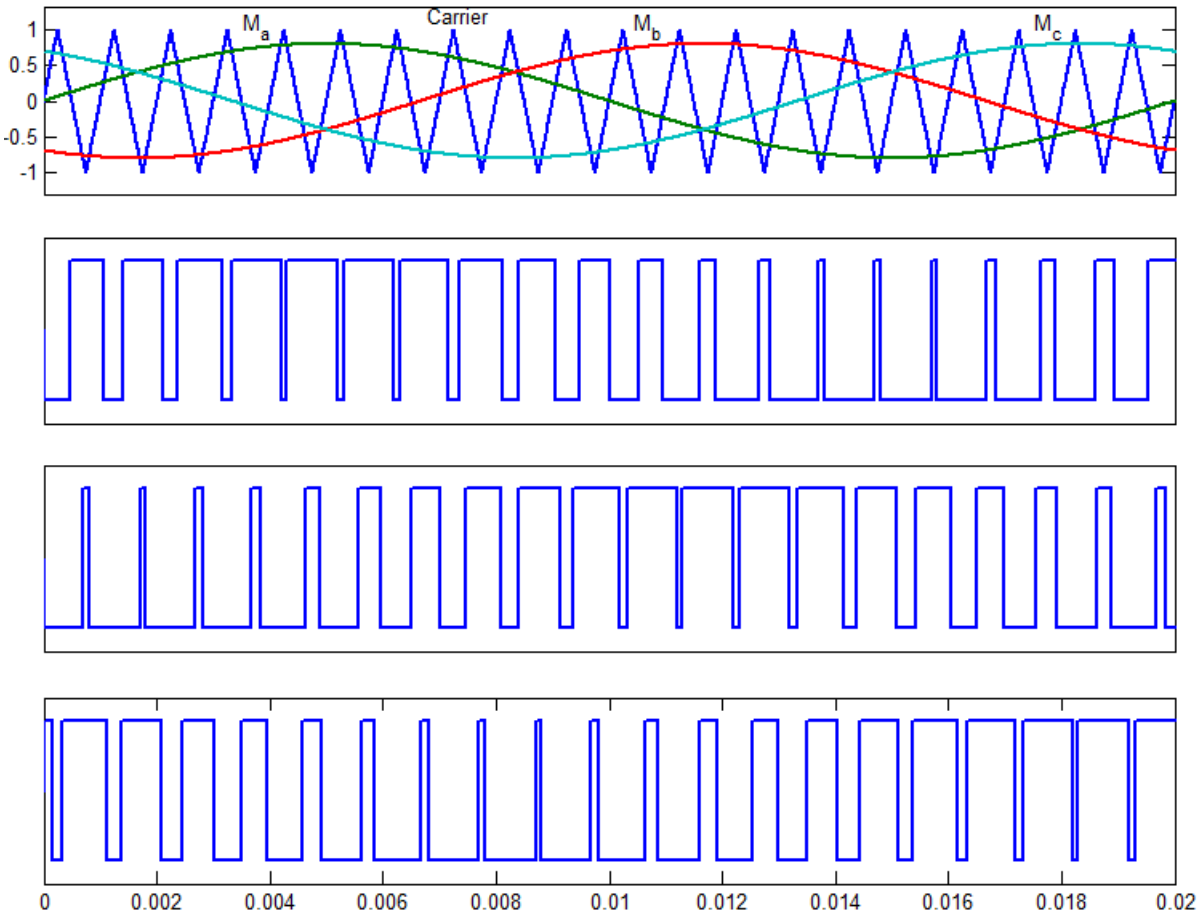

Figure 3.6 Sine-triangle modulation for the three-phase waveform with three switched waveform legs: a, b and c

However, one of the shortcomings of SPWM, total harmonic distortion (THD) is higher than space vector modulation (SVM).

3.4.2 Space Vector Modulation

Space vector modulation is a technique that has become popular in control systems and is widely applied in three-phase grid-connected inverters. SVM is considered the best PWM technique due to features such as its ability to provide 15% higher output voltage compared with sinusoidal PWM [141]. Other advantages are that the switching frequency is constant, there is increased DC link voltage utilization, the output harmonic spectrum is well defined and the switching patterns are ideal [142]. In addition, SVM has additional degrees of freedom in the hexagon compared with SPWM [141]. It can be argued that SVM is a more sophisticated modulation technique than others due to its many advantages, as shown in Table 3.1

Table 3.1 Comparison of SVM and SPWM modulation techniques

SVM	SPWM
Less total harmonic distortion	High total harmonic distortion
DC supply voltage increased by 15%	Unable to fully utilize DC supply voltage
Supports advanced vector control implementation	Does not support advanced vector control implementation
Facilitates free degrees of freedom throughout the entire hexagon	There are no degrees of freedom in implementation

SVM can be designed as a single unit. This unit has eight switching levels and each switching state describes the voltage space vector as a point in two-dimensional complex vector mapping in the $\alpha\beta$ plane. Figure 3.7 shows the vector's hexagonal shape in SVM. The shape is divided into six non-zero switching sectors from $U_1$to U_6, where U_0 and U_7 lie at the original point of the hexagon. The switching sector states of SVM use the combination of the switching states to approximate the reference vector. The position of the reference vector $\overline{U_S}$ can be determined by the angular position θ in the hexagon and can lie anywhere, as shown in Figure 3.7. There is angle phase displacement of 60° between the sectors with an equal magnitude of $2/3\,V_{dc}$.

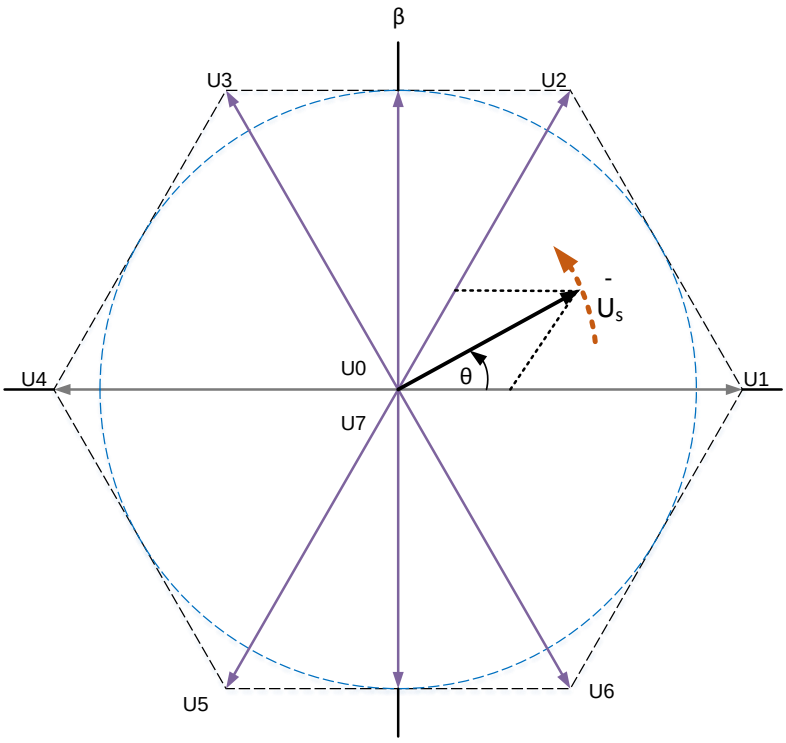

Figure 3.7 Space vector hexagon

In this technique, the three-phase reference voltages U_a, U_b, and U_c are converted to a complex two-phase orthogonal $\alpha - \beta$ plane using Clark's transformation, as shown in the following equations:

$$\overline{U_S} = 2/3\,[U_a + aU_b + a^2U_c] \tag{3.9}$$

where $\overline{U_S}$ is the reference voltage vector and $a = e^{j\,(\frac{2\pi}{3})}$ in exponential form and thus:

$$\overline{U_S} = \left|\overline{U_S}\right| \exp j\theta = U_\alpha + jU_\beta \tag{3.10}$$

The exponential form can easily be changed to $-(\frac{1}{2} + j\,\frac{\sqrt{3}}{2})$ in rectangular form:

$$U_\alpha = 2/3\left[U_a + U_b \cos\frac{2\pi}{3} + U_c \cos\frac{2\pi}{3}\right] \tag{3.11}$$

$$U_\beta = 2/3\left[U_b \sin\frac{2\pi}{3} + U_c \sin\frac{2\pi}{3}\right] \tag{3.12}$$

Equations (3.11) and (3.12) can be written in matrix form:

$$\overline{U_S} = \begin{bmatrix} U_\alpha \\ U_\beta \end{bmatrix} = \begin{bmatrix} 2/3 & -1/3 & -1/3 \\ 0 & 1/\sqrt{3} & -1/\sqrt{3} \end{bmatrix} \begin{bmatrix} U_a \\ U_b \\ U_c \end{bmatrix} \tag{3.13}$$

The phase voltage values corresponding to different switching states are given in Table 3.2. SVM can be classified depending on the voltage in each state.

Table 3.2 The phase voltage levels for different switching states

State	Switch On	V_a	V_b	V_c
U0	1, 3, 5	0	0	0
U1	1, 4, 6	$(2/3)V_{dc}$	$-(1/3)V_{dc}$	$-(1/3)V_{dc}$
U2	1, 3, 6	$(1/3)V_{dc}$	$(1/3)V_{dc}$	$-(2/3)V_{dc}$
U3	2, 3, 6	$-(1/3)V_{dc}$	$(2/3)V_{dc}$	$-(1/3)V_{dc}$
U4	2, 3, 5	$-(2/3)V_{dc}$	$(1/3)V_{dc}$	$(1/3)V_{dc}$
U5	2, 4, 5	$-(1/3)V_{dc}$	$-(1/3)V_{dc}$	$(2/3)V_{dc}$
U6	1, 4, 5	$(1/3)V_{dc}$	$-(2/3)V_{dc}$	$(1/3)V_{dc}$
U7	2, 4, 6	0	0	0

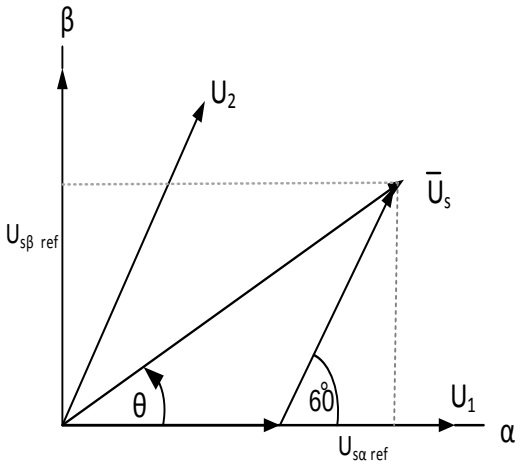

Figure 3.8 Reference voltage vector

In Figure 3.8 the reference voltage vector $\overline{U_s}$ has the components $U_{s\alpha\,ref}$ in the α domain and $U_{s\beta\,ref}$ in the β domain, which can adjust the state vectors U_1 and U_2. The reference voltage vector $\overline{U_S}$ can be calculated as:

$$\overline{U_S}\sin\theta = U_2\sin 60^o \tag{3.14}$$

$$U_2 = |\overline{U_S}|\frac{\sin\theta}{\sin 60^o} = \frac{2}{\sqrt{3}}|\overline{U_S}|\sin\theta \tag{3.15}$$

$$U_1 = |\overline{U_S}|\cos\theta - U_2\cos 60^o \tag{3.16}$$

$$U_1 = |\overline{U_S}|\cos\theta - \frac{2}{\sqrt{3}}|\overline{U_S}|\sin\theta\cos 60^o \tag{3.17}$$

$$U_1 = |\overline{U_S}|\ \frac{2}{\sqrt{3}}(\ \frac{\sqrt{3}}{2}\cos\theta - \sin\theta\cos 60^o) \tag{3.18}$$

$$U_1 = |\overline{U_S}|\ \frac{2}{\sqrt{3}}(\ sin60^o\cos\theta - \sin\theta\cos 60^o) \tag{3.19}$$

$$U_1 = \frac{2}{\sqrt{3}}|\overline{U_S}|\sin(60^\circ - \theta) \tag{3.20}$$

$$U_2 = \frac{2}{\sqrt{3}}|\overline{U_S}|\sin(\theta) \tag{3.21}$$

3.4.3 Hysteresis Band PWM Modulation

Hysteresis modulation has been used in some applications for three-phase inverters because of its ease of implementation and faster transient response than other methods [64]. The operating principle of the control system depends on the output of the three-phase current of the inverter compared with the reference phase current. Hence, the results of three-phase errors are used at the same time to feed the PWM through hysteresis comparators. The output pulse is controlled by a hysteresis current controller employing a switch status up and down counter. If the phase current exceeds the upper band, the upper switch is turned ON and the lower switch is turned OFF. On the other hand, if the phase current is below the lower limit, the lower switch will turn ON and the upper switch will turn OFF.

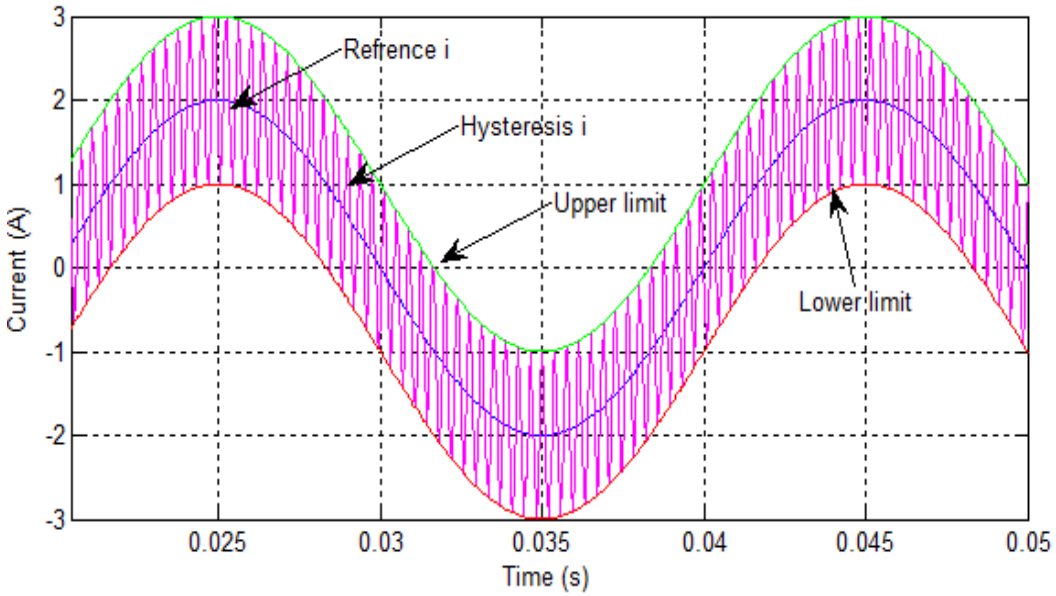

Figure 3.9 Hysteresis band PWM control

The hysteresis adaption mechanism for this scheme can be described as:

$$i_u = i_m(t) + \Delta i \tag{3.22}$$

$$i_l = i_m(t) - \Delta i \tag{3.23}$$

where i_u is the upper band, i_l is the lower band and i_m is the reference current for the phases a, b, and c. Δv is the hysteresis band limit during the switching period.

However, there are several drawbacks to hysteresis current control. One of these drawbacks is that the hysteresis bandwidth can cause losses between the phases and can produce high switching frequency and high current ripple.

3.4.4 Third-harmonic injection PWM

Third-harmonic injection PWM has been used to improve the SPWM technique by adding a third harmonic to the modulation signal. It follows the same SPWM implementation. The difference between third-harmonic and sinusoidal PWM is that the reference of the third harmonic not sinusoidal but includes third harmonic components as shown in Figure 3.10. The third harmonic injection can be injected with a ratio of 25% of the fundamental. This will increase the amplitude of the DC supply by 15% more than sinusoidal PWM [26]. The reference

signal is composed of the fundamental and the third harmonic and can be obtained from the following equation:

$$f(\omega t) = \frac{2}{\sqrt{3}}\sin(\omega t) + \frac{1}{3\sqrt{3}}\sin(3\omega t) \tag{3.24}$$

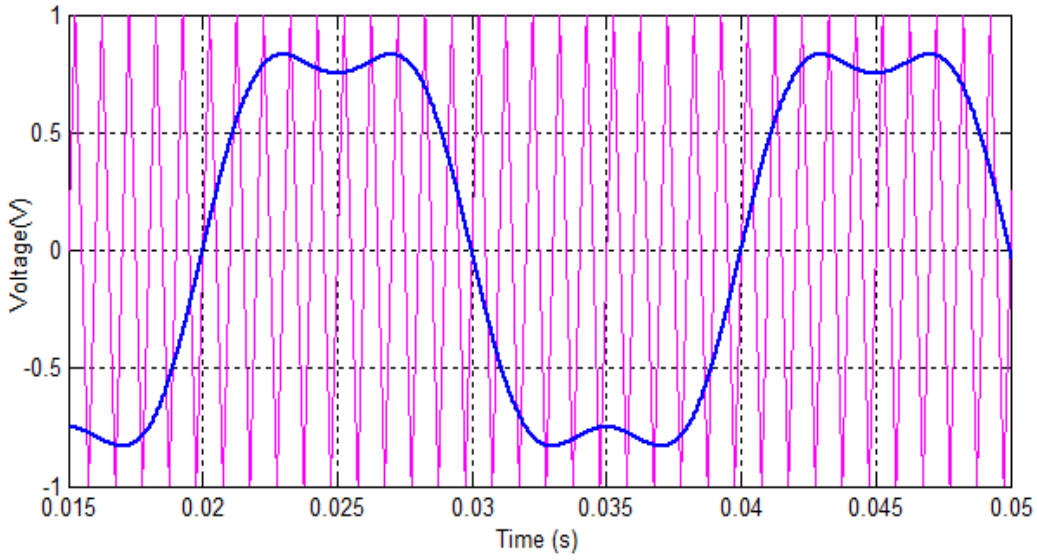

Figure 3.10 Third-harmonic injection waveform with carrier waveform

3.5 Passive Component Design

In grid-connected applications, a wide range of harmonics and noise have been found to affect the switching frequency. For this reason, filter design is an essential part of eliminating the noise and high-frequency harmonics. The traditional simple L-filter is a typical filter used to connect three-phase inverters to the grid due to its ease of use. One of the features of the L-filter is that resonant frequency can be avoided as the utility grid is mostly inductive. However, the drawbacks of this filter are its very high cost and anexcessive voltage drop across the inductor, hindering its use. In contrast, the use of other higher order filters, such as LCL filters, has been shown to improve the power quality of the current injected into the grid and provide better attenuation of harmonic currents, therefore leading to reduced filter sizes compared with lower order L and LC filters [14].

In this thesis, the LCL filter was chosen. The differential equation representing the LCL filter can be obtained from the per-phase equivalent circuit, as shown in Figure 3.11. The filter is

defined by the inverter-side inductor L_1 and the filter capacitor C_1. L_2 is the grid-side inductor and R_1 and R_2 are the resistive load.

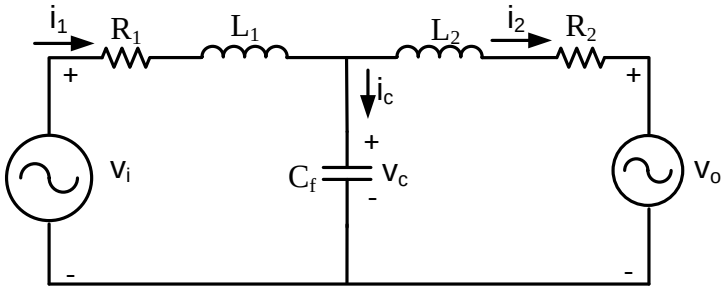

Figure 3.11 Single-phase equivalent circuit LCL filter

The LCL filter can be designed and analysed in different configuration schemes. The simple model represents LCL parameters including the ohmic losses in the passive components.

$$V_i - V_c = \frac{di}{dt}L_1 + R_1 i_1 \tag{3.23}$$

$$V_c - V_o = \frac{di}{dt}L_2 + R_2 i_2 \tag{3.24}$$

$$V_c = \frac{1}{C_f}\int i_C \, dt \tag{3.25}$$

The previous equations can be written in the state space model in the (S) domain using a wye-connected model as follows: Note: assume initial conditions are all 0.

$$V_i(s) - V_c(s) = s\, I_1 L_1(s) + R_1 I_1(s) \tag{3.26}$$

$$V_c(s) - V_o(s) = s\, I_2 L_2(s) + R_2 I_2\,(s) \tag{3.27}$$

$$V_c(s) = \frac{1}{SC_f} I_C(s) \tag{3.28}$$

Therefore, transfer functions can be obtained from Equations (3.26), (3.27) and (3.28) respectively:

$$\frac{I_1(s)}{V_i(s) - V_C(s)} = \frac{1}{R_1 + sL_1} \tag{3.29}$$

$$\frac{V_C(s)}{I_s(s)} = \frac{1}{sC} \tag{3.30}$$

$$\frac{I_2(s)}{V_C(s) - V_O(s)} = \frac{1}{R_2 + sL_2} \tag{3.31}$$

Here, the series resistors R_1 and R_2 are ignored due to their small size for the sake of simplicity. The transfer function of the LCL filter is given by:

$$I_1(s)\left[sL_1 + \frac{sL_2\left(\frac{1}{sC_f}\right)}{sL_2 + \left(\frac{1}{sC_f}\right)}\right] = V_i(s) \tag{3.32}$$

$$I_1(s)\left[sL_1 + \frac{L_2/C_f}{s^2L_2C_f + 1/s\,C_f}\right] = V_i(s) \tag{3.33}$$

$$\frac{I_1(s)}{V_i(s)} = \frac{1}{sL_1 + (\frac{L_2/C_f}{sL_2 + 1/sC_f})} \tag{3.34}$$

$$I_2(s) = I_1(s) \cdot \frac{1/sC_f}{sL_2 + 1/sC_f} \tag{3.35}$$

$$\frac{I_2(s)}{I_1(s)} = \frac{1/sC_f}{sL_2 + 1/sC_f} \tag{3.36}$$

$$G(s) = \frac{I_1(s)}{V_i(s)} \cdot \frac{I_2(s)}{I_1(s)}$$

$$G(s) = \frac{1}{sL_1 + (\frac{L_2/C_f}{sL_2 + 1/sC_f})} \cdot \frac{1/sC_f}{(sL_2 + 1/sC_f\,)} \tag{3.37}$$

$$G(s) = \frac{1/L_1L_2C_f}{s\left(s^2 + \frac{L_1+L_2}{L_1L_2C_f}\right)} \tag{3.38}$$

To make the transfer function of Equation (3.38) simpler, it can be written as:

$$\frac{I_2(s)}{V_i(s)} = \frac{1}{\left(s^3 C_f L_1 L_2\right) + s(L_1 + L_2)} \tag{3.39}$$

Thus, $I_2(s)$ is the output current and $V_i(s)$ is the input voltage of the inverter in the s-domain.

The behaviour of the LCL filter can be obtained from the Bode plot response of the system. Figure 3.12 illustrates the Bode plot of the un-damped filter. The gain margin is obtained at cut-off frequency. The LCL filter can achieve high performance at high frequency with an attenuation rate of -60 dB/dec.

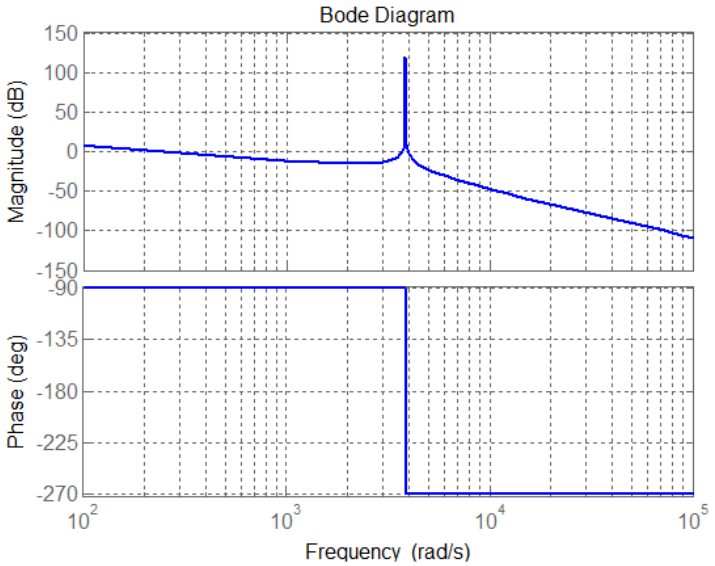

Figure 3.12 LCL filter Bode diagram

In spite of these advantages of the LCL filter, it has a resonance peak at the resonance frequency from the inverter or from the grid as can be seen in Figure 3.12. To overcome this issue, passive or active damping is used to enhance the impedance response. Commonly, a resistor is added in series with the filter capacitor or in parallel with the grid-side inductor to dampen the high frequency in the filter.

The equivalent circuit of the third order LCL filter with damping resistor which is connected in series to the filter capacitor is shown Figure 3.13. However, it should be noted that the larger the passive damping resistor the greater the inhibition, but also the greater the losses.

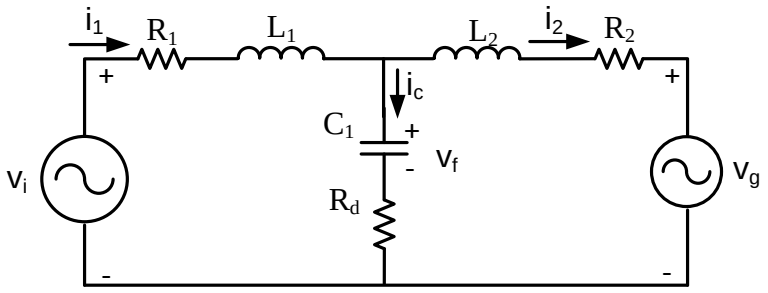

Figure 3.13 Equivalent circuit of single-phase LCL filter with damping resistor

The new transfer function of the system after considering the damping factor will then become:

$$G(s) = \frac{I_1(s)}{V_i(s)} \cdot \frac{I_2(s)}{I_1(s)} \tag{3.40}$$

$$I_1(s) \cdot sL_1 + \frac{sL_1 \cdot (R_\mathrm{d} + 1/sC_f)}{sL_2 + R_\mathrm{d} + 1/s\,C_f} = V_i(s) \tag{3.41}$$

$$\frac{I_1(s)}{V_i(s)} = \frac{1}{sL_1 + \frac{SL_2(R_\mathrm{d} + 1/SC_f)}{SL_2 + R_\mathrm{d} + 1/SC_f}} \tag{3.42}$$

$$\frac{I_2(s)}{I_1(s)} = \frac{(R_\mathrm{d} + 1/sC_f)}{SL_2 + R_\mathrm{d} + 1/s\,C_f} \tag{3.43}$$

$$G(s) = \left(1 \Big/ \frac{sL_1 + sL_2(R_\mathrm{d} + 1/sC_f)}{sL_2 + R_\mathrm{d} + 1/s\,C_f}\right) \cdot \left(\frac{R_\mathrm{d} + 1/sC_f}{sL_2 + R_\mathrm{d} + 1/sC_f}\right) \tag{3.44}$$

$$\frac{I_2(s)}{V_i(s)} = \frac{sCR_d + 1}{s(S^2CL_1L_2 + sCR_d(L_1 + L_2) + s(L_1 + L_2))} \tag{3.45}$$

The behaviour of the passively damped LCL filter can be determined as in Figure 3.14 which illustrates the Bode plot of the damped LCL filter. In this figure, the value of system frequency ω is limited by the phase lag of the LCL filter. The LCL filter can achieve high performance at high frequency with an attenuation rate of -60 dB/dec.

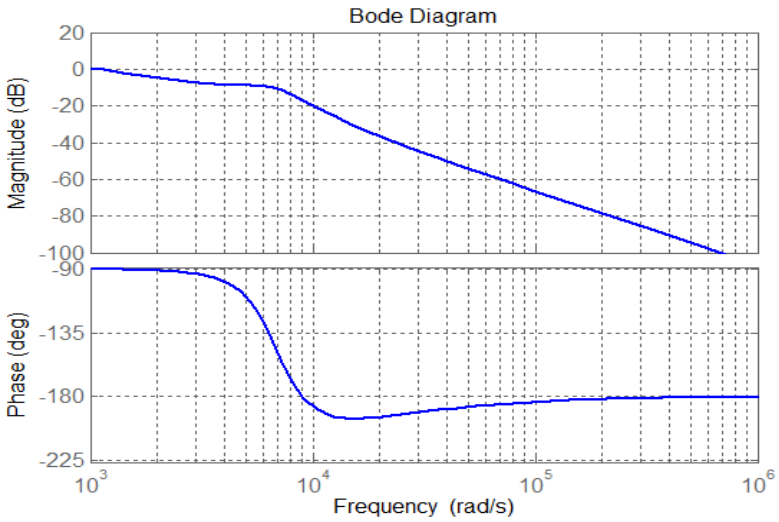

Figure 3.14 LCL filter with damping resistor

In addition, the LCL filter can be converted to the discrete z-domain to test its stability and all the system by using the root locus technique, which is discussed in Chapter 4.

3.6 Chapter Summary

This chapter introduces the working principle of a three-phase grid-connected inverter. The most common three-phase grid connected-inverter is a two-level inverter (VSI). This inverter consists of six switches with freewheeling diodes. The three-phase grid-connected inverter is used to interface the PV panels which generates DC voltage into appropriate AC voltage for the utility grid. In fact, there are two different stages. The single stage where PV panels are connected in series or parallel to achieve certain voltage and current level. The dual-stage topology where the model is separated into two steps, the first step is a DC-DC converter which used in this application to boost the voltage to the higher desirable values and the second is a DC-AC inverter to converts the DC value to the three-phase AC values. In additions, the modelling of the pulse width modulation PWM was discussed. There are different types of PWM switching technique, such as sinusoidal PWM, SVM, hysteresis band PWM and third harmonic elimination PWM. Among them, SVM is found to be the most suitable method for grid-connected inverters. In addition, the design of the passive components of the grid filter was presented. Different filters were discussed and the LCL filters have been shown to improve the power quality of the current injected into the grid and provide better attenuation of harmonic currents, therefore leading to reduced filter sizes compared with lower order L and LC filters.

Chapter 4. Grid Synchronization and Control of the Three-phase Gird-connected Inverter

4.1 Introduction

In this chapter, grid synchronization of the three-phase grid-connected inverter during normal and abnormal grid conditions. In the unbalanced grid condition, the dynamic behaviour of the system becomes progressively worse. AC components will cause power oscillation and increased harmonic components in the system. Yet, this technique is not effectual if there is an abnormal condition in the system, or if there should be any disruption in the network. Owing to the negative-sequence terms, there will be oscillatory errors arising; consequently, the dynamic behavior develops into something that is progressively worse. Based on the literature review as discussed in chapter 1 and chapter 2, a method of decomposition is used in this thesis to decompose the positive and negative sequence components.

The next section of this chapter investigates the main current control used for the three-phase grid connected inverter. Current control is one of the most important challenges which needs to be addressed. The main function of current control is to ensure that the reference signal is followed by the measured signal. Many different current control techniques have been utilized in order to achieve a better quality of the current waveform. In the three-phase system, current control can be implemented in various ways such as Proportional Integral (PI) current control in the synchronous rotating reference frame *dq*, and Proportional Resonance (PR) current control in the stationary reference frame $\alpha\beta$.

4.2 Decomposition of the Symmetrical Components

Under abnormal grid conditions such as unsymmetrical voltage sags or swells, one or more of the phase voltage drops or rises. As a result, the grid current and voltage lose their sinusoidal and balanced appearance which makes the control system more challenging.

In this case, the negative sequence component is used to overcome the effect of the fault in the injected current. Hence, it is necessary to use the method of decomposition to overcome important issues regarding the operation of the three-phase inverter during unbalanced grid conditions.

In normal grid conditions, the three-phase symmetrical component voltage has the same frequency and amplitude with respect to the phase angle which is shifted in a clockwise direction by 120° degrees. In general, a three-phase voltage can be written as:

$$v_a(t) = \sqrt{2}V_{rms}\cos(\omega t) \tag{4.1}$$

$$v_b(t) = \sqrt{2}\,\mathrm{V_{rms}}\cos(\omega t - 120^{\circ}) \tag{4.2}$$

$$v_c(t) = \sqrt{2}V_{rms}\cos(\omega t - 240^{\circ}) \tag{4.3}$$

Sometimes it is useful to present this information using the magnitude and phase angle as presented in phase rotation as:

$$v_a = V_{rms}\angle 0° \tag{4.4}$$

$$v_b = V_{rms}\angle -120° \tag{4.5}$$

$$v_c = V_{rms}\angle -240° \tag{4.6}$$

Thus, the sum of three balanced voltages should be zero:

$$v_a + v_b + v_c = v_{rms}(1\angle 0° + 1\angle -120° + 1\angle 120°) \tag{4.7}$$

As a consequence, if there is any deviation from the above formula it will represent an abnormal condition. This can happen when any difference in magnitude or deviation from the designated phase angles is normally referred to as unbalanced. It must be noted that the difference between the magnitude of the phase voltages is the most frequently occurring form of unbalance under a normal mode of operation, and change in the phase normally occurs under faulty conditions. To overcome this problem, using the symmetrical component method in the three-phase system can convert the set of the three-phase voltages as well as the three-phase current into a linear combination of the positive sequence components, the negative sequence, and the zero sequence.

The symmetrical component can be written as

$$v_{abc} = \begin{bmatrix} v_a \\ v_b \\ v_c \end{bmatrix} = \sum_{i=1}^{n} (v_{abc}{}^{+} + v_{abc}{}^{-} + v_{abc}{}^{0}) \tag{4.8}$$

Where

$$v_{abc}{}^{+} = V^{+n}\begin{bmatrix}\cos(\omega t + \delta^{+}) \\ cos\left(\omega t + \delta^{+} - \frac{2\pi}{3}\right) \\ cos\left(\omega t + \delta^{+} + \frac{2\pi}{3}\right)\end{bmatrix} \quad (4.9)$$

$$v_{abc}{}^{-} = V^{-n}\begin{bmatrix}\cos(\omega t + \delta^{-}) \\ cos\left(\omega t + \delta^{-} - \frac{2\pi}{3}\right) \\ cos\left(\omega t + \delta^{-} + \frac{2\pi}{3}\right)\end{bmatrix} \quad (4.10)$$

$$v_{abc}{}^{0} = V^{0n}\begin{bmatrix}\cos(\omega t + \delta^{0}) \\ cos(\omega t + \delta^{0}) \\ cos(\omega t + \delta^{0})\end{bmatrix} \quad (4.11)$$

Figure 4.1 shows a positive, negative, and zero sequences. These components can be represented by v^{+}, v^{-} in a term of root mean square while the zero sequence has the same magnitude and in the phase of each other, rotating in the same direction of the positive sequence.

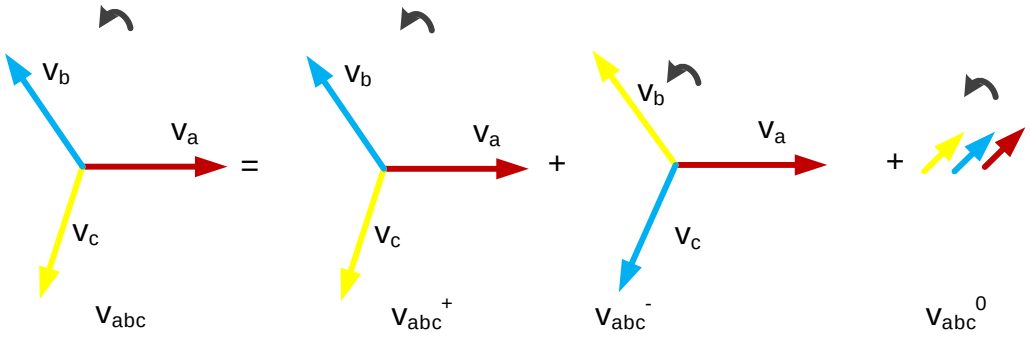

Figure 4.1 The positive, negative and zero sequences system

It should be noted that the three-phase grid-connected inverter applications are using three wire connections, therefore the zero sequence component can be neglected since it is the only component that can flow in neutral. As a result, the set of the positive and negative sequence voltage represent two balanced systems in which the order of rotation between various phases representing the phase voltages have been reversed. This means:

$$v_a{}^{+} + v_b{}^{+} + v_c{}^{+} = v^{+}(1\angle 0 + 1\angle 240° + 1\angle 120°) \quad (4.12)$$

$$v_a{}^{-} + v_b{}^{-} + v_c{}^{-} = v^{-}(1\angle 0 + 1\angle 120° + 1\angle 240°) \quad (4.13)$$

The equations (4.12) and (4.13) can be expressed in the phasor matrix:

$$[V_{\pm 0}]=\begin{bmatrix}V_+\\V_-\\V_0\end{bmatrix}=\frac{1}{3}\begin{bmatrix}1 & \alpha & \alpha^2\\1 & \alpha^2 & \alpha\\1 & 1 & 1\end{bmatrix}\begin{bmatrix}V_a\\V_b\\V_c\end{bmatrix} \quad (4.14)$$

α is an operator defined as the reference for resulting symmetrical components which is $\alpha = e^{j2\pi/3}$, or can be expressed in rectangular form as $\alpha = \frac{-1}{2} + j\frac{\sqrt{3}}{2}$.

where $j = \sqrt{-1}$ or 90° rotator.

Likewise, the inverse transformation of (4.14) is addressed to be

$$\begin{bmatrix}V_a\\V_b\\V_c\end{bmatrix}=\frac{1}{3}\begin{bmatrix}1 & 1 & 1\\\alpha^2 & \alpha & 1\\\alpha & \alpha^2 & 1\end{bmatrix}\begin{bmatrix}V_+\\V_-\\V_0\end{bmatrix} \quad (4.15)$$

The voltage vector matrix of (4.15) can be expressed in the stationary *α, β* reference frame. The voltage and the current are now decomposed to the positive sequence signal (PSS) and negative sequence signal (NSS). Moreover, each of the two-phase voltages and two-phase currents can be presented in

$$v_\alpha = v_\alpha^+ + v_\alpha^- \ , \ v_\beta = v_\beta^+ + v_\beta^- \quad (4.16)$$

$$i_\alpha = i_\alpha^+ + i_\alpha^- \ , \ i_\beta = i_\beta^+ + i_\beta^- \quad (4.17)$$

In the stationary reference frame, the component matrix can be reformulated from complex operator *α* to signify the time delay in the period (T_0) by phase shift 90°. Figure 4.2 shows the symmetrical component decomposition of a two-phase system in the stationary reference frame *α, β*.

Part a) shows the relationship between the positions of *α, β* for both positive and negative sequence components with respect to the phase angle 90°. Parts b) and c) show the decomposition of *α, β.* The red vectors are the unbalanced components *α, β* of positive and negative sequence components where the blue vectors are the result of both balance and unbalance *α, β.*

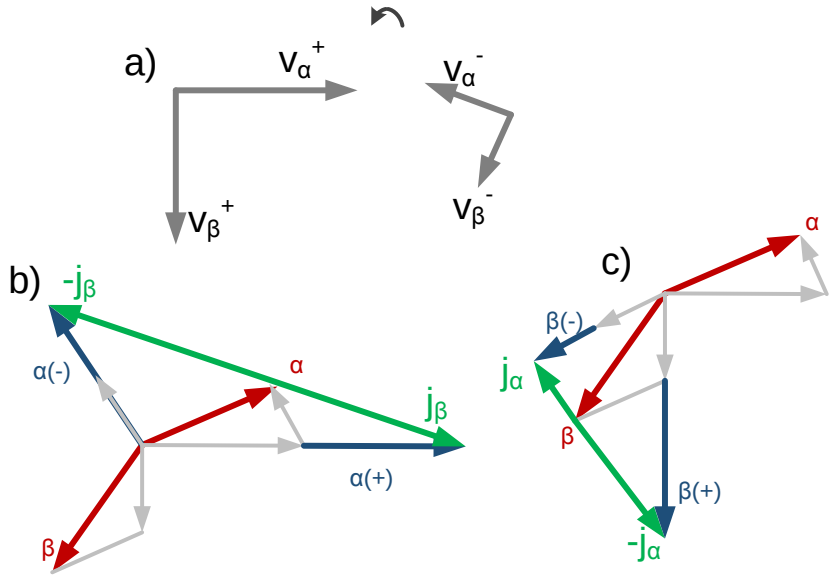

Figure 4.2 The symmetric components decomposition two-phase system

Hence, the two-phase symmetric components decomposition can be represented as:

$$\begin{bmatrix} v_\alpha^+ \\ v_\alpha^- \end{bmatrix} = \frac{1}{2}\begin{bmatrix} 1 & j \\ 1 & j^{-1} \end{bmatrix}\begin{bmatrix} v_\alpha \\ v_\beta \end{bmatrix} \tag{4.18}$$

$$\begin{bmatrix} v_\beta^+ \\ v_\beta^- \end{bmatrix} = \frac{1}{2}\begin{bmatrix} j & 1 \\ j^{-1} & 1 \end{bmatrix}\begin{bmatrix} v_\alpha \\ v_\beta \end{bmatrix} \tag{4.19}$$

As a result, the input signal frequency ω and the period T_0 the phase shift -j operator can be defined as ($\frac{T_0}{4}$) delay in the time domain. It can be said that the positive voltage β (v_β^+) is achieved by averaging the normal voltage orthogonal β with a quarter cycle delay ($\frac{T_0}{4}$) of the normal voltage orthogonal α. Moreover, the positive voltage α (v_α^+) is also obtained by averaging the normal voltage orthogonal $\alpha$with a quarter cycle delay ($\frac{T_0}{4}$) of the normal voltage orthogonal β.

The equation for the α and β components for positive-sequence can be written as:

$$v_\alpha^+(t) = \frac{1}{2}\left(v_\alpha(t) - v_\beta\left(t - \frac{T_0}{4}\right)\right) \tag{4.20}$$

$$v_\beta^+(t) = \frac{1}{2}\left(v_\beta(t) + v_\alpha\left(t - \frac{T_0}{4}\right)\right) \tag{4.21}$$

The negative-sequence can be obtained from the following equation:

$$\mathrm{v}_{\alpha}^{-}(t) = \frac{1}{2}\,(v_{\alpha}(t) + v_{\beta}(t - \tfrac{T_0}{4})) \tag{4.22}$$

$$\mathrm{v}_{\beta}^{-}(t) = \frac{1}{2}\,(v_{\beta}(t) - v_{\alpha}(t - \tfrac{T_0}{4})) \tag{4.23}$$

The equations (4.20), (4.21), (4.22) and (4.23) can be written as the vector of positive and negative sequence components in complex form:

$$\underline{\mathrm{v}}^{+\alpha\beta}(t) = \frac{1}{2}\,(\underline{\mathrm{v}}^{\alpha\beta}(t) + j\underline{\mathrm{v}}^{\alpha\beta}\left(t - \frac{T_0}{4}\right)) \tag{4.24}$$

$$\underline{\mathrm{v}}^{-\alpha\beta}(t) = \frac{1}{2}\,(\underline{\mathrm{v}}^{\alpha\beta}(t) - j\underline{\mathrm{v}}^{\alpha\beta}\left(t - \frac{T_0}{4}\right)) \tag{4.25}$$

The equations demonstrate that by delaying the voltage vector by a quarter of the period ($\frac{T_0}{4}$), a vector constituted of similar positive sequence components with negative sequence component. respecting the equal amplitude and contrary sign.

However, to implement this method in the practical work in the software of the DSP for the three-phase grid-connected inverter, the method of decomposition should be written in the discrete domain. The equations are as follows:

$$\underline{\mathrm{v}}^{+\alpha\beta}(KT_s) = \frac{1}{2}\,(\underline{\mathrm{v}}^{\alpha\beta}(KT_s) + j\underline{\mathrm{v}}^{\alpha\beta}(KT_s - T_s n_0)) \tag{4.26}$$

$$\underline{\mathrm{v}}^{-\alpha\beta}(KT_s) = \frac{1}{2}\,(\underline{\mathrm{v}}^{\alpha\beta}(KT_s) - j\underline{\mathrm{v}}^{\alpha\beta}(KT_s - T_s n_0)) \tag{4.27}$$

where T_s is the sampling time and n_0 is the discrete delay of $\frac{T_0}{4}$ of the sampling time T_s.

However, despite several advantages of using the time delay method such as it is easy to implement in the DSP and its fast response, some disadvantages can be found in this method. One of the drawbacks is that the delay of period t by $\frac{T}{4}$ have an effect in real-time implementation and therefore, some errors appear. In addition, this method requires more data storage in the DSP.

To enhance this method of time delay, a low-pass filter is implemented in order to shift the cycle by a quarter-time delay of the sampling time for the first filter and the same method for

the second filter [107]. The result of the filter can obtain a 90° lag and can be easily implemented in the DSP. The two low-pass filters can be written as:

$$H_1(s) = \left(\frac{\omega_0}{s+\omega_0}\right), \quad H_2(s) = \left(\frac{\omega_0}{s+\omega_0}\right) \tag{4.28}$$

Equation (4.28) can be decomposed and written as:

$$H(s) = \left(\frac{\omega_0}{s+\omega_0}\right)\left(\frac{\omega_0}{s+\omega_0}\right) = \frac{{\omega_0}^2}{(s+\omega_0)^2} \tag{4.29}$$

where ω_0 is the angular velocity.

The behaviour of the filter can be obtained from the Bode plot response of the system. Figure 4.3 shows the Bode plot diagram of the adaptive filter of the decomposition signal. It is illustrated that only -6 *(dB)* attention at ω_0 with a phase lag of 90° is achieved. The amplitude attenuation is 0.5 .

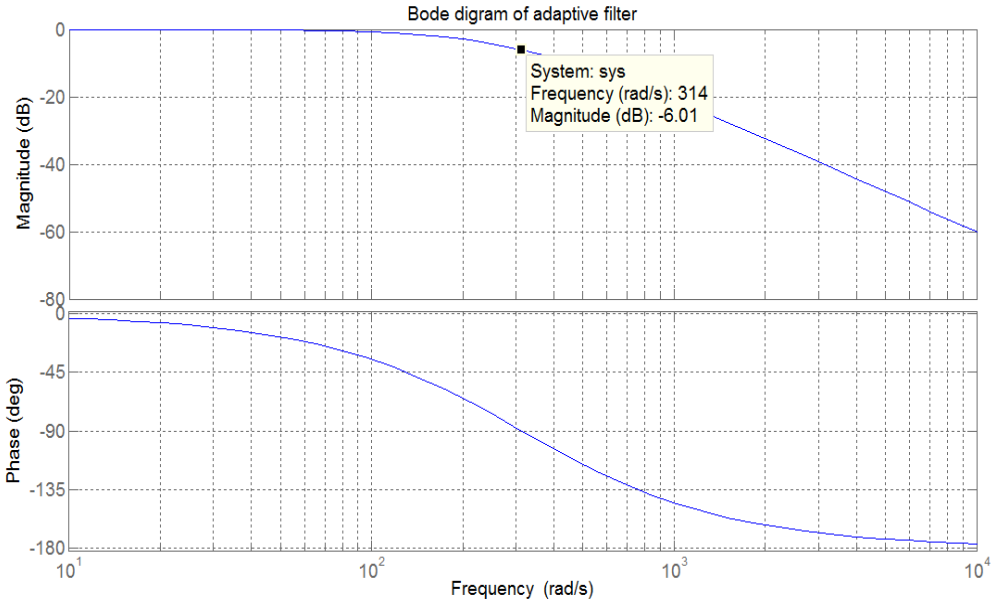

Figure 4.3 The bode plot of the low pass filter

In order to implement this method in the digital signal processor (DSP), a filter should be converted to a discrete formula. This can be done by using the forward Euler method for one filter $H_1(s)$ and the backward Euler method for the second filter $H_2(s)$. To simplify the discretization of the filter, a two-cascaded equation is implemented in the DSP code.

The forward Euler and the backward Euler discretization for $H_1(s)$ and $H_2(s)$ respectively are shown in the following equations below:

$$H_1(s) = \left(\frac{\omega_0}{s+\omega_0}\right) \tag{4.30}$$

$$H_1(z) = H_1(s)\Big|_{\frac{1}{s}=\frac{zT_S}{z-1}}$$

$$H_1(s) = \frac{\omega_0}{(z-1/T_s)+\omega_0} = \frac{\omega_0 T_s}{z-1+\omega_0} \tag{4.31}$$

$$H_1(s) = \frac{\omega_0 T_s}{z-(1-\omega_0 T_s)} = \frac{\omega_0 T_s z^{-1}}{1-z^{-1}(1-\omega_0 T_s)} \tag{4.32}$$

$$H_2(s) = \left(\frac{\omega_0}{s+\omega_0}\right) \tag{4.33}$$

$$H_2(z) = H_2(s)\Big|_{\frac{1}{s}=\frac{zT_S}{z-1}}$$

$$H_2(s) = \frac{\omega_0}{(z-1/zT_s)+\omega_0} = \frac{\omega_0 T_s}{(z-1+zT_s\omega_0/zT_s)} \tag{4.34}$$

$$H_2(z) = \frac{z\omega_0 T_s}{z(1+\omega_0 T_s)-1} = \frac{(\omega_0 T_s/(1+\omega_0 T_s)z}{z-(\frac{1}{1+\omega_0 T_s})} \tag{4.35}$$

$$H_2(z) = \frac{y(z)}{x(z)} = \frac{\omega_0\, T_s}{(1+\omega_0\, T_s)-\, z^{-1}} \tag{4.36}$$

$$y(z) + \omega_0\, T_s\, y(z) - \; z^{-1}y(z) = \omega_0\, T_s\; x(z) \tag{4.37}$$

$$y(z)\,(1+\omega_0\, T_s) - \; z^{-1}y(z) = \omega_0\, T_s\; x(z) \tag{4.38}$$

$$y(z) = \frac{1}{1+\omega_0\, T_s}\,[\, z^{-1}y(z) + \omega_0\, T_s\; x(z)\,] \tag{4.39}$$

where $x(z)$ is the filter input and $y(z)$ is the filter output. ω_0 is the angular velocity and T_s is the sampling time.

The difference equation in the time domain becomes:

$$y(k) = \frac{1}{1 + \omega_0 T_s}\{ y(k-1) + \omega_0 T_s \; x(z) \tag{4.40}$$

Note that $z^{-1}y(z) = y(k-1)$. The difference equation realization of two cascaded filters [107]. To obtain the final full discrete form of the filters, the final difference equations can be written as:

$$y(k) = \omega_0 T_s \left(\frac{1}{2} x\,(k-1) - y(k-1) \right) + y(k-1) \tag{4.41}$$

$$z(k) = \omega_0 T_s \left(\frac{1}{2} y\,(k-1) - z(k-1) \right) + z(k-1) \tag{4.42}$$

Where *x(k)* is original α and β voltage sequence, *y(k)* is the output of the first filter $H_1(s)$ and *z(k)* is the output of the second filter $H_2(s)$.

The decompression structure of the filter can be easily shown from the block diagram in Figure 4.4.

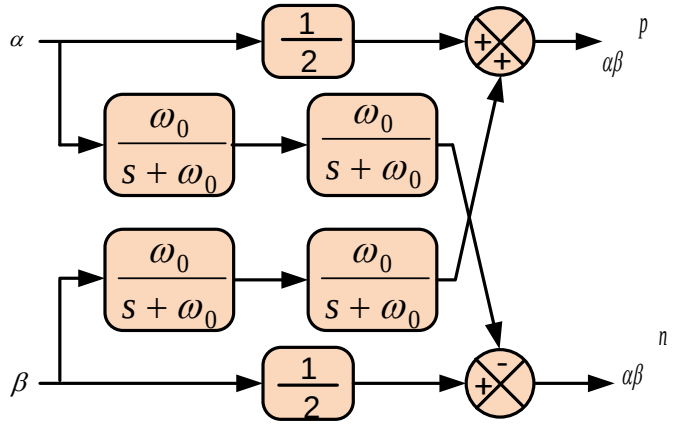

Figure 4.4 Block diagram of positive and negative decomposition

4.3 Current Control of the Three-phase Grid-connected Inverter

Many different current control techniques have been utilized in order to achieve the best quality of the current waveform. In the three-phase system, current control can be implemented in various ways such as Proportional Integral (PI) current control in the synchronous rotating reference frame *dq*, and Proportional Resonance (PR) current control in the stationary reference

frame $\alpha\beta$. Figure 4.5 shows the single line diagram of the three-phase grid-connected inverter using a PI controller.

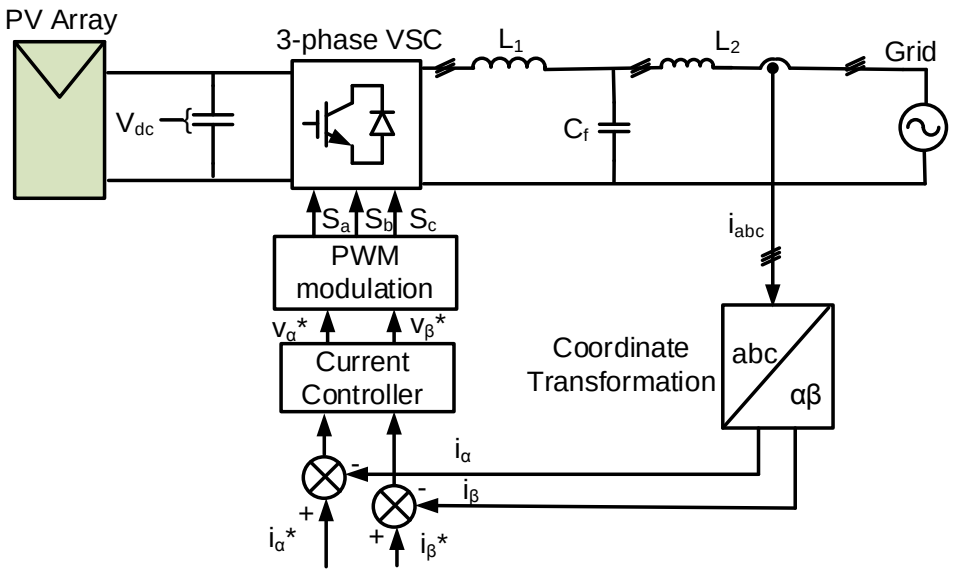

Figure 4.5 single line diagram of three-phase grid-connected inverter with current control scheme

4.3.1 Proportional Integral (PI) Current Controller in the Synchronous Reference Frame

Traditionally, Proportional Integral (PI) current control is the most common current method used to control the output current. In the three-phase system, the three-phase reference frame *abc* coordinates are transformed into *dq* synchronous coordinates in a rotating reference frame. Figure 4.6 shows the circuit diagram of the three-phase grid-connected inverter using a PI current controller. The block diagram of the control approach utilizes a cascaded PI current control structure. The control consists of an outer loop of the voltage control and internal control for the current control. This structure increases the performance of the control system.

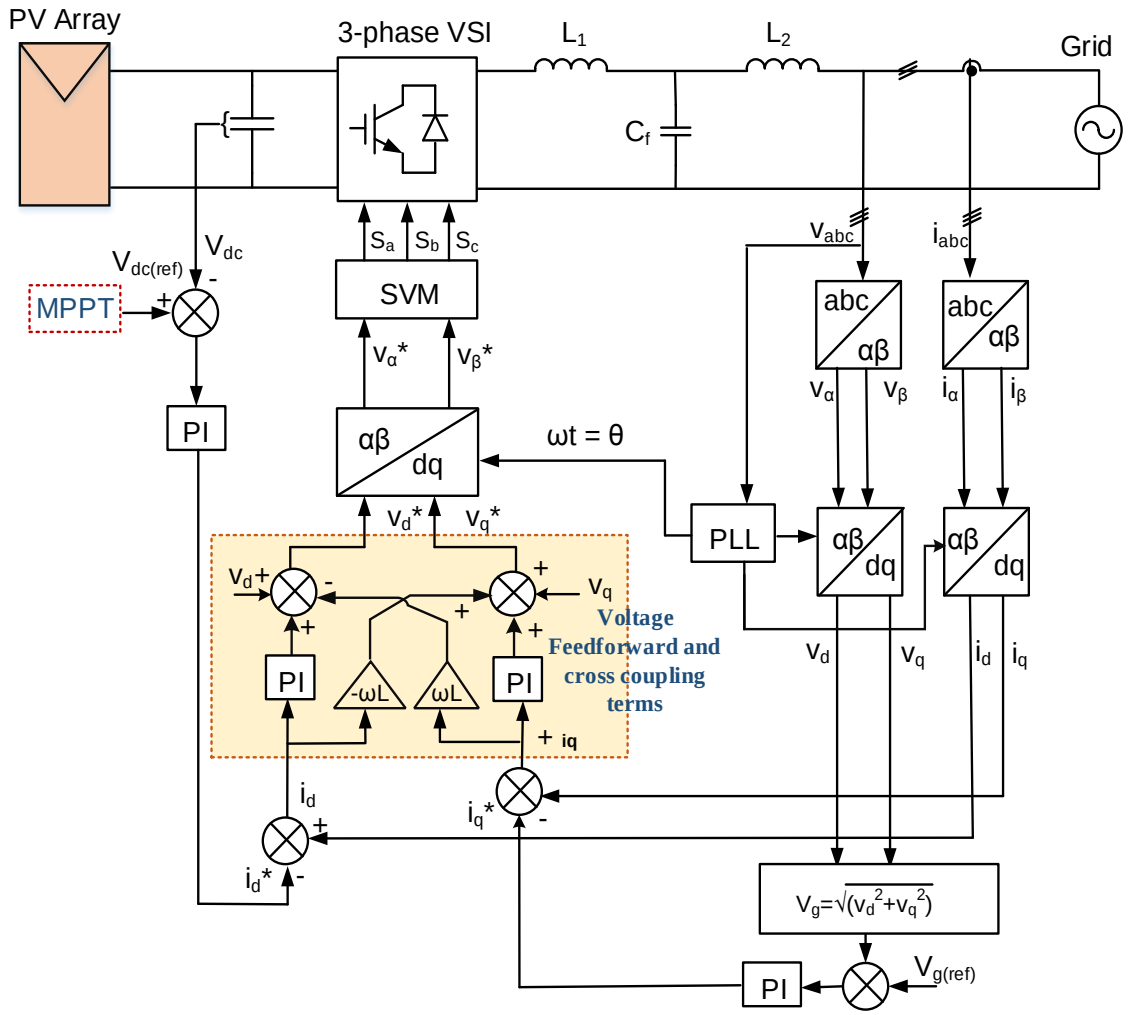

Figure 4.6 PI controller in synchronous reference scheme

To control the three-phase grid-connected inverter current using a PI controller, the three-phase reference frame *abc* coordinates are transformed into *dq* synchronous coordinates in a rotating reference frame with angular frequency using the transformation matrix, as shown in equations (4.43) and (4.44) [52].

$$\begin{bmatrix} v_d \\ v_q \\ 0 \end{bmatrix} = \begin{bmatrix} \cos\theta & \cos(\theta - \frac{2\pi}{3}) & \cos(\theta + \frac{2\pi}{3}) \\ \sin\theta & \sin(\theta - \frac{2\pi}{3}) & \sin(\theta + \frac{2\pi}{3}) \end{bmatrix} \begin{bmatrix} v_a \\ v_b \\ v_c \end{bmatrix} \tag{4.43}$$

$$\begin{bmatrix} i_d \\ i_q \end{bmatrix} = \begin{bmatrix} \cos\theta & \cos(\theta - \frac{2\pi}{3}) & \cos(\theta + \frac{2\pi}{3}) \\ \sin\theta & \sin(\theta - \frac{2\pi}{3}) & \sin(\theta + \frac{2\pi}{3}) \end{bmatrix} \begin{bmatrix} i_a \\ i_b \\ i_c \end{bmatrix} \tag{4.44}$$

To control the grid voltage at the point of common coupling (PCC), the greatness of the measured voltage in αβ frame is considered according to the following equation:

$$|V_{PCC}| = \sqrt{V_{gd}^2 + V_{gq}^2} \tag{4.45}$$

Note that the magnitude of V_{PCC} is compared with the magnitude of the reference voltage $v_{g(ref)}$ in per-unit (pu). The output of the grid voltage PI controller is the current reference i_q^*. In normal grid conditions, the unity power factor can be obtained by making i_q^* equal to zero. On the other hand, the calculated i_d and i_q were compared with their reference set-point currents i_d^* and i_q^* and controlled by the PI controllers. The PI controller is capable of decreasing the error in the generated waveform. The PI controller can be subdivided into two terms; proportional gain (k_p) and integral gain (k_i). The proportional gain has to be adjusted sufficiently to reduce the error input in the controller leading to an increase in the speed response of the current controller. The integral gain is responsible for decreasing the distance of the settling time in the waveform. The controller can be modelled using the following equation:

$$u(t) = k_p e(t) + k_i \int_0^t e(t)dt \tag{4.46}$$

Where k_p is the proportional gain,k_i is the integral gain of the controller, and $e(t)$ is the steady-state control error. A schematic diagram of the PI control scheme is shown in Figure 4.7.

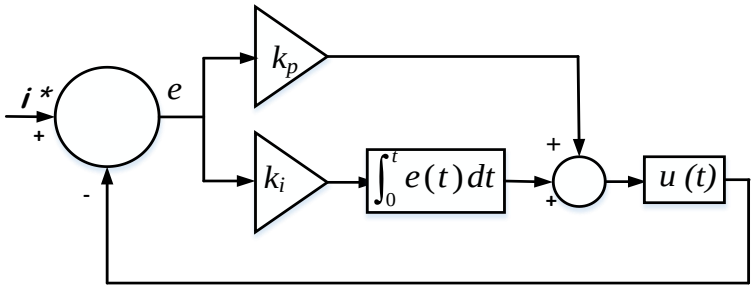

Figure 4.7 PI control scheme in the time domain

In addition, the calculated i_d and i_q were paralleled with the reference set-point current i_d^* and i_q^* measured by the PI controllers to create the *d* and *q* components of the moderating voltage v_d^* and v_q^* in the synchronous orientation frame (SRF). This is reassigned to the standing location frame by an inverse Park conversion, shown in equation (4.47).

$$\begin{bmatrix} v_d^* \\ v_q^* \end{bmatrix} = \begin{bmatrix} \cos\theta & -\sin\theta \\ \sin\theta & \cos\theta \end{bmatrix} \begin{bmatrix} v_\alpha^* \\ v_\beta^* \end{bmatrix} \tag{4.47}$$

The grid voltage feed-forward procedures are occasionally related in grid-connected purposes to relieve some of the weight on the PI controller itself thus developing the response of the AC tracking system [143]. The current in the synchronous reference frame can be described from the single-phase equivalent circuit in *d* and *q* components as follows:

$$\begin{bmatrix} v_d^* \\ v_q^* \end{bmatrix} = L\frac{d}{dt}\begin{bmatrix} i_d \\ i_q \end{bmatrix} + L\omega\begin{bmatrix} -i_q \\ i_d \end{bmatrix} + R\begin{bmatrix} i_d \\ i_q \end{bmatrix} + \begin{bmatrix} e_d \\ e_q \end{bmatrix} \tag{4.48}$$

where v_d^* and v_q^* are the inverter voltages in *d* and *q* components, e_d and e_q are the grid voltages, R and L are the total resistors and inductance of the grid filter.

From equation (4.42), there is a clear cross-coupling of the currents in the d-axis and q-axis. Stereotypically, such cross-coupling can make unwelcome disruption which disturbs the dynamic retort of the system as each axis concurrently impacts upon the other [144]. Due to this, a voltage feed-forward de-coupling strategy is added, as shown in Figure 4.6 [39].

On the other hand, the PI controller can be described in the state space transfer and is defined as follows [53]:

$$G_{pi}(s) = k_p + \frac{k_i}{s} \tag{4.49}$$

Where, k_p is the proportional gain and k_i is the integral gain of the controller.

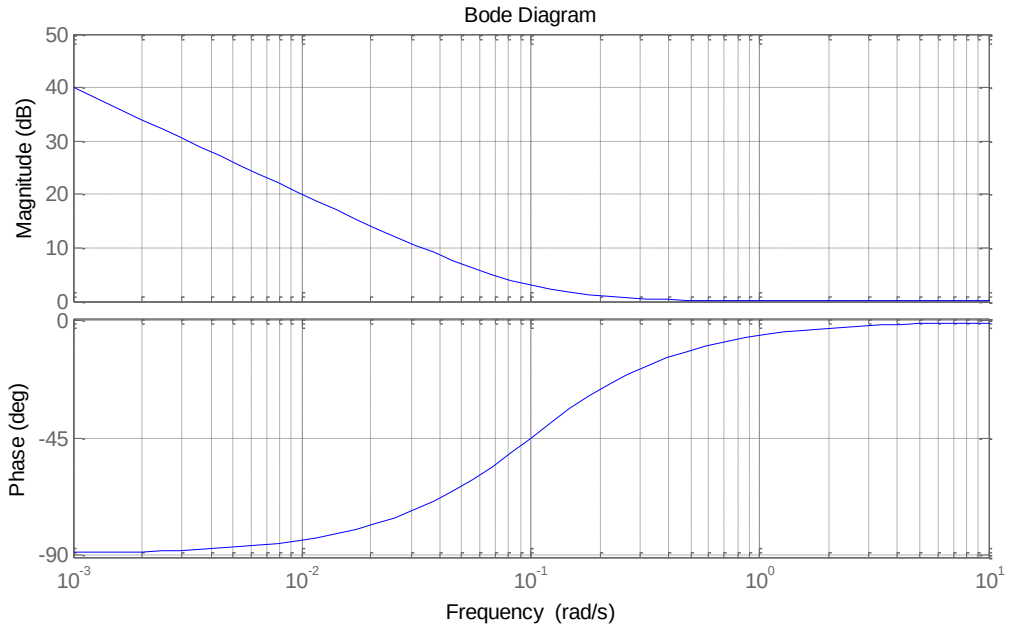

Figure 4.8 PI controller Bode diagram

Figure 4.8 illustrates the concept of PI controller by using the Bode plots diagram. It is expected that the PI controller magnitude break down goes to zero with -40 dB/dec and goes flat as soon as it reaches the poles. As a result, the infinite gain at dc and a high gain at the low frequency will be shown. Therefore, the PI controller will ensure good tracking of the error and good low-frequency rejection.

In addition, in order to implement the PI controller in the DSP, a digital formula in the discrete domain is obtained to implement it in real time. To do so, the PI control is converted from the continuous-time domain to the discrete-time domain. The PI controller equation in the time domain is:

$$y(t) = k_p\, e(t) + \ k_i \int e(t)\, dt \qquad (4.50)$$

where $y(t)$ is the output of the controller, $e(t)$ is the input error of the controller, k_p is the proportional gain and k_i is the integral gain.

Thus, PI controller can be converted to discrete domain using the Backward Euler method as following:

$$\frac{1}{s} = \frac{T_s}{1 - z^{-1}}$$
$$s = \frac{1 - z^{-1}}{T_s} \tag{4.51}$$

The PI controller in discrete form is as follows:

$$\frac{dy}{dt} = k_p\left(\frac{d.e}{dt} + \frac{k_i}{k_p}e\right) \tag{4.52}$$

$$\frac{y(K) - y(K-1)}{T_s} = k_p\left(\frac{e(k) - e(k-1)}{T_s} + \frac{k_i}{k_p}e(k)\right) \tag{4.53}$$

$$y(K) - y(K-1) = k_p\left(e(k) - e(k-1) + \frac{k_i}{k_p}T_s.e(k)\right) \tag{4.54}$$

$$y(K) = y(K-1) + k_p\left(e(k)\left[1 + \frac{k_i}{k_p}T_s\right] - e(k-1)\right) \tag{4.55}$$

4.3.2 Stability of Proportional Integral (PI) Current Controller

In order to test the stability of the system and obtain the impact of the PI controller in the system, the Bode plot and root locus of the closed loop of the PI controller are obtained. First of all, the whole system will be converted into a transfer function to test the stability of the system. The control block diagram is shown in Figure 4.9. The open loop and closed loop system transfer functions are addressed. The control system has used the Bode plot for the open loop and root locus for the closed loop. The root locus is one of the methods used to design a closed loop control system.

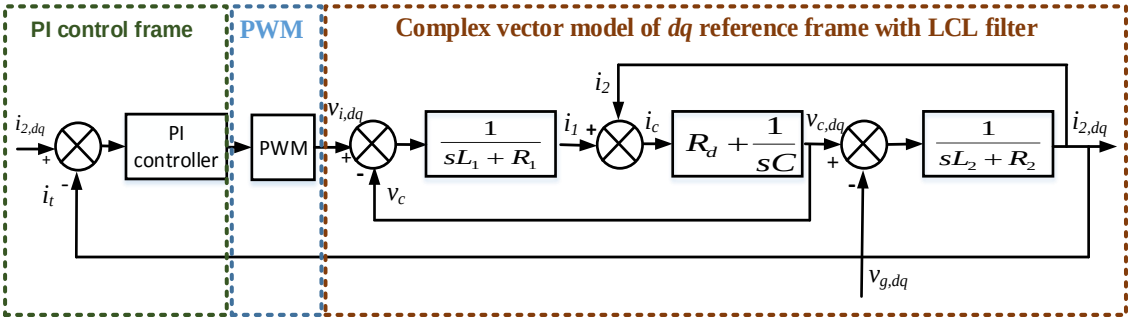

Figure 4.9 Closed loop of an inverter with LCL filter using PI controller

The Bode blot analysis of the PI controller is based on the open loop transfer function of the system. The cascaded system PI controller with the LCL filter is represented in the open loop system. Following equations are describing the control diagram open loop transfer functions:

$$G(s) = G_{PI}(s).G_{PWM}(s).G_{LCL}(s) \tag{4.56}$$

The transfer function of the PWM is given by:

$$G_{PWM}(s) = \frac{1}{1.5T_s s + 1} \tag{4.57}$$

where; T_s is the sampling time of the system. In addition, the transfer function of the LCL filter is given by:

$$G_{LCL}(s) = \frac{SCR_d + 1}{S(S^2CL_1L_2 + SCR_d(L_1 + L_2) + S(L_1+L_2))} \tag{4.58}$$

Figure 4.10 shows the Bode plots of the open loop system using the PI controller of the open loop system. It illustrates that the system is fairly uniform across the resonance frequency. It can be said that the system has a fast response and the stability of the system is confirmed. In addition, in order to see the stability of the system, it is necessary to plot the root locus for this system. In this technique, the plots close the loop poles in the complex plane to provide stability in the system. Equation (4.52) becomes:

$$G(s) = \frac{G(s)}{1 + G(s)} \tag{4.59}$$

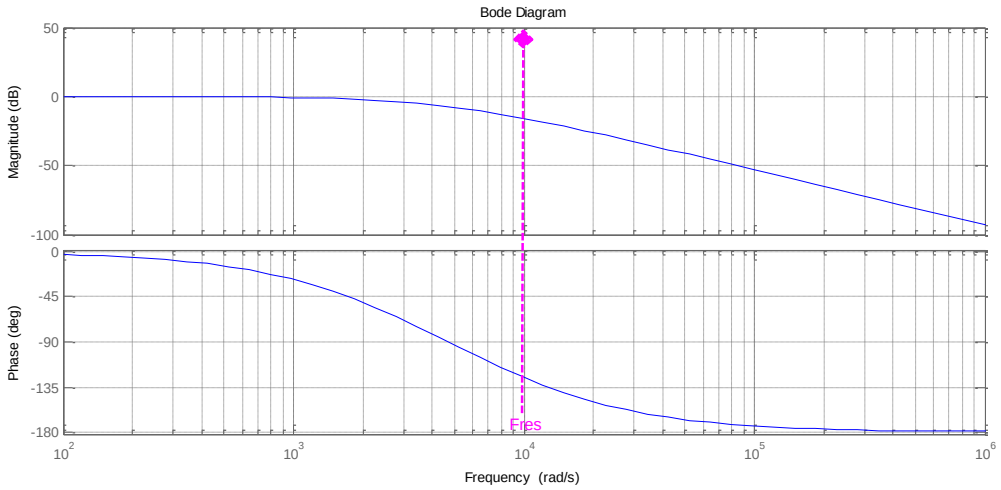

Figure 4.10 Bode plot of the open loop system

Figure 4.11 shows the root locus of the closed loop system using the PI controller. In this figure, the stability is determined by the position of the proportional gain k_p. It can be seen that there are no poles on the right-hand side of the complex planes which ensures that the system is stable. Based on the result, the value of the proportional gain k_p is chosen to be $k_p = 6$ to maintain stability. This indicates that the system is stable for a high enough control gain. In addition, the control gains can rise to dampen poles to maximum proportional gain k_p that will give a marginal stability is $k_p = 15$.

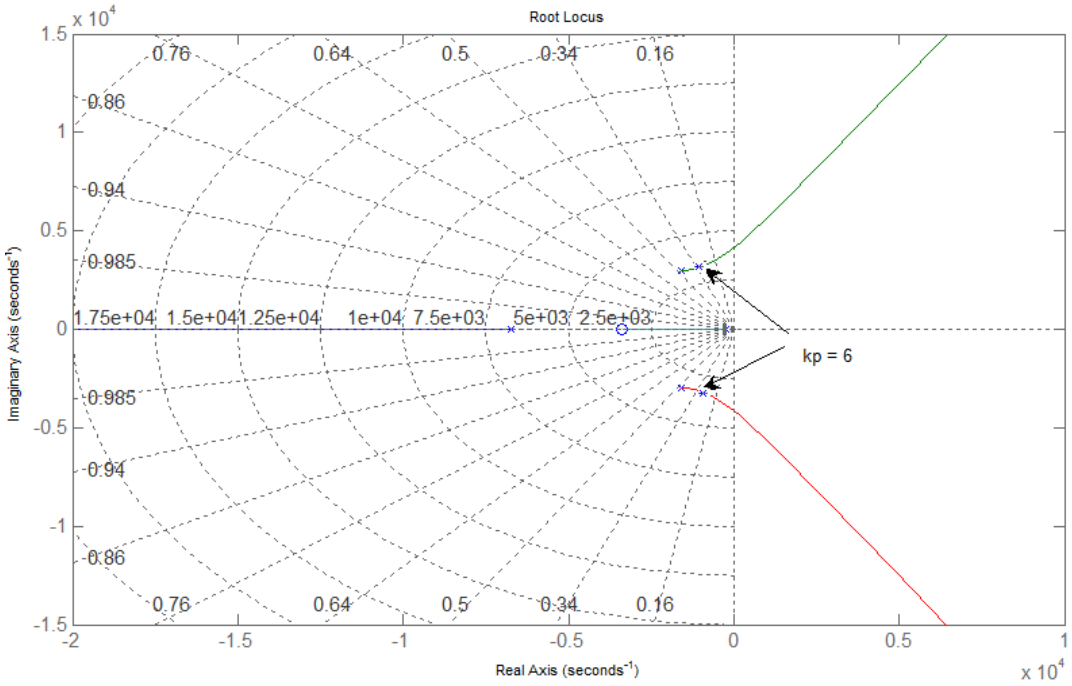

Figure 4.11 Root locus of the PI controller

4.4 Proportional Resonance Current Control in the Stationary Reference Frame

The PR current control block diagram is revealed in the stationary reference frame as seen in Figure 4.12. It is seen as obligatory to alter the alternating current and voltage waveforms from the three-phase *abc* coordinate components to two-phase *αβ* components utilizing the Clarke transformation, as shown in equations (4.60) and (4.61) [39, 145].

$$\begin{bmatrix} v_\alpha \\ v_\beta \end{bmatrix} = \frac{2}{3}\begin{bmatrix} 1 & -\frac{1}{2} & -\frac{1}{2} \\ 0 & \frac{\sqrt{3}}{2} & -\frac{\sqrt{3}}{2} \end{bmatrix}\begin{bmatrix} v_a \\ v_b \\ v_c \end{bmatrix} \tag{4.60}$$

$$\begin{bmatrix} i_\alpha \\ i_\beta \end{bmatrix} = \frac{2}{3}\begin{bmatrix} 1 & -\frac{1}{2} & -\frac{1}{2} \\ 0 & \frac{\sqrt{3}}{2} & -\frac{\sqrt{3}}{2} \end{bmatrix}\begin{bmatrix} i_a \\ i_b \\ i_c \end{bmatrix} \tag{4.61}$$

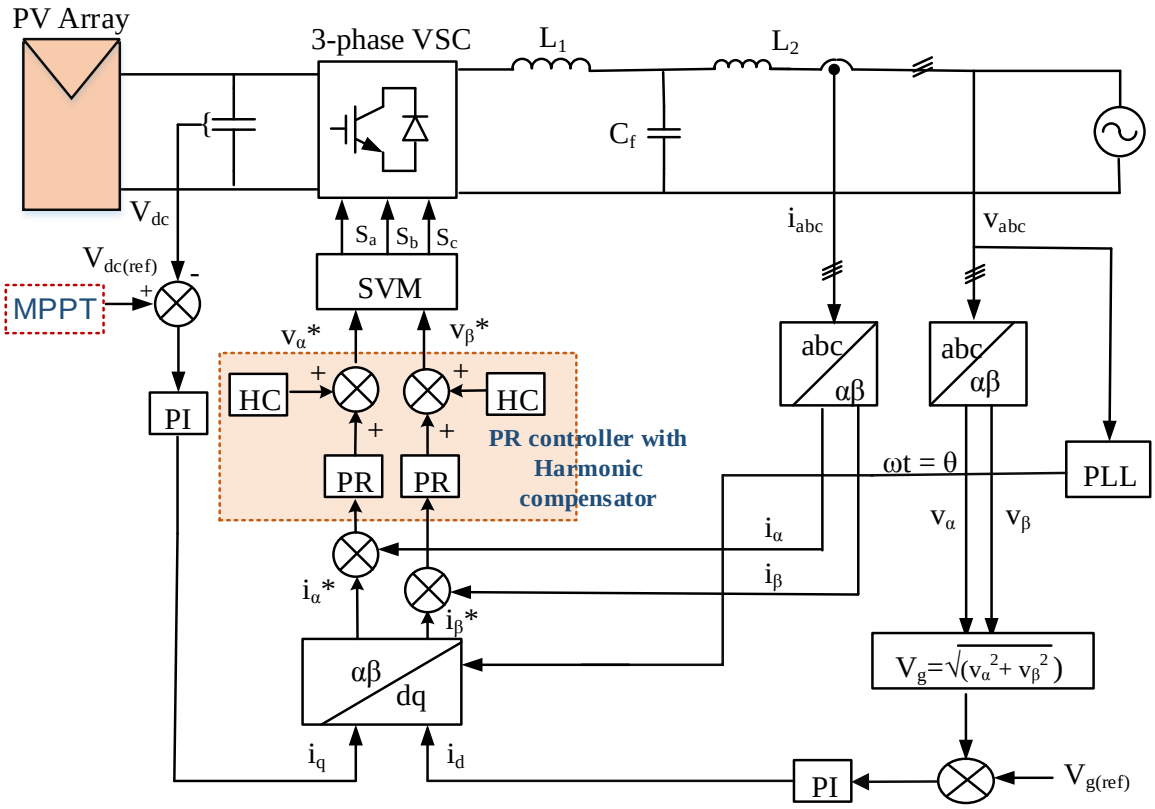

Figure 4.12 PR controller in the stationary reference frame control

To control the voltage at the grid side at the point of common coupling (PCC), the magnitude of the measured voltage in the $\alpha\beta$ frame is considered by using the equations below:

$$\begin{bmatrix} v_\alpha \\ v_\beta \end{bmatrix} = \frac{2}{3}\begin{bmatrix} 1 & -\frac{1}{2} & -\frac{1}{2} \\ 0 & \frac{\sqrt{3}}{2} & -\frac{\sqrt{3}}{2} \end{bmatrix}\begin{bmatrix} v_a \\ v_b \\ v_c \end{bmatrix} \tag{4.62}$$

$$|V_{PCC}| = \sqrt{V_{g\alpha}^2 + V_{g\beta}^2} \tag{4.63}$$

Note that the magnitude of V_{PCC} is compared with the reference voltage $v_{g(ref)}$ magnitude in per-unit (*pu*). In normal grid conditions, the unity power factor can be obtained by making $i_q{}^*$ equal to zero. On the other hand, the calculated i_d and i_q were compared with their reference set-point currents $i_d{}^*$ and $i_q{}^*$ and controlled by the PI controllers. Here, the PR controller is capable of decreasing the error in the generated waveform. The PR controller can be subdivided into two parts; proportional gain (k_p) and integral gain (k_i). The proportional gain k_p has to be adjusted sufficiently to determine the controller response and reduce the error input of the controller. The integral gain k_i is responsible for decreasing the distance of the settling time in

the waveform and controlling the bandwidth around it. The controller can be modelled using the following equation:

$$u(t) = K_p e(t) + K_i \cos \omega t \int_0^t e(t)dt \tag{4.64}$$

where K_p is the proportional gain, K_i is the integral gain of the controller, and $e(t)$ is the steady-state control error. The transfer function of the ideal PR controller is given by the equation:

$$G_{PR}(\mathrm{s}) = K_p + K_i \frac{s}{(s^2 + \omega_o{}^2)} \tag{4.65}$$

where ω_o is the resonant (line) frequency. Due to the high noticeable advance at the fundamental frequency ω, a balanced state error can be characteristically detached via the PR controller.
A chart diagram of the PR control scheme is presented in Figure 4.13.

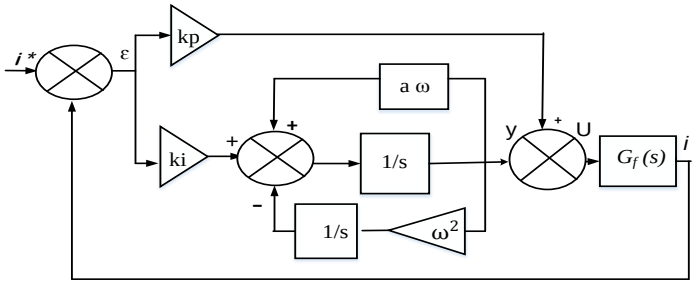

Figure 4.13 Control Diagram of PR controller implementation

Nevertheless, to circumvent the problem of obtaining an infinite gain at the resonant frequency, a non-ideal PR controller which is given in the following equation can be used instead:

$$G_{PR}(\mathrm{s}) = K_p + K_i \frac{2\omega_c s}{(s^2 + 2\omega_c s + \omega_o{}^2)} \tag{4.66}$$

where k_p is the proportional gain, k_i is the integral gain of the controller, ω_0 is the resonance frequency, and ω_c is the cut off frequency and $\omega_c \ll \omega_0$.

Figure 4.14 shows the Bode plots diagram for PR controller in both causes ideal and non-ideal. It clearly shows that the non-ideal PR controller has less gain in the narrow frequency over the entirety of the resonance frequency compared with an ideal one.

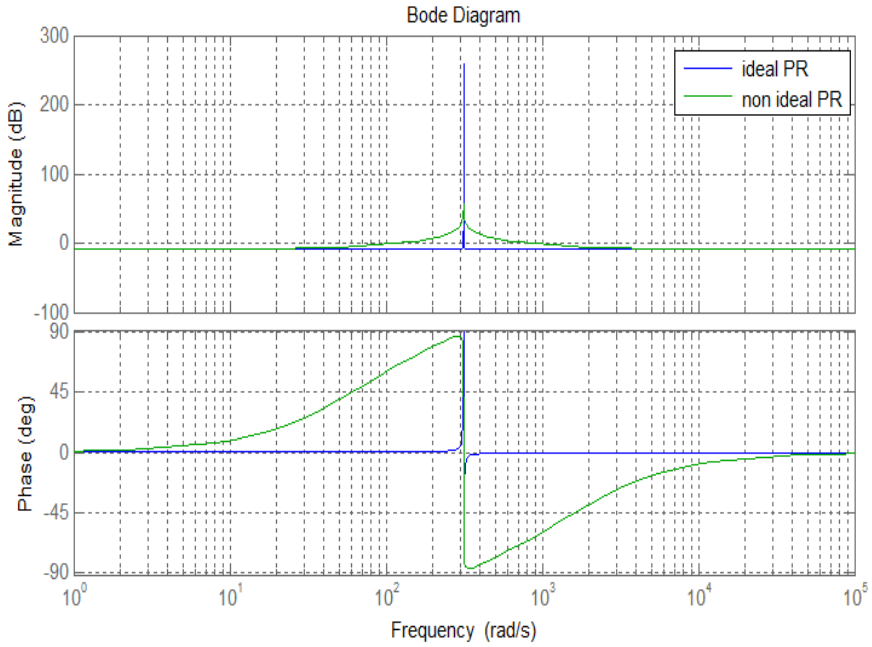

Figure 4.14 The Bode plots of ideal PR and non-ideal PR controller

The considered i_α and i_β are compared with the references i_α^* and i_β^* and controlled by the PR controller to derive the reference set-point voltages v_α^* and v_β^*. These references are in the stationary reference frame, and unlike the PI controller are ac quantities and are applied directly to the space vector modulation (SVM) without any transformation blocks. In order to create a more robust PR controller, a harmonic compensator (HC) is designed in analogous lines with the main PR regulator scheme. It can be said that the HC has no impact on the competence of the rudimentary PR controller. Nevertheless, it has a substantial bearing on the low order harmonic frequency. The HC can be executed by the equation below:

$$G_{HC}(s) = \sum_{h=5,7} \frac{2\ K_{ih}\ s}{s^2 + (\omega h)^2} \tag{4.67}$$

where K_{ih} is the individual resonant gain, h is the harmonic order.

Importantly, the PR controller can be converted to a discrete domain and implemented in low-cost digital signal processor (DSP) technology in order to avoid algebraic loops during the implementation. One of the methods is the generalized discrete equivalent of the PR controller by transformed to the z domain using the Backward Euler in (4.68). By assuming the error is x, the discrete z-domain can be written as follow.

$$H(z) = H(s)\Big|_{\frac{1}{s} = \frac{T_S}{z-1}} \tag{4.68}$$

$$\frac{\mathrm{y(k)}}{x} = \frac{K_i s}{(s^2+{\omega_o}^2)}$$

$$y(k+2) = 2y(k+2) - \left(1+{\omega_o}^2{T_s}^2\right)y_2(k) + k_i T_s[x(k+1) - x(k)] \tag{4.69}$$

$$y = 2yz^{-1} - \left(1+{\omega_o}^2{T_s}^2\right)z^{-2}y_2(k) + k_i T_s[z^{-1} - z^{-2}]x(k) \tag{4.70}$$

$$y - 2yz^{-1} + \left(1+{\omega_o}^2{T_s}^2\right)z^{-2}y_2(k) = k_i T_s[z^{-1} - z^{-2}]x(k) \tag{4.71}$$

$$y(k)(1 - 2z^{-1} + \left(1+{\omega_o}^2{T_s}^2\right)z^{-2}) = x(k)\, k_i T_s[z^{-1} - z^{-2}] \tag{4.67}$$

$$H_1(z) = \frac{y(k)}{x(k)}$$
$$H_1(z) = k_i T_s \frac{z^{-1} - z^{-2}}{1 - 2z^{-1} + \left(1+{\omega_o}^2{T_s}^2\right)z^{-2}} \tag{4.72}$$

where $y(k)$ is the output of the controller and ω_o is the resonant frequency, T_s is switching time.

For non-ideal PR controller can be converted as follow:

$$H_1(z) = H_1(s)\Big|_{\frac{1}{s} = \frac{T_s}{z-1}}$$
$$\frac{\mathrm{y(k)}}{x} = \frac{2K_i\omega_c s}{(s^2 + 2\omega_c s + {\omega_o}^2)} \tag{4.73}$$

$$y(k) - 2y(k-1) + y(k-2) + 2\omega_c\big(y(k) - y(k-1)\big) + {\omega_o}^2 y(k){T_s}^2 = 2k_i\omega_c T_s[x(k) - x(k-1)] \tag{4.74}$$

$$(1 + 2\omega_c T_s + {\omega_o}^2)y(k) = (2 + 2\omega_c T_s)\, y(k-1) + y(k-2) + 2k_i\omega_c T_s[x(k) - x(k-1)] \tag{4.75}$$

$$\mathrm{y(k)} = \frac{1}{1 + 2\omega_c \mathrm{T_s} + \omega_o}[(2 + 2\omega_c \mathrm{T_s})\, \mathrm{y(k-1)} - \mathrm{y(k-2)} + 2\mathrm{k_i}\omega_c \mathrm{T_s}[\mathrm{x(k)} - \mathrm{x(k-1)}] \tag{4.76}$$

$$H_1(z) = \frac{y(k)}{x(k)}$$
$$H_1(z) = \frac{1}{1 + 2\omega_c T_s + \omega_o}[(2 + 2\omega_c T_s)z^{-1} - z^{-2} + 2k_i\omega_c T_s[x(k) - x(k-1)] \tag{4.77}$$

where ω_c is the cut-off frequency and ω_o is the resonant frequency.

4.4.1 Stability Analysis of Proportional Resonance (PR) Current Controller

Consequently, the stability of the system is used here to impact the PR controller. First, the control system has used the Bode plot for the open loop and the root locus for the closed loop. The whole system will be converted into a transfer function to test the stability of the system. Figure 4.15 shows the closed loop block diagram of the system using the PR controller.

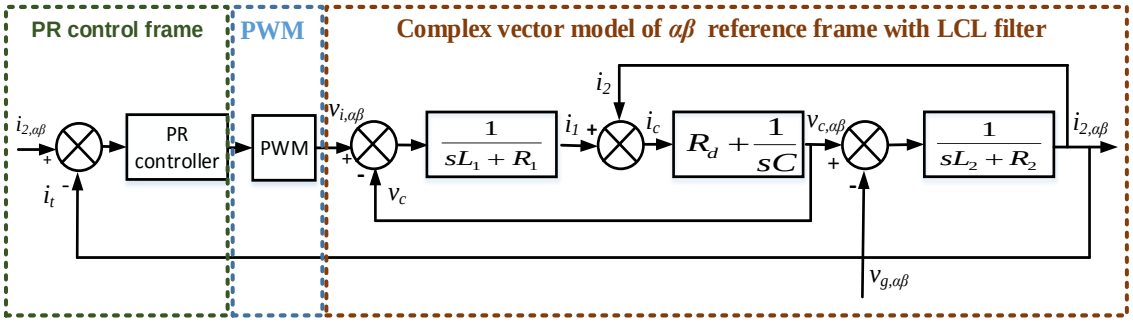

Figure 4.15 Closed loop of an inverter with LCL filter using PR controller

The cascaded system PR controller with the LCL filter is represented first in the open loop system. The following equations describe the control diagram open loop transfer functions:

$$G(s) = G_{PR}(s).G_{PWM}(s).G_{LCL}(s) \tag{4.78}$$

Figure 4.16 shows the Bode plot of the open loop system using the PR controller. Since the PR controller has the proportional part, the system has a fast response and the time can be merged with a variation of the k_p. Due to the resonance part with integral components, it is shown that there is better damping capability around the fundamental frequency ω_o. Figure 4.17 shows the root locus of the closed loop system using the PR controller. In this figure, the system is flexible and stability is determined by the position of the proportional gain k_p. In addition, no poles are recorded on the right-hand side of the complex planes which ensures that the system is stable. Based on the result, the value of the proportional gain k_p is chosen to be $k_p = 6$ to maintain stability. This indicates that the system is stable for a high enough control gain. In addition, the control gains can rise to dampen poles to maximum proportional gain k_p that will give a marginal stability is $k_p = 15$ before it becomes unstable.

The proportional gain is $k_p = 6$ that indicates that the proportional gain can be high. Therefore, the controller proportional gain can be increased up to the $k_p = 15$

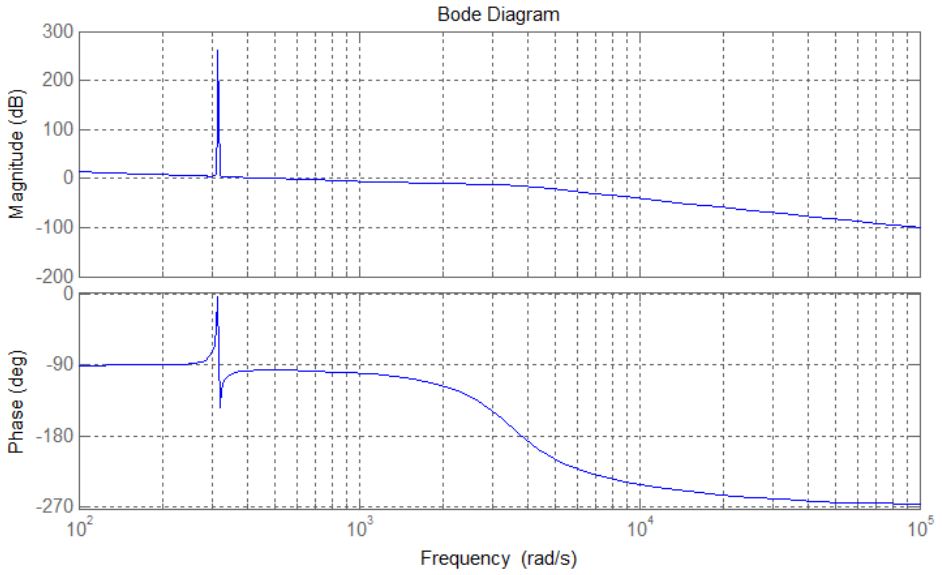

Figure 4.16 The bode blot of the open loop system

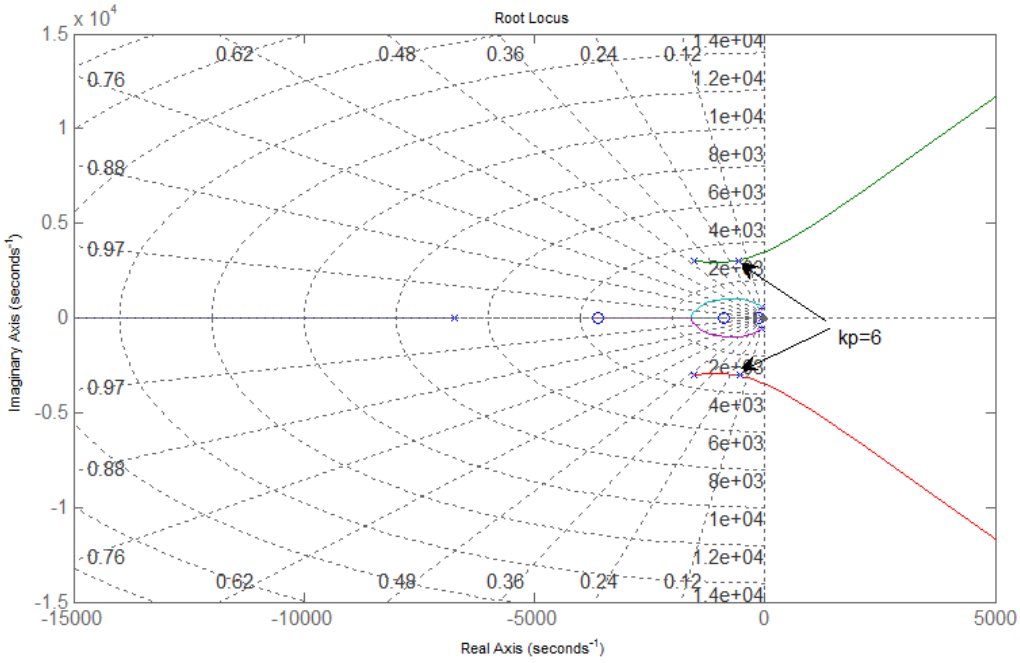

Figure 4.17 The root locus of the closed loop system

4.5 Chapter Summary

This chapter introduces the grid synchronization of the three-phase grid-connected inverter during normal and abnormal grid conditions. In abnormal grid condition, the dynamic behaviour of the system becomes progressively worse. Therefore, a method of decomposition is used in the thesis to decompose the positive and negative sequence components and achieve balance output current. This can be done based on the time delay method. Two filters are implemented in order to shift the cycle by a quarter-time delay of the sampling time for the first filter and the same method for the second filter. The result of the filters can obtain a 90° lag and can be easily implemented in the DSP.

In the three-phase system, current control can be implemented in various ways. The Proportional Integral (PI) current control in the synchronous rotating reference frame *dq*, and Proportional Resonance (PR) current control the stationary reference frame $\alpha\beta$ are the most current control techniques. The implementation of the industrially accepted PI controller, along with the developing PR controller; accepted in grid-connected renewable energy applications, has injected the current under abnormal conditions under any circumstance such as grid fault. Thus, the current control techniques based on the most suitable strategies that could achieve better results during normal and abnormal conditions in the thesis are: positive and negative sequence control *(*PNSC*)* and balance positive sequence control (BPSC).

Chapter 5. Simulation and Experimental Results for PI and PR Current Controller

5.1 Introduction

In this chapter, simulation and experimental results for the three-phase grid-connected inverter are presented using PI and PR current controllers. The first part looks at the inverter controlled using a PI controller. The second section looks at the inverter controlled using PR controller. Performance evaluation of the controllers based on harmonic distortion and dynamic response of the system is also demonstrated.

The system is applied and modelled first in Matlab/Simulink tools version 2012, taking into account the normal and abnormal grid operating conditions. The model comprises the three-phase inverter powered from PV array, with an LCL filter connected to the utility grid. The three-phase grid current is transformed to reference frame and fed to the appropriate controller. The control structure is based on cascaded PI or PR current control. The control techniques consist of an external voltage control loop and internal current control loop. This structure increases the performance of the control system. The control variable is used to generate the PWM signal using Space Vector Modulation (SVM); this being the most common modulation approach based on space vector in the stationary reference frame $\alpha\beta$ plane.

This chapter also describes the experimental hardware equipment for the three-phase grid-connected inverter. It contains an overview of the hardware used. The system comprises the three-phase inverter powered from a DC source and an LCL filter connected to the three-phase inverter. The three-phase grid current is transformed to the reference frame and fed to the appropriate controller. The current control structure is based on PI or PR current control.

5.1 Simulation Model of the System

This section is shown the simulation model of the three-phase grid-connected inverter. To determine the parameters of the simulation, the following equations are used based on the [146-148].

The DC link voltage is derived from the equation (5.1):

$$V_{dc} = \frac{2\sqrt{2}}{mi\sqrt{3}\,V_L} \tag{5.1}$$

where V_{dc} is the dc link voltage, V_L is the line voltage, mi is the modulation index.

The inductances and capacitance values of the LCL filter are calculated from the base values using (5.2) and (5.30) respectively.

$$Z_b = \frac{{V_{LL}}^2}{P} \tag{5.2}$$

$$C_b = \frac{1}{Z_b \omega_n} \tag{5.3}$$

where V_{LL} is the line to line voltage, P is the active power, Z_b is the base impedance, C_b is the base capacitance and ω_n is the grid frequency.

The filter capacitor is a relation between the allowable fraction of the reactive power at rated voltage and current expressed as:

$$C_f = x_1 C_b \tag{5.4}$$

where C_f is the filter capacitor, x_1 is the allowable fraction and has been chosen to be 5%.

To design the inverter-side inductor (L_1), which L_1 is chosen to reduce the ripple in the current. The allowable current ripple should be considered as the percentage of the inverter current and is given by:

$$\Delta i_L = \frac{V_d}{2L_1 f_s} \tag{5.5}$$

where Δi_L is the allowable per-unit ripple in the line current and f_s is the switching frequency. The value of Δi_L is chosen to be equal to 10% of the line current

$$\Delta\, i_L = x_2\, i_L \tag{5.6}$$

where i_L is the output inverter current, x_2 is allowable current ripple and has been chosen to be 25%.

The inverter-side inductor L_1 is given by:

$$L_1 = \frac{V_{dc}}{(8 * f_s * \Delta i_L)} \tag{5.7}$$

where f_s is the switching frequency. In addition, the grid-side inductor L_2 is designated as a segment of the inverter-side inductance which is accountable for the diminution of the majority of the switching ripple. Consequently, L_2 is a function of the inverter-side inductor L_1 and can be calculated as:

$$L_2 = x_3 L_1 \tag{5.8}$$

Where x_3 is the ratio index between the inductance at the inverter-side and grid-side.

$$C_f = xC_b \tag{5.9}$$

where C_b is the base filter capacitor.

The resonant frequency of the LCL filter can be calculated as:

$$f_{res} = \frac{1}{2\pi}\sqrt{\frac{L_1 + L_2}{L_1 L_2 C_f}} \tag{5.10}$$

This resonant frequency is chosen to be at least 10 times the line frequency but less than half of the switching frequency [150].

From the above equations, the nominal operating parameters used in the simulation model are listed in Table 5.1.

Table 5.1 Three-phase inverter simulation parameters

Parameter	Value
Rated power, P	100kW
Inverter side inductance, L_1	5 mH
Inverter side inductance, L_2	3 mH
Grid voltage -line to line, V_g	415 V
DC voltage, V_{dc}	760 V
DC capacitor, C_{dc}	2000 µF
Switching & Sampling frequency, f_s	10 kHz
Filter capacitor, C_f	92 µF

Figure 5.1 shows the simulation model in the Simulink environment modelled using the calculated parameters of Table 5.1. Figure 5.2 shows the PLL, voltage and current transformations. The simulation results were obtained from Matlab/Simulink software package under normal and abnormal grid operating conditions with constant grid voltage magnitude, constant frequency and constant power from the PV array.

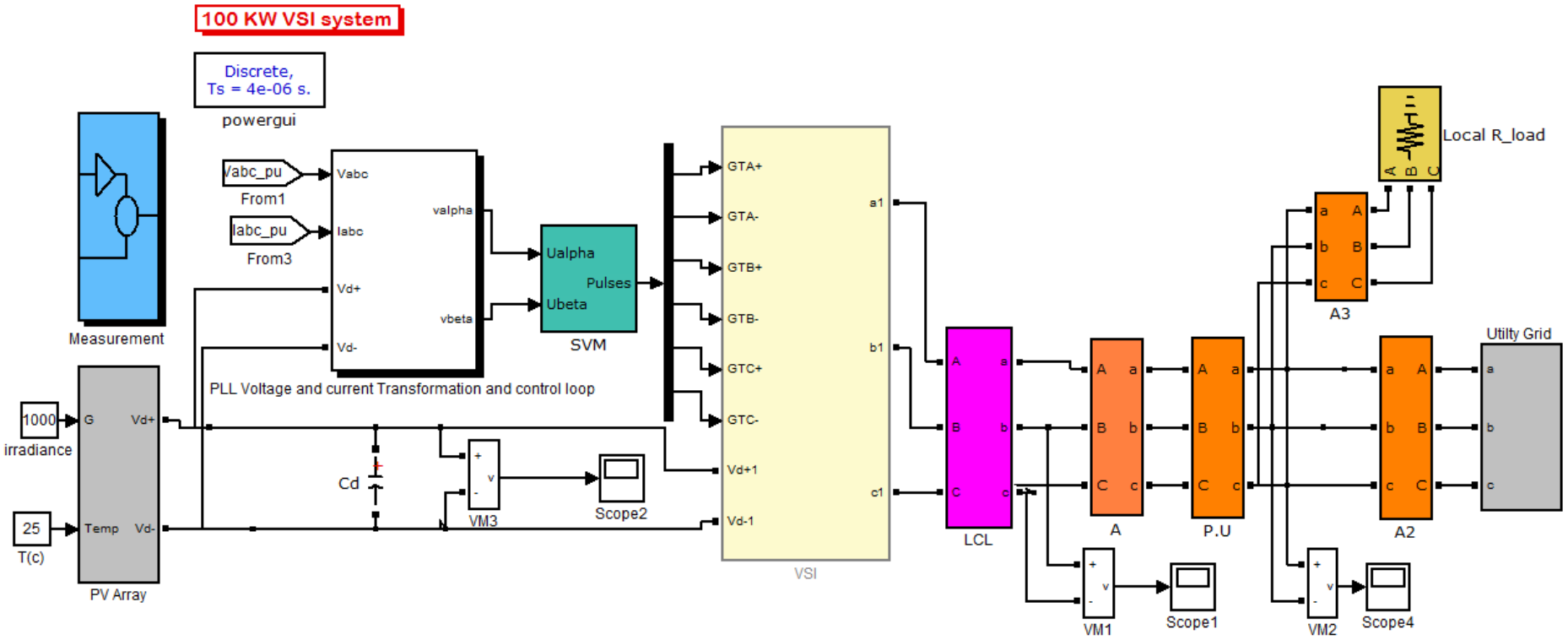

Figure 5.1 Simulink model of the three-phase grid-connected inverter

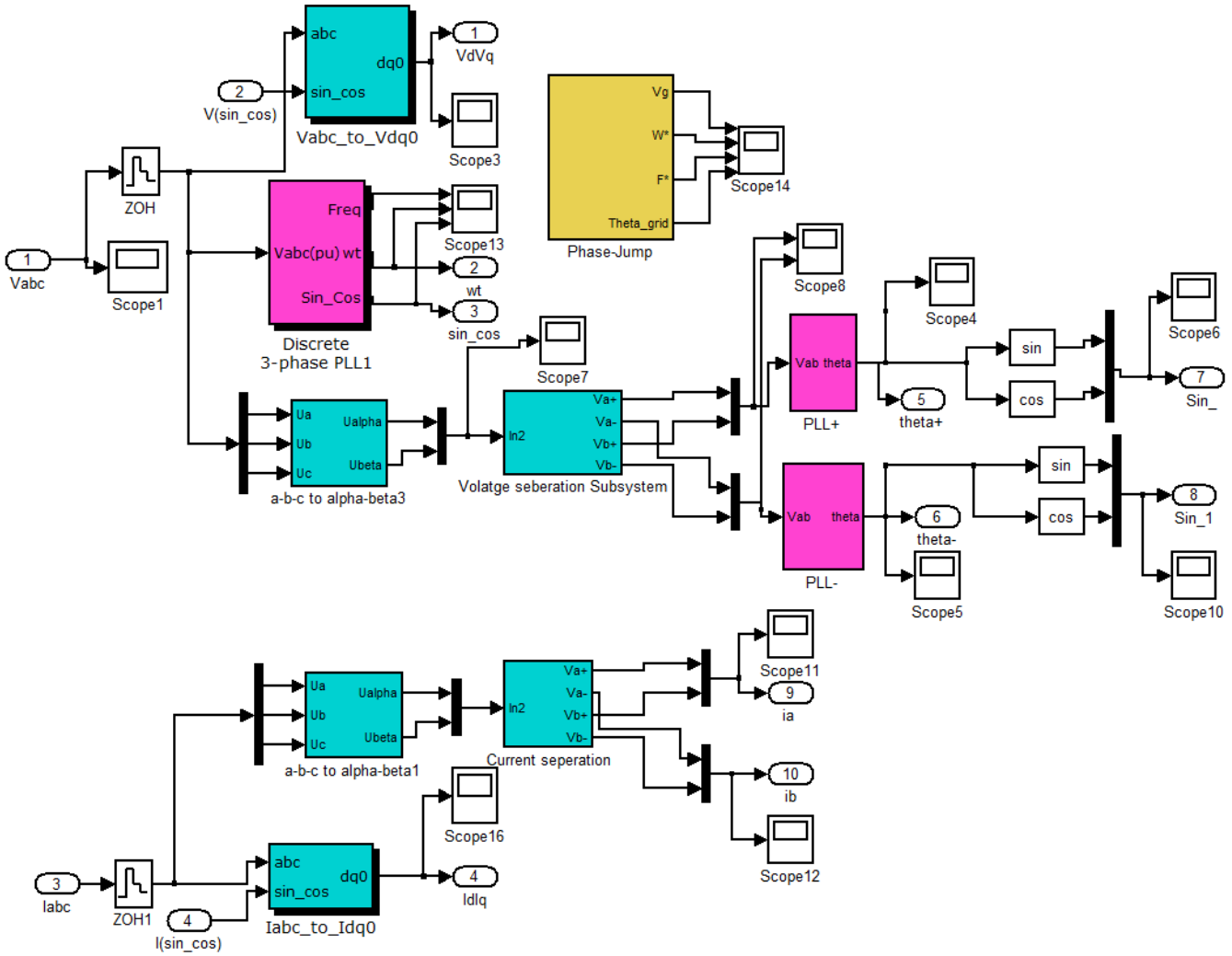

Figure 5.2 PLL, voltage and current transformations

5.2 Simulation Results

Figure 5.3 and Figure 5.4 show the three-phase grid voltage waveform and the three-phase current waveform. As can be seen from the figures, both waveforms are sinusoidal with low harmonic content. The voltage amplitude is 350 V whilst the current amplitude is 140 A. The value of PI controller parameters is shown in Table 5.2 .

Table 5.2 PI controller parameters

Parameter	The proportional gain k_p	The integral gain k_i
DC voltage controller	1.0	0.1
Grid voltage controller	7	0.0001
d-axis current controller	6	0.5
q-axis current controller	6	0.5

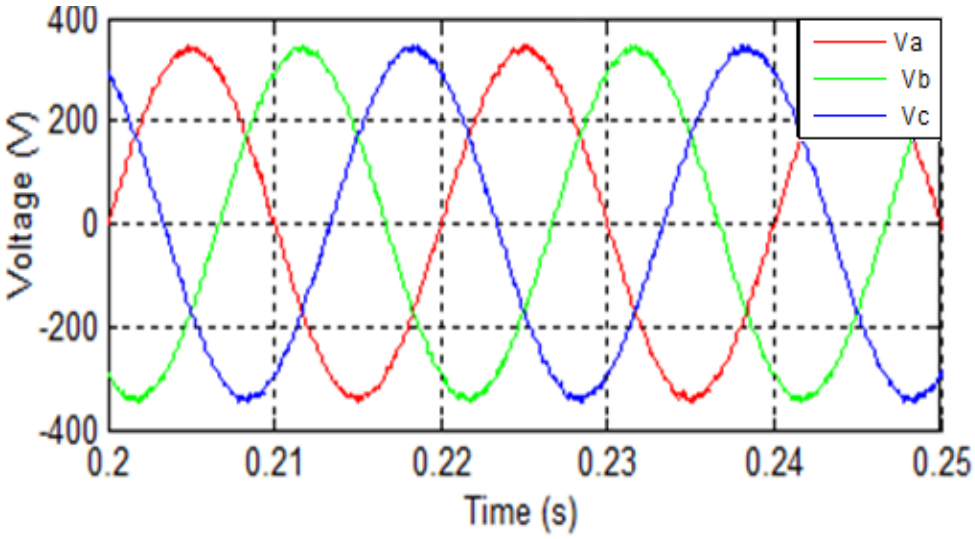

Figure 5.3 The three-phase grid voltage

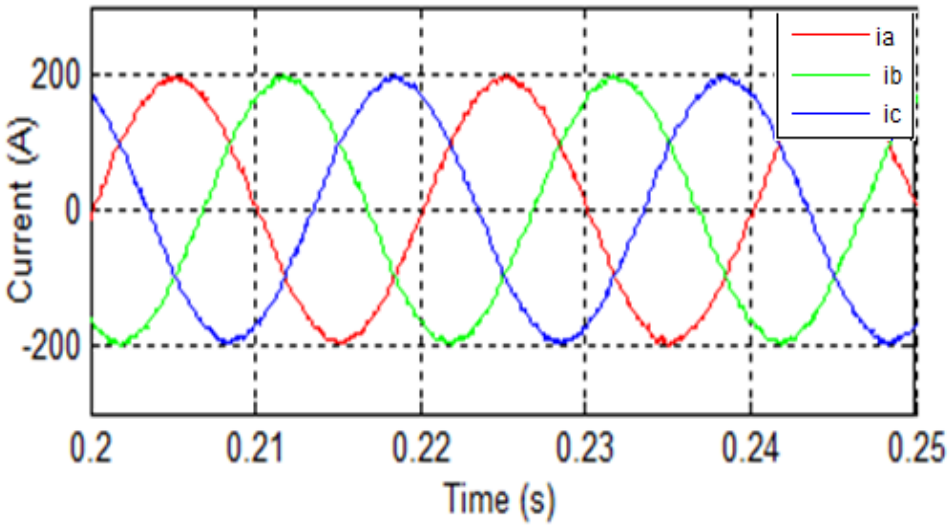

Figure 5.4 The three-phase grid current

Figure 5.5 shows the measured D.C voltage from the PV source. The DC link voltage is stable with a magnitude of 760V. Figure 5.6 illustrates the PI controller waveform of the reference and the measured DC-link voltage. The PI controller is tuned to obtain zero phase error. Therefore, the measured DC-link voltage follows the reference waveform.

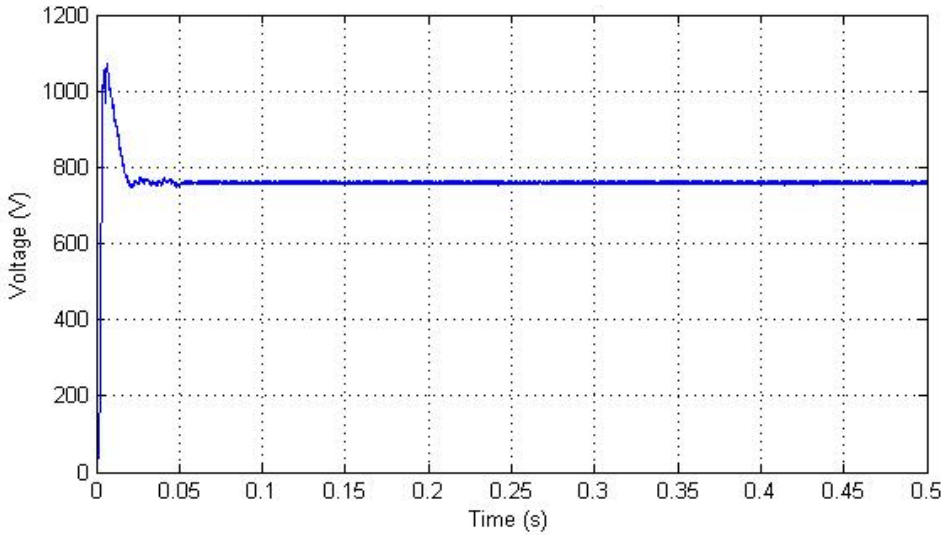

Figure 5.5 Measured DC voltage

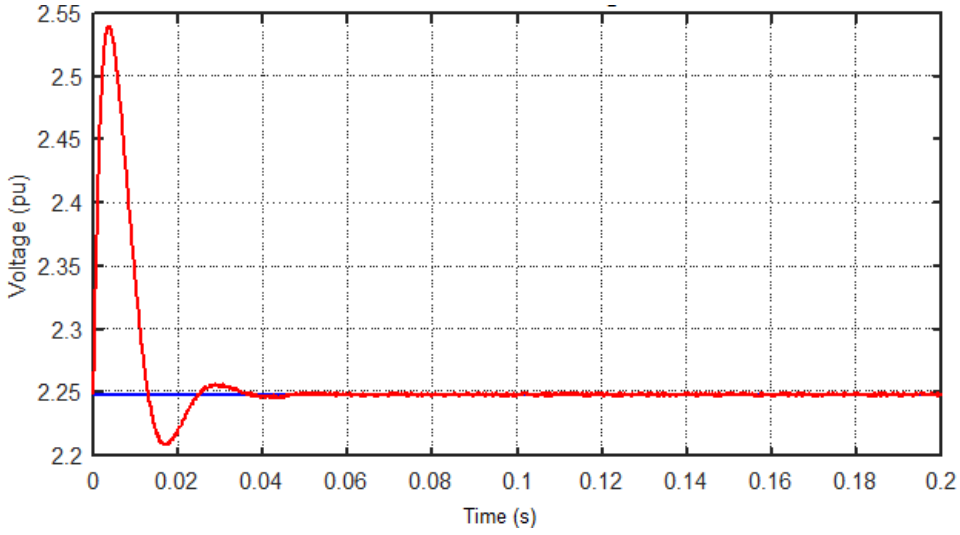

Figure 5.6 Measured PI controller for DC voltage

Figure 5.7 and Figure 5.8 shows the reference and the measured current waveform for the current controller for the *d-axis* and the *q-axis* current, i_d and i_q respectively. In the controller, the current values are expressed in per-unit with the peak value of the nominal current used as the base value. The PI controller is manually tuned method using trial and error to obtain zero error between the reference and the actual current, and the results show that this was achieved. The current reference for i_q is set to zero so that there is no reactive power applied to the inverter and the grid to achieve unity power factor. To observe the dynamic response of the system, the PI controller was tested under step response as shown in Figure 5.9. The controller shows the good performance current i_d follows the reference current i_{d-ref} with less overshoot and settling time.

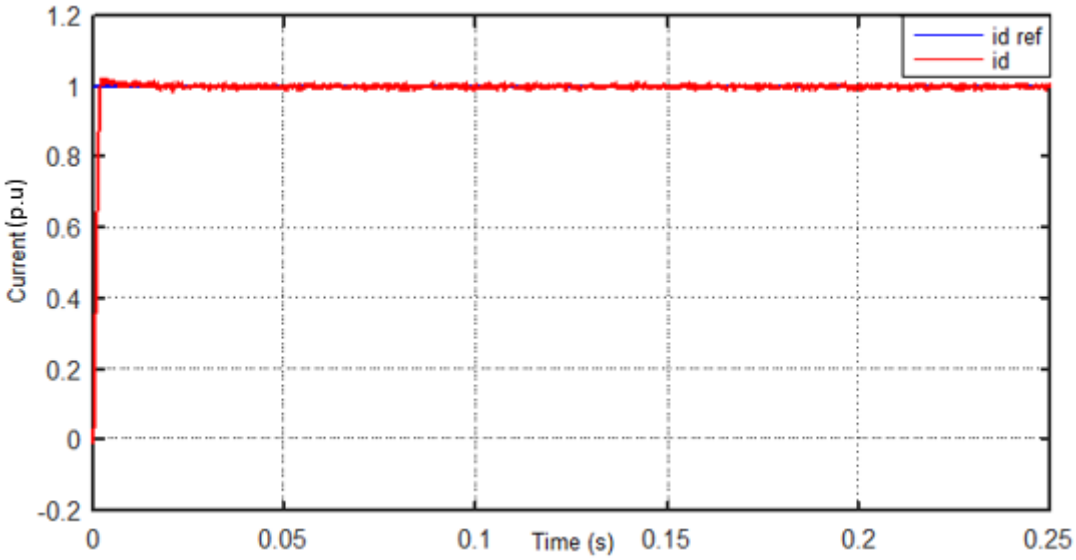

Figure 5.7 Reference and measured d-axis current

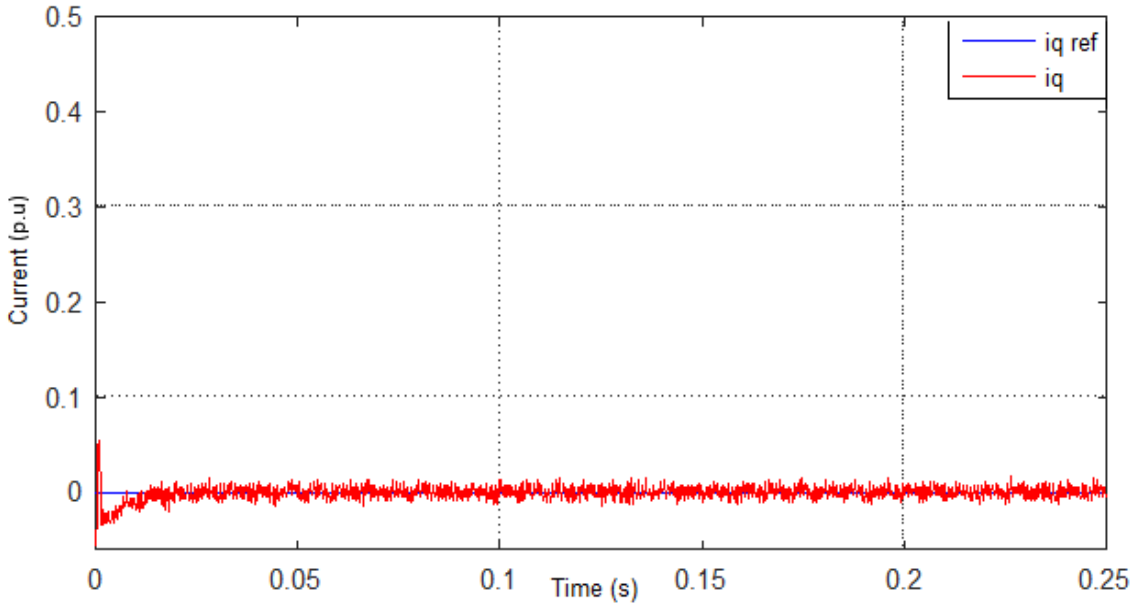

Figure 5.8 Reference and measured q-axis current

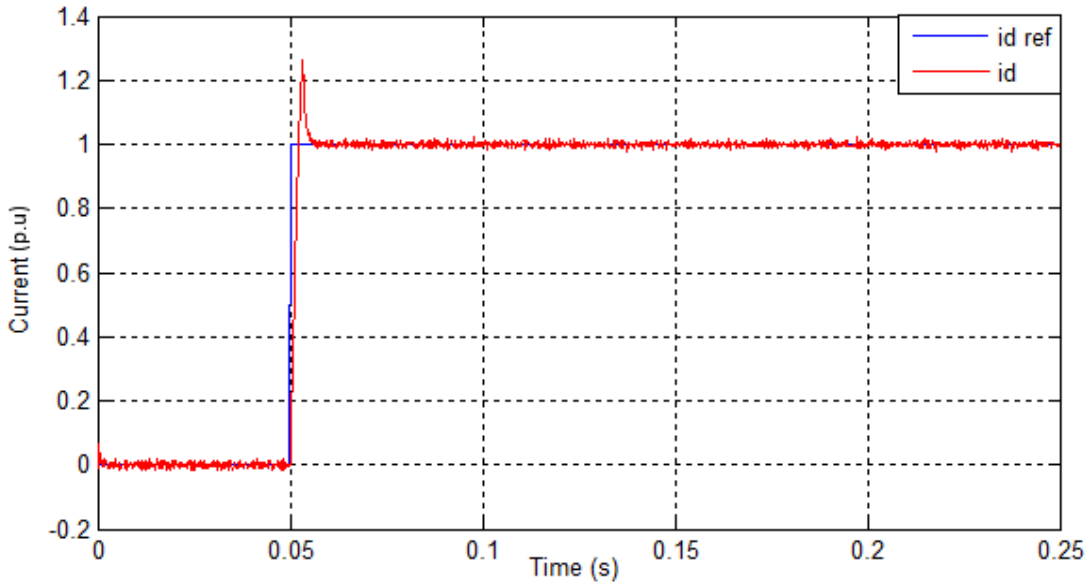

Figure 5.9 The step response of the reference and measured current i_d

Figure 5.10 shows that the magnitude of active power and the reactive power. The active power is at its nominal value of 100 kW while the reactive power is zero. This confirms that the active power is controlled by i_d and the reactive power is controlled by i_q and the control of the two currents is decoupled.

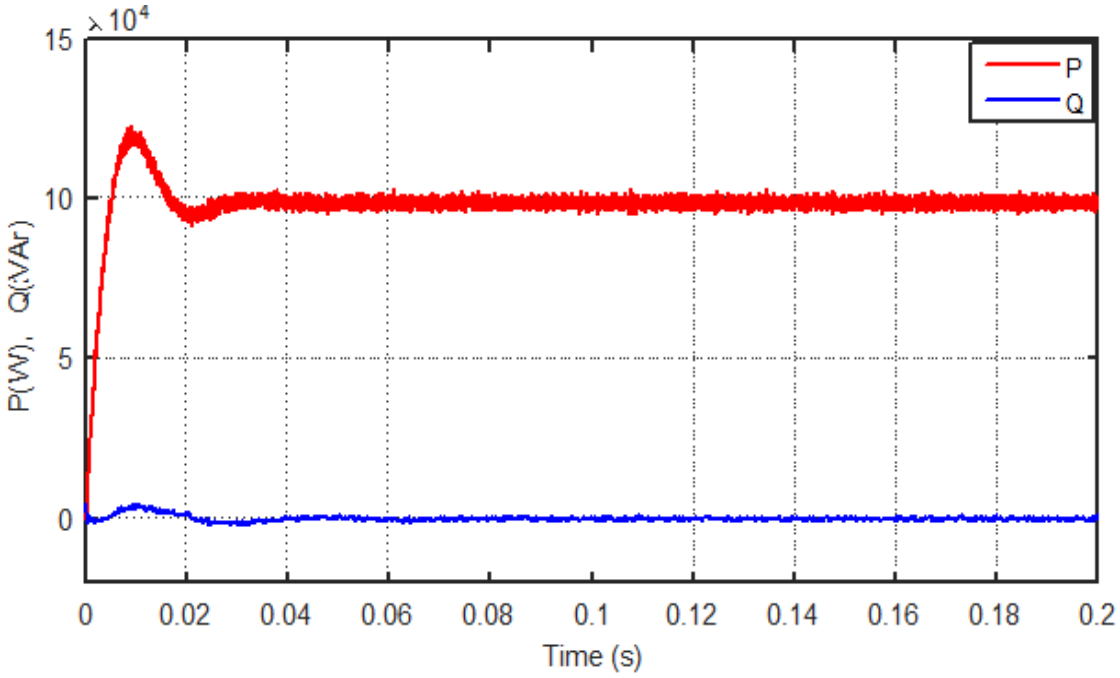

Figure 5.10 The active and reactive power waveform

5.2.1 PI controller under abnormal grid conditions

This section investigates the performance of the control technique under abnormal grid conditions. The abnormal grid conditions are faults which lead to voltage sags or swell at the inverter terminals. Most common of abnormal conditions and power quality refers to voltage sags. Two possible scenarios have been considered, the first one considers is a balanced three-phase fault leading to a voltage sag of 75% of the rated voltage for the time interval of 0.1-0.15 seconds and voltage swell of 30% from 0.17-0.19 seconds. Whilst the second case analyses an unbalanced voltage sag of 90% of the nominal voltage applied to two phases of the gird-connected inverter.

5.2.1.1 PI controller under balanced voltage sag

Figure 5.11 shows the three-phase voltage waveform during the balanced voltage sag and swell disturbance. It can be seen that the voltage magnitude in all the phases is reduced equally, but the waveforms are not distorted. Figure 5.12 shows the three-phase current waveform during the balanced voltage sag and swell. There is an increase in the magnitude of the current during the fault at a time interval of 0.1-0.15 seconds and decreased from 0.17-0.19 seconds. This is because the same amount of active power has to flow from the PV array to the grid before and during the voltage sag. Therefore, when the voltage decreases, the current has to increase to maintain the flow of active power.

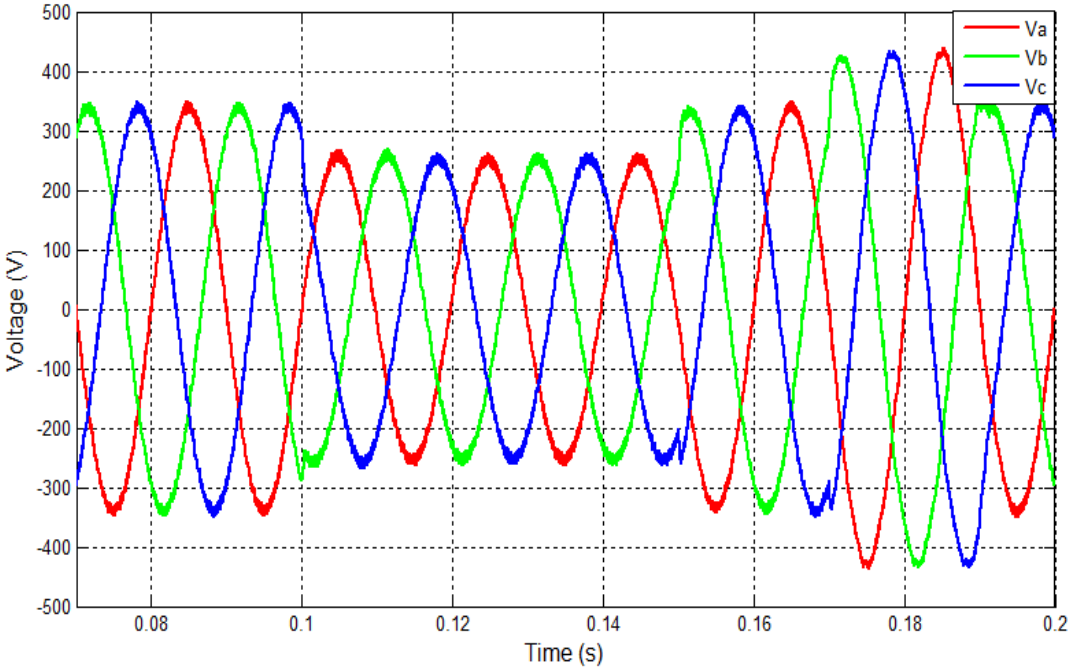

Figure 5.11 The three-phase voltage waveform under balanced voltage sags and swell

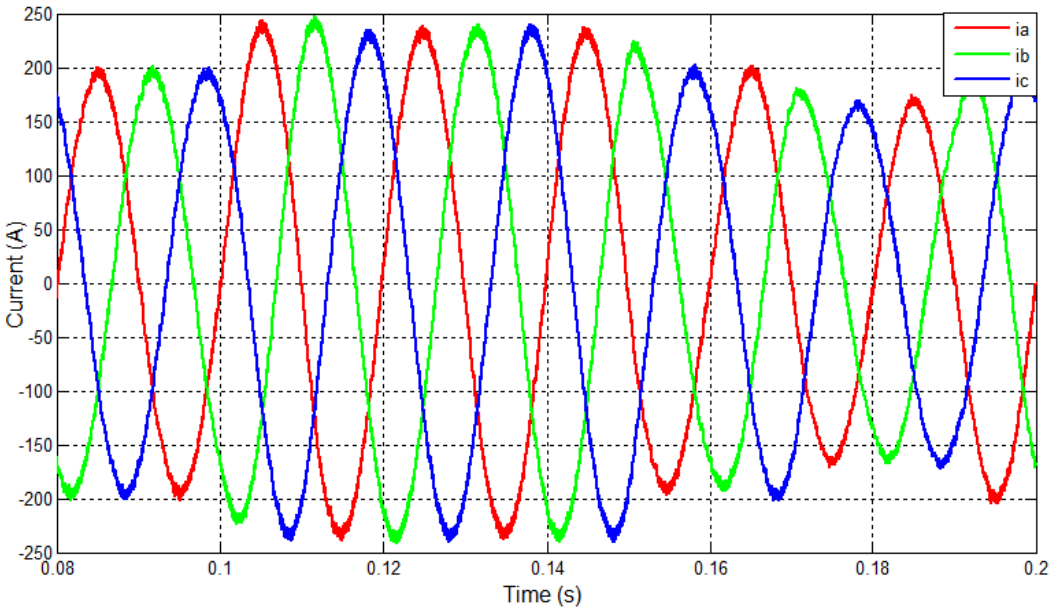

Figure 5.12 The three-phase current waveform under balanced voltage sags and swell

Figure 5.13 shows the reference and actual current $i_d{}^*$ and i_d respectively. The reference current is determined by the outer DC voltage controller, to control the active power flowing from the PV array to the grid. During the voltage sag, the current reference rises, to compensate

for the decreased voltage at the point of common coupling (PCC), and the actual current increases following the reference.

Figure 5.14 shows the reference and actual current i_q^* and i_q respectively. The reference current is obtained from the outer loop PCC voltage controller. Before the voltage sag, the actual voltage at the PCC is equal to the reference voltage and the reference current i_q^* is equal to zero. During this time, there is no reactive power flow between the inverter and the grid. During the voltage sag, the voltage at the PCC is less than the reference voltage, and the current reference i_q^* becomes equal to -0.5 pu. The actual current follows the reference, and this means that reactive power will flow from the inverter to the grid, and help to increase the voltage at the PCC during the voltage sag. The waveforms for the current controller values show that the measured current follows the reference current accurately during the voltage sag. Therefore, the controller is not sensitive to the voltage sag. The FFT of the current waveform shows a THD of 2.01% in Figure 5.15.

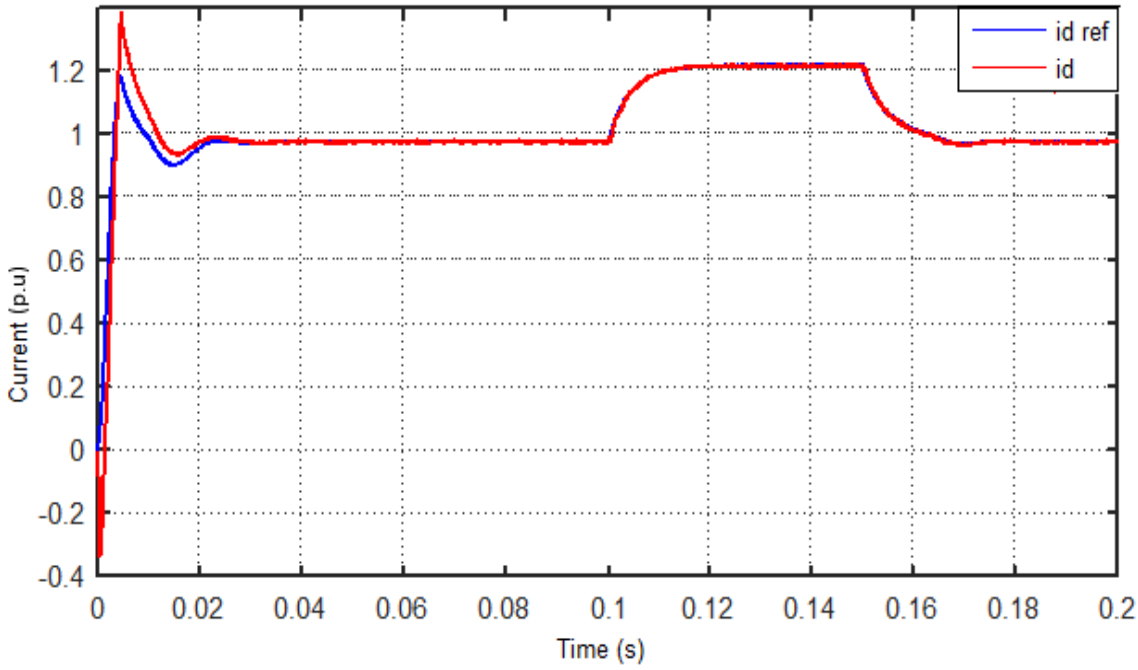

Figure 5.13 The reference and measured d-axis current i_d for PI controller

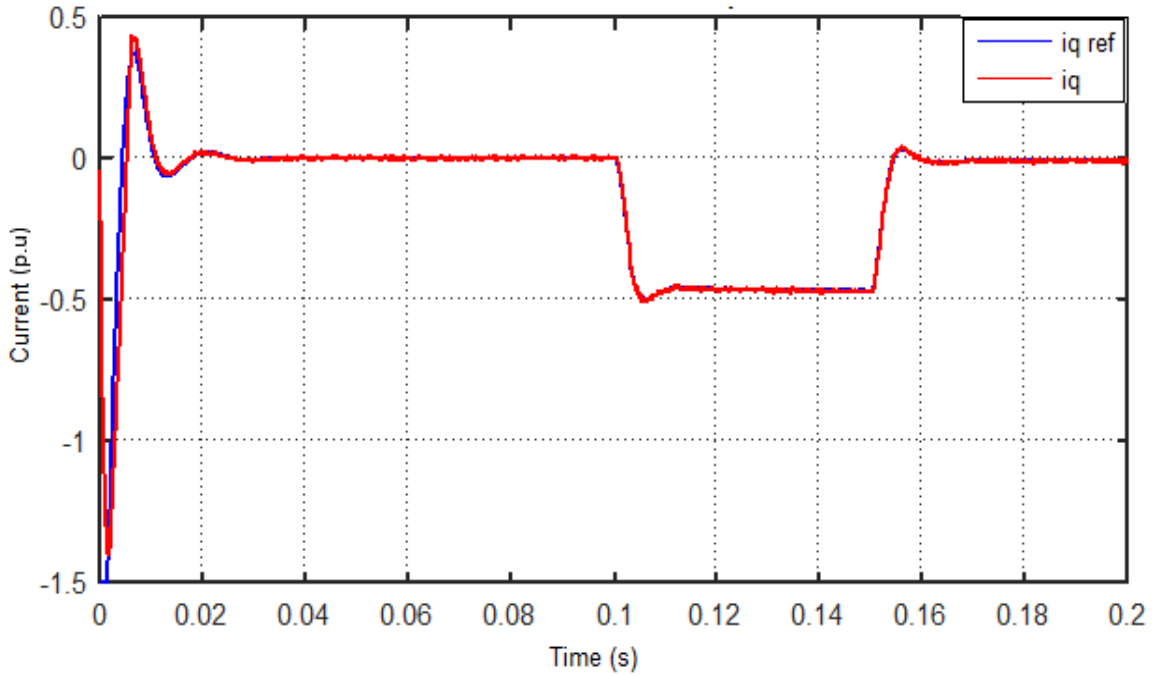

Figure 5.14 The reference and measured i_q for PI controller

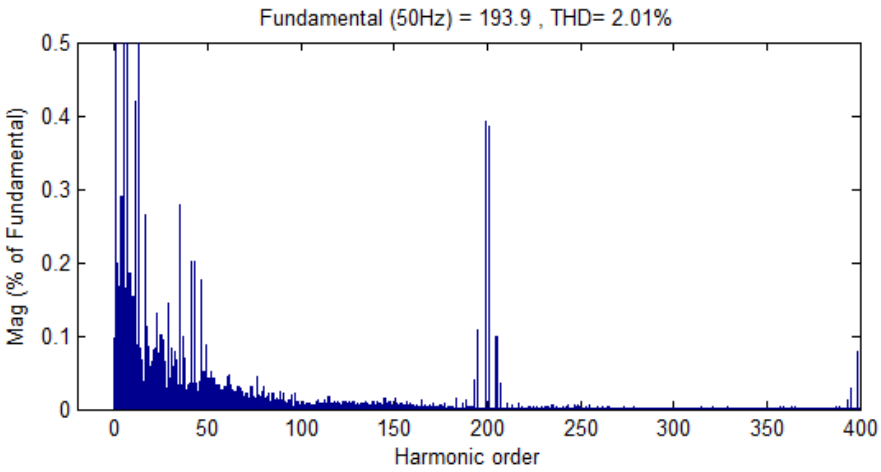

Figure 5.15 The FFT of the current waveform using PI controller

5.2.1.2 PI controller under unbalanced voltage sag

Unbalanced abnormal conditions include unbalanced voltage sags. During a voltage sag, the phase voltage decreases to between 10% and 90% of its nominal value for the duration of the fault causing the voltage sag. In an unbalanced voltage sag, the phase voltage decreases in one

or two phases. Figure 5.16 shows the three-phase voltage waveform during an unbalanced voltage sag. In this figure, two phases have been affected by voltage sag. In this case, the current will be distorted as shown in Figure 5.17. This is because the unbalanced voltage consists of positive-sequence and negative-sequence components, and the current will also consist of the same components. To deal with this matter, the current has been decomposed into positive and negative sequence components based on delayed signal cancellation method. It is worth noticing that after the decomposition, the injected current into the grid is balanced and is not distorted as shown Figure 5.18. The current components in the positive-sequence controller are also shown in Figure 5.19. It can be concluded that the measured current follows the reference current.

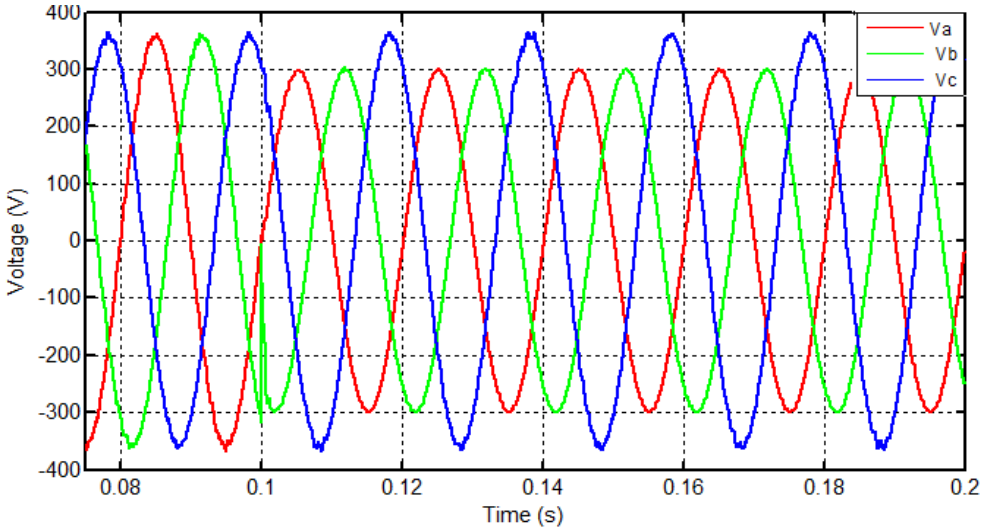

Figure 5.16 The three-phase voltage under unbalanced conditions

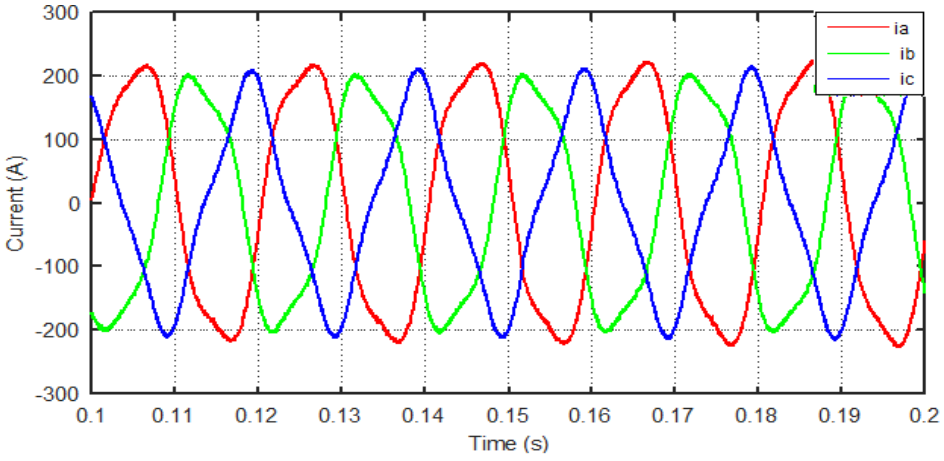

Figure 5.17 The three-phase distorted current waveform under unbalanced conditions

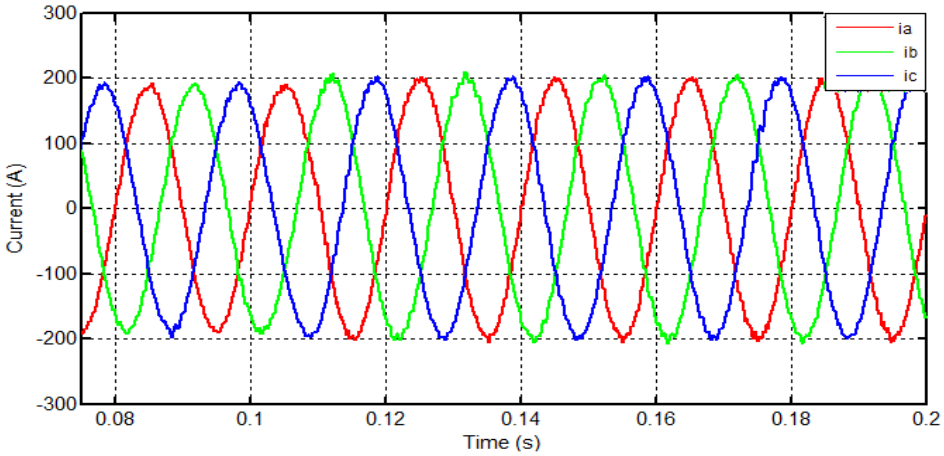

Figure 5.18 The three-phase current waveform under unabalnced grid conditions using decompestion method

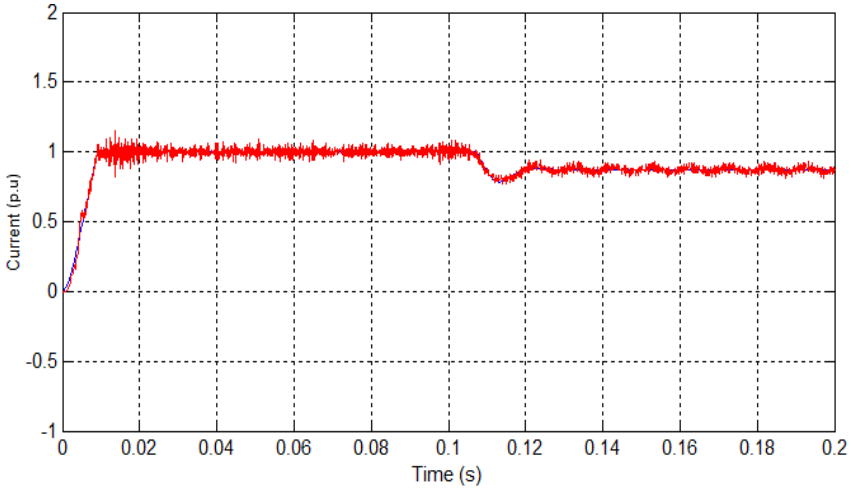

Figure 5.19 The reference and measured i_d for in the positive-sequence controller under unabalnced grid conditions

5.3 Simulation Results of PR Current Control in the Stationary Reference Frame

In this section, the three-phase grid system has been controlled using PR current controller. Figure 5.20 and Figure 5.21 show the three-phase voltage and current waveform, respectively, for the inverter, obtained using the PR controller in steady-state. Using this approach, the PR controller with a harmonic compensator generates smoother waveforms in terms of the distortion. Table 5.3 shows the controller parameters of the PR controller.

Table 5.3 PR controller parameters

Parameter	The proportional gain k_p	The integral gain k_i
DC voltage controller	1.0	0.011
Grid voltage controller	5	0.0022
α-axis current controller	3	1000
β-axis current controller	3	1000

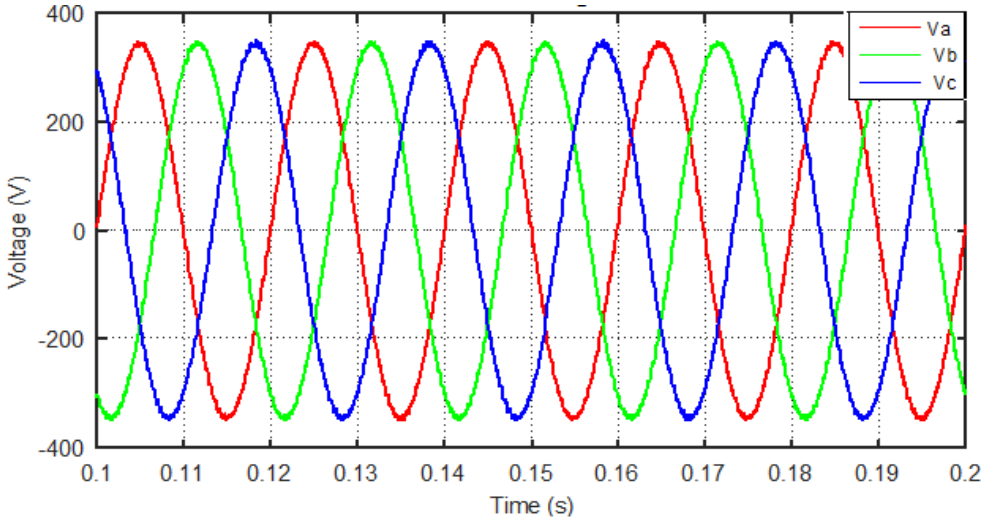

Figure 5.20 Measured phase voltage waveform

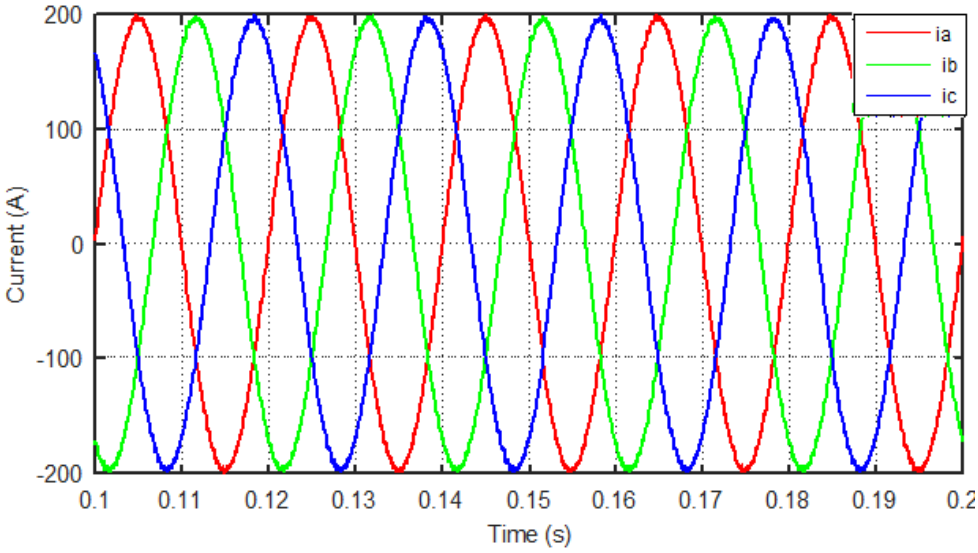

Figure 5.21 Phase current waveform

In addition, Figure 5.22 and Figure 5.23 show the alpha and beta current in the stationary reference frame. The control parameters are manually tuned using trial and error to obtain the smallest error between the reference and the measured current. The measured current in the stationary reference frame alpha and beta follow the reference current effectively as shown in the figures.

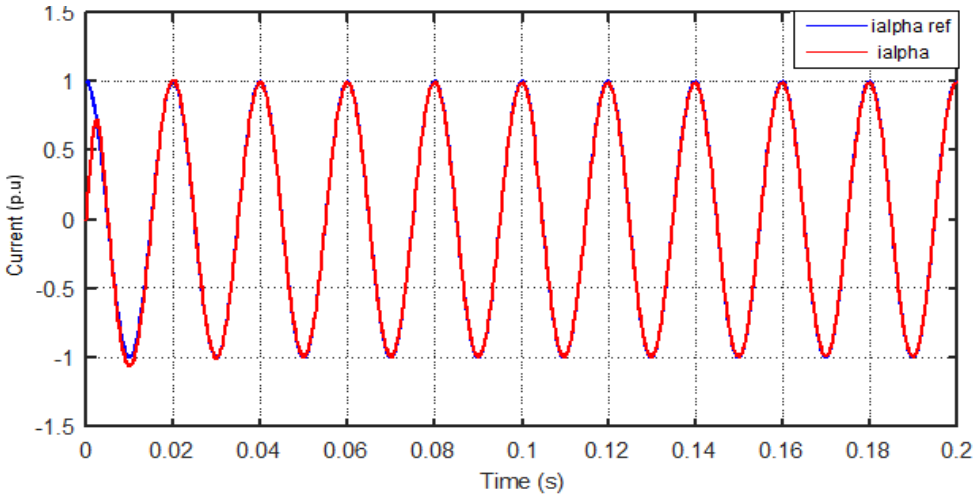

Figure 5.22 The alpha current in the stationary reference frame

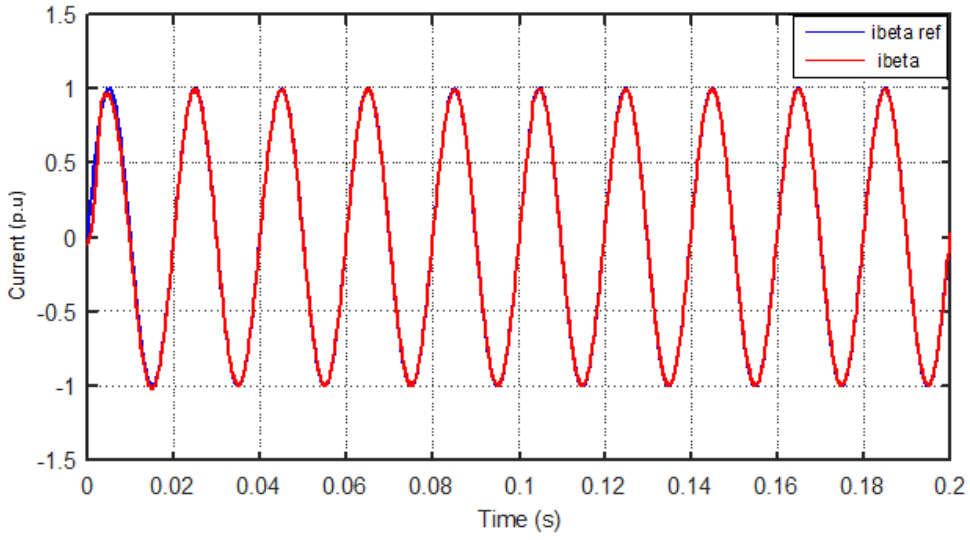

Figure 5.23 The beta current in the stationary reference frame

5.3.1 PR controller under abnormal grid conditions

The performance of the PR controller has been experienced in abnormal grid condition considering two cases. In the first case, three-phase voltage sag is applied at a time of 0.15 sec as shown in Figure 5.24. Figure 5.25 shows the current waveform under voltage sag. It can be seen from the Figure 5.24 and Figure 5.25 that the result is satisfactory in both transient and steady state.

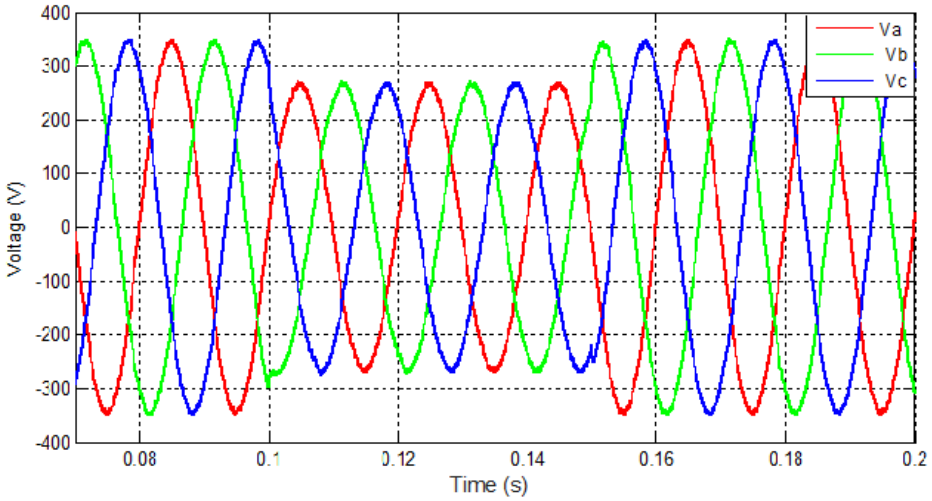

Figure 5.24 The three-phase grid voltage waveform under voltage sags

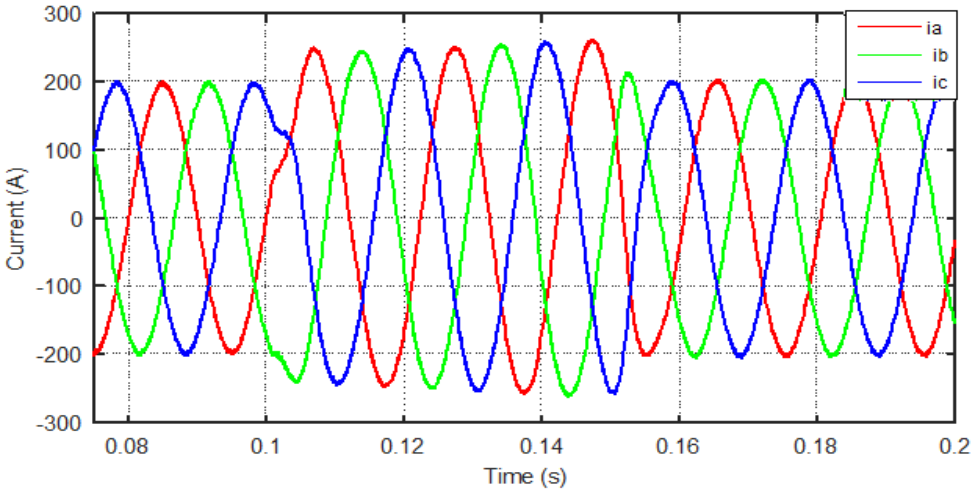

Figure 5.25 The three-phase current using PR controller

Despite the PR controller offers good performance during abnormal grid conditions. However, a sudden change in the grid such as the drop or the increased in the voltage could show a rise in regard to the error between the reference signal and the controlled signal. This, in turn, would seemingly cause a noticeable divergence from its nominal value in the transient response. In

this regard, the implementation of the PR controller is unable to keep up with the upsurge in the error, which weakens the controller functioning. The stationary reference frame alpha and beta are shown in Figure 5.26 and Figure 5.27, which illustrate the error between the reference and the measured current is approximately 8% when there is a sudden decrease or sudden increase in the voltage. Figure 5.28 shows the FFT analysis of the current waveform using PR controller. It can be seen that the THD and harmonics speccturm of the phase current is smaller compared with that the THD and harmonics speccturm of PI controller in Figure 5.15.

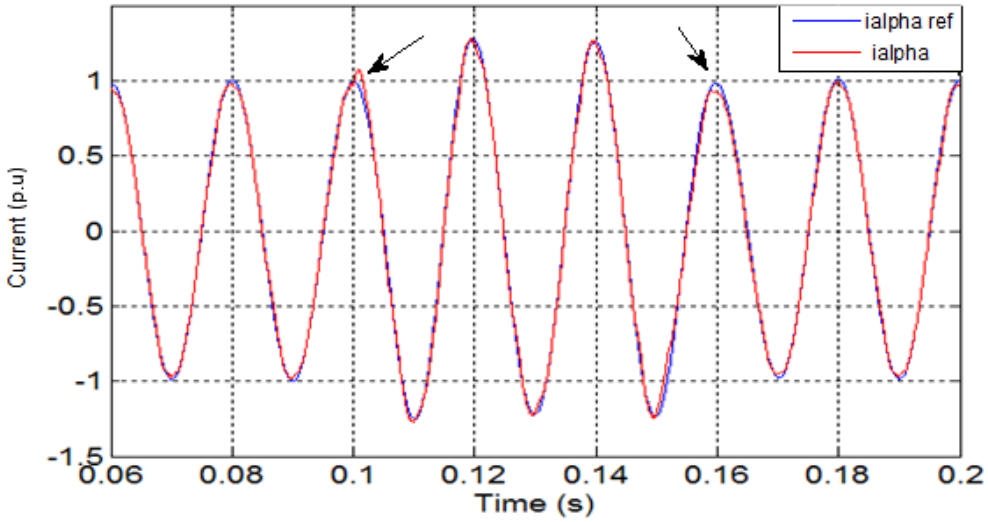

Figure 5.26 The alpha current waveform

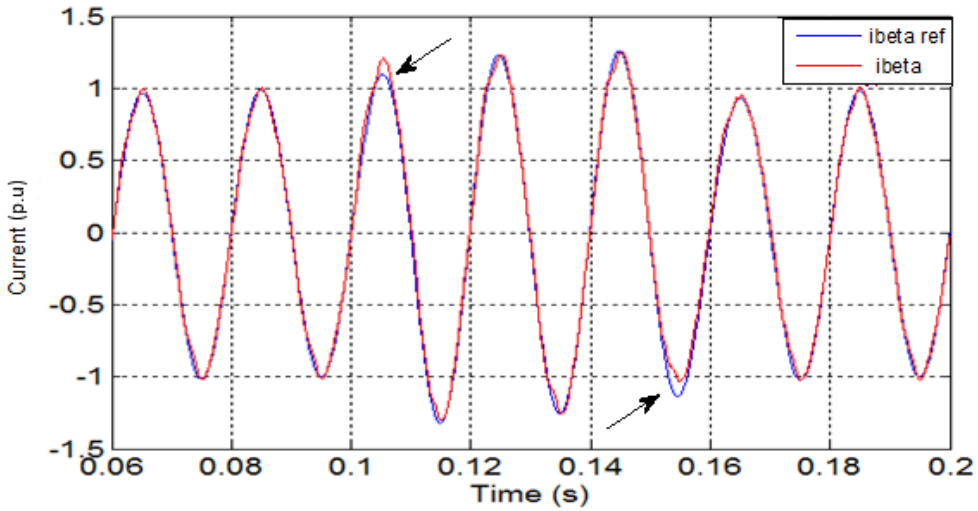

Figure 5.27 The beta current waveform

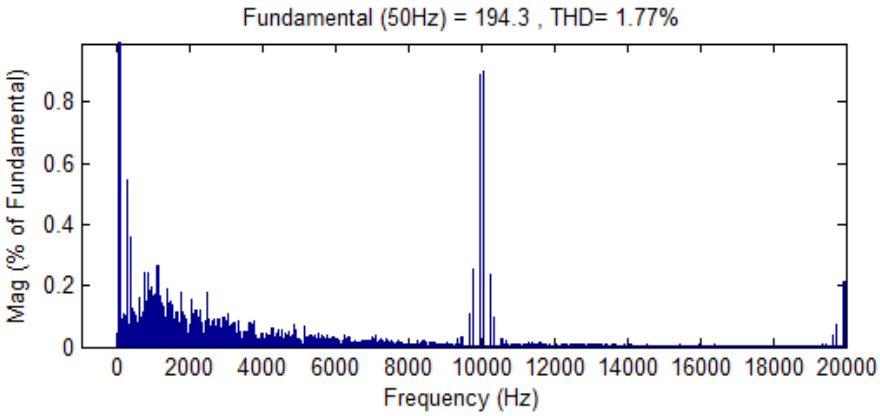

Figure 5.28 The FFT of the current waveform using PR controller

To overcome this problem, an improvement in the current control using a novel adaptive PR controller based on look-up-table is implemented and demonstrated in chapter 6.

5.4 Hardware Equipment for the Three-phase Grid-connected Inverter

Figure 5.29 shows an overview of the three-phase inverter rig and supporting equipment. The experimental rig consists of a metal case, DC source, supply variac transformer and RL loads. A large metal case is used for the purpose of putting all the components together, as can be seen in Figure 5.30. The metal case contains a three-phase inverter, control board, and gate drive which were all built in Newcastle University's electronics laboratory. To supply the low voltage electronics, an auxiliary power supply unit (PSU) is included in the equipment enclosed in the case. For short-circuit, current protection, a miniature circuit breaker (MCB), and fuses rated at different current values are used. The metal case is grounded to ensure safety from earth fault currents. Contactors with delay timers are used to connect the inverter to the DC power supply, and to the grid respectively. The DC contactor is switched first to charge the DC link capacitor with and after the set delay, during which the DC link capacitor gets fully charged, the AC contactor can be switched on. The equipment inside the case is shown in Figure 5.30. Three LEM CAS6NP current sensors are used to measure the current which is fed back to the controller through a sensor interface board and an analogue-to-digital converter (ADC). The grid voltage is measured using 6 AD215AY isolated voltage sensors which measure the voltage at the point of common coupling (PCC) between the inverter and the grid, and at the grid side of the variac. The voltage measured at the grid side of the variac is used to synchronize the inverter to the grid using a PLL.

Figure 5.29 Three-phase grid-connected inverter test rig

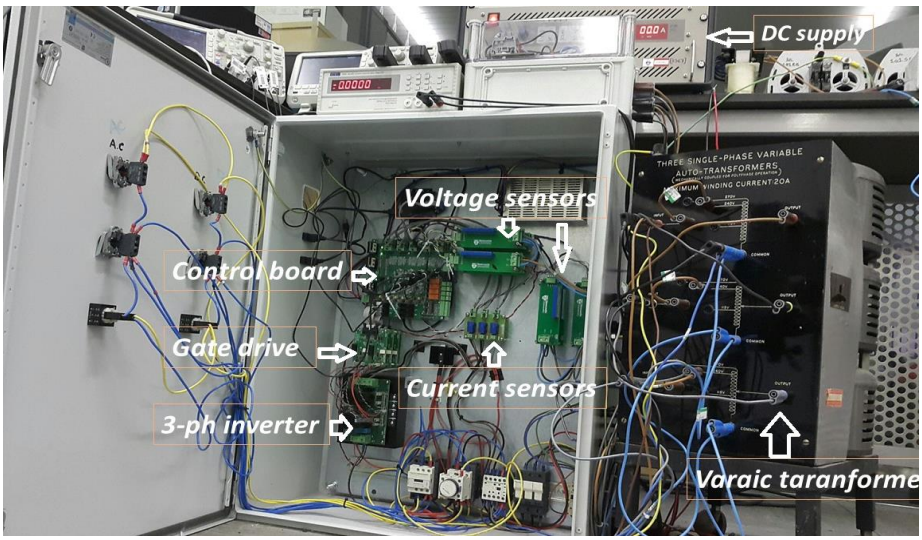

Figure 5.30 The three-phase inverter rig metal cage from inside

Since the project concerns a three-phase grid-connected inverter, it has been connected to the grid via a 415 V mains supply in the experimental study. In this case, a supply variac transformer and isolation transformer are interfaced between the grid and the rig as shown in Figure 5.29.

The three-phase variac transformer is used in order to effectively regulate the voltage from the mains supply to the experimental grid-connected PV inverter system. In addition, it allows the DC link voltage to be used at low values instead of using the conversion ratio between DC/AC applications. However, the variac is a non-isolated transformer which has no protection from any feedback of the DC current into the mains supply. Thus, to overcome this issue, an isolation

transformer is connected between the grid's mains supply and the variac transformer. The connection is Δ-Y.

In addition, Figure 5.29 shows the LCL filter connected the rig. An LCL filter has been used in the experiment to smoothe the output waveform from the AC side of the inverter and thus reduce the harmonic of the switching frequency.

Two three-phase inductances are tapped to five different readings in order to test the effect of various values of inductances. The inductor L_1, is tapped from 0.3mH to 0.8mH and L_2, is tapped from 0.1mH to 0.3mH with a rating current of 15A. Different values of inductances and capacitances have been tested and the most suitable values chosen for a 10kHz switching frequency.

5.5 Control Board and DSP

In the practical tests, the three-phase grid connected inverter uses a Texas Instrument eZdsp F28335 Digital Signal Processor (DSP) which uses an algorithm to produce various series of digital pulses patterns. This DSP generates high processing speeds that allow control of the power electronic switches dependent on the results of sophisticated mathematical calculations. The F28335 DSP is connected to the general interface control board as shown in Figure 5.31. The general interface board has been designed and built at Newcastle University by Dr. David Atkinson and has following features:

- It is modified to have six drive interfaces and allow six pairs of PWM output, meaning that it can be used in multilevel converter applications.
- It has six voltage window detectors for the interface of the ten sensors which can be used in case of any excessive voltage or current occurring.
- The analogue signal is transformed to a digital signal via an analogue-digital converter (ADC).
- The digital signal can also be converted to the real time from the four digital-analogue Converter (DAC) channels on the board.

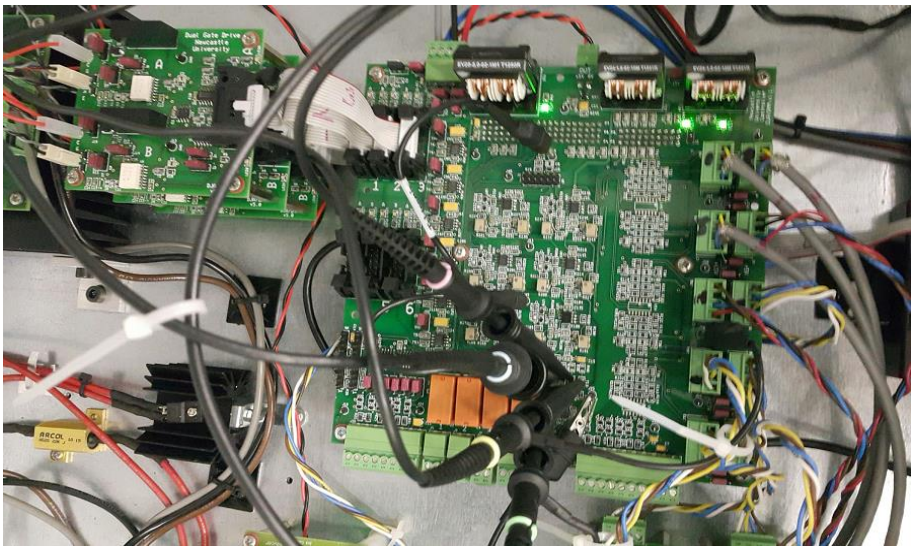

Figure 5.31 Newcastle University control board

Once the functions have been coded, the controller can communicate with the LabVIEW program via an RS232 serial interface port in order to be monitored and tested by the user in real-time. A LabVIEW software control program is chosen because it provides a safe technique for communication with the rig during the test operation in online applications as shown in Figure 5.32. A LabVIEW control panel is programmed to enable/disable the microcontroller functions such as sending a reset signal to the microprocessor by pressing buttons.

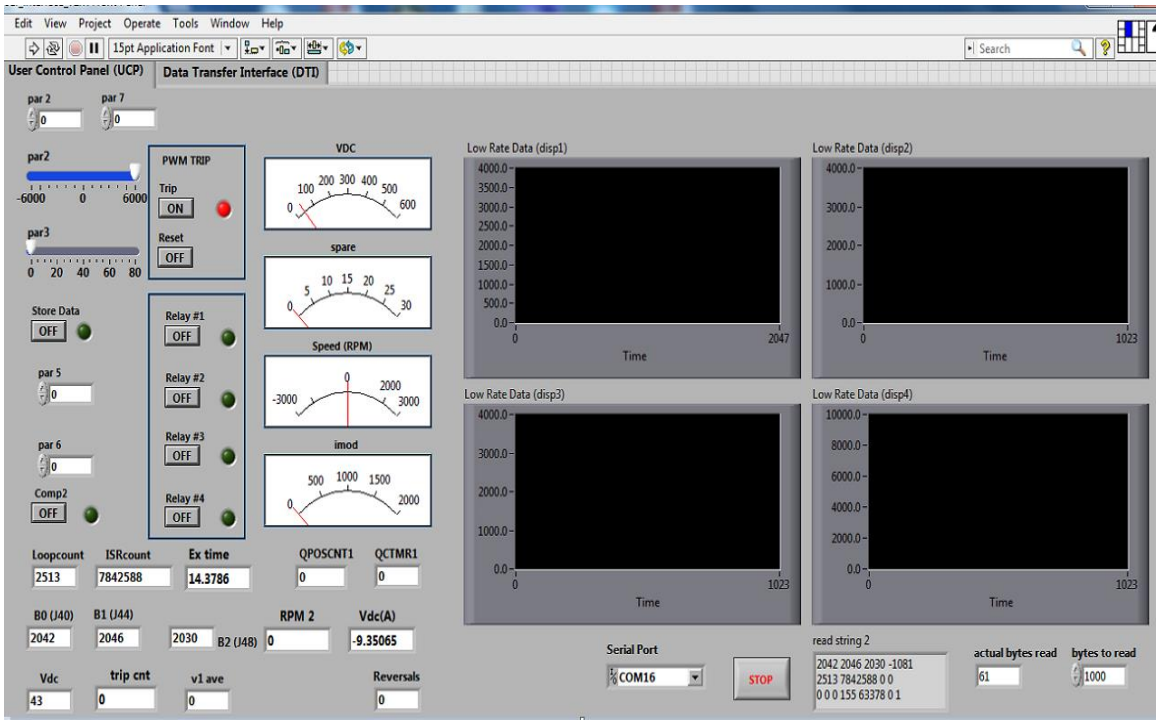

Figure 5.32 Screen shot of LabVIEW

5.6 Power Wiring Diagram

The experimental system is designed and installed to provide interaction between PV sources and the utility grid in the UG lab bay A. Figure 5.33 shows a general overview of the power wiring diagram for the rig. A three-phase inverter is supplied by a DC source and connected to the LCL filter. The rig has two DC switching contactor (D_1 and D_2) from the DC side and one contactor (A) from the AC side along with the main MCB for safety and emergency purposes. When the DC link is switched on, a high inrush current will flow into the DC link circuit. A timer delay is connected to the contactor (D_2) to hold it for a few seconds in order to allow the DC capacitors to charge up. A resistor is connected in parallel with the contactor and a diode is connected on the DC side to prevent the reversal of the current into the DC power supply. In addition, the rig has one voltage sensor on the DC link voltage, three voltage sensors in the AC side and three current sensors also on the AC side. In order to protect the DC link capacitors from excessive current, a fast fuse is placed before the output of the three-phase inverter which has the ability to blow up in case of over-current.

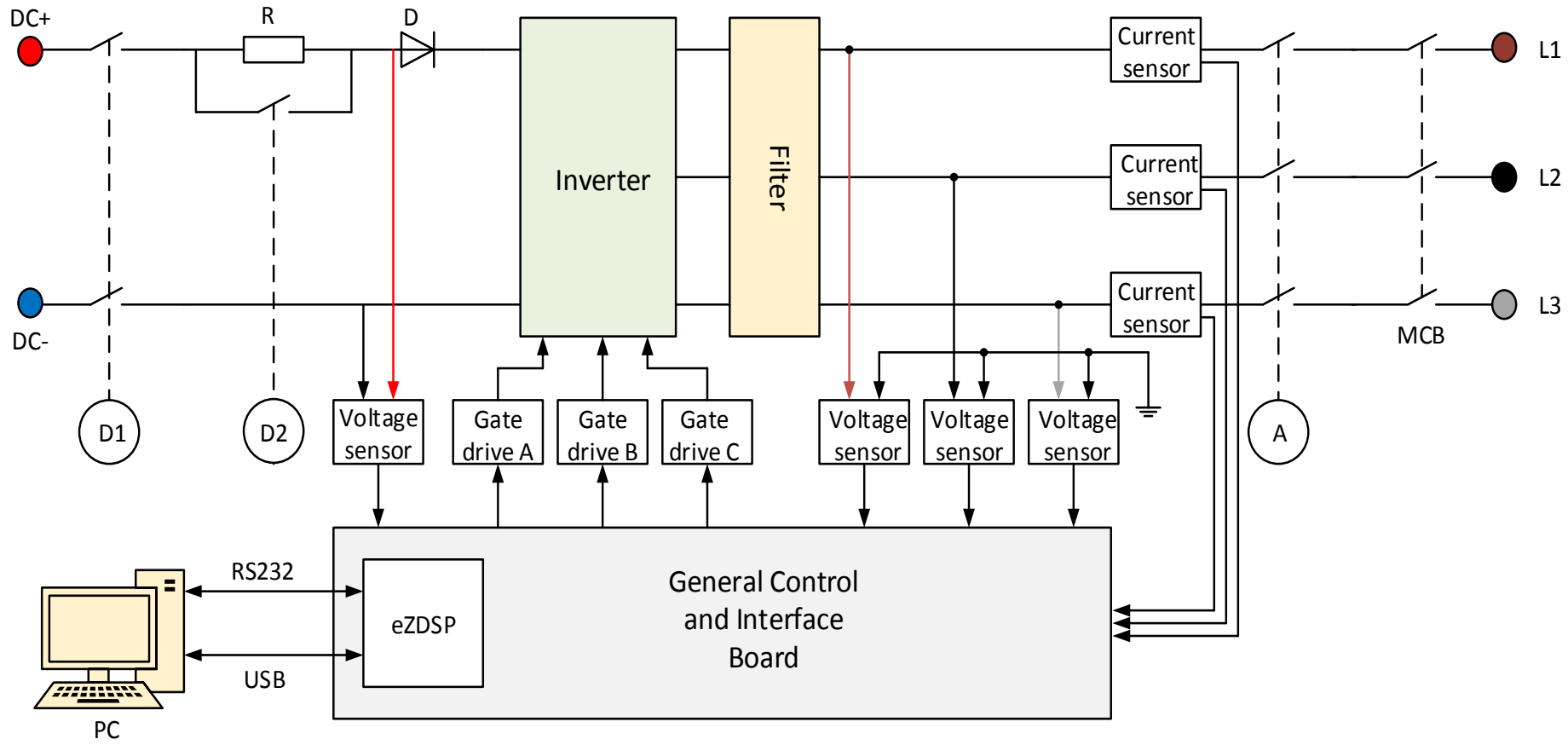

Figure 5.33 Power wiring diagram

5.7 Grid Connection Sequence

In order to connect the three-phase inverter to the grid, the following procedures are employed:

1. All AC and DC switches are switched off.
2. The three-phase variac is set to zero voltage to make sure that no voltage is applied to the system.
3. The program code is run and it is checked that the phase-locked loop is working.
4. The DC supply is switched on to charge the capacitors and after a few seconds, the AC side is switched on.
5. The three-phase variac is gradually increased and DC link voltage is established to feed the inverter input until it reaches the maximum allowable values. However, the current demand is still kept at zero.
6. The LabVIEW control program is switched on and the current demand is gradually increased in order to deliver the current to the grid network.

5.8 Experimental Results of PI and PR Controller

To validate the control technique for the system in the laboratory, the system is scaled down and has been tested, the specifications of the system parameters have been accurately chosen based on mathematical equations [146-148]. The experimental parameters are calculated based on equations (5.1) to (5.10). The nominal operating parameters are shown in Table 5.4.

Table 5.4 Three phase inverter practical parameters

Parameter	Value
The output power	300W
Grid voltage (line to line) V_L	40 V
Inverter side inductance	0.6 m H
Grid side inductance	0.175 m H
DC-link voltage	50 V
DC capacitor	1500 µF
Switching frequency	10 kHz
Sampling frequency	10 kHz
filter capacitor	20 µF

5.8.1 Experimental result of PI current control

The harmonic content of the grid voltage was stable throughout the course of the measurements. Figure 5.34 and Figure 5.35 show the three-phase voltage and the current waveform using the PI current control technique. The results were obtained under normal steady-state grid operating conditions with a constant grid voltage magnitude, constant frequency and constant power from the DC power supply. As can be seen from the figures, both waveforms are sinusoidal with low harmonic content. The same effect is also observed in the low ripple in the current result.

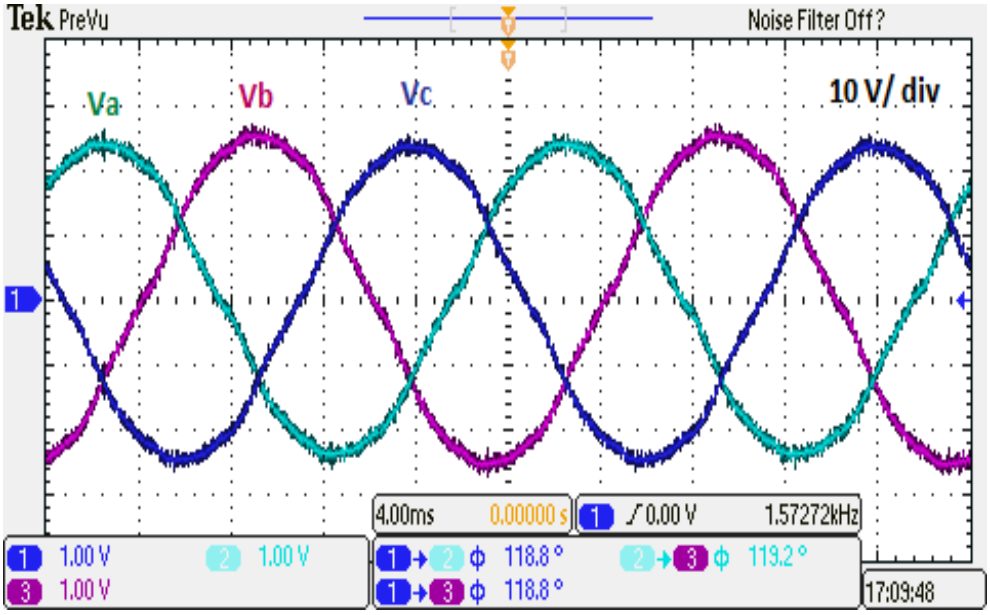

Figure 5.34 Three-phase voltage waveform at PCC

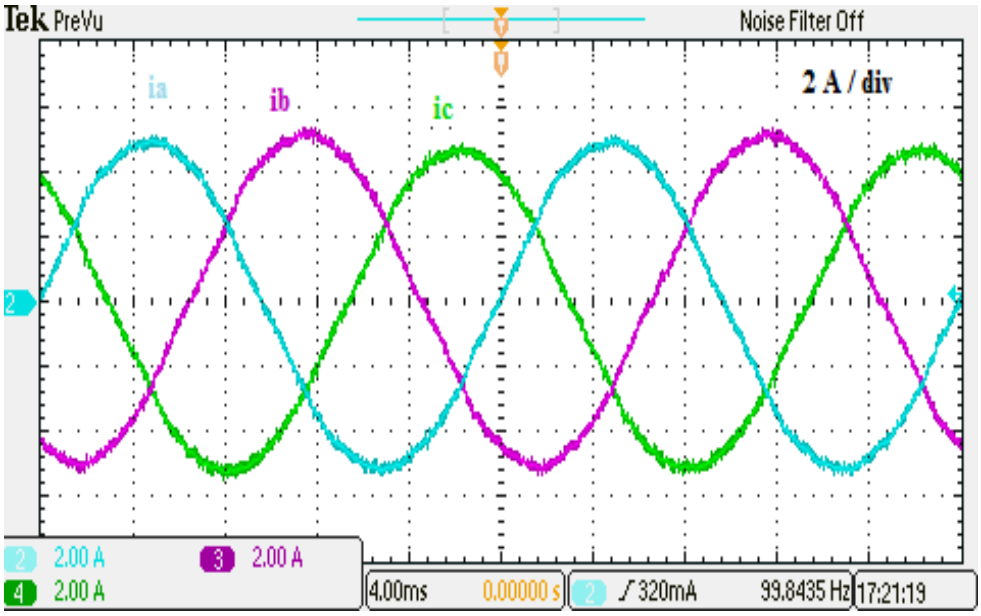

Figure 5.35 Three-phase current waveform using PI controller

Figure 5.36 shows the reference and measured i_d and i_q of the PI controller. It can be seen, that the measured current i_d follows the reference current i_{d-ref} and the current i_q follows the reference current i_{q-ref}. This demonstrates that the controller is working effectively.

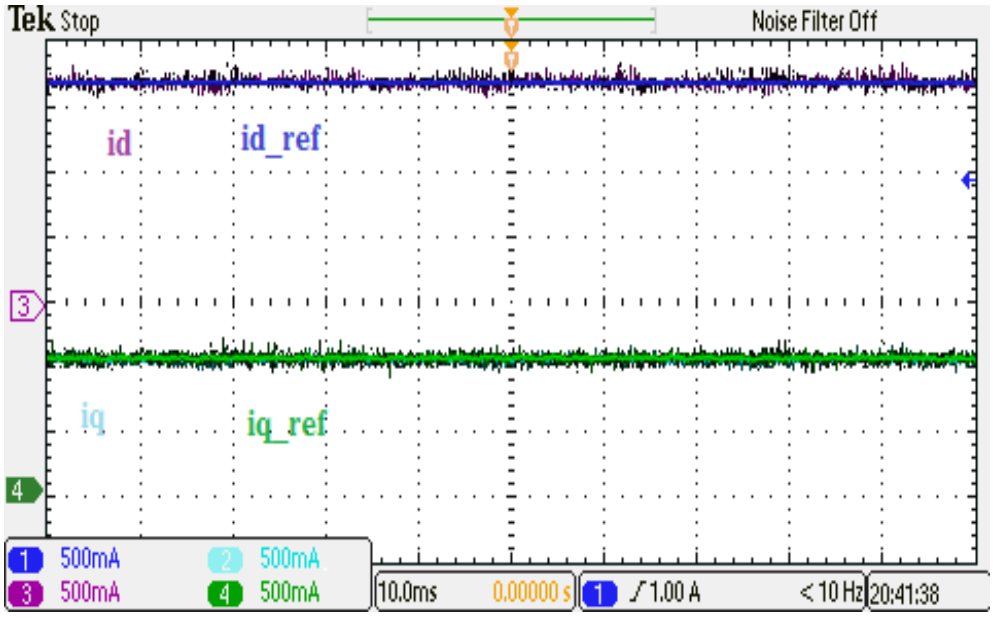

Figure 5.36 The reference and measured i_d and i_q

To observe the dynamic response of the system and the control performance compared with the simulation results, the PI controller was tested by applying step reference current as shown in the Figure 5.37. The controller shows the good performance with current i_d following the reference current i_{d-ref} with only a small overshoot and settling time 0.2 sec.

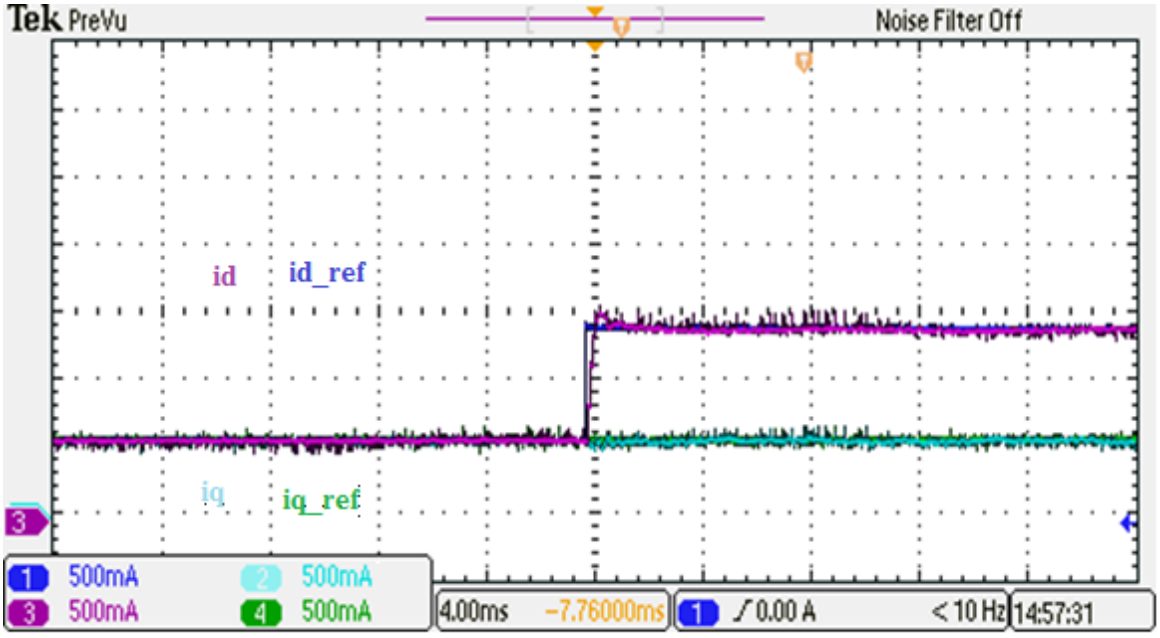

Figure 5.37 The reference and measured i_d and i_q under step response

5.8.2 Experimental result of PR current control

In addition, the performance of the PR controller was tested in a grid-connected system. Figure 5.38 shows the three-phase current waveform with phase-a of the grid voltage, which demonstrates that the PR current controller with harmonic compensator generates smoother waveforms in terms of the distortion and this indicates that PR controller works effectively.

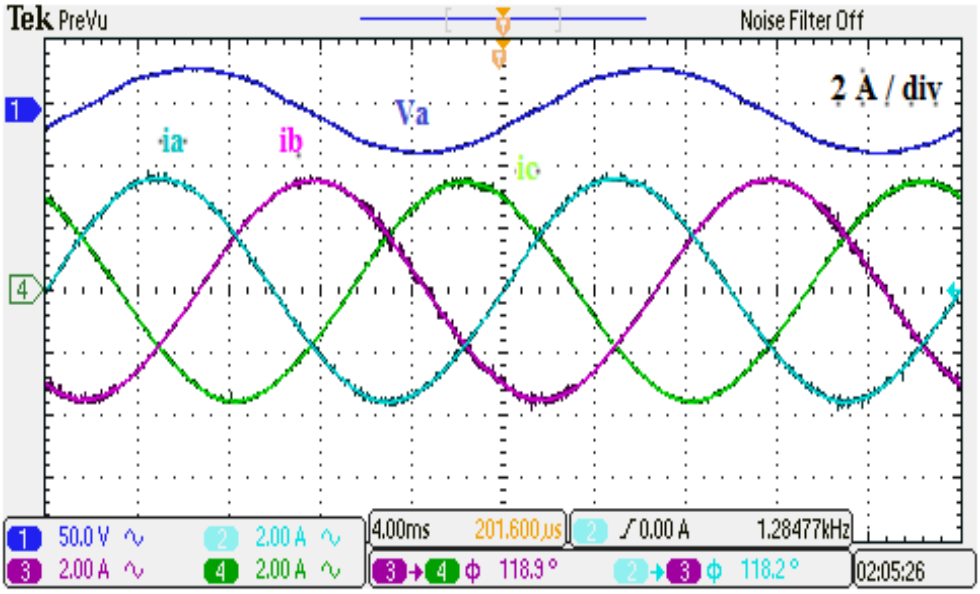

Figure 5.38 The three-phase current waveform with grid voltage using PR controller

Figure 5.39 shows the reference and measured alpha α current waveform and the reference and measured beta β current waveforms respectively. There is a phase shift of 90 degrees between the alpha and the beta current. In addition, both results case show that perfect tracking is achieved.

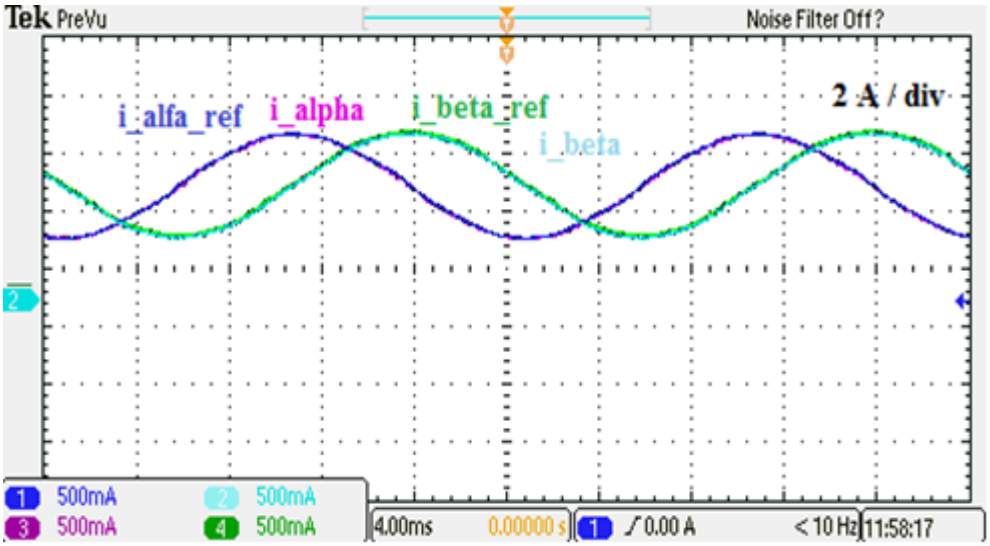

Figure 5.39 The reference and measured alpha and beta currents waveform

The next results show the step response of the three-phase output current of the inverter waveform connected to the grid using the PR current controller. This test was performed to observe the dynamic response, stability, and performance of the control system. Figure 5.40 shows the three-phase current waveform with step response. In this figure, the quality of the output current waveform is shown. Figure 5.41 shows the reference and measured alpha α current waveform with step response. The transit and the dynamic responses with fast response has been considered.

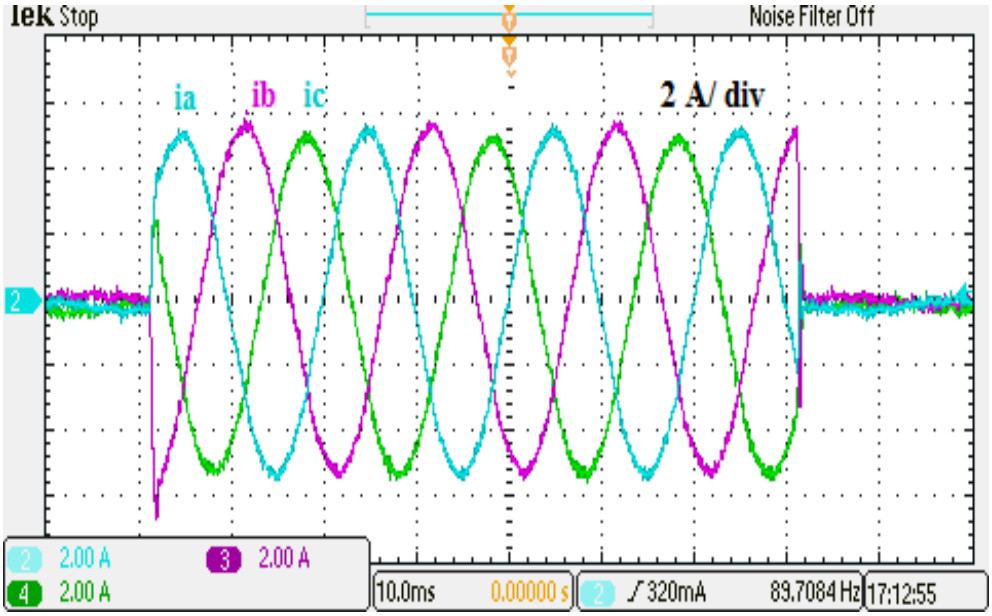

Figure 5.40 The current waveform with step response

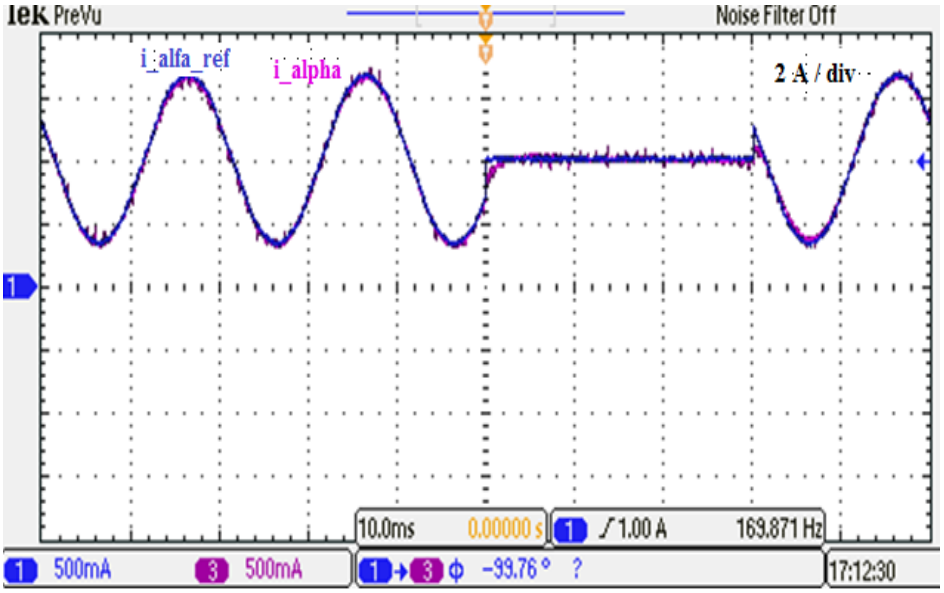

Figure 5.41 The alpha reference and measured current waveform with response

By adding the harmonic compensator to the PR controller, an attenuation of the current waveform in terms of total harmonic distortion THD is obtained as shown in Figure 5.42. The results here involve Fast Fourier Transform (FFT) analysis to show a reduction harmonics in and good performance is clear in terms of accurate tracking and a fast dynamic response. According to the IEEE standard 929, the odd harmonics from 3^{rd} to 9^{th} should be lower than 4% and from 11^{th} to 15^{th} should be lower than 2%. In Figure 5.42, the highest harmonics are the 5^{th} and 7^{th} which are 1%, while the 11^{th}, 13^{th} and 15^{th} are less than 0.3%. Therefore, the controller meets the standard requirements.

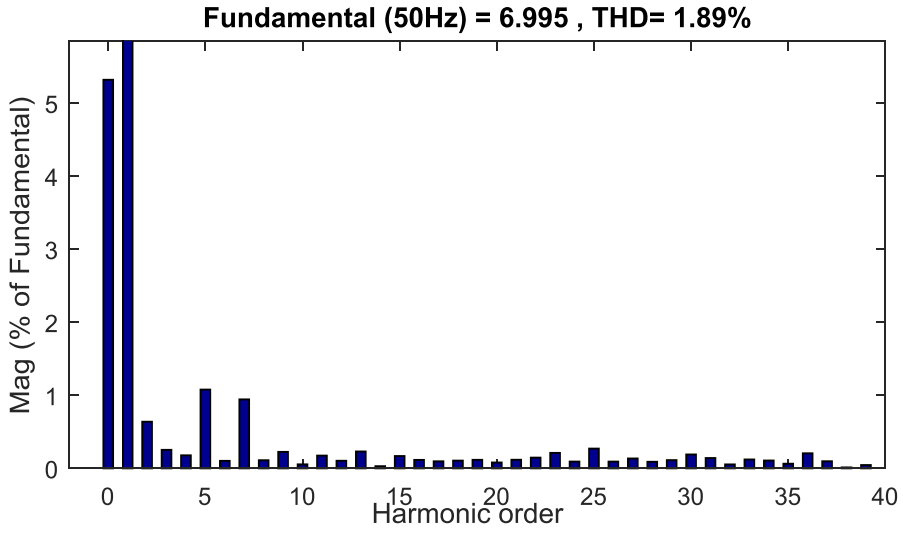

Figure 5.42 The THD of the current waveform of PR controller with HC

5.9 Unbalanced Grid Connected Result

The aim of this research is to study the behaviour of the three-phase grid-connected inverter during normal and abnormal conditions such as voltage sag or voltage swell. Therefore, the ability to control the current under unbalanced grid condition is important. To do this, the current control compensates for unbalanced condition and allows the system during the fault.

As stated before, unbalanced conditions occurring in the grid can affect the current waveform in both PI controller in the synchronous reference frame and PR controller in the stationary reference frame. The controller has been tested in the response of different unbalanced conditions with different voltage sags as well. The first test is carried out based on a line-to-ground fault. The second method uses a line-to-line fault giving an unbalanced voltage sag. In addition, the controller has been tested with different amplitudes of unbalanced voltage sag. As a result of that voltage sag, the phase-locked loop output is distorted. In order to deal with unbalanced grid conditions, the positive and negative sequences must be compensated for extracted and controlled. As discussed earlier in chapter 4, positive and negative sequence decomposition is used to overcome the effects of unbalanced conditions.

5.9.1 PI current control for unbalanced grid condition

The system is controlled first by the PI controller using the conventional single synchronous reference frame (S-SRF). To control the system using a PI controller, the three-phase reference

frame *abc* coordinates are transformed into *dq* synchronous coordinates in a rotating reference frame with angular frequency. Figure 5.43 shows the unbalanced voltage grid. It is illustrated that the phase *a* is lower than phase *b* and phase *c*. With this control method, the PI controller shows a poor control waveform and cannot deal with the unbalanced conditions due to the increase of oscillations in the current signals as shown in Figure 5.44. It can be noted that PI controller is shown poor performance due to cross-coupling between *d* and *q* coordinators and needs decoupling term between the d and q coordinators and the voltage feedforward. However, by using voltage feed-forward the control is shown to improve slightly but still suffers from the unbalance as shown in Figure 5.45. As a result, the use of the control approach led to an unstable system and the total harmonic distortion is over than the IEEE standards.

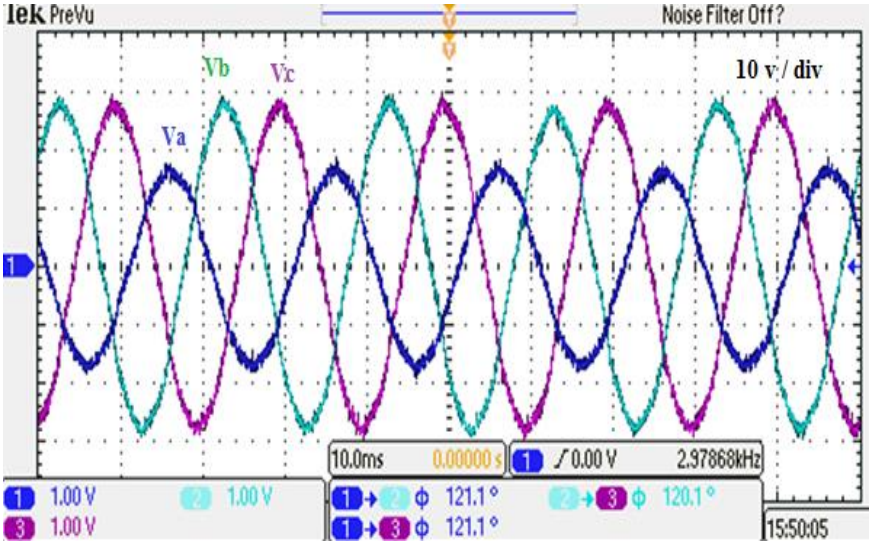

Figure 5.43 Three-phase unbalanced voltage

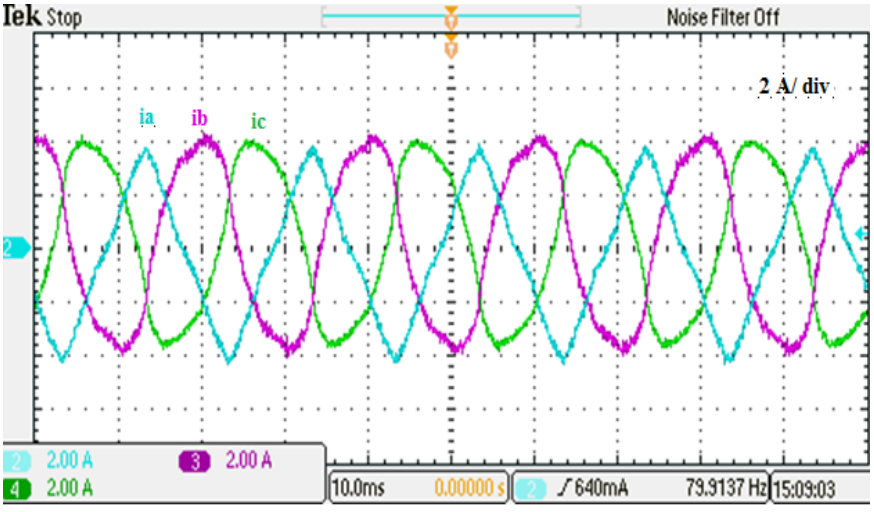

Figure 5.44 Three-phase current waveform under unbalance condition

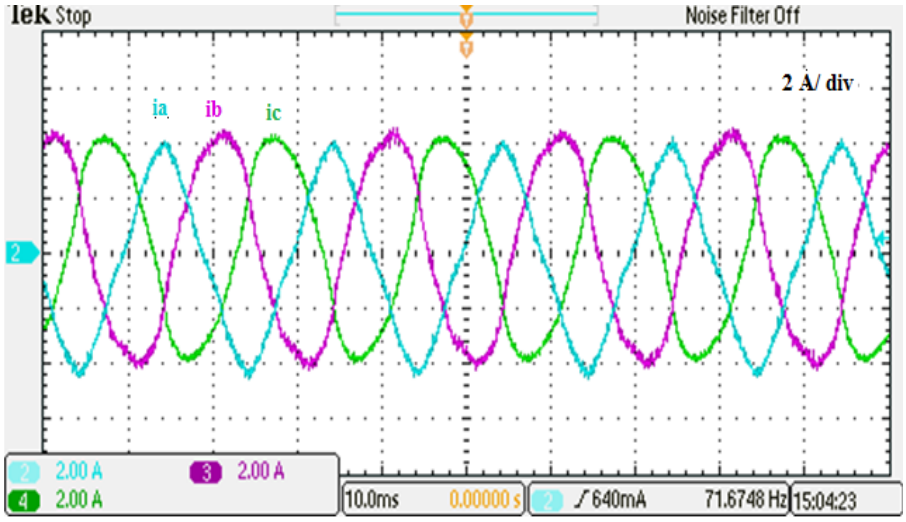

Figure 5.45 Three-phase current under unbalance condition with feed-forward voltage

5.9.2 Dual frame control under unbalanced condition

In an unbalanced system, the nature of the injected current to the grid is different than in normal grid conditions. During the grid unbalance conditions, the grid is distorted by unbalanced voltage sag in one phase or more phases. In ordered to ride through the unbalance of the voltage, the current injected into the grid includes the negative sequence components to enhance the quality of the waveform. The first method is a dual positive and negative sequence components d-q PI controller in the dual synchronous reference frame and the second one is α-β PR controller in the stationary reference frame.

5.9.2.1 Dual PI controller in the synchronous reference frame:

The current control is used both positive and negative sequence components based on positive and negative current control. The measured current injection to the grid is expressed in dq^+ and dq^- reference current as shown in the Figure 5.46. The effect of the cross-coupling between the positive and negative sequence reference frame is shown in the Figure 5.46. It is also clear that the measured current is able to track the reference accurately.

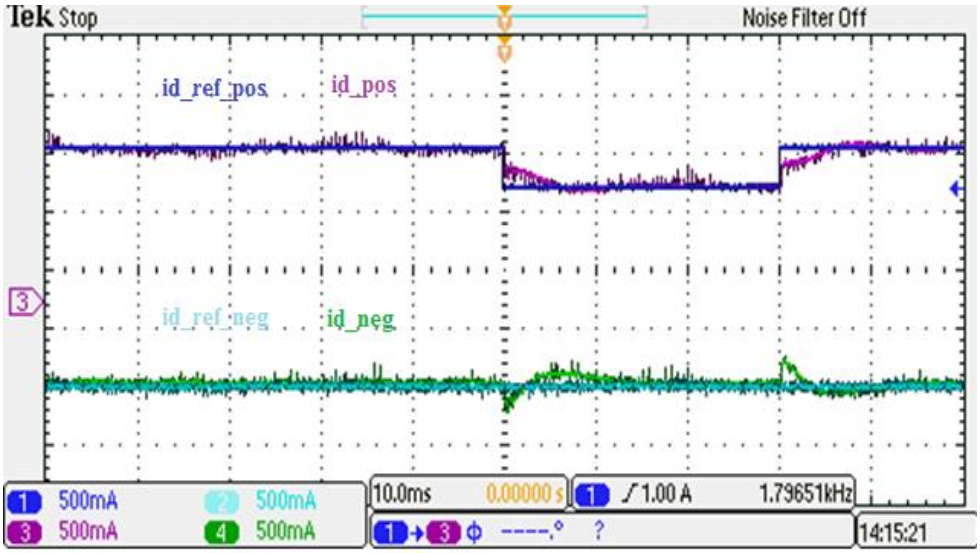

Figure 5.46 The reference and measured dq^+ and dq^-

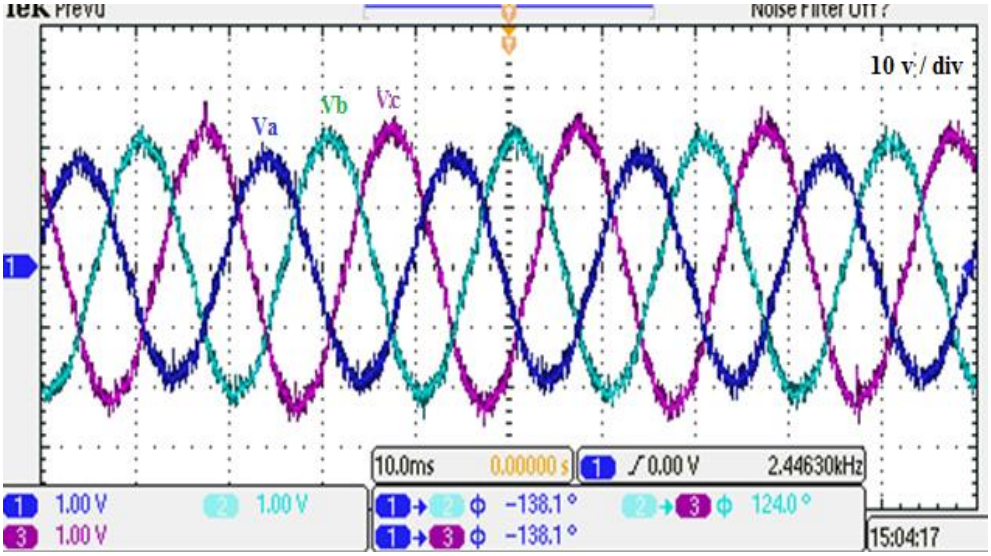

Figure 5.47 The three-phase unbalanced voltage in phase a

Figure 5.47 shows the three-phase unbalanced voltage in phase and Figure 5.48 shows the three-phase current waveform. This demonstrates that the control system is working effectively and can deal with unbalanced grid conditions using the dual PI control technique. The output current waveform is stable. The synchronous controller builds two control loops to control unbalanced current, one of the positive sequence components and the other for negative sequence components.

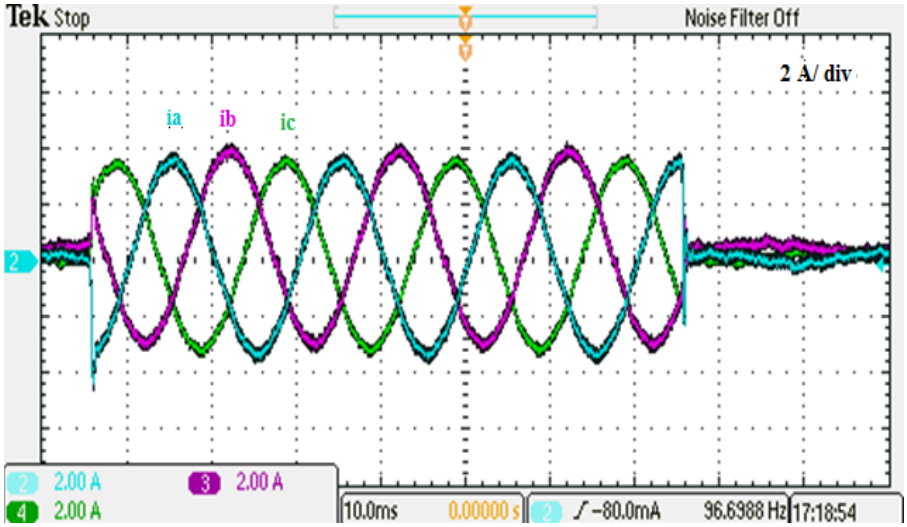

Figure 5.48 The three-phase current waveform

Figure 5.49 shows the FFT of the current waveform using the dual PI controller under unbalanced grid conditions. The total harmonic distortion is 3.95% which is within the limits specified by IEEE standard.

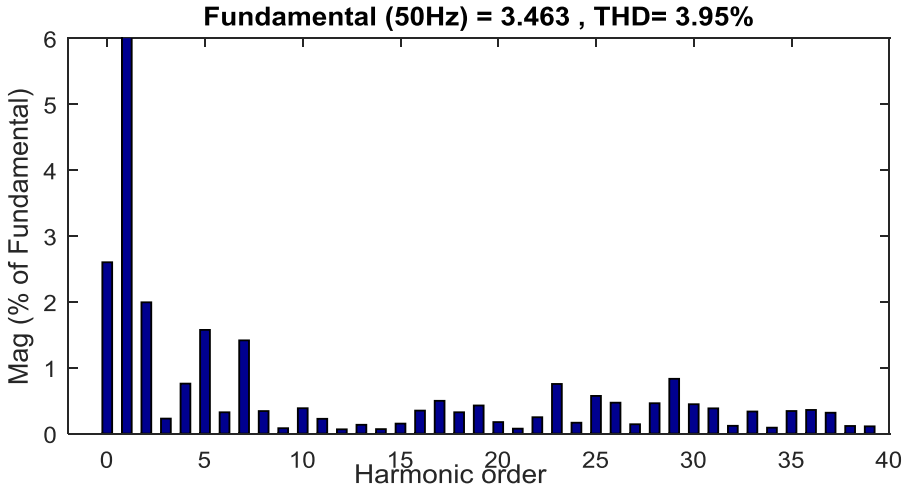

Figure 5.49 The FFT of the current waveform using dual PI controller

In addition to the unbalanced method, the controller has also been tested with an unbalanced line-to-line fault to check the robustness of the system. Figure 5.50 shows the three-phase voltage with unbalanced line-to-line voltage sags.

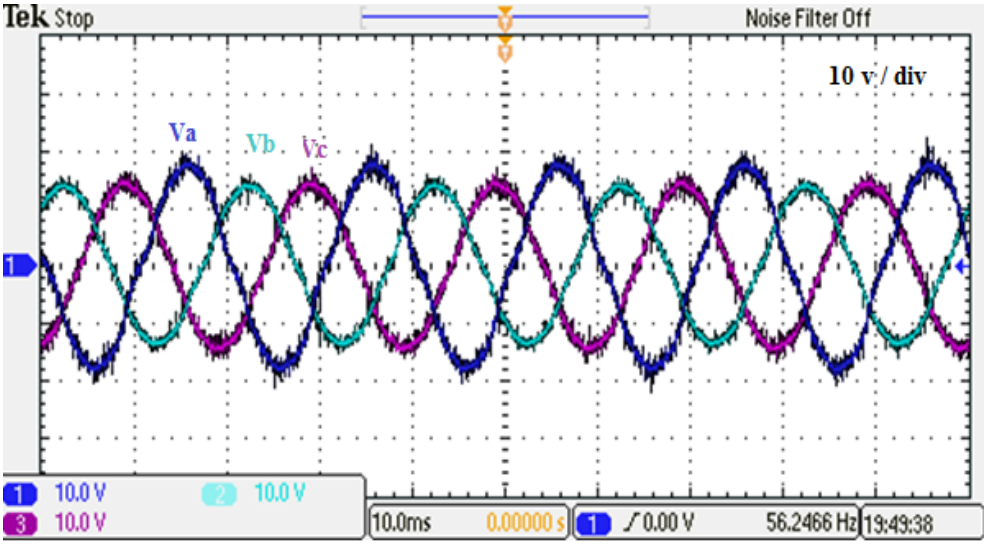

Figure 5.50 The three-phase voltage with unbalanced line to line voltage sags.

Figure 5.51 shows the three-phase current waveform. The output current shows a small overshoot which is normal in PI controller and smooth waveform. It can be seen there is no effect of the unbalanced voltage to the quality of the current waveform.

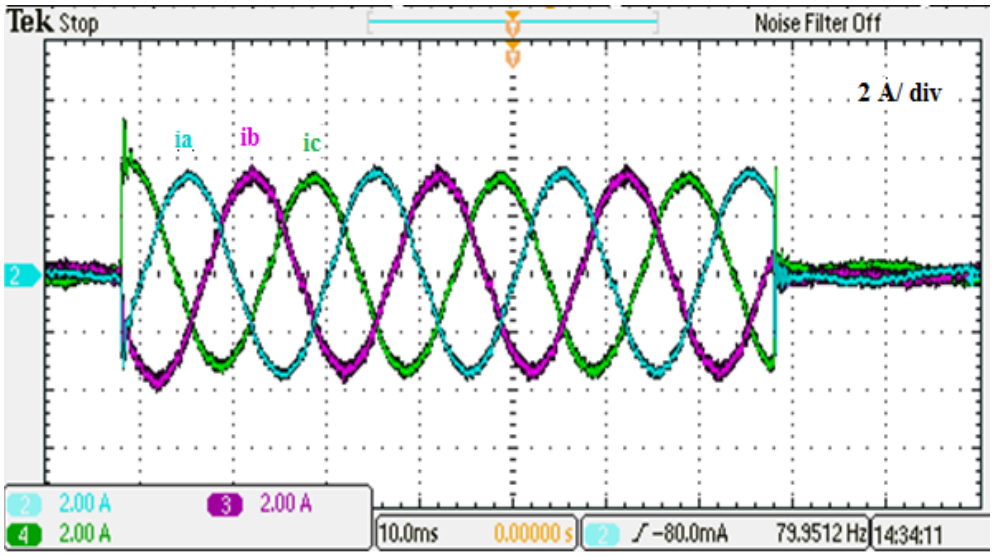

Figure 5.51 The three-phase current waveform.

5.9.3 PR current controller for unbalanced grid condition:

In this section, the system has been controlled using PR current controller under unbalanced grid conditions. Figure 5.52 and Figure 5.53 show the voltage and current waveform for the three-phase using PR controller respectively. Using this approach, the PR controller with harmonic compensator generates smoother waveforms in terms of the distortion. This proves

that the control system is working with unbalanced grid conditions using the conventional PR control technique. The output current waveform is maintained stable during the unbalance. It is worth noting that no need to builds two control loops to control unbalanced currents like PI current control which it used two control loops, one for the positive sequence components and the other for negative sequence components. Figure 5.54 shows the reference and measured alpha and beta current using conventional PR controller waveforms.

Although the PR controller offers satisfactory performance during abnormal grid conditions. It can be noticed in Figure 5.54, an error between the reference signal and the controlled signal in the alpha and beta current using conventional PR controller waveforms. In this regard, the implementation of the PR controller is unable to keep up with the upsurge in the error, which weakens the controller functioning. To get beyond this concern, an enhancement in the current control using a novel adaptive PR controller is implemented and demonstrated in the next chapter.

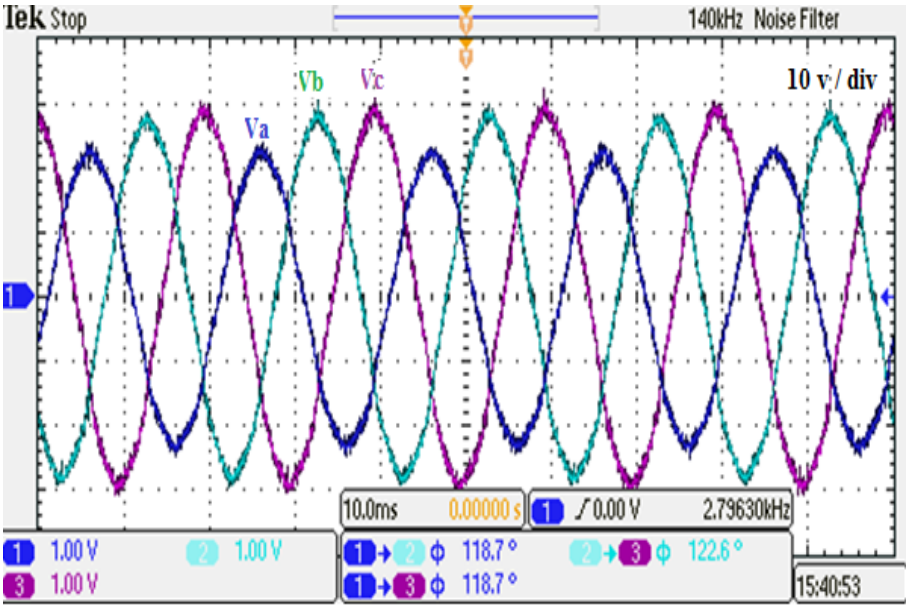

Figure 5.52 Three-phase voltage with unbalance voltage sag

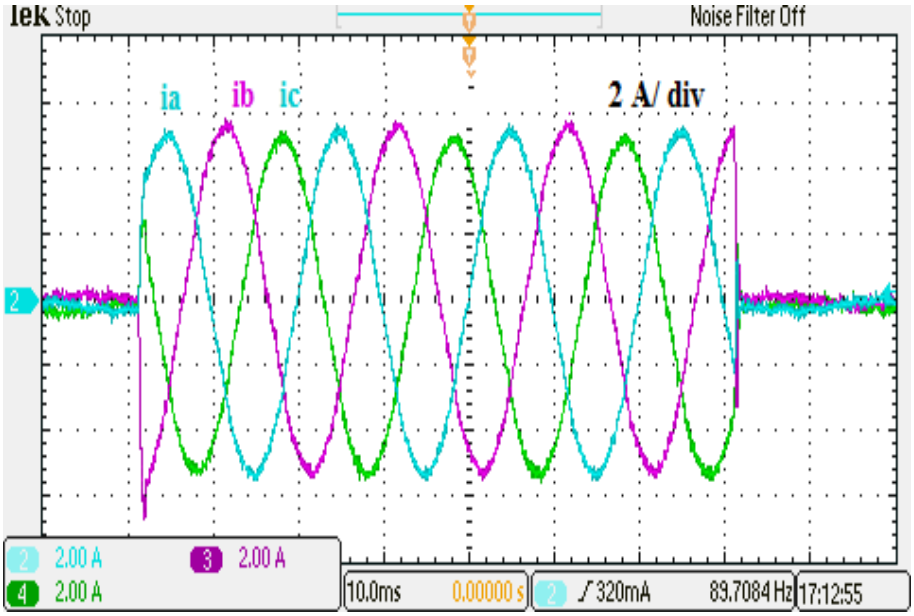

Figure 5.53 The three-phase current waveform with unbalance voltage sag in phase a

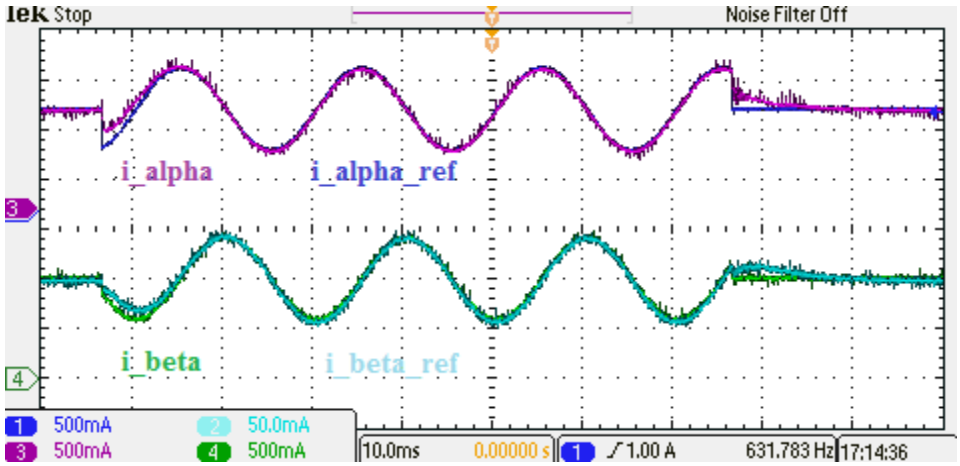

Figure 5.54 The reference and measured alpha and beta current using conventional PR controller waveforms

Figure 5.55 shows the total harmonic distortion of the current waveform. The FFT analysis is able to record a low value of the THD which is 3.25% which is less than maximum THD in PI controller in Figure 5.49 which is 3.95%.

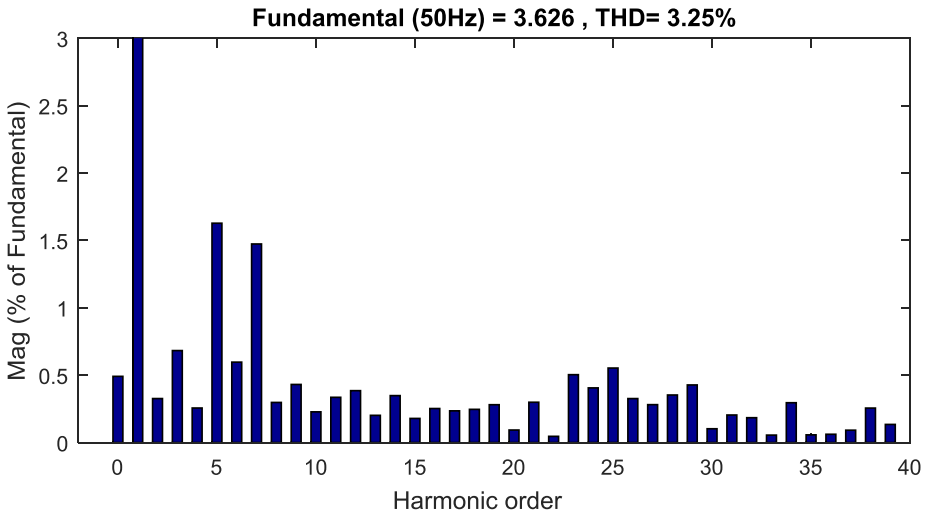

Figure 5.55 The FFT waveform of the current waveform

5.10 Chapter Summary

In this chapter, the influence regarding the current control scheme for the three-phase grid-connected inverter has been considered. The simulation and experimental results for the three-phase grid-connected inverter were presented using PI and PR current controllers. In the three-phase grid-connected system, current control can be implemented in various ways such as the synchronous rotating reference frame *dq*, and the stationary reference frame $\alpha\beta$ in a rotating reference frame with angular frequency using Clarks's and Park's transformations.

The current control schemes used are the PI and PR controllers under normal and abnormal conditions. The simulation and practical results show that the PI and PR current controllers are able to control the system in general under normal grid conditions but suffer in abnormal conditions.

PI current control is a straightforward tunning method to use within the control system. However, the PI current controller suffered from some drawbacks. *d* and *q* coordinators are decoupled due to cross-coupling terms between them. The PI current controller requires more transformation from three-phase to two-phase, which therefore requires more space in a DSP. PI current control is poor for eliminating low order harmonics, for that reason, the feedforward control method is applied in the control system to be able to reduce the grid current harmonics caused by grid voltage distortion without changing the dynamic response.

Under abnormal grid conditions, the PI controller needs to control the positive and negative voltage sequence separately, which makes the controller more complicated than before.

PR current control as another control method working in in the stationary reference frame. PR current control is a straightforward method and has the capability to eliminate the steady state error in normal grid conditions. In addition, PR controller can implement harmonic compensator without changing the dynamic response. α and β coordinators are not decoupled to each other. In abnormal grid conditions, PR controller can only control the positive voltage sequence since both the positive and negative voltage components have the same fundamental frequency. However, under abnormal grid conditions, the controlled signal instigating significant deviation from its nominal value and causes an error which weakens controller performance. As a result, a novel adaptive PR controller was implemented and tested in both balanced and unbalanced grid conditions in the simulation and verified experimentally in the following chapter.

Chapter 6. Adaptive PR Controller

6.1 Introduction

In this chapter, the proposed adaptive PR controller is presented. The aim of this chapter is to validate and prove the advantages of the proposed control approach in terms of stability and minimizing the error between the measured and the reference controllers in the current waveform during normal and abnormal grid conditions. The proposed technique is implemented with the eZdsp F28335 and verified experimentally in normal and abnormal grid conditions. The proposed control method is able to achieve better waveform with less overshoot and less total harmonic distortion compared to PI controller and conventional PR controller.

6.2 Adaptive PR Controller

During abnormal grid conditions, the error between the references should be minimized to within a very small limit. This requires appropriate adaptive control. In general, as k_p and k_i increase, the gain and the bandwidth of the system is also increased. However, as the gain increases, instability in the system can occur.

In the transient response, a large value of the k_p leads to an increase in the gains of all frequency components, while k_i decreases the settling time and helps reduce steady-state error and therefore the higher the loop bandwidth, the better the transient performance [151]. When the level of error suddenly increases beyond the maximum allowed variation of desired values in the transient response, the adaptive controller will auto-tune the value of both the k_p and k_i using interpolation in a look-up-table of the PR controller.

In this study, the adaptive PR controller strategy is used to regulate stationary gains regarding proportional and integral elements of the PR controllers. The online adaptation is founded on a look-up table, which is used to inform the controller parameters using the following equations:

$$k_p(k+1) = k_p(k) + \Delta k_p(k) \tag{6.1}$$

$$k_i(k+1) = k_i(k) + \Delta k_i(k) \tag{6.2}$$

where $k_p(k)$ and $k_i(k)$ are the reference values of the adaptive PR controller gains. $\Delta k_p(k)$ and $\Delta k_i(k)$ are chosen based on the error $|e|$ using the following method:

- If $|e|$ is higher than the 8 %, a large $(\Delta k_p(k), \Delta k_i(k))$ is chosen.
- If $|e|$ is higher than the 5 % and less than 8%, a medium $(\Delta k_p(k), \Delta k_i(k))$ is chosen.
- If $|e|$ is less than the 5 %, a low $(\Delta k_p(k), \Delta k_i(k))$ is chosen.

The high gain will make the system response faster and increase the robustness of the controller during the transient response. The proposed algorithm for the control adaption technique can be seen in Figure 6.1 and proposed adaptive PR controller scheme is shown in Figure 6.2. In this figure, the reaction of the adaptive system against the error e will be within the desired gains which ensures that the system is stable. Based on the result, the value of the adaptive gain will increase until the error is reduced to maintain stability. This indicates that the system will be stable for a high enough control gain. In addition, to achieve balanced and sinusoidal grid currents during unbalanced grid conditions, the positive-sequence component of the grid is used for synchronization (BPSC).

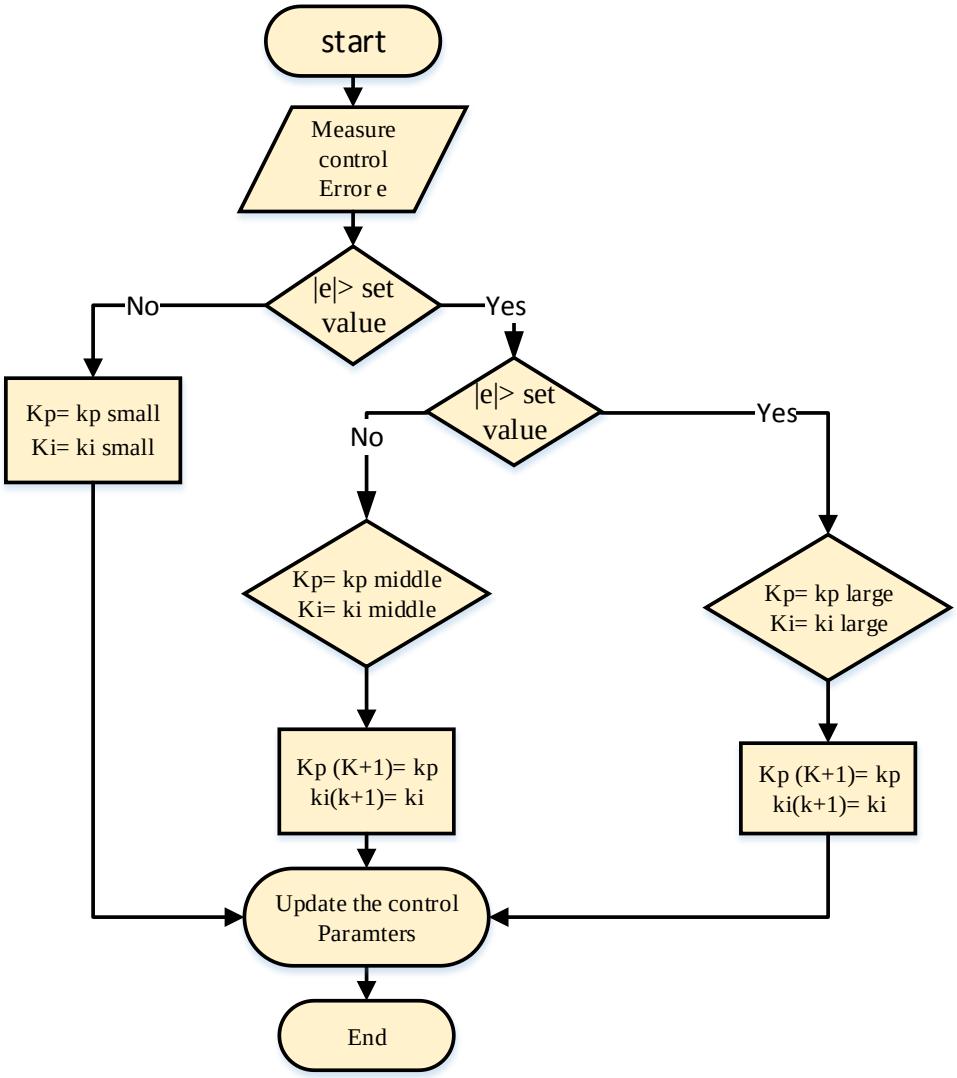

Figure 6.1 Flow chart of the proposed adaptive PR controller

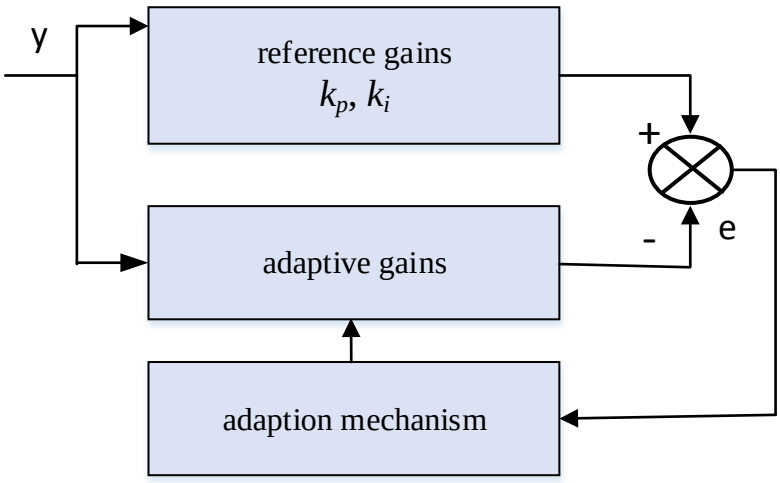

Figure 6.2 proposed adaptive PR controller structure

6.3 Simulation Results of Adaptive PR Controller under Abnormal Grid Condition

In cases of unbalanced grid conditions, the controller has been tested with different voltage sags. As a result, the controlled signal starting could promote a rise in the error between the reference signal, and the controlled signal which can be identified as creating aberration from its nominal value. To overcome this concern, the adaptive PR control techniques have been used in the stationary reference frame to control the current based on look-up-table is implemented to obtain the optimal values of the control parameters. It establishes and associates the enactment of the adaptive PR controller during standard and irregular grid voltage conditions.

The performance of the adaptive PR controller has been implemented in abnormal grid condition. The adaptation mechanism applied allows low PR controller gains until there is a sudden change in the grid conditions. This means the error will appear eventually. If the error is less than the set value which is 5%, the adaptation mechanism still used low PR controller gains. If the error is higher than 5% and less than 8%, the adaptation mechanism will use medium PR controller gains and the new parameters are applied. If the error is higher than 8%, the adaptation mechanism will use larger PR controller gains and the new parameters are applied as can be seen in table Table 6.1. Figure 6.3 shows a screenshot of the adaptive PR controller in the Simulink.

Table 6.1 Adaptive PR controller simulation parameters

Parameter	The proportional gain k_p	The integral gain k_i
α-axis, β-axis current controllers (low)	1	500
α-axis, β-axis current controllers (medium)	3	1000
α-axis, β-axis current controllers (large)	6	1500

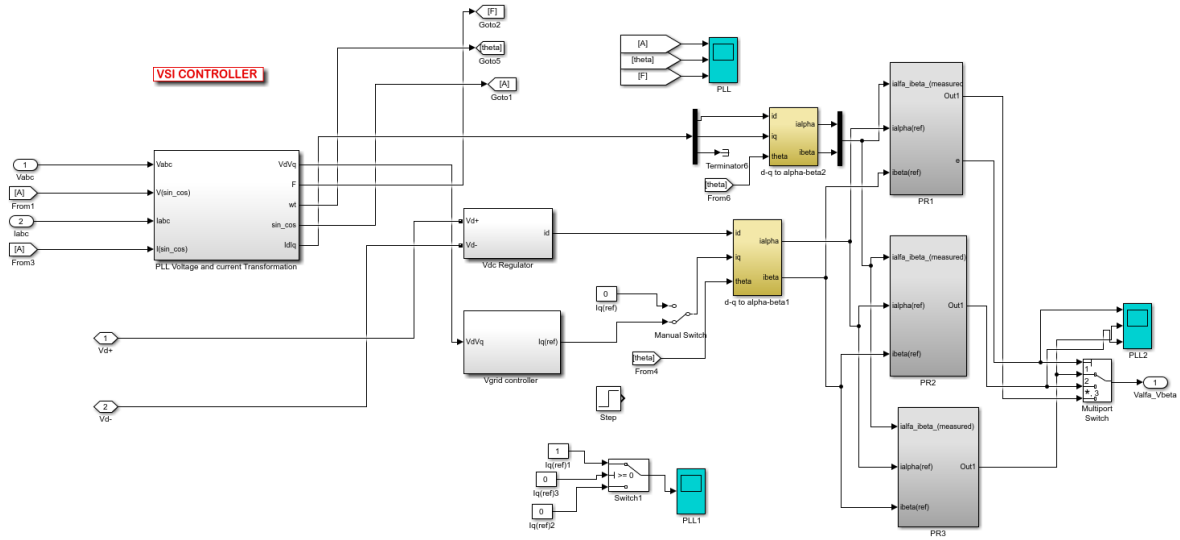

Figure 6.3 Screenshot of the adaptive PR controller

In order to test the controller dynamic performance under unbalanced conditions, three-phase voltage sag, single phase voltage sag and two-phase voltage sag fault conditions are investigated. Figure 6.4 and Figure 6.5 show the voltage and current waveform under voltage sag 30% for all phases. By applying the adaptation mechanism based on the error at the starting of the transient response, at a time of 0.15 sec, the k_p and k_i are varied from their set values in the look-up-table based on the error. The adaptation mechanism has been chosen the medium control gains. It can be seen from Figure 6.4 that the voltage drops when a voltage sag happens in the system at 0.1 sec until 0.15 sec. Figure 6.5 shows that the current has increased when the sudden voltage occurs at 0.1 sec in order to balance the active power transfer from the PV source.

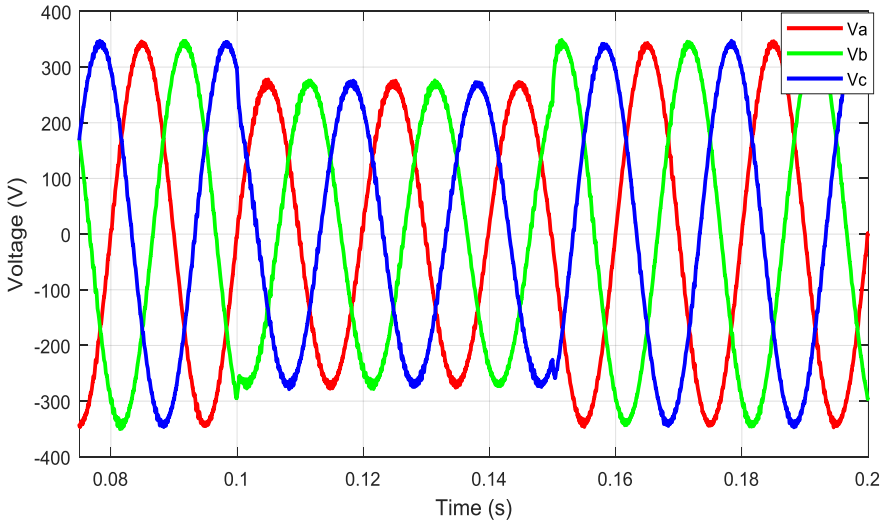

Figure 6.4 The voltage waveform with 30% voltage sag

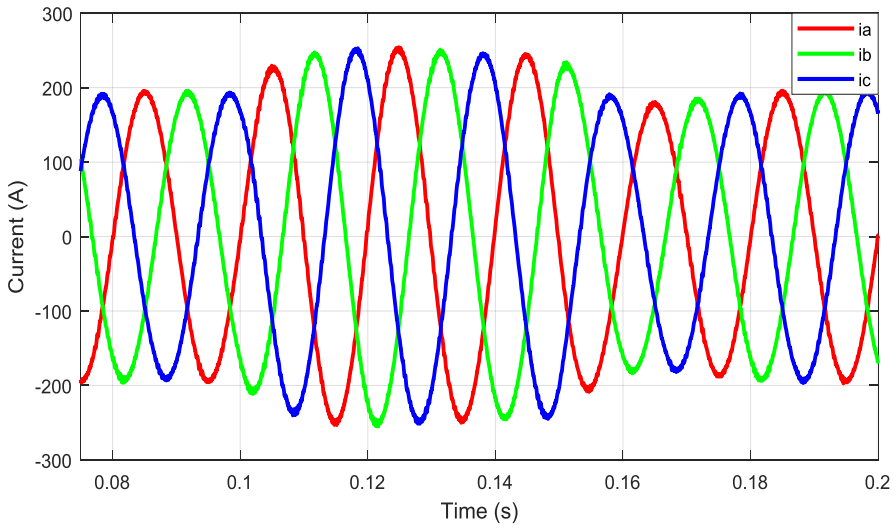

Figure 6.5 The current waveform with 30% voltage sag

Figure 6.6 and Figure 6.7 shows the stationary reference frame alpha and beta current respectively for adaptive PR controller with medium controls gains. The adaptation mechanism based on the error at the starting of the transient response, at a time of 0.15 sec, the k_p and k_i are varied from their set values in the look-up-table based on the error. As can be seen from the figures, the measured current follows the reference current during steady state and transient states and the result is satisfactory in both transient and steady-state. It can be noticed that the when the control gains increased in the adaptive method, the settling time is reduced as well as the error is reduced between the reference and measured alpha and beta current waveforms compared to the conventional PR controller in Figure 5.26 and Figure 5.27, which illustrate the error between the reference and the measured current is approximately 8%.

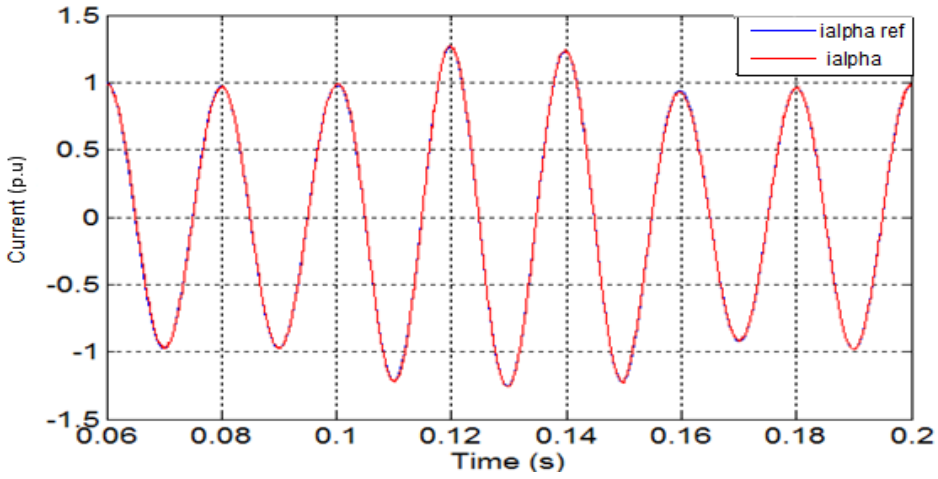

Figure 6.6 The adaptive PR controller alpha current using medium gains

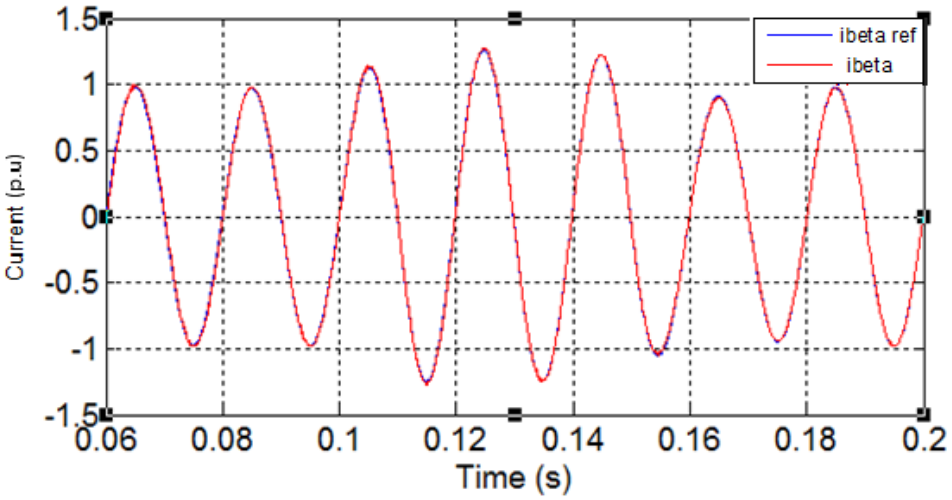

Figure 6.7 The beta current waveform for adaptive PR controller using medium gains

Figure 6.8 shows the voltage waveform during unbalanced grid condition with 50% voltage sag. Due to the clear unbalanced in phase *a* at 0.15 sec, the adaptation mechanism starting control the system and choose high gains. Unlike the PI controller, only one PR controller is needed to control the three-phase inverter under unbalanced grid condition. Here in the adaptive PR controller, the current components in the positive-sequence components is applied based on the adaptation mechanism as shown in Figure 6.9. As a result, it is observed that the current waveform is not affected by faults in the voltage and the control will work as designed and not distorted anymore.

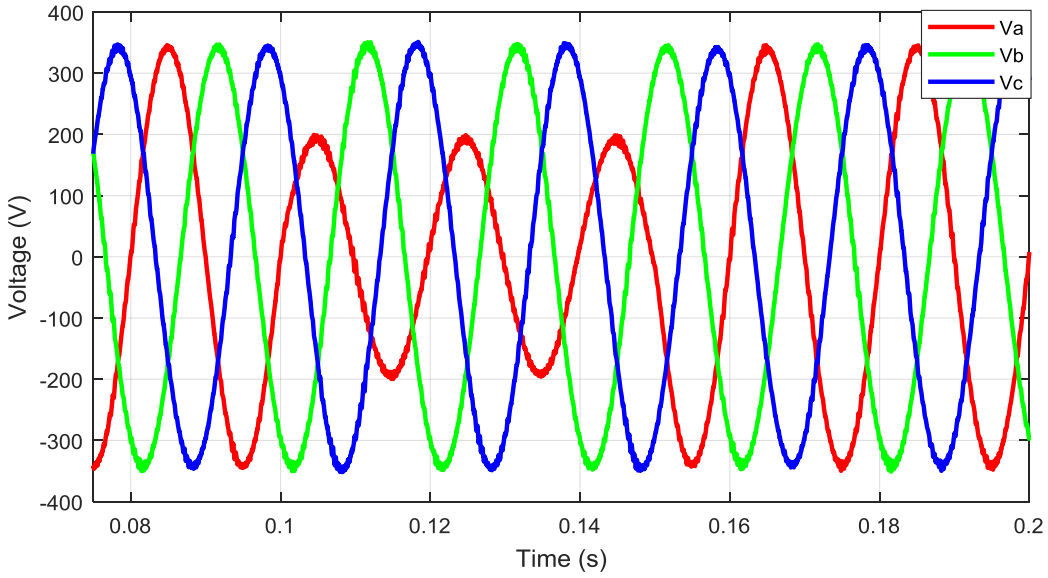

Figure 6.8 The single phase-to-ground voltage sags

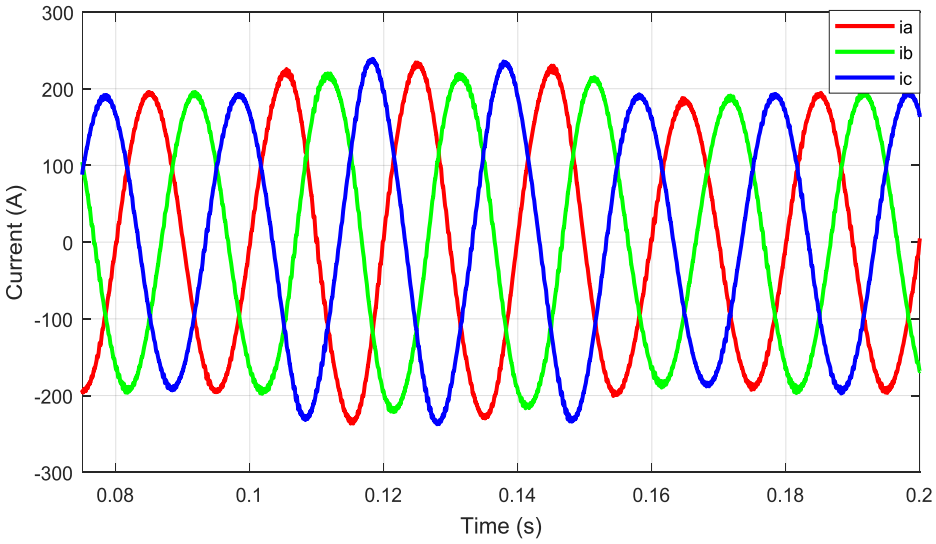

Figure 6.9 The three-phase current waveform under unbalanced voltage sags

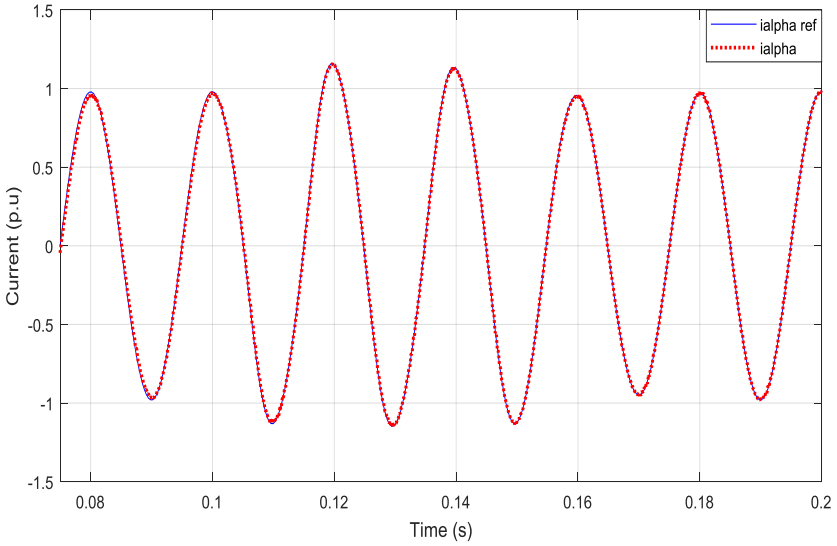

Figure 6.10 The adaptive PR controller alpha current using medium gains

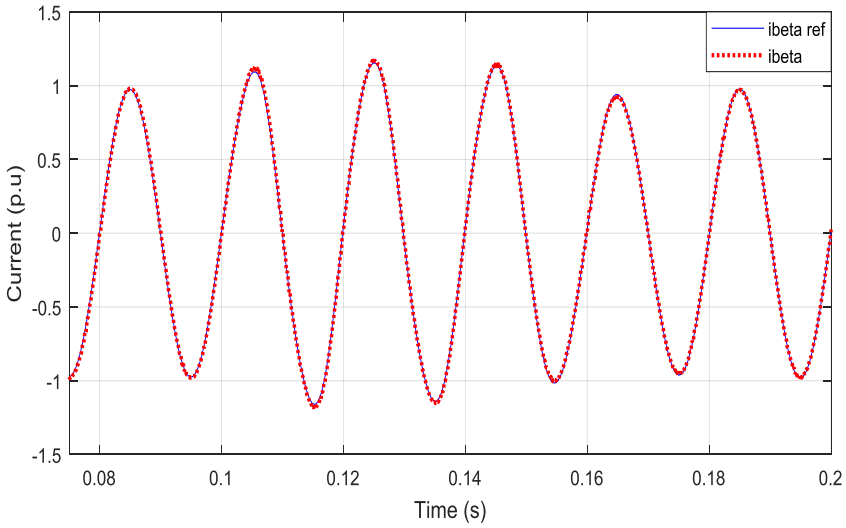

Figure 6.11 The beta current waveform for adaptive PR controller using medium gains

To further validate the performance of the adaptive PR controller, another case was investigated based on unbalanced two-phase voltage sag as shown in Figure 6.12. Before introducing the adaptive PR controller, the current waveforms were distorted due to the unbalanced voltage and the effect of the unbalanced is visible as shown Figure 6.13. However, the control system will be significantly improving by obtaining the adaptive PR controller. The adaptive PR controller is applied and the output current waveform is shown in Figure 6.14. The control gains, k_p and $k_i$were tuned depended on the error while observing the system response. The error over the limit and the test was carried out using the high gains. It can, therefore, be determined that the adaptive PR controller is able to achieve good performance during both balanced and unbalanced voltage sags.

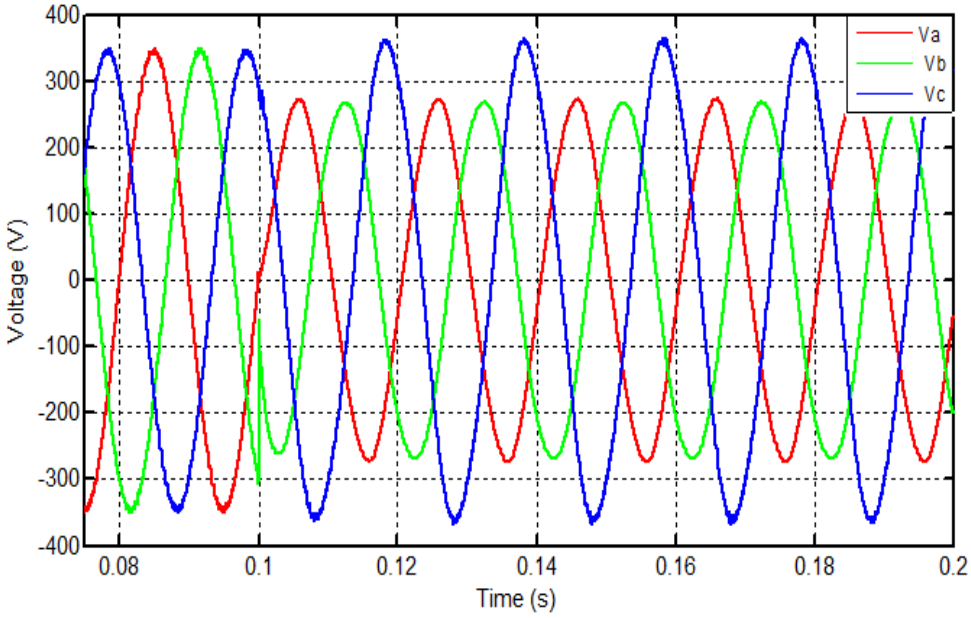

Figure 6.12 The two-phase-to-ground voltage sag

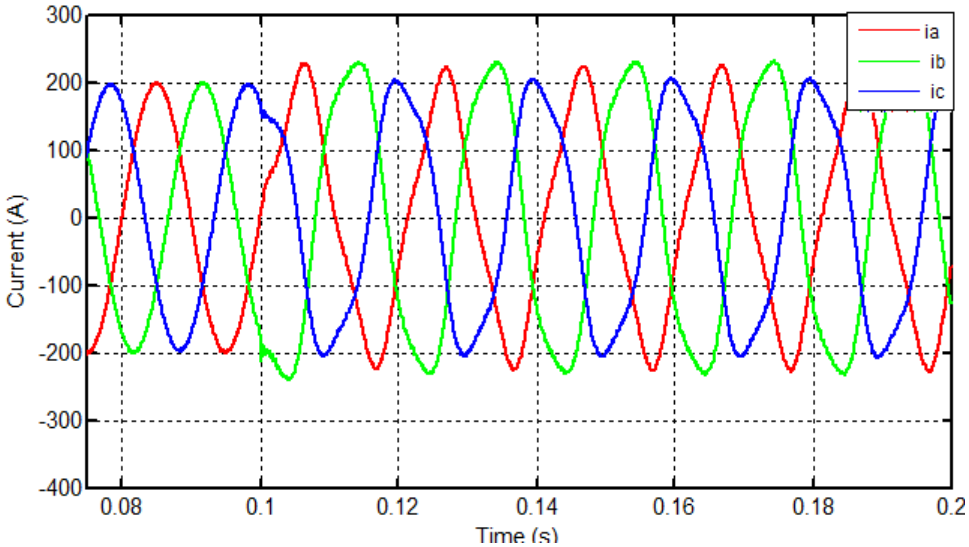

Figure 6.13 The distorted current waveform under unbalanced line to line fault

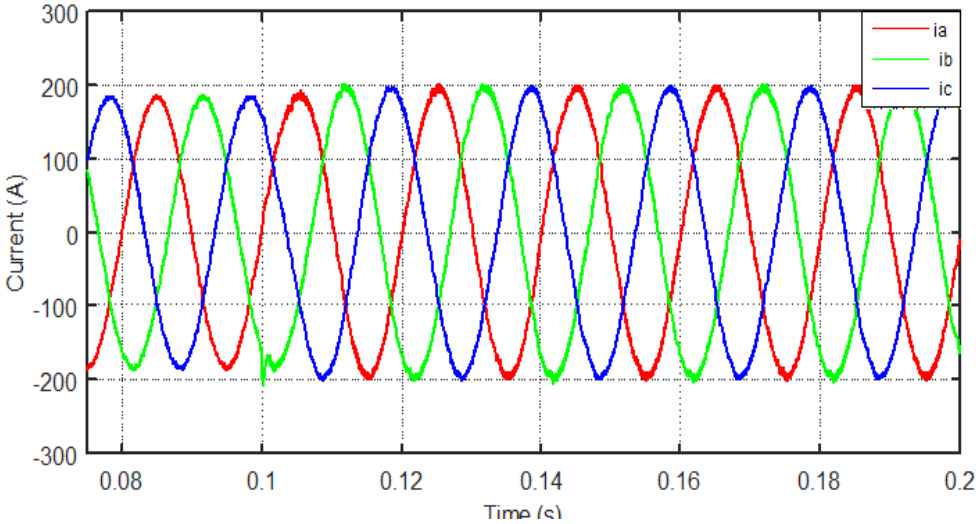

Figure 6.14 The three-phase current waveform under unbalanced conditions

Figure 6.15 and Figure 6.16 show the reference and measured alpha and beta current respectively. It can be seen that the measured current follows the reference in both cases. It can be concluded that the measured current follows the reference current even in unbalanced grid conditions.

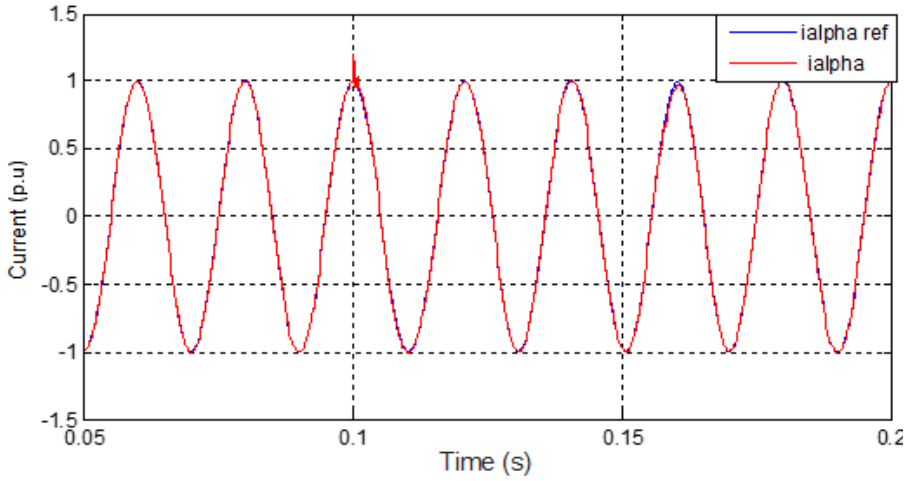

Figure 6.15 The stationary reference frame alpha current

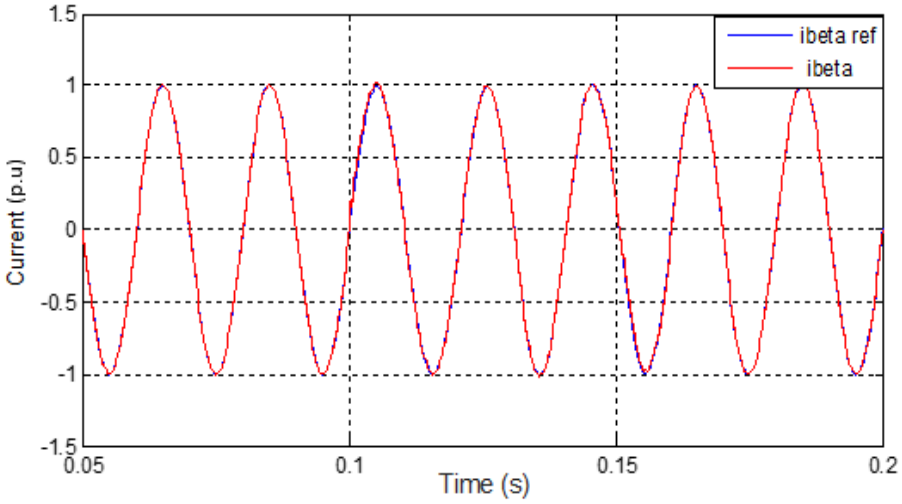

Figure 6.16 The stationary reference frame beta current

6.4 Experimental Results of the Adaptive PR Controller

To validate the control technique for the system in the laboratory, as explained earlier in chapter 5, the system is scaled down and has been tested. The results were obtained under unbalanced grid conditions such as the line to ground fault voltage sags and line-to-line voltage sags. Table 6.2 shows the adaptive PR controller parameters. Note, the controller parameters were adjusted depends on actual values of the adaptation mechanism of the PR controller. This section is carried out in real-time under different faults conditions using different PR controller gains according to the system response.

Table 6.2 Adaptive PR controller practical parameters k_p, k_i

Parameter	The proportional gain k_p	The integral gain k_i
α-axis, β-axis current controllers (low)	213	131
α-axis, β-axis current controllers (medium)	231	219
α-axis, β-axis current controllers (large)	236	324

6.4.1 Line to ground fault voltage sags

The test is carried out in real-time by subjecting the system under different fault conditions using different PR controller gains according to the system response to the error. Figure 6.17 shows the three-phase voltage with the unbalanced line to ground voltage sag in phase a by 20%. In this case, in order to ride through the unbalance fault of the voltage, the current injected into the grid via adaptive PR controller with low PR controller gains since the error was under 5%. By applying an adaption control technique which has the auto-tuning of the control parameters based on Table 6.2, the effectiveness of the controller is verified according to the system response. The adaptive includes the positive sequence components based on balance positive sequence control strategy to enhance the quality of the waveform.

Figure 6.18 shows the three-phase current waveform using an adaptive PR controller with low gains. To test the effectiveness of the adaptive control with low gains, the step response is applied. It should be noted that, the current waveform is smother and the control technique not effected from the unbalanced in the grid. It can be shown that the adaptive controller is compensating the voltage drops in phase *a*. By testing the total harmonic distortion in the current waveform in Figure 6.19. The THD is 2.22% which is lower the conventional PR controller in Figure 5.55 which is 3.25% and lower than the IEEE standard of 5%.

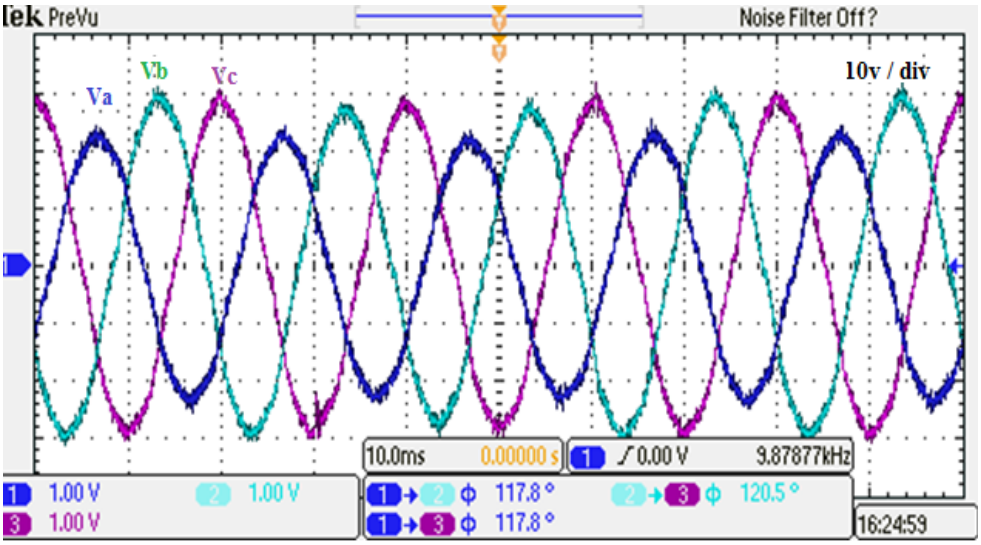

Figure 6.17 Three-phase voltage with unbalance voltage sag in phase a by 20%

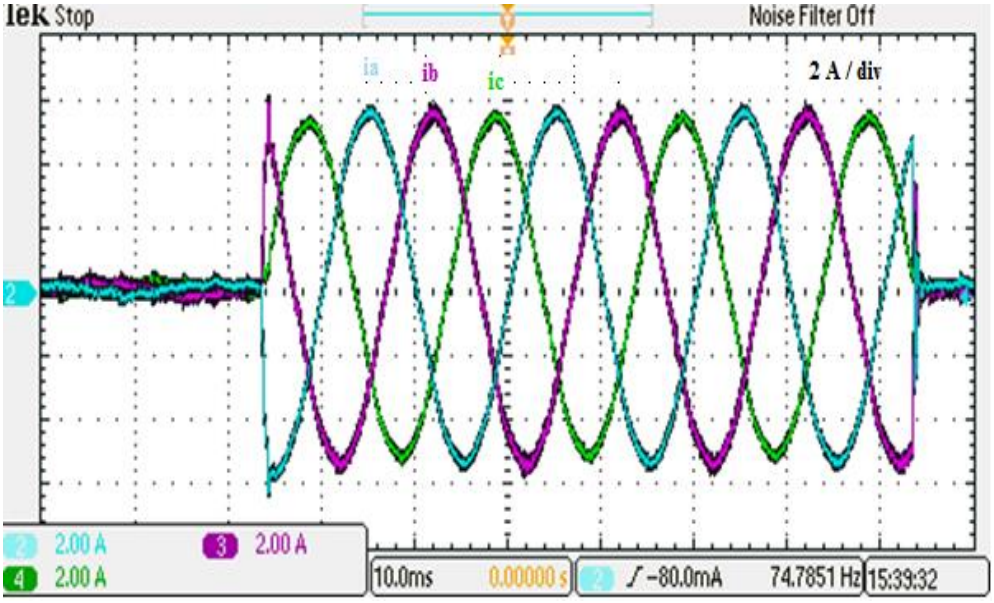

Figure 6.18 Three-phase current waveform using adaptive PR controller

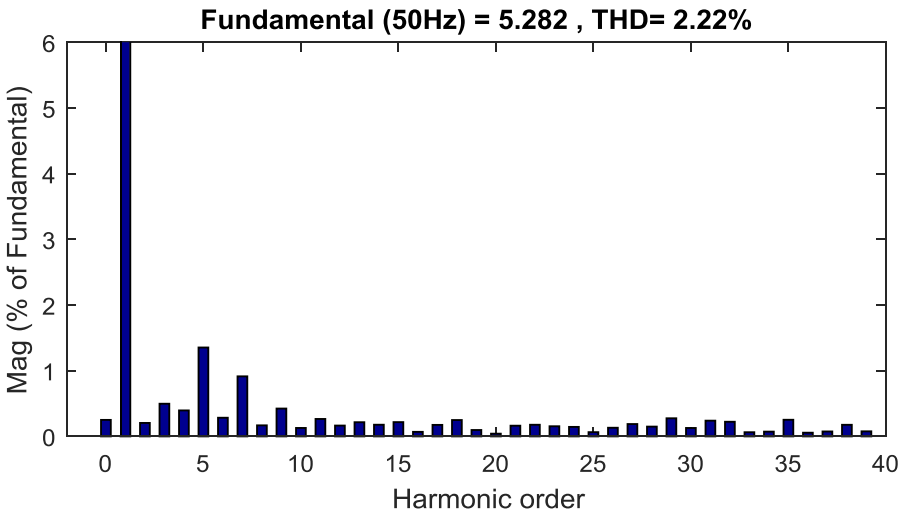

Figure 6.19 The FFT of the current waveform

In the following figures, the control has been used with the adaptive mechanism when the voltage sag has been reduced to 30%. In this case, due to the error is higher than the desired values, the adaptive control applied medium gains from the look-up-table as can be seen in Figure 6.20. Figure 6.21 shows the three-phase current waveform, the current waveform still is balanced and achieves a good response. Figure 6.22 shows the overall total harmonic distortion for the current waveform which is 2.03 %. It can be seen that the average THD is less than the conventional PR controller in Figure 5.55 with a value 3.25% and the PI controller in

Figure 5.49 with value 3.95% which is a noticeable reduction although the current control is using higher gains.

In addition, Figure 6.23 shows the reference and measured alpha and beta current waveforms using the adaptive method with medium gains. It can be noticed that the when the control gains increased in the adaptive method, the settling time is reduced as well as can reduce the error between the reference and measured alpha and beta current waveforms compared to the conventional PR controller in Figure 5.54.

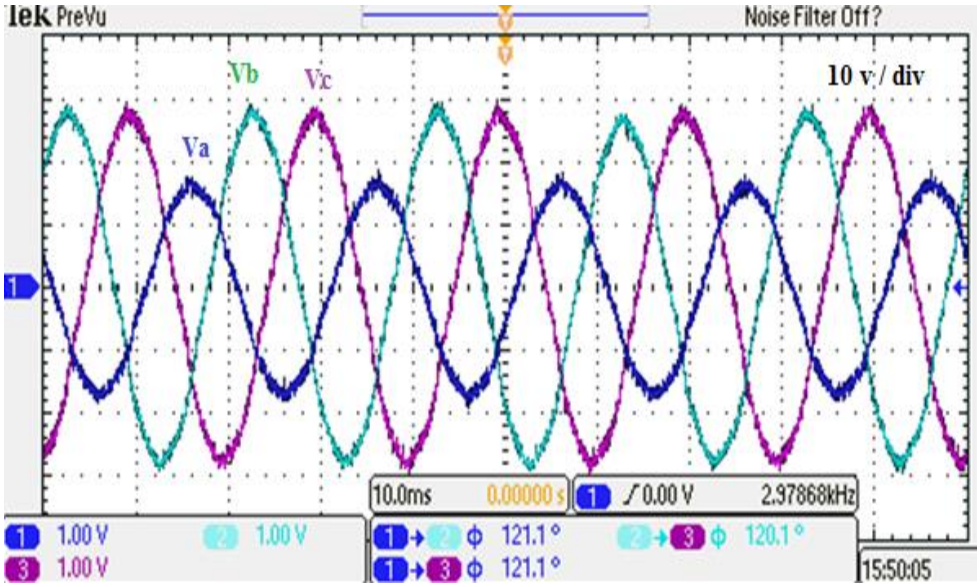

Figure 6.20 Three-phase voltage with unbalance voltage sag in phase a by 30%

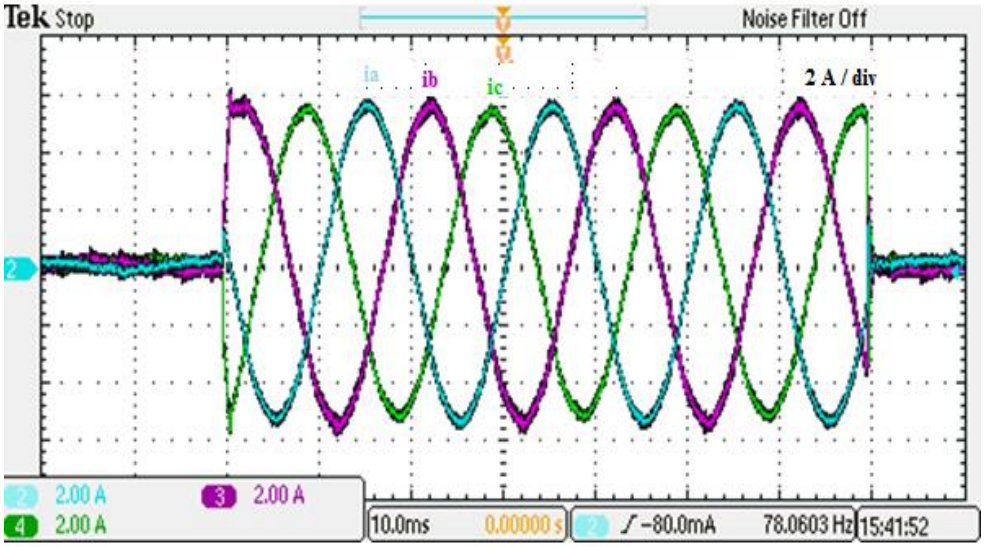

Figure 6.21 The three-phase current waveform with unbalance voltage sag in phase a by using medium adaptive controls gains

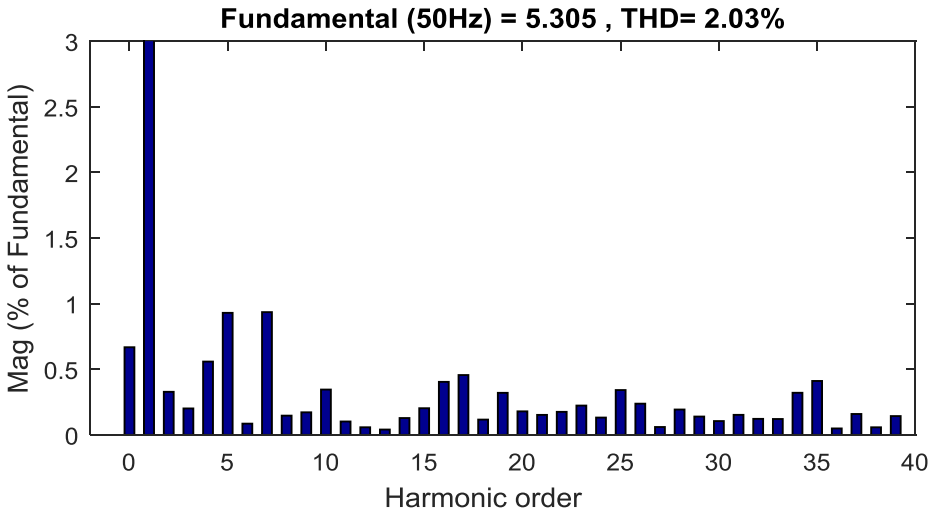

Figure 6.22 The FFT of the current waveform using medium adaptive controls gains

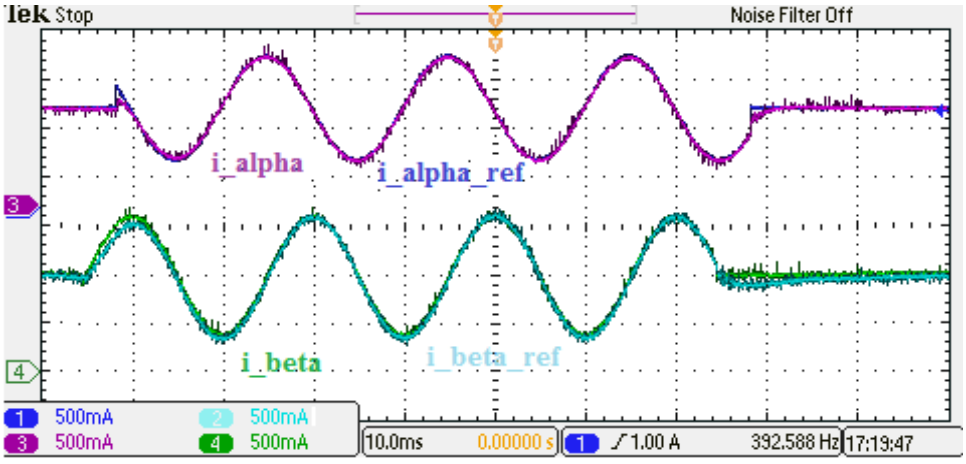

Figure 6.23 The reference and measured alpha and beta current using medium gains of the adaptive PR controller

Even if the unbalance is increased in the voltage waveform as shown in Figure 6.24, which illustrates the unbalance three-phase voltage waveform with 50% voltage sag in phase a, therefore the error will increase beyond the demands values. As a result, the control will detect the control high gains. Figure 6.25 shows the three-phase current waveform, as can be seen, the current waveform is balanced and a good response achieved. The total harmonic distortion for the current waveform can be seen in Figure 6.26 which has a magnitude of 2.20%.

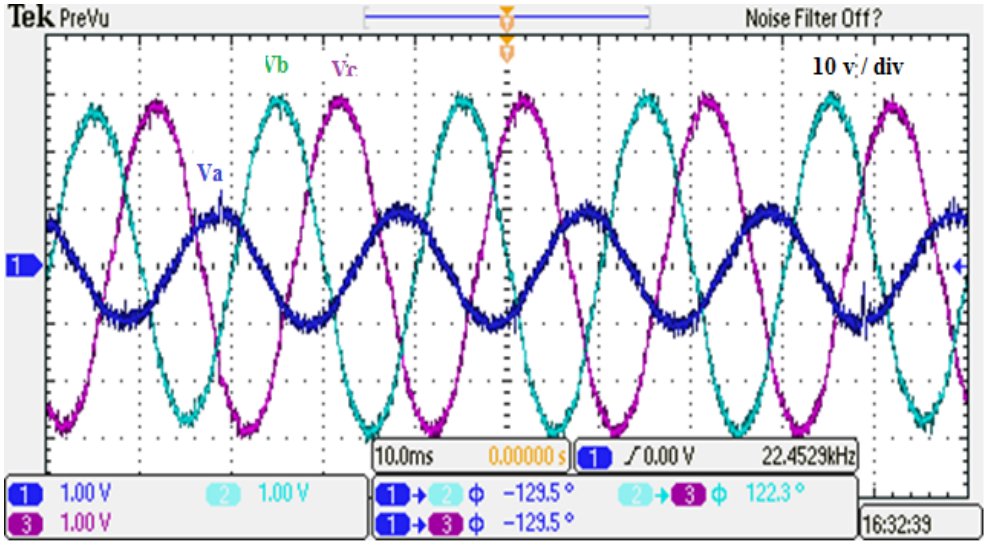

Figure 6.24 Three-phase voltage with 50% unbalance voltage sag in phase a using higher gains for the adaptive PR control

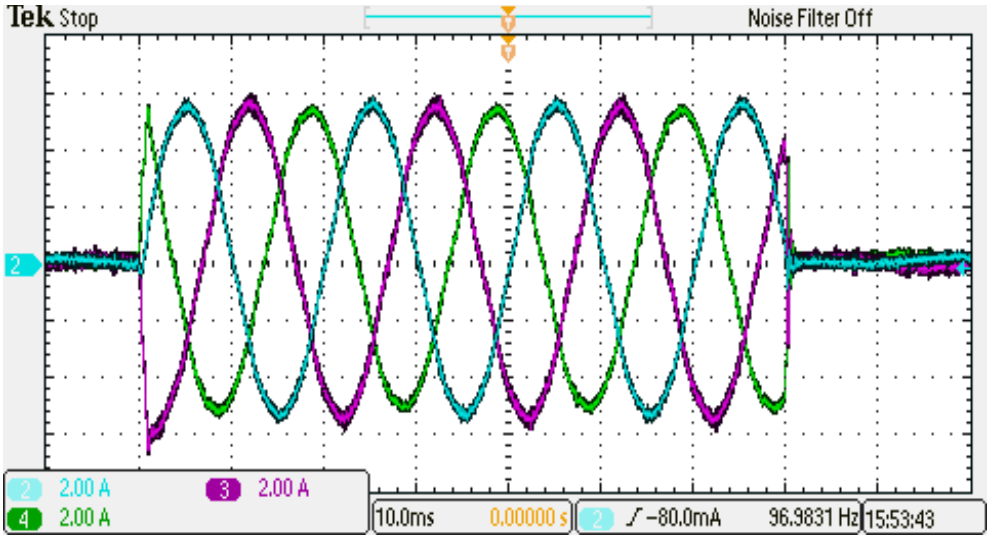

Figure 6.25 The three-phase current waveform with 50% unbalance voltage sag in phase a

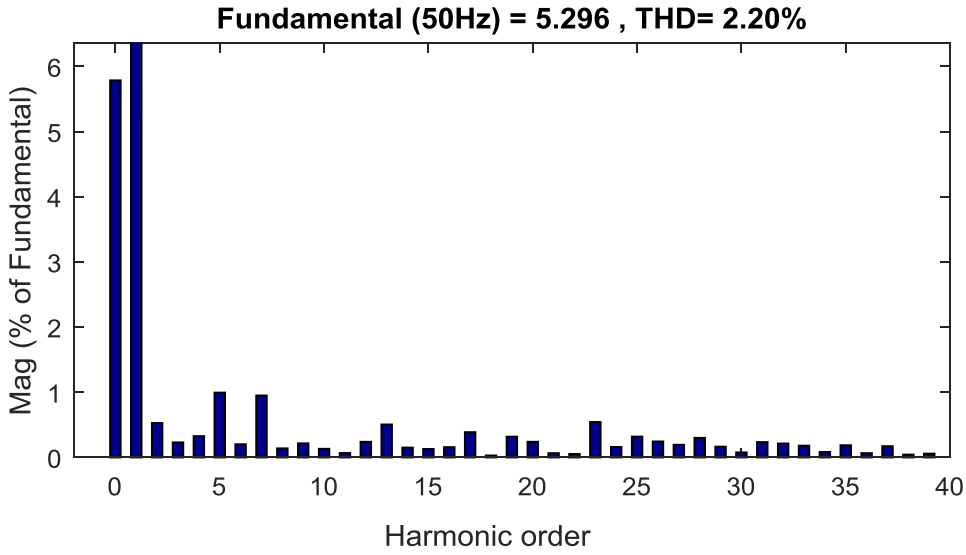

Figure 6.26 The FFT current waveform using higher adaptive controls gains

6.4.2 Two Line to line fault voltage sags

The control system has also been tested during unbalanced grid conditions. In this case, two line-to-line faults have been applied in phase *b* and *c* by diffrent voltage sags. This leads to a higher voltage in phase *a* than in phases b and c, in the output of the voltage waveform, as can be seen in Figure 6.27 which shows the unbalanced three voltage waveforms with line-to-line faults.

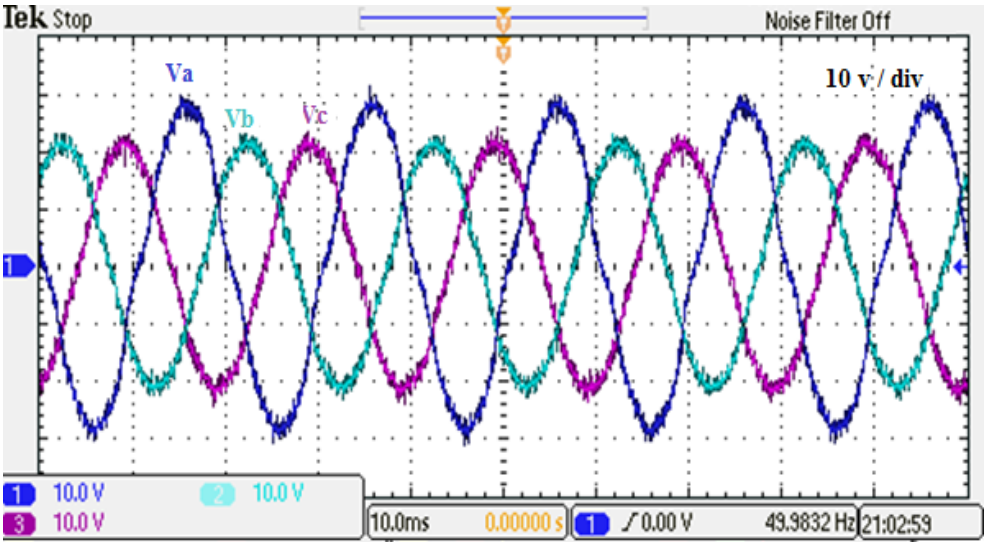

Figure 6.27 The unbalanced three-phase voltage with line to line voltage sags

Figure 6.28 shows the three-phase current waveform with the line to line voltage sags using low adaptive control gains. The adaptive control technique is still achieving sinusoidal output current under unbalanced grid conditions as shown in Figure 6.28. Figure 6.29 shows the reference and measured alpha and beta current waveforms using the adaptive method with low gains. As illustrated, the measured current follows the reference in both controllers even in unbalanced grid conditions.

In addition, Figure 6.30 show the effectiveness of the adaptive PR controller with step response. The measured current follows the reference. Figure 6.31 shows the FFT analysis of the current waveform, which indicates low harmonic distortion and effective compensation of the working current with a value 1.93 %. It should be noted that the proposed controller has shown a significant reduction of the THD compared with PI controller and PR controller. The THD is 3.25% when controlled via PR controller in Figure 5.55 and 3.95% when controlled by PI controller in Figure 5.49. As a result, it can be said that the adaptive PR controller ride through the abnormal grid conditions better than the PI controller and conventional PR controller and the lower value of THD can be achieved.

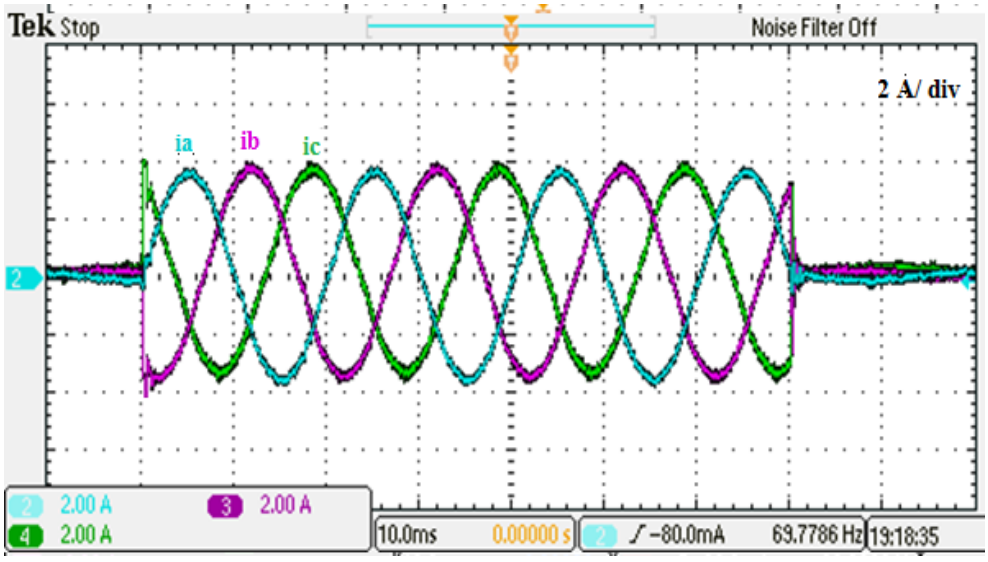

Figure 6.28 The three-phase current waveform with line to line voltage sags using low control gains

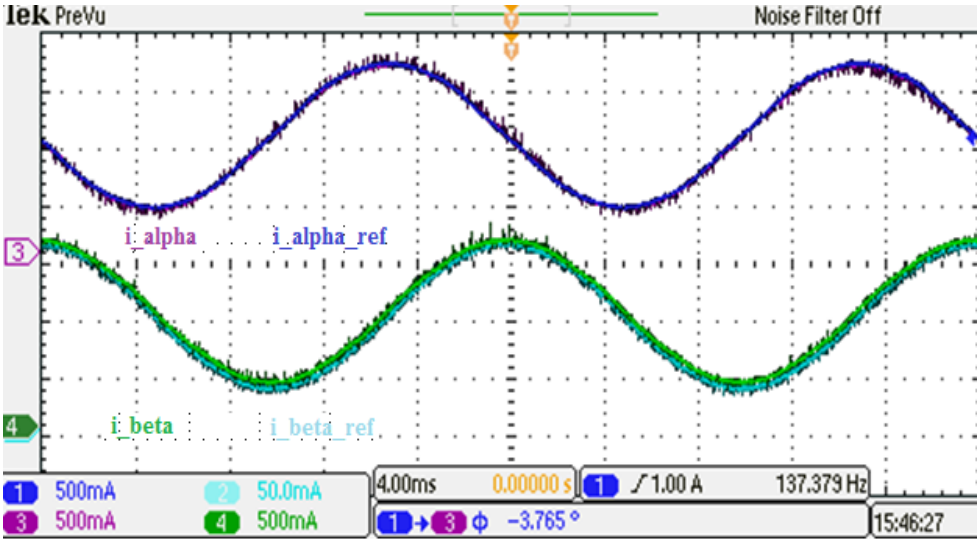

Figure 6.29 The reference and measured alpha and beta current using medium gains of the adaptive PR controller

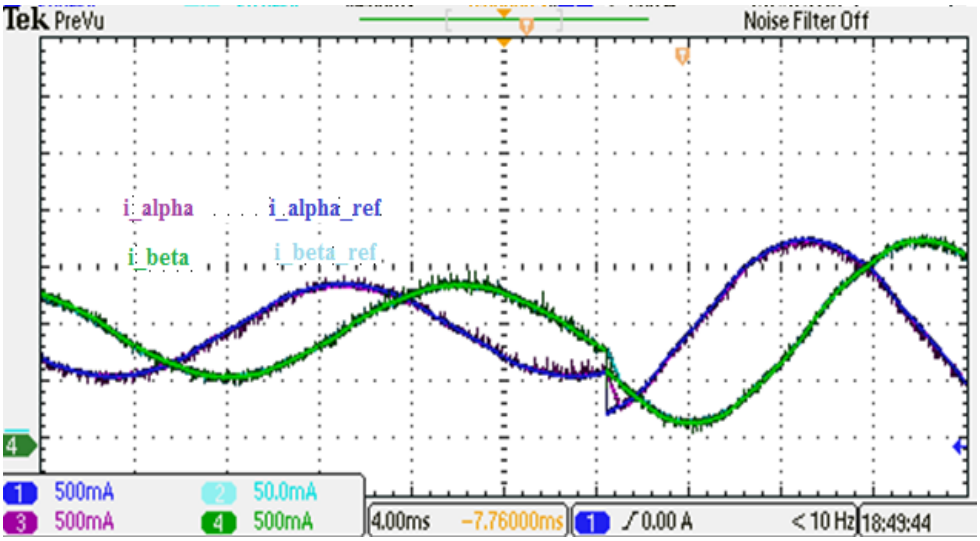

Figure 6.30 The reference and measured alpha and beta current with step response

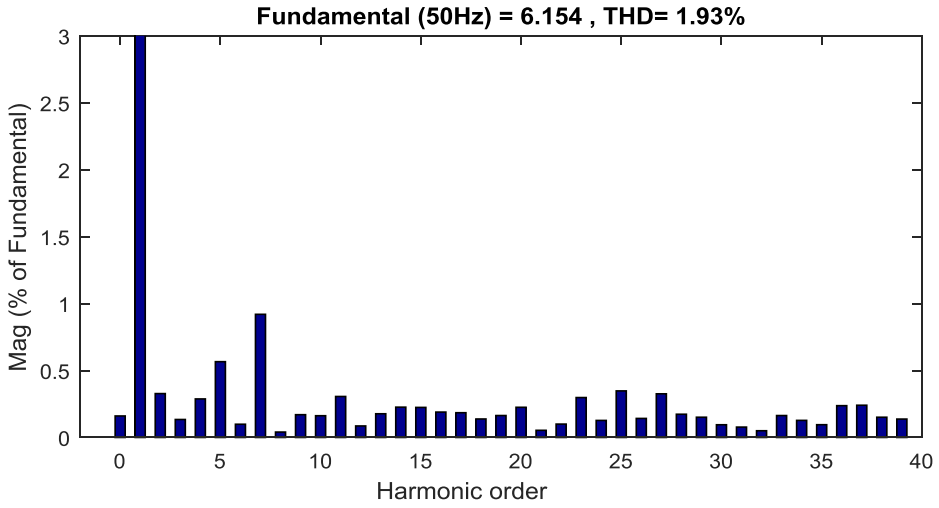

Figure 6.31 The FFT of the current waveform two line-to-line faults

6.5 Chapter Summary

When the abnormal occurred in the gird, the implementation of the current controller cannot match the rise in error, in turn, this lessens controller performance weakening. To get beyond this concern, this chapter introduced the adaptive PR control techniques in the stationary reference frame $\alpha\beta$ rotating reference frame with angular frequency to control the current. A Novel method for adaptive PR controller for abnormal conditions in the grid using a look-up table. The adaptive controller will auto-tune the value of both the k_p and k_i on-line. The adaptation mechanism applied allows low k_p and k_i gains work until there is a sudden change in the grid conditions. If the error is less than the set value which is 5%, the adaptation mechanism still used low PR controller gains. However, if the error is higher than 5% and less than 8%, the adaptation mechanism will use medium PR controller gains and the new parameters are applied. If the error is higher than 8%, the adaptation mechanism will use larger PR controller gains and the new parameters were applied.

The proposed control technique demonstrates good control of the waveform under balanced and unbalanced grid conditions. The control techniques have been successfully implemented and tested in both normal and abnormal grid conditions in the simulation and verified experimentally. The results clearly show that the desired output current is well regulated, with zero steady-state error. PR controller can implement harmonic compensator without changing the dynamic response. The FFT analysis of the average total harmonic distortion analysis of the

current waveform indicates are well within acceptable limits and show low harmonic distortion and effective compensation and less over_shoot of the working current with lower values compared with the conventional PI and PR controllers.

Chapter 7. Particle Swarm Optimization

7.1 Introduction

In this chapter, the proposed adaptive Particle Swarm Optimisation (PSO) is presented to control the three-phase grid connected inverter. PSO is a self-commissioning tuning process method which tunes the parameters of the controllers to manage different normal and abnormal conditions and the transitions among them. PI and PR controllers have been widely used for speed and position control in many various applications. PSO is the powerful technique for solving a problem and can increase the performance of the system.

Compared to GA and ANN, PSO can operate much more easily and faster to optimize and making it well suited for real-time control applications which experience time-varying disturbances. Moreover, it is a stable optimization method that is relatively easy to implement, because there are few parameters to adjust and it does not impose a significant computational.

7.2 Particle Swarm Optimization

Particle Swarm Optimisation (PSO) is a mathematical method that generates a specific implementation of an iterative optimisation technique which is stimulated by the conduct of a swarm of birds, fish or bees moving in the search space at a random velocity [126]. It has been used in many applications such as industry, electronic, digital communication and control systems to give an optimal optimization solution. Since then, many modifications have been made in PSO. Shi and Elbert proposed a new scheme by adding a new parameter called inertia weight to achieve higher performance. The inertia weight ω which is linearly decreasing during iteration in addition to another common type of PSO [152, 153]. PSO is initialized with a society of particles where all particles are located at random positions and each particle represents a potential solution to a problem and adjusts its own "flying experience" in a particular defined boundary space. The concept of PSO has been represented by the theory of the position and the velocity of the particles. Basically, each particle is represented by a position particle index vector; $X_i^n = [x_{i1}, x_{i2}, x_{i3} \dots x_{in}]$ and velocity vector; $V_i^n = [v_{i1}, v_{i2}, \dots v_{in}]$, where i is the particle number, and $n= (1,2,3, \dots, N)$ is the iteration number. The particles initial velocity and position are updated using the following equations:

$$V_{id}^{n+1} = \omega . V_{id}^{n} + c_1 . rand(\ \ ) . \left(X_{pbest}^{n} - X_{id}^{n}\right) + c_2 . rand(\ \ ) . \left(X_{gbest}^{n} - X_{id}^{n}\right) \quad (7.1)$$

$$X_{i}^{n+1} = X_{id}^{n} + V_{id}^{n+1} \quad (7.2)$$

Here, in every iteration, the best recorded previous position vector is defined as, X_{pbest}^{n}, whilst the best particle amongst all particles is referred to as the best recorded global position vector, X_{gbest}^{n}. Also, c_1 and $c_2$are acceleration constants, $rand(\ \ )$is a random value between 0 and 1, and ω is an inertia weight used to balance between 'global' and 'local' search capabilities.

The flowchart of the optimization process of the PSO algorithm is shown in Figure 7.1. Initially, the position and the velocity of the particles are initialised. After that, the iterative optimization process begins, and the position and the velocity of the particles are updated every iteration. The movement of each particle within the search space is calculated according to a given performance function that assesses the fitness of the particle. The position of each particle can be changed based on its own local best P_{best} and the global best of the full swarm population G_{best}. The process continues until the predefined number of iterations is met. The process is also terminated when predefined stopping criteria are satisfied or no significant improvement is achieved over a number of iterations.

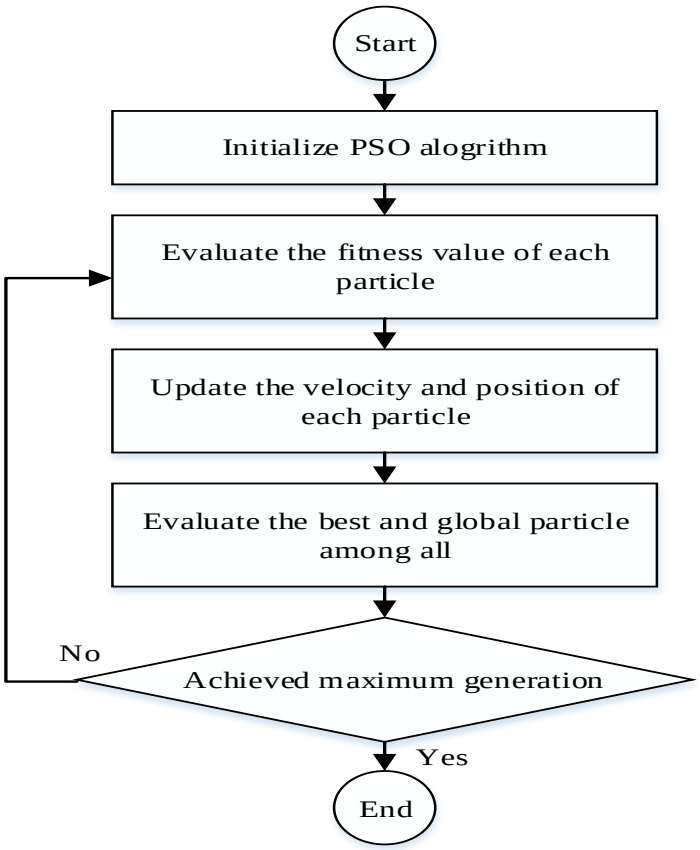

Figure 7.1 Particle Swarm Optimisation flowchart (PSO)

7.3 Proposed Control Parameters Optimization Scheme Using PSO

The selection of current control strategy has a large impact on the dynamic response, accuracy, steady-state error and robustness of the system. In this work, real-time optimization of a cascaded control system, the voltage control includes two PI controllers; one for the DC link voltage control and the other for grid voltage control. The measured voltages are compared with the desired output voltage $v_{dc(ref)}$ in the DC voltage control and $v_{g(ref)}$ in the grid voltage control. As such, the outputs of the voltage controller serve as the current references for the d-q current control. The three-phase grid current is transformed to the reference frame and fed to the appropriate controller. The current control structure is based on PI or PR current control. Figure 7.2 shows the PSO in the synchronous reference frame using a PI controller.

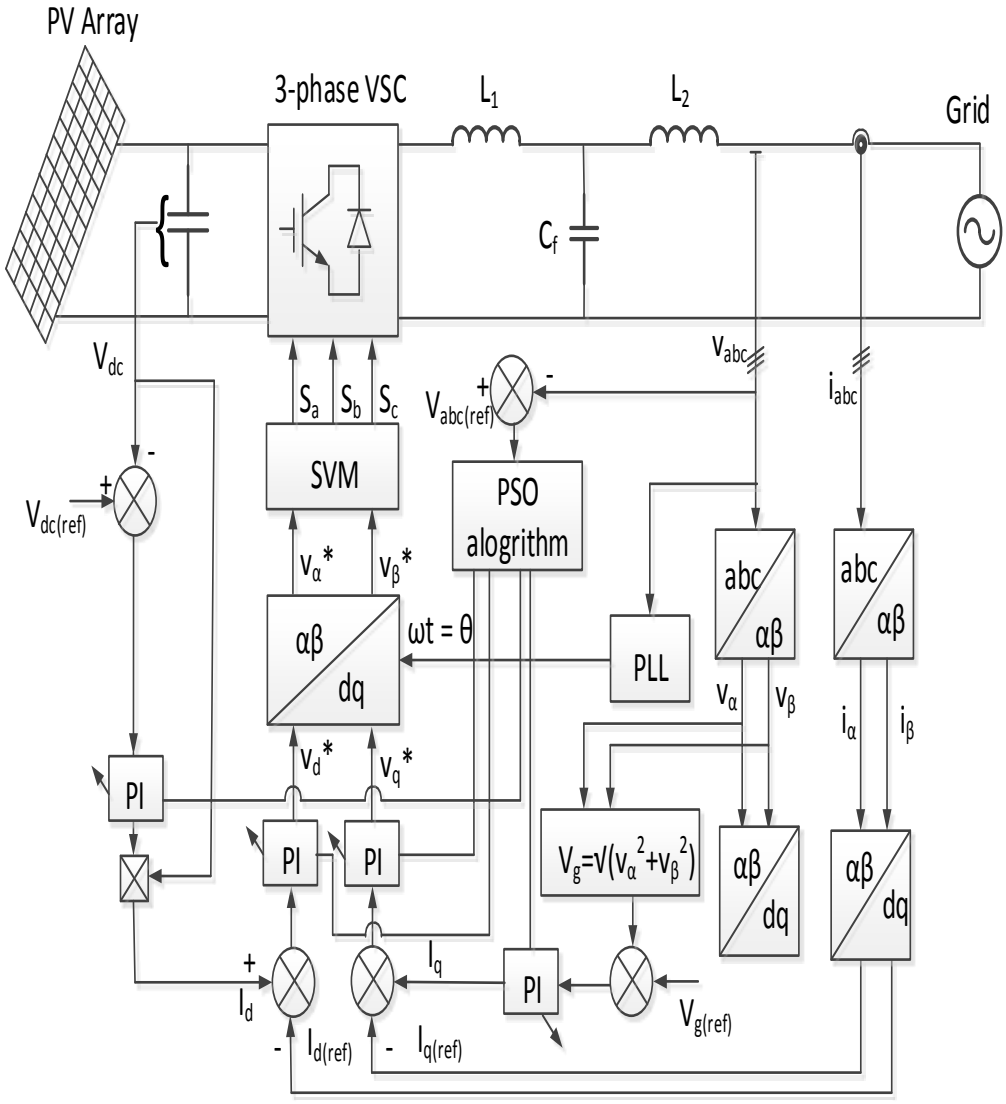

Figure 7.2 PSO optimization in the synchronous reference frame

In addition, PSO can be applied in the stationary reference frame using PR controller as shown in Figure 7.3. In both cases, the PSO algorithm is employed for self-tuning the control parameters by using the integral time absolute error (ITAE) as a cost function. The optimum solution is determined by the cost function calculation. The most commonly utilized cost functions are integral based such as the ITAE, integral of squared error (ISE) and integral of time multiplied by squared error (ITSE) [135], [136]. In this thesis, the ITAE is used.

$$TEA = \int_0^{\infty} t\left|e(t)\right| dt \tag{7.3}$$

where *e(t)* is the difference between the reference and actual values. The cost function is minimised using equations (7.1) and (7.2) throughout the optimisation process. The block diagram of the optimization process is shown in Figure 7.4.

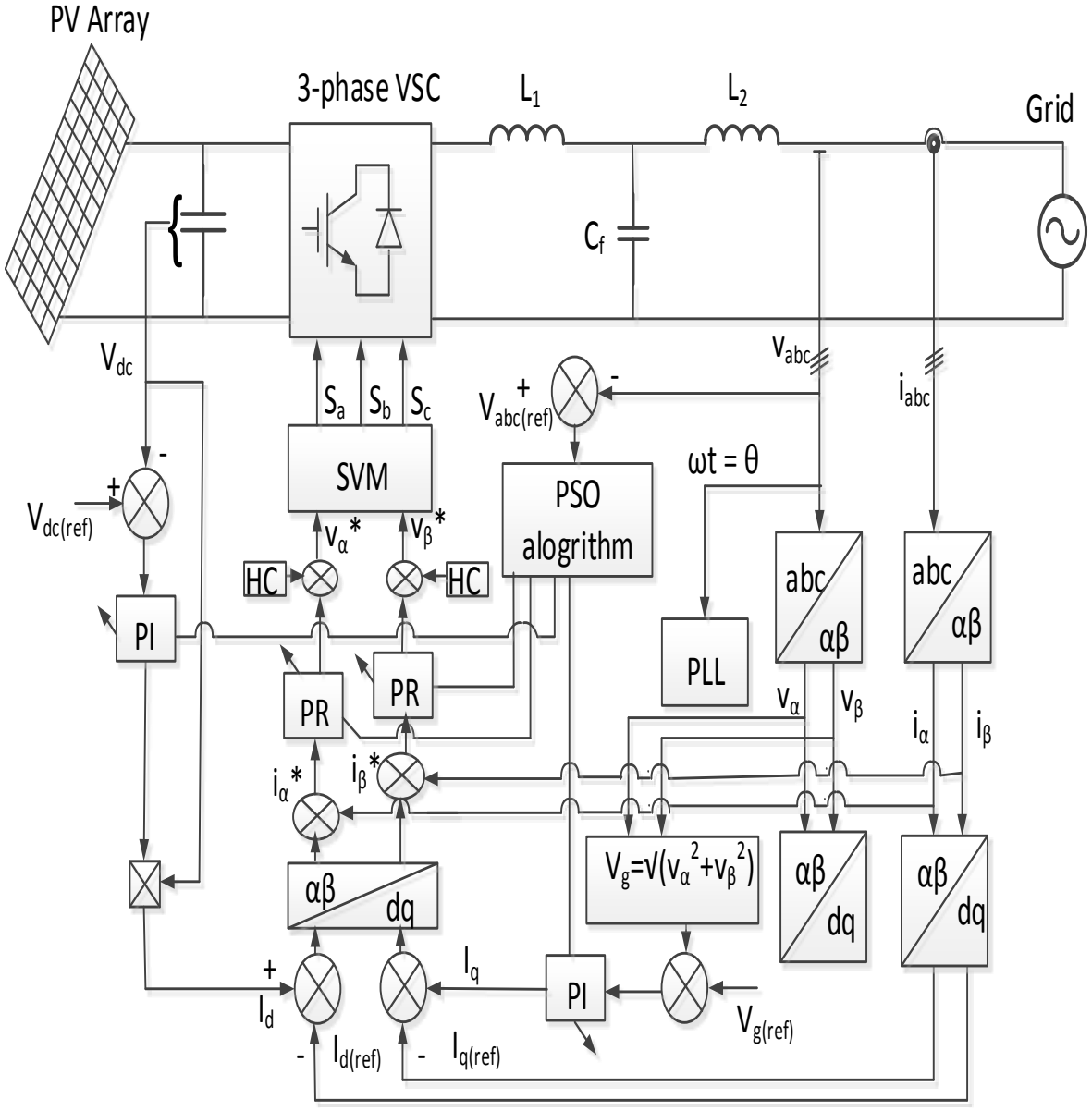

Figure 7.3 Optimization in the stationary reference frame using PR controller

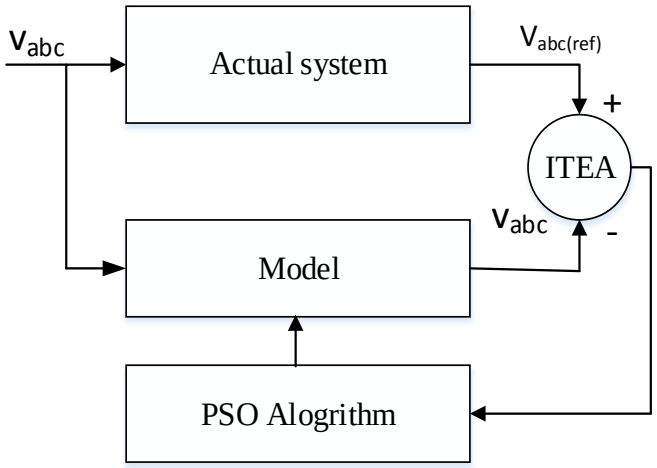

Figure 7.4 General structure of the PSO optimization algorithm

Ultimately, each particle has a candidate solution for the PI or PR controller parameters K_p and K_i.

7.4 Simulation Results of Using PSO Method

In this section, stochastic optimization control method using Particle Swarm Optimisation (PSO) is employed to select the optimal values of the controller gains. The PSO is based on a specific implementation of an iterative optimisation technique inspired by animal swarm behaviour.

During the optimization process, the control parameters of the three-phase grid-connected inverter are updated every iteration. Figure 7.5 and Figure 7.6 show the three-phase grid voltage and current waveforms respectively suing PSO optimization in the synchronous reference frame which based on PI control method. In order to analyse the inverter performance during abnormal grid condition such as the three-phase voltage sags, the system is designed accurately throughout the entire voltage sag event of 75% over a 0.1 to 0.15 second period. Figure 7.5 and Figure 7.6 show that PSO based control parameter tuning produces high-quality output grid voltage and current waveforms with low ripple and harmonic content.

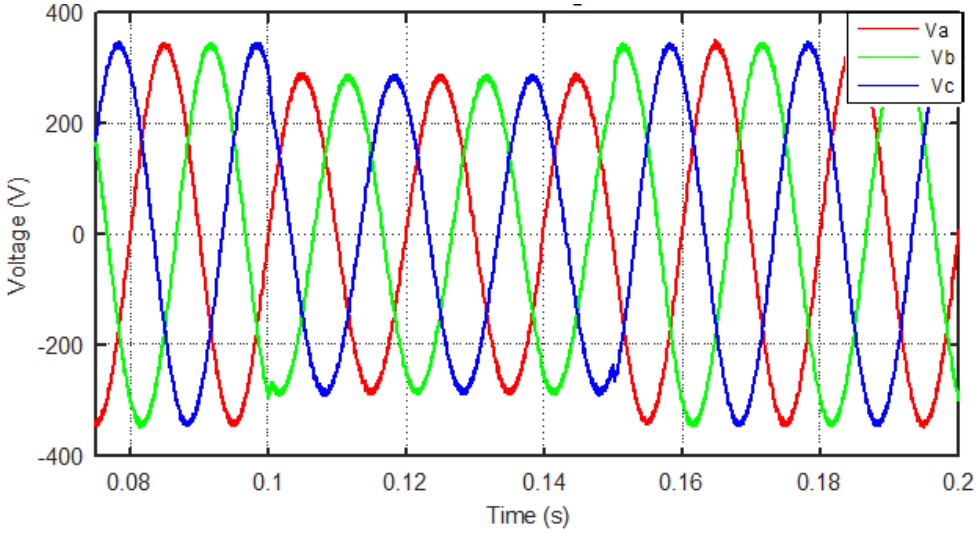

Figure 7.5 The three-phase voltage waveform using PSO

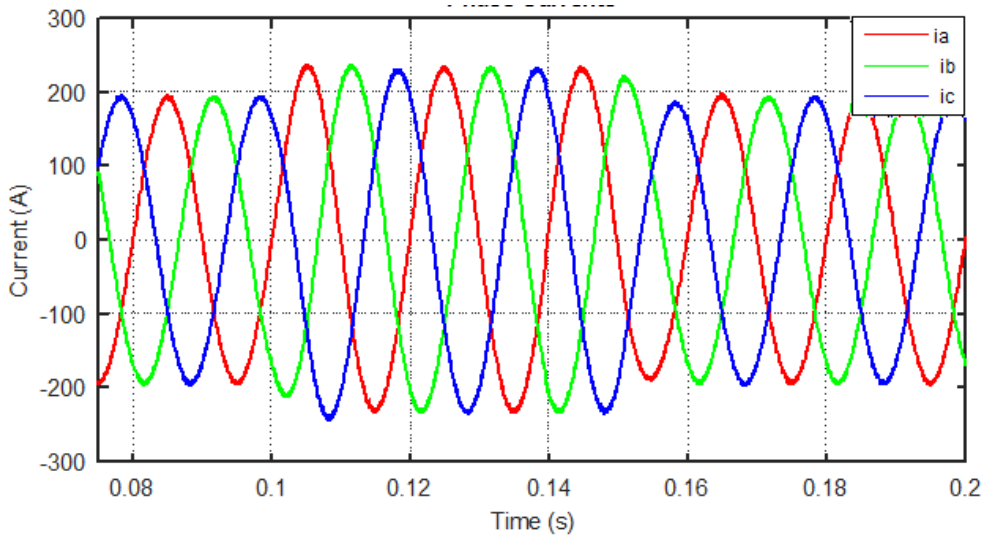

Figure 7.6 The three-phase current waveform Using PSO

Figure 7.7 and Figure 7.8 show, respectively, the waveforms of i_d and i_q current components when the PI controller is employed in the synchronous reference frame using PSO. During the abnormal conditions, there is an increase in the magnitude of the current. This is because the same amount of active power has to flow from the PV array to the grid before and during the voltage sag. Therefore, when the voltage decreases, the current has to increase to maintain the flow of active power.

In summary, the measured current follows the reference current accurately throughout the entire voltage sag event. Note that PSO tuning method achieves fast dynamic response and short settling time compared with the conventional method of tuning PI controller in Figure 5.13 and Figure 5.14.

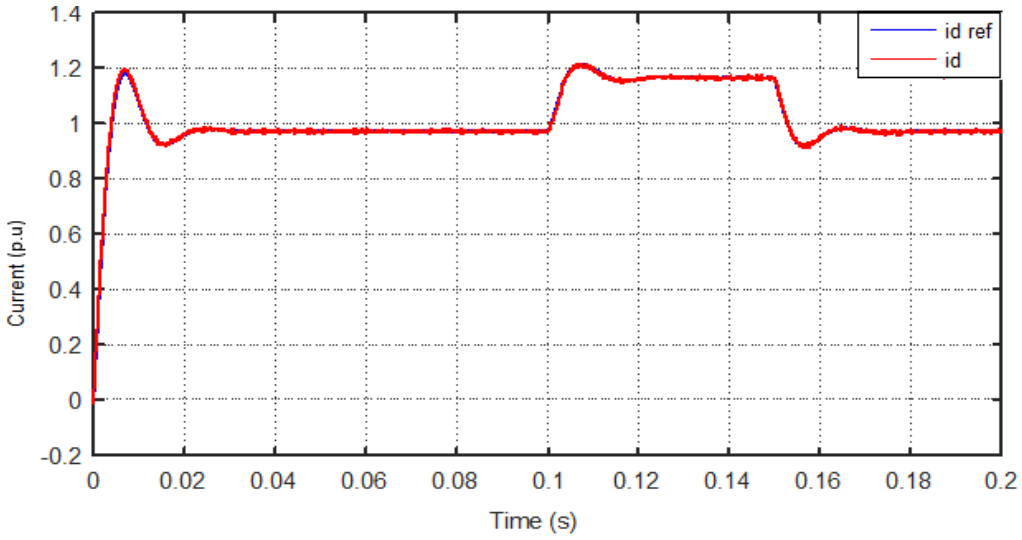

Figure 7.7 The reference and measured i_d current using PSO

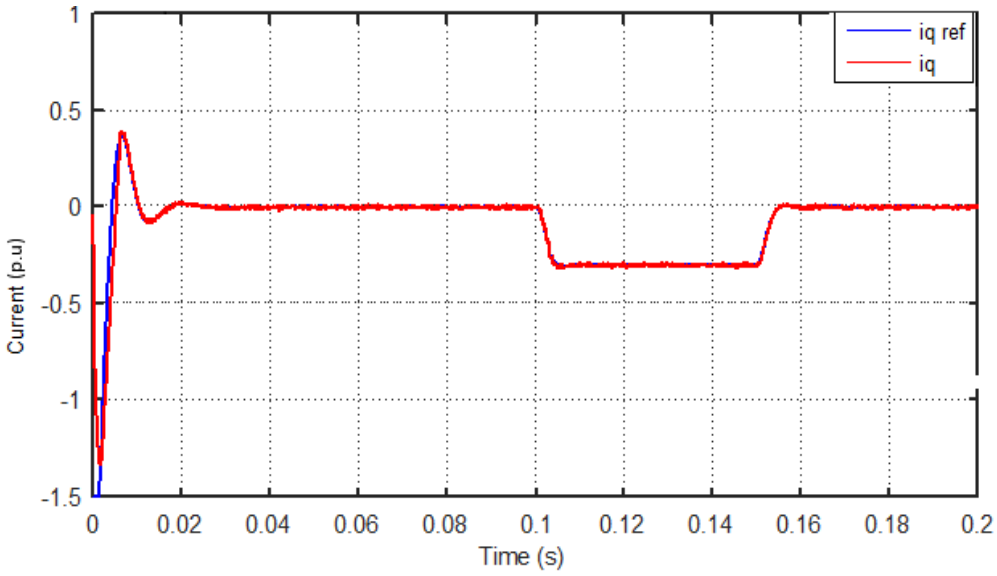

Figure 7.8 The reference and measured i_q current using PSO

Similarly, the PSO method is also used in tuning the controller parameters of the PR controller. Figure 7.9 and Figure 7.10 show, respectively, i_α and i_β current waveforms when PSO is used to tune the parameters of PR controller in the stationary reference frame. As shown, the measured current precisely tracks the reference current.

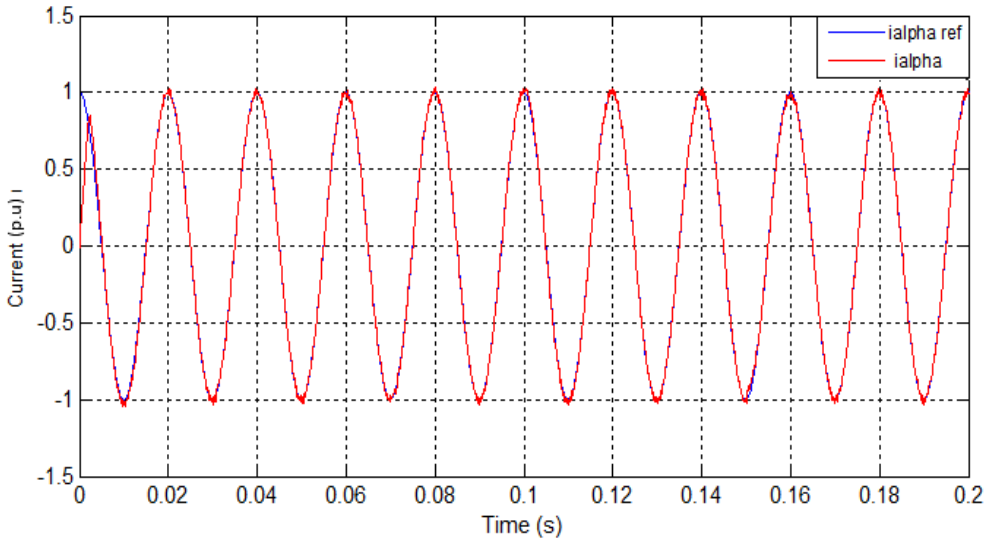

Figure 7.9 The reference and measured i-alpha using PSO

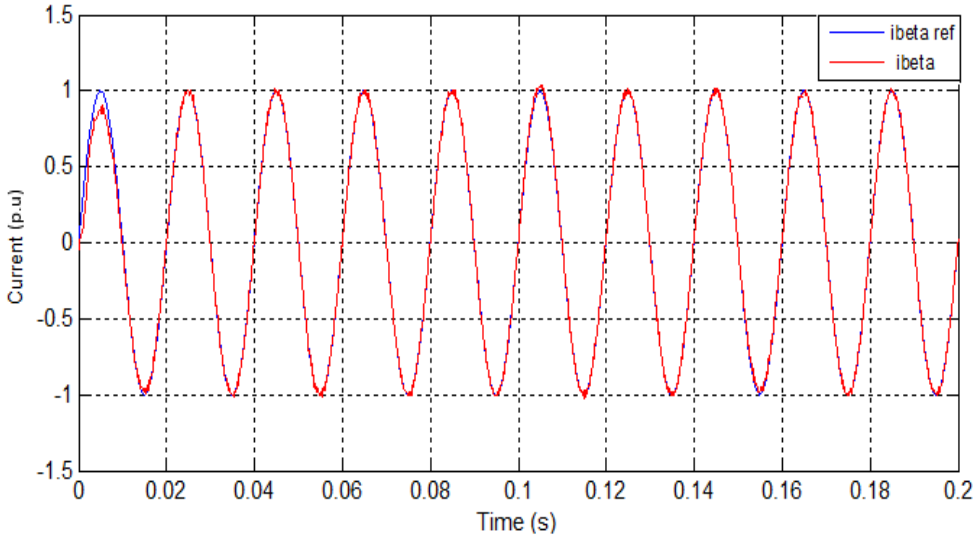

Figure 7.10 The reference and measured i-beta using PSO

7.4.1 Simulation Results of Using PSO under Unbalanced Grid Conditions

In order to test the controller dynamic performance of the control technique under unbalanced conditions, the principle of the PSO has been applied in PR controller in the stationary reference frame under unbalanced grid condition as shown in Figure 7.11 where a line to ground fault voltage sag is applied in the system.

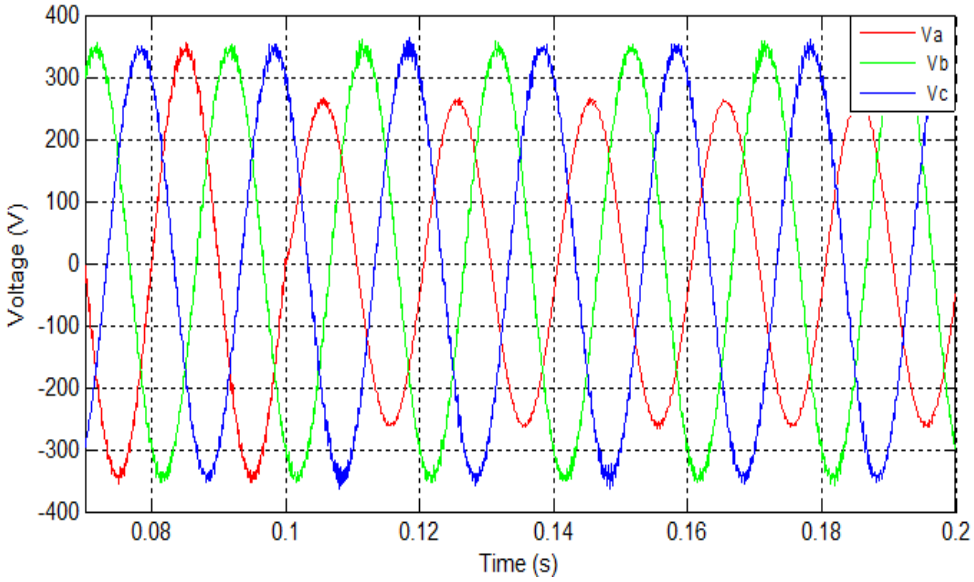

Figure 7.11 The unbalanced voltage waveform

It was observed in Figure 7.12 that the current waveform is not affected by the fault of the voltage and the injected current to the grid is balanced and is not distorted as shown control will work as desired.

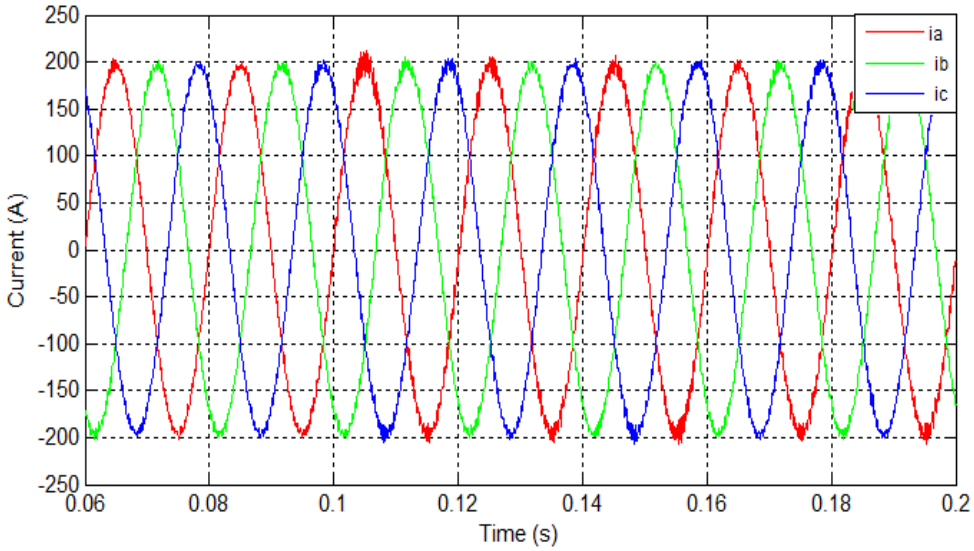

Figure 7.12 The three-phase current waveform

Figure 7.13 and Figure 7.14 show, respectively, i_α and i_β current waveforms. The measured current in the stationary reference frame alpha and beta follow the reference current effectively as shown in the figures. The result is satisfactory in both figures.

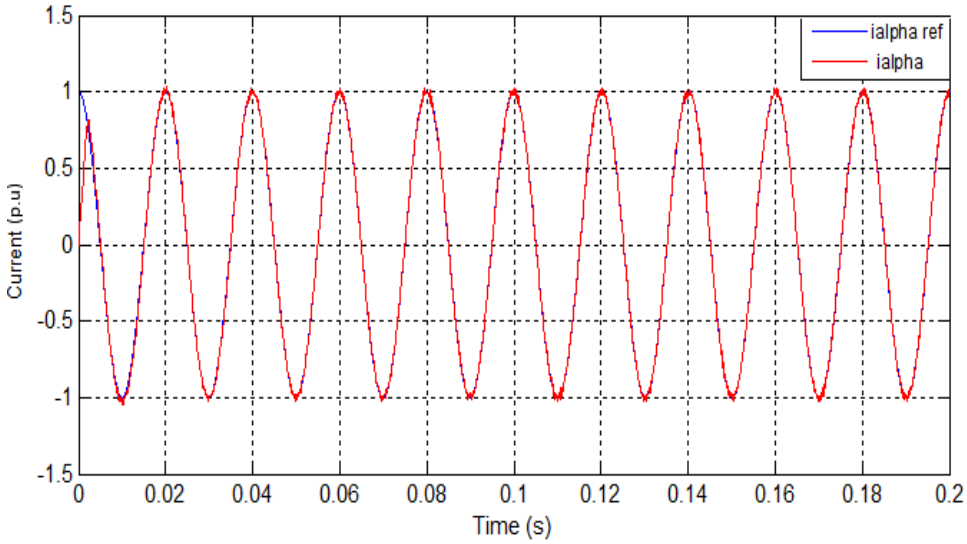

Figure 7.13 The reference and measured i_alpha under unbalance condition

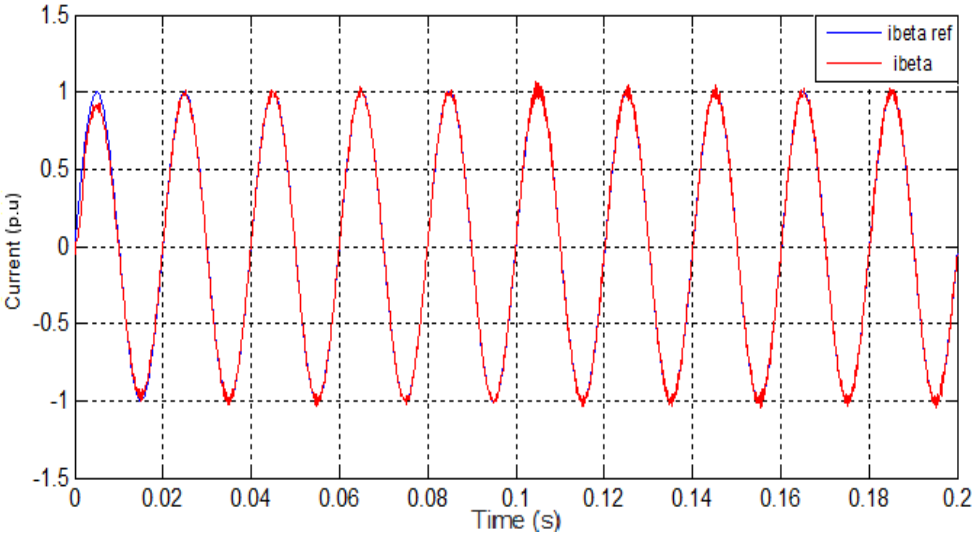

Figure 7.14 The reference and measured i_beta under unbalance condition

Here, in every iteration, the position and the velocity of the particles are initialised. The best recorded previous position vector is defined based on the control parameters k_p and k_i. The process continues until the predefined number of iterations is met. The following Table 7.1 gives the update regarding the control parameters in every iteration. The process is also terminated when predefined stopping criteria are satisfied or no significant improvement is achieved over a number of iterations.

Table 7.1 Iteration numbers the control parameters

No of iteration	k_p	K_i
1	7.812	999.9734
2	7.756	999.965
3	7.361	999.944
4	6.4813	999.8632
5	6.4123	999.8630
6	6.4120	999.7256
7	6.210	999.7112
8	5.4918	999.5735
9	5.4813	999.3682
10	5.4813	999.1632

Figure 7.15 shows the convergence error curve where the integral absolute error signal has been reduced to almost zero after few iterations when PSO is used in PR controller in the stationary reference frame. Figure 7.16 shows the FFT of the current waveform shows a very low THD of 0.59% when PSO is employed to tune the parameters of PR controller in the stationary reference frame. The ripple of the waveform is very small compared with the fundamental frequency. The FFT analysis of the measured current shows much lower THD value of 0.59% whilst 1.7% and 2.01% THDs are obtained with conventional PR controller and PI controller, respectively

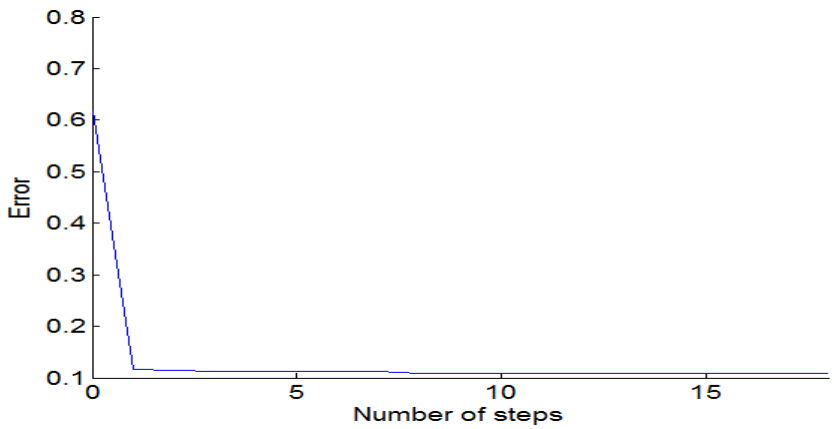

Figure 7.15 The error convergence curve

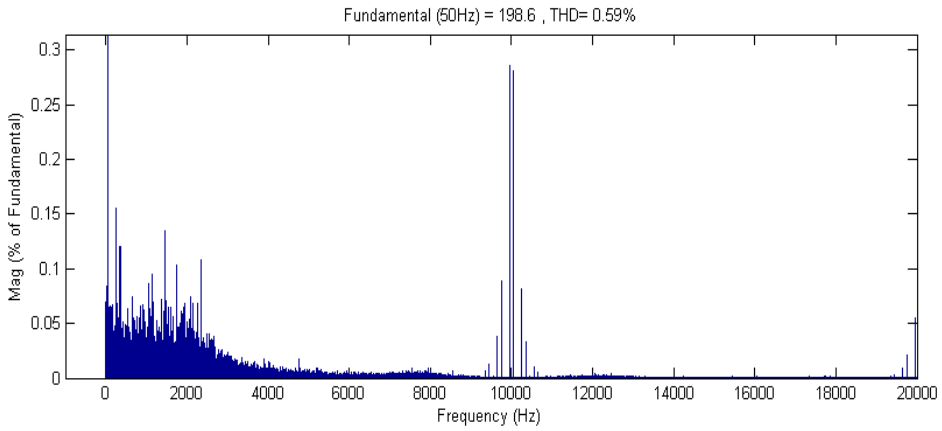

Figure 7.16 The FFT of the phase current waveform using PSO

7.5 Chapter Summary

In this chapter, the control parameter optimization of a three-phase grid-connected inverter using PSO is presented. When tuned with PSO, the controller demonstrates stability over a wide range of operating conditions and shows a fast dynamic response and good steady-state performance compared with the conventional method of tuning PI and PR controller. The effectiveness of the proposed optimization method using PSO is demonstrated by simulation results of a three-phase grid-connected inverter during normal and abnormal grid conditions. The proposed method can be employed without significantly increasing system complexity and cost and does not require any additional hardware. However, due to the time limitation, the proposed method not yet implemented in the laboratory and worth investigating in the future study.

Chapter 8. Conclusion and Future work

8.1 Introduction

It is likely that the aggressive use of non–renewable resources has produced major issues such as the production of more pollution and greenhouse gas emissions. From this point, researchers have encouraged organizations to use alternative renewable sources such as photovoltaic and the wind turbine to generate clean energy.

Photovoltaic, widely abbreviated as solar PV, is a fast growing element of renewable the market. PV generates DC voltage into appropriate AC voltage for the utility grid via three-phase grid-connected PV inverter. Three-phase grid-connected PV inverter is connected to the grid filter to reduce the harmonics inserted into the utility grid. It is aiming to inject the sinusoidal current intto the utility grid and to be able to deal with any abnormal conditions that occur in the grid and causes the disturbances through the electric power system.

Thus, these disturbances can be caused in the utility grid by short circuit faults like the line to ground fault, voltage sags, voltage swell and injected harmonics. This thesis investigated in detail the influence of the present control scheme of a three-phase grid-connected inverter given both normal and abnormal grid conditions.

8.2 Conclusion

There are two critical issues in the control of the three-phase inverter connected to the grid during abnormal condition. Firstly, grid synchronization is required to be more accurate and should be able to deal with any current controller in the grid-connected inverter. Moreover, this controller also needs to work perfectly with the symmetrical components of the grid voltage when the system is unbalanced and proper control of the sequences of both positive and negative current components injected to the grid is required.

Secondly, depending on the desired performance of the three-phase grid-connected inverter, the reference current generated by the current controller during abnormal conditions has three status levels: balanced, unbalanced or distorted and can cause undesired overcurrent tripping. Although there are many techniques used to control the three-phase grid-connected inverters,

most of the stake on the same structures which should be taken into account during normal and abnormal conditions.

In the three-phase grid-connected inverter, current control can be implemented in various ways. The Proportional Integral current control in the synchronous rotating reference frame *dq* and Proportional Resonance current control the stationary reference frame *αβ* are the most current control techniques. The implementation of the industrially accepted PI controller, along with the developing PR controller; accepted in grid-connected renewable energy applications, has injected the current under abnormal conditions under any circumstance such as grid fault, where the grid current varies from the normal operating case. Thus, the current control techniques based on the most suitable strategies that could achieve better results during normal and abnormal conditions in the thesis are: positive and negative sequence control *(*PNSC*)* and balance positive sequence control (BPSC).

This thesis delivers a straightforward method that decomposes the voltage and current, placing them into respective positive and negative sequence components that in turn are based on adaptive delayed filters with one-quarter period deferral. This filter presented in regard to the adaptive control strategy performance, producing good power quality (unity power factor and low THD performance) it can only be confirmed through imitation and results based on experimentation.

In keeping with the claims of other studies, simulation and practical studies have confirmed that the PR controller shows better performance under normal operating conditions.

The PI current controller indicates good performance and is easy to control. However, it results in a steady state error which cannot be eliminated when used with sinusoidal references. On the other hand, the PR controller has the capability to eradicate steady-state error by offering extra gain at the particular resonant frequency of the controlled signal

The PI controller has lowly functioning connected to cross-coupling between *d* and *q* components of grid current and needs decoupling term between the d and q coordinators and the voltage feedforward. However, the PR controller is used in the stationary reference frame α-β coordinates are not cross-coupled and consequently, no decoupling is required. In terms of the required processing and memory resources, the PI current controller requires additional mathematical transformation from the stationary reference frame to synchronous reference

frame. However, with the PR current control Park's transformation is not needed and hence the complexity of the control is reduced.

On the other hand, PR controller has the capability to implement harmonic compensator (HC) in parallel with PR controller without effect the dynamic response of the system and increase the quality of the quality of the control.

As well as under normal grid conditions, the current controller should be designed to operate under abnormal grid condition such as short circuit faults, voltage sags, voltage swell. These faults can be produced by abnormal situations in the grid such as direct starting of large motors, transformer energizing and capacitor bank charging. During this abnormality, one or more of phase voltage is reduced or increased than the nominal level at the point of common coupling (PCC) and causes unbalanced voltage waveform. The unbalanced voltage could be: single phase to ground faults, two-phase to phase to ground fault and unbalanced three-phase to ground faults. Therefore, unbalance grid conditions have the most significant impact in terms of increased current harmonics and ripple in the output power leading to the reductions in power quality.

To deal with these issues, the current control must be stable as during normal conditions. Under abnormal operating conditions, a method of the decomposing the voltage and current into its positive and negative sequence components is usually used. The PI current controller needs to control both the positive and negative voltage sequence while with the PR controller just the positive voltage sequence is required reducing the control complexity.

Under abnormal grid conditions, the controlled signal instigating substantial divergence from its nominal value. The implementation of the orthodox controller cannot remain in line with the rise in the error accordingly weakening which weakens controller performance. To get beyond this concern, this shows an enhancement in present-day control using a novel adaptive PR controller. The adaptive PR control techniques have been used in the stationary reference frame to control the current. The control techniques have been successfully implemented and tested in both balanced and unbalanced grid conditions in the simulation and verified experimentally. The online adaptation is based on a look-up table which is used to update the controller gains.

The proposed control technique is able to provide truncated total harmonic distortion THD in the injected current even during the occurrence of abnormal grid conditions compared with PI and PR controllers. The FFT analysis of the measured current shows much lower THD value

of 1.93% whilst 3.25% and 3.95% THDs are obtained with conventional PR controller and PI controller, respectively. The proposed method also achieves lower overshoot and settling time as well as smaller steady-state error. Overall, it can be suggested that the adaptive PR controller can provide an enhanced output power regulation, thus is better equipped with the result of grid faults, or procedure in weak grid environments.

Despite the fact that both PI and PR controllers are relatively straightforward to tune, and are sometimes capable of dealing with many time-varying conditions, most disturbances associated with grid-connected inverter technology, such as (grid voltage dip or changes in network impedance) are significantly more challenging and depends on the designer to obtain the best performance.

This research also presented an adaptive controller tuned using PSO is presented to optimize the parameters of both PI and PR controllers for the three-phase grid-connected inverter**.** Particle Swarm Optimisation is a self-commissioning tuning process method which tunes the parameters of the controllers to manage different normal and abnormal conditions and the transitions among them. PSO can operate easily and fast to optimize and is well suited for real-time control applications which experience time-varying disturbances. It is a stable optimization method that is relatively easy to implement because there are few parameters to adjust and it does not impose a significant computational. PSO is a powerful technique for solving a problem and can enhance the performance of the system.

When tuned with PSO, the controller demonstrated constancy over an expansive range of operating situations and showed a fast dynamic response and good steady-state performance compared with conventional methods of tuning PI controller and PR controller. The effectiveness of the proposed optimization method using PSO is demonstrated by simulation results of a three-phase grid-connected inverter. The results showed that with PSO parameter tuning, the current THD is reduced to 0.59% compared to 1.77% when parameters are tuned with trial and error. The proposed method can be employed without significantly increasing system complexity and cost and does not require any additional hardware.

8.3 Future Work

This research has investigated the performance of the current control techniques on the three-phase grid-connected inverter. Although a comprehensive investigation of the impact abnormal grid conditions, further investigation to take into account the load resistance in the control

scheme is considered to be worthwhile. Therefore, in continuation of this research, the following areas might be of interest for further work:

- A method of advanced optimization control techniques to control the three-phase grid-connected application in practical work such as PSO and GA.
- PSO can be integrated
- The optimization of reactive power sharing control strategies with active power control.
- In unbalanced conditions, the voltage control with reactive power compensation. The other option can be carried out to apply STATCOM system, therefore, bus voltage will be balanced.

References

[1] L. Wuhua and H. Xiangning, "Review of Nonisolated High-Step-Up DC/DC Converters in Photovoltaic Grid-Connected Applications," *IEEE Trans. Ind Electron.,* vol. 58, pp. 1239-1250, 2011.

[2] S. B. Kjaer, J. K. Pedersen, and F. Blaabjerg, "A review of single-phase grid-connected inverters for photovoltaic modules," *IEEE Transactions on Industry Applications,* vol. 41, pp. 1292-1306, 2005.

[3] R. E. P. N. f. t. s. Century, "Renewables 2016 Global Status Report ", (Paris: REN21 Secretariat)2016.

[4] N. Statistics, "Renewable sources of energy: Chapter 6, Digest of United Kingdom Energy Statistics (DUKES)," D. o. E. C. Change, Ed., ed: U.K goverment- Energy Statistics 2015.

[5] I. I. E. Agency, "Snapshot of Global PV Markets," The International Energy Agency (IEA)2015.

[6] A. H. Almasoud and H. M. Gandayh, "Future of solar energy in Saudi Arabia," *Journal of King Saud University - Engineering Sciences,* vol. 27, pp. 153-157, 2015.

[7] SUNPOWER. (6 March). *King Abdullah University, Saudi Arabia*. Available: https://global.sunpower.com/solar-case-studies/kaust-saudi-arabia/

[8] T. Yun Tiam and D. S. Kirschen, "Impact on the Power System of a Large Penetration of Photovoltaic Generation," in *Power Engineering Society General Meeting, 2007. IEEE*, 2007, pp. 1-8.

[9] T. Stetz, F. Marten, and M. Braun, "Improved Low Voltage Grid-Integration of Photovoltaic Systems in Germany," *Sustainable Energy, IEEE Transactions on,* vol. 4, pp. 534-542, 2013.

[10] S. Kouro, J. Rodriguez, B. Wu, S. Bernet, and M. Perez, "Powering the Future of Industry: High-Power Adjustable Speed Drive Topologies," *IEEE Industry Applications Magazine,* vol. 18, pp. 26-39, 2012.

[11] B. Tamyurek, "A High-Performance SPWM Controller for Three-Phase UPS Systems Operating Under Highly Nonlinear Loads," *IEEE Transactions on Power Electronics,* vol. 28, pp. 3689-3701, 2013.

[12] E. K. Kim, F. Mwasilu, H. H. Choi, and J. W. Jung, "An Observer-Based Optimal Voltage Control Scheme for Three-Phase UPS Systems," *IEEE Transactions on Industrial Electronics,* vol. 62, pp. 2073-2081, 2015.

[13] P. Rodriguez, J. Pou, J. Bergas, I. Candela, R. Burgos, and D. Boroyevich, "Double Synchronous Reference Frame PLL for Power Converters Control," in *Power Electronics Specialists Conference, 2005. PESC '05. IEEE 36th*, 2005, pp. 1415-1421.

[14] M. Liserre, F. Blaabjerg, and S. Hansen, "Design and control of an LCL-filter-based three-phase active rectifier," *IEEE Trans. Ind App.,* vol. 41, pp. 1281-1291, 2005.

[15] S. Chakraborty, B. Kramer, and B. Kroposki, "A review of power electronics interfaces for distributed energy systems towards achieving low-cost modular design," *Renewable and Sustainable Energy Reviews,* vol. 13, pp. 2323-2335, 2009.

[16] T. Kerekes, M. Liserre, R. Teodorescu, C. Klumpner, and M. Sumner, "Evaluation of Three-Phase Transformerless Photovoltaic Inverter Topologies," *Power Electronics, IEEE Transactions on,* vol. 24, pp. 2202-2211, 2009.

[17] "IEEE Recommended Practice for Utility Interface of Photovoltaic (PV) Systems," *IEEE Std 929-2000,* p. i, 2000.

[18] "IEEE Recommended Practice for Utility Interface of Residential and Intermediate Photovoltaic (PV) Systems," *ANSI/IEEE Std 929-1988,* p. 0_1, 1987.

[19] M. A. Elgendy, B. Zahawi, and D. J. Atkinson, "Operating Characteristics of the P&O Algorithm at High Perturbation Frequencies for Standalone PV Systems," *IEEE Transactions on Energy Conversion,* vol. 30, pp. 189-198, 2015.

[20] R. Kadri, J. P. Gaubert, and G. Champenois, "An Improved Maximum Power Point Tracking for Photovoltaic Grid-Connected Inverter Based on Voltage-Oriented Control," *Industrial Electronics, IEEE Transactions on,* vol. 58, pp. 66-75, 2011.

[21] X. Weidong, F. F. Edwin, G. Spagnuolo, and J. Jatskevich, "Efficient Approaches for Modeling and Simulating Photovoltaic Power Systems," *Photovoltaics, IEEE Journal of,* vol. 3, pp. 500-508, 2013.

[22] J. Rodriguez, S. Bernet, P. K. Steimer, and I. E. Lizama, "A Survey on Neutral-Point-Clamped Inverters," *IEEE Transactions on Industrial Electronics,* vol. 57, pp. 2219-2230, 2010.

[23] A. Nabae, I. Takahashi, and H. Akagi, "A New Neutral-Point-Clamped PWM Inverter," *IEEE Transactions on Industry Applications,* vol. IA-17, pp. 518-523, 1981.

[24] B. Xiao, L. Hang, J. Mei, C. Riley, L. M. Tolbert, and B. Ozpineci, "Modular Cascaded H-Bridge Multilevel PV Inverter With Distributed MPPT for Grid-Connected Applications," *IEEE Transactions on Industry Applications,* vol. 51, pp. 1722-1731, 2015.

[25] F. Wu, X. Li, F. Feng, and H. B. Gooi, "Modified Cascaded Multilevel Grid-Connected Inverter to Enhance European Efficiency and Several Extended Topologies," *IEEE Transactions on Industrial Informatics,* vol. 11, pp. 1358-1365, 2015.

[26] M. H. Rashid, *Power electronics: Circuits, devices & applications, International Edition*. United States. : Pearson Education Inc, 2004.

[27] P. Channegowda and V. John, "Filter Optimization for Grid Interactive Voltage Source Inverters," *IEEE Transactions on Industrial Electronics,* vol. 57, pp. 4106-4114, 2010.

[28] W. Li, X. Ruan, D. Pan, and X. Wang, "Full-Feedforward Schemes of Grid Voltages for a Three-Phase <formula formulatype="inline"> <img src="/images/tex/749.gif" alt="LCL"> </formula>-Type Grid-Connected Inverter," *IEEE Transactions on Industrial Electronics,* vol. 60, pp. 2237-2250, 2013.

[29] R. Teodorescu, M. Liserre, and P. RodrÃguez, *Grid Converters for Photovoltaic and Wind Power Systems*: Wiley, 2011.

[30] T. Erika and D. G. Holmes, "Grid current regulation of a three-phase voltage source inverter with an LCL input filter," *IEEE Transactions on Power Electronics,* vol. 18, pp. 888-895, 2003.

[31] G. Shen, D. Xu, L. Cao, and X. Zhu, "An Improved Control Strategy for Grid-Connected Voltage Source Inverters With an LCL Filter," *IEEE Transactions on Power Electronics,* vol. 23, pp. 1899-1906, 2008.

[32] F. Liu, Y. Zhou, S. Duan, J. Yin, and B. Liu, "Parameter Design of a Two-Current-Loop Controller Used in a Grid-Connected Inverter System With LCL Filter," *IEEE Transactions on Industrial Electronics,* vol. 56, pp. 4483-4491, 2009.

[33] M. H. Bierhoff and F. W. Fuchs, "Active Damping for Three-Phase PWM Rectifiers With High-Order Line-Side Filters," *IEEE Transactions on Industrial Electronics,* vol. 56, pp. 371-379, 2009.

[34] J. Dannehl, F. W. Fuchs, S. Hansen, and P. B. Thogersen, "Investigation of Active Damping Approaches for PI-Based Current Control of Grid-Connected Pulse Width Modulation Converters With LCL Filters," *IEEE Transactions on Industry Applications,* vol. 46, pp. 1509-1517, 2010.

[35] Rodri, x, P. guez, A. Luna, Mu, x00F, R. S. oz-Aguilar, I. Etxeberria-Otadui, R. Teodorescu, and F. Blaabjerg, "A Stationary Reference Frame Grid Synchronization System for Three-Phase Grid-Connected Power Converters Under Adverse Grid Conditions," *IEEE Trans, Power Electron.,* vol. 27, pp. 99-112, 2012.

[36] F. Mur, V. Cardenas, J. Vaquero, and S. Martinez, "Phase synchronization and measurement digital systems of AC mains for power converters," in *Power Electronics Congress, 1998. CIEP 98. VI IEEE International*, 1998, pp. 188-194.

[37] J. W. Choi, Y. K. Kim, and H. G. Kim, "Digital PLL control for single-phase photovoltaic system," *Electric Power Applications, IEE Proceedings -,* vol. 153, pp. 40-46, 2006.

[38] F. M. Gardner, *Phaselock Techniques* vol. 2nd edition: Wiley-Interscience, 1979.

[39] F. Blaabjerg, R. Teodorescu, M. Liserre, and A. V. Timbus, "Overview of Control and Grid Synchronization for Distributed Power Generation Systems," *Industrial Electronics, IEEE Transactions on,* vol. 53, pp. 1398-1409, 2006.

[40] H. Guan-Chyun and J. C. Hung, "Phase-locked loop techniques. A survey," *IEEE Trans, Ind. Appl.,* vol. 43, pp. 609-615, 1996.

[41] A. Timbus, M. Liserre, R. Teodorescu, and F. Blaabjerg, "Synchronization methods for three phase distributed power generation systems - An overview and evaluation," in *Power Electronics Specialists Conference, 2005. PESC '05. IEEE 36th*, 2005, pp. 2474-2481.

[42] D. Jovcic, "Phase locked loop system for FACTS," *IEEE Trans, on Power Systems,* vol. 18, pp. 1116-1124, 2003.

[43] M. Weinhold, "A new control for optimal operation of a three-phase voltage dc link PWM converter," in *Proc. PCIM Conf* 1991, pp. 371-371.

[44] L. A. Serpa, S. Ponnaluri, P. M. Barbosa, and J. W. Kolar, "A Modified Direct Power Control Strategy Allowing the Connection of Three-Phase Inverters to the Grid Through LCL Filters," *IEEE Transactions on Industry Applications,* vol. 43, pp. 1388-1400, 2007.

[45] N. Alford and J. FrÃ©chet, *Proceedings of the Eighth Saudi Students Conference in the UK*: World Scientific Publishing Company, 2015.

[46] J. R. Rodriguez, J. W. Dixon, J. R. Espinoza, J. Pontt, and P. Lezana, "PWM regenerative rectifiers: state of the art," *IEEE Trans, Ind. Appl.,* vol. 52, pp. 5-22, 2005.

[47] M. Liserre, F. Blaabjerg, and S. Hansen, "Design and control of an LCL-filter-based three-phase active rectifier," *IEEE Trans, Ind. Appl.,* vol. 41, pp. 1281-1291, 2005.

[48] "IEEE Standard for Interconnecting Distributed Resources With Electric Power Systems," *IEEE Std 1547-2003,* pp. 0_1-16, 2003.

[49] "Draft Application Guide for IEEE Standard 1547, Interconnecting Distributed Resources with Electric Power Systems," *IEEE Unapproved Draft Std P1547.2/D10, Mar 2008,* 2008.

[50] M. P. Kazmierkowski and M. A. Dzieniakowski, "Review of current regulation methods for VS-PWM inverters," in *Industrial Electronics, 1993. Conference Proceedings, ISIE'93 - Budapest., IEEE International Symposium on*, 1993, pp. 448-456.

[51] W. Leonhard, *Control of Electrical Drive*. Berlin, Germany: Springer-Verlag, 1996.

[52] J. Svensson, "Synchronisation methods for grid-connected voltage source converters," *IEE Proceedings - Generation, Transmission and Distribution,* vol. 148, pp. 229-235, 2001.

[53] K. J. Åström and T. Hägglund, *Advanced PID Control*: ISA-The Instrumentation, Systems, and Automation Society, 2006.

[54] R. Teodorescu, F. Blaabjerg, U. Borup, and M. Liserre, "A new control structure for grid-connected LCL PV inverters with zero steady-state error and selective harmonic compensation," in *Applied Power Electronics Conference and Exposition, 2004. APEC '04. Nineteenth Annual IEEE*, 2004, pp. 580-586 Vol.1.

[55] R. Teodorescu, F. Blaabjerg, M. Liserre, and P. C. Loh, "Proportional-resonant controllers and filters for grid-connected voltage-source converters," *IEE Proceedings - Electric Power Applications,* vol. 153, pp. 750-762, 2006.

[56] R. Teodorescu and F. Blaabjerg, "Flexible control of small wind turbines with grid failure detection operating in stand-alone and grid-connected mode," *IEEE Transactions on Power Electronics,* vol. 19, pp. 1323-1332, 2004.

[57] S. Fukuda and T. Yoda, "A novel current-tracking method for active filters based on a sinusoidal internal model [for PWM invertors]," *IEEE Transactions on Industry Applications,* vol. 37, pp. 888-895, 2001.

[58] S. Byeong-Mun, K. Youngroc, C. Hanju, and L. Hakju, "Current harmonic minimization of a grid-connected photovoltaic 500kW three-phase inverter using PR control," in *Energy Conversion Congress and Exposition (ECCE), 2011 IEEE*, 2011, pp. 1063-1068.

[59] A. Nicastri and A. Nagliero, "Comparison and evaluation of the PLL techniques for the design of the grid-connected inverter systems," in *Industrial Electronics (ISIE), 2010 IEEE International Symposium on*, 2010, pp. 3865-3870.

[60] M. Castilla, J. Miret, J. Matas, L. G. de Vicua, and J. M. Guerrero, "Linear Current Control Scheme With Series Resonant Harmonic Compensator for Single-Phase Grid-Connected Photovoltaic Inverters," *Industrial Electronics, IEEE Transactions on,* vol. 55, pp. 2724-2733, 2008.

[61] M. Liserre, R. Teodorescu, and F. Blaabjerg, "Multiple harmonics control for three-phase grid converter systems with the use of PI-RES current controller in a rotating frame," *Power Electronics, IEEE Transactions on,* vol. 21, pp. 836-841, 2006.

[62] R. Teodorescu, F. Blaabjerg, M. Liserre, and P. C. Loh, "Proportional-resonant controllers and filters for grid-connected voltage-source converters," *Electric Power Applications, IEE Proceedings,* vol. 153, pp. 750-762, 2006.

[63] S. Buso, L. Malesani, and P. Mattavelli, "Comparison of current control techniques for active filter applications," *IEEE Transactions on Industrial Electronics,* vol. 45, pp. 722-729, 1998.

[64] M. Mohseni and S. M. Islam, "A New Vector-Based Hysteresis Current Control Scheme for Three-Phase PWM Voltage-Source Inverters," *IEEE Trans. Power Electron.,* vol. 25, pp. 2299-2309, 2010.

[65] T. Orłowska-Kowalska, F. Blaabjerg, and J. Rodríguez, *Advanced and Intelligent Control in Power Electronics and Drives*: Springer International Publishing, 2014.

[66] T. Noguchi, H. Tomiki, S. Kondo, and I. Takahashi, "Direct power control of PWM converter without power-source voltage sensors," *IEEE Transactions on Industry Applications,* vol. 34, pp. 473-479, 1998.

[67] M. Malinowski, M. P. Kazmierkowski, S. Hansen, F. Blaabjerg, and G. D. Marques, "Virtual-flux-based direct power control of three-phase PWM rectifiers," *IEEE Transactions on Industry Applications,* vol. 37, pp. 1019-1027, 2001.

[68] R. Wu, S. B. Dewan, and G. R. Slemon, "Analysis of a PWM AC to DC voltage source converter under the predicted current control with a fixed switching frequency," *IEEE Transactions on Industry Applications,* vol. 27, pp. 756-764, 1991.

[69] Z. Song, W. Chen, and C. Xia, "Predictive Direct Power Control for Three-Phase Grid-Connected Converters Without Sector Information and Voltage Vector Selection," *IEEE Transactions on Power Electronics,* vol. 29, pp. 5518-5531, 2014.

[70] A. Bouafia, J. P. Gaubert, and F. Krim, "Predictive Direct Power Control of Three-Phase Pulsewidth Modulation (PWM) Rectifier Using Space-Vector Modulation (SVM)," *IEEE Transactions on Power Electronics,* vol. 25, pp. 228-236, 2010.

[71] M. Castilla, J. Miret, J. L. Sosa, J. Matas, V. de, x00F, and L. G. a, "Grid-Fault Control Scheme for Three-Phase Photovoltaic Inverters With Adjustable Power Quality Characteristics," *Power Electronics, IEEE Transactions on,* vol. 25, pp. 2930-2940, 2010.

[72] E. E. Juarez and A. Hernandez, "An analytical approach for stochastic assessment of balanced and unbalanced voltage sags in large systems," *Power Delivery, IEEE Transactions on,* vol. 21, pp. 1493-1500, 2006.

[73] M. Bollen, J. R. Gordon, S. Djokic, K. Stockman, J. Milanovic, R. Neumann, G. Ethier, and F. Zavoda, "Voltage dip immunity of equipment and installations - status and need for further work," in *Electricity Distribution (CICED), 2010 China International Conference on*, 2010, pp. 1-8.

[74] L. Tzung-Lin, H. Shang-Hung, and C. Yu-Hung, "D-STATCOM With Positive-Sequence Admittance and Negative-Sequence Conductance to Mitigate Voltage Fluctuations in High-Level Penetration of Distributed-Generation Systems," *IEEE Trans. Ind. Electron.,* vol. 60, pp. 1417-1428, 2013.

[75] M. Savaghebi, A. Jalilian, J. C. Vasquez, and J. M. Guerrero, "Autonomous Voltage Unbalance Compensation in an Islanded Droop-Controlled Microgrid," *IEEE Trans. Ind. Electron.,* vol. 60, pp. 1390-1402, 2013.

[76] A. Sannino, J. Svensson, and T. Larsson, "Power-electronic solutions to power quality problems," *Electric Power Systems Research,* vol. 66, pp. 71-82, 2003.

[77] "IEEE Recommended Practice for Monitoring Electric Power Quality," *IEEE Std 1159-1995,* p. i, 1995.

[78] F. Salha, F. Colas, and X. Guillaud, "Dynamic performance analysis of a LC-filter grid-connected gas turbine under voltage-sag operation," in *Advanced Electromechanical Motion Systems & Electric Drives Joint Symposium, 2009. ELECTROMOTION 2009. 8th International Symposium on*, 2009, pp. 1-6.

[79] J. Miret, M. Castilla, A. Camacho, L. G. d. Vicu, x00F, and J. Matas, "Control Scheme for Photovoltaic Three-Phase Inverters to Minimize Peak Currents During Unbalanced Grid-Voltage Sags," *IEEE Transactions on Power Electronics,* vol. 27, pp. 4262-4271, 2012.

[80] E. Fuchs and M. A. S. Masoum, *Power Quality in Power Systems and Electrical Machines*: Elsevier Science, 2011.

[81] L. Chia-Tse, H. Che-Wei, and C. Po-Tai, "A Low-Voltage Ride-Through Technique for Grid-Connected Converters of Distributed Energy Resources," *IEEE Trans, Ind. Electron.,* vol. 47, pp. 1821-1832, 2011.

[82] J. Miret, A. Camacho, M. Castilla, L. G. de Vicuna, and J. Matas, "Control Scheme With Voltage Support Capability for Distributed Generation Inverters Under Voltage Sags," *IEEE Trans, Power Electron.,* vol. 28, pp. 5252-5262, 2013.

[83] A. Camacho, M. Castilla, J. Miret, A. Borrell, and L. Garcia de Vicuna, "Active and Reactive Power Strategies With Peak Current Limitation for Distributed Generation Inverters During Unbalanced Grid Faults," *IEEE Trans, Ind. Electron.,* vol. 62, pp. 1515-1525, 2015.

[84] D. Graovac, V. Katic, and A. Rufer, "Power Quality Problems Compensation With Universal Power Quality Conditioning System," *IEEE Trans, Power Del.,* vol. 22, pp. 968-976, 2007.

[85] F. Barrero, S. Martinez, F. Yeves, F. Mur, and P. M. Martinez, "Universal and reconfigurable to UPS active power filter for line conditioning," *IEEE Trans, Power Del.,* vol. 18, pp. 283-290, 2003.

[86] S. George and V. Agarwal, "A DSP Based Optimal Algorithm for Shunt Active Filter Under Nonsinusoidal Supply and Unbalanced Load Conditions," *IEEE Trans, Power Electron.,* vol. 22, pp. 593-601, 2007.

[87] B. Singh and J. Solanki, "An Implementation of an Adaptive Control Algorithm for a Three-Phase Shunt Active Filter," *Industrial Electronics, IEEE Transactions on,* vol. 56, pp. 2811-2820, 2009.

[88] W. Fei, J. L. Duarte, and M. A. M. Hendrix, "Grid-Interfacing Converter Systems With Enhanced Voltage Quality for Microgrid Application—Concept and Implementation," *IEEE Trans, Power Electron.,* vol. 26, pp. 3501-3513, 2011.

[89] M. Castilla, J. Miret, A. Camacho, J. Matas, and L. Garcia de Vicuna, "Voltage Support Control Strategies for Static Synchronous Compensators Under Unbalanced Voltage Sags," *IEEE Trans, Ind. Electron.,* vol. 61, pp. 808-820, 2014.

[90] L. Kuang, L. Jinjun, W. Zhaoan, and W. Biao, "Strategies and Operating Point Optimization of STATCOM Control for Voltage Unbalance Mitigation in Three-Phase Three-Wire Systems," *IEEE Trans, Power Del.,* vol. 22, pp. 413-422, 2007.

[91] L. Tzung-Lin, H. Shang-Hung, and C. Yu-Hung, "D-STATCOM With Positive-Sequence Admittance and Negative-Sequence Conductance to Mitigate Voltage Fluctuations in High-Level Penetration of Distributed-Generation Systems," *IEEE Trans, Ind. Electron.,* vol. 60, pp. 1417-1428, 2013.

[92] P. Rodriguez, J. Pou, J. Bergas, J. I. Candela, R. P. Burgos, and D. Boroyevich, "Decoupled Double Synchronous Reference Frame PLL for Power Converters Control," *IEEE Transactions on Power Electronics,* vol. 22, pp. 584-592, 2007.

[93] H. Awad, J. Svensson, and M. J. Bollen, "Tuning software phase-locked loop for series-connected converters," *IEEE Transactions on Power Delivery,* vol. 20, pp. 300-308, 2005.

[94] J. Svensson, M. Bongiorno, and A. Sannino, "Practical Implementation of Delayed Signal Cancellation Method for Phase-Sequence Separation," *IEEE Transactions on Power Delivery,* vol. 22, pp. 18-26, 2007.

[95] V. Kaura and V. Blasko, "Operation of a phase locked loop system under distorted utility conditions," *IEEE Transactions on Industry Applications,* vol. 33, pp. 58-63, 1997.

[96] C. Se-Kyo, "A phase tracking system for three phase utility interface inverters," *IEEE Transactions on Power Electronics,* vol. 15, pp. 431-438, 2000.

[97] P. Rodriguez, L. Sainz, and J. Bergas, "Synchronous double reference frame PLL applied to a unified power quality conditioner," in *Harmonics and Quality of Power, 2002. 10th International Conference on*, 2002, pp. 614-619 vol.2.

[98] P. Rodriguez, J. Pou, J. Bergas, J. I. Candela, R. P. Burgos, and D. Boroyevich, "Decoupled Double Synchronous Reference Frame PLL for Power Converters Control," *Power Electronics, IEEE Transactions on,* vol. 22, pp. 584-592, 2007.

[99] L. Kyoung-Jun, L. Jong-Pil, S. Dongsul, Y. Dong-Wook, and K. Hee-Je, "A Novel Grid Synchronization PLL Method Based on Adaptive Low-Pass Notch Filter for Grid-Connected PCS," *IEEE Trans, Industrial Electronics,* vol. 61, pp. 292-301, 2014.

[100] Y. F. Wang and Y. W. Li, "Analysis and Digital Implementation of Cascaded Delayed-Signal-Cancellation PLL," *IEEE Transactions on Power Electronics,* vol. 26, pp. 1067-1080, 2011.

[101] H. Geng, D. Xu, and B. Wu, "A Novel Hardware-Based All-Digital Phase-Locked Loop Applied to Grid-Connected Power Converters," *IEEE Transactions on Industrial Electronics,* vol. 58, pp. 1737-1745, 2011.

[102] P. Rodr, x00Ed, guez, A. Luna, R. S. Mu, x00F, A. oz, I. Etxeberria-Otadui, R. Teodorescu, and F. Blaabjerg, "A Stationary Reference Frame Grid Synchronization System for Three-Phase Grid-Connected Power Converters Under Adverse Grid Conditions," *IEEE Transactions on Power Electronics,* vol. 27, pp. 99-112, 2012.

[103] Y. Zhou, P. Bauer, J. A. Ferreira, and J. Pierik, "Operation of Grid-Connected DFIG Under Unbalanced Grid Voltage Condition," *IEEE Transactions on Energy Conversion,* vol. 24, pp. 240-246, 2009.

[104] F. A. S. Neves, M. C. Cavalcanti, H. E. P. de Souza, F. Bradaschia, E. J. Bueno, and M. Rizo, "A Generalized Delayed Signal Cancellation Method for Detecting Fundamental-Frequency Positive-Sequence Three-Phase Signals," *Power Delivery, IEEE Transactions on,* vol. 25, pp. 1816-1825, 2010.

[105] W. Yi Fei and L. Yun Wei, "Three-Phase Cascaded Delayed Signal Cancellation PLL for Fast Selective Harmonic Detection," *Industrial Electronics, IEEE Transactions on,* vol. 60, pp. 1452-1463, 2013.

[106] "A New Single-Phase PLL Structure Based on Second Order Generalized Integrator," in *Power Electronics Specialists Conference, 2006. PESC '06. 37th IEEE*, 2006, pp. 1-6.

[107] A. Kulka, "''Sensorless digital control of grid connected three phase converters for renewable sources'', PhD Thesis," PhD, Norwegian University of Science and Technology, 2009.

[108] J. A. Suul, A. Luna, P. Rodriguez, and T. Undeland, "Voltage-Sensor-Less Synchronization to Unbalanced Grids by Frequency-Adaptive Virtual Flux Estimation," *IEEE Transactions on Industrial Electronics,* vol. 59, pp. 2910-2923, 2012.

[109] P. Rioual, H. Pouliquen, and J. P. Louis, "Regulation of a PWM rectifier in the unbalanced network state using a generalized model," *IEEE Trans, Power Electron.,* vol. 11, pp. 495-502, 1996.

[110] S. Hong-Seok and N. Kwanghee, "Dual current control scheme for PWM converter under unbalanced input voltage conditions," *IEEE Trans, Ind. Electron.,* vol. 46, pp. 953-959, 1999.

[111] S. Yongsug and T. A. Lipo, "Control scheme in hybrid synchronous stationary frame for PWM AC/DC converter under generalized unbalanced operating conditions," *IEEE Transactions on Industry Applications,* vol. 42, pp. 825-835, 2006.

[112] I. Etxeberria-Otadui, U. Viscarret, M. Caballero, A. Rufer, and S. Bacha, "New Optimized PWM VSC Control Structures and Strategies Under Unbalanced Voltage Transients," *Industrial Electronics, IEEE Transactions on,* vol. 54, pp. 2902-2914, 2007.

[113] P. Rodriguez, A. V. Timbus, R. Teodorescu, M. Liserre, and F. Blaabjerg, "Flexible Active Power Control of Distributed Power Generation Systems During Grid Faults," *Industrial Electronics, IEEE Transactions on,* vol. 54, pp. 2583-2592, 2007.

[114] P. Rodriguez, A. V. Timbus, R. Teodeorescu, M. Liserre, and F. Blaabjerg, "Independent PQ Control for Distributed Power Generation Systems under Grid Faults," in *IEEE Industrial Electronics, IECON 2006 - 32nd Annual Conference on*, 2006, pp. 5185-5190.

[115] F. Wang, J. L. Duarte, and M. A. M. Hendrix, "Design and analysis of active power control strategies for distributed generation inverters under unbalanced grid faults," *Generation, Transmission & Distribution, IET,* vol. 4, pp. 905-916, 2010.

[116] A. V. Timbus, P. Rodriguez, R. Teodorescu, M. Liserre, and F. Blaabjerg, "Control Strategies for Distributed Power Generation Systems Operating on Faulty Grid," in *Industrial Electronics, 2006 IEEE International Symposium on*, 2006, pp. 1601-1607.

[117] M. Castilla, J. Miret, J. L. Sosa, J. Matas, V. de, x00F, and L. G. a, "Grid-Fault Control Scheme for Three-Phase Photovoltaic Inverters With Adjustable Power Quality Characteristics," *IEEE Trans, Power Electron.,* vol. 25, pp. 2930-2940, 2010.

[118] C. Lascu, L. Asiminoaei, I. Boldea, and F. Blaabjerg, "High Performance Current Controller for Selective Harmonic Compensation in Active Power Filters," *IEEE Transactions on Power Electronics,* vol. 22, pp. 1826-1835, 2007.

[119] A. Vidal, F. D. Freijedo, A. G. Yepes, P. Fernandez-Comesana, J. Malvar, O. Lopez, and J. Doval-Gandoy, "Assessment and Optimization of the Transient Response of Proportional-Resonant Current Controllers for Distributed Power Generation Systems," *Industrial Electronics, IEEE Transactions on,* vol. 60, pp. 1367-1383, 2013.

[120] Q. Bi, W.-J. Cai, Q.-G. Wang, C.-C. Hang, L. Eng-Lock, Y. Sun, K.-D. Liu, Y. Zhang, and B. Zou, "Advanced controller auto-tuning and its application in HVAC systems," *Control Engineering Practice,* vol. 8, pp. 633-644, 2000.

[121] A. Rubaai and P. Young, "EKF-Based PI-/PD-Like Fuzzy-Neural-Network Controller for Brushless Drives," *Industry Applications, IEEE Transactions on,* vol. 47, pp. 2391-2401, 2011.

[122] A. Rubaai, M. J. Castro-Sitiriche, and A. R. Ofoli, "Design and Implementation of Parallel Fuzzy PID Controller for High-Performance Brushless Motor Drives: An Integrated Environment for Rapid Control Prototyping," *Industry Applications, IEEE Transactions on,* vol. 44, pp. 1090-1098, 2008.

[123] Y. del Valle, G. K. Venayagamoorthy, S. Mohagheghi, J. C. Hernandez, and R. G. Harley, "Particle Swarm Optimization: Basic Concepts, Variants and Applications in Power Systems," *Evolutionary Computation, IEEE Transactions on,* vol. 12, pp. 171-195, 2008.

[124] M. S. A. Dahidah, G. Konstantinou, and V. G. Agelidis, "A Review of Multilevel Selective Harmonic Elimination PWM: Formulations, Solving Algorithms, Implementation and Applications," *Power Electronics, IEEE Transactions on,* vol. 30, pp. 4091-4106, 2015.

[125] J. Vikramarajan, *Particle swarm optimizer: Economic dispatch with valve point effect using various Pso techniques*. Hamburg: Anchor Acadmic Puplishing, 2014.

[126] J. Kennedy and R. Eberhart, "Particle swarm optimization," in *Neural Networks, 1995. Proceedings., IEEE International Conference on*, 1995, pp. 1942-1948 vol.4.

[127] S. Yuhui and R. Eberhart, "A modified particle swarm optimizer," in *Evolutionary Computation Proceedings, 1998. IEEE World Congress on Computational Intelligence., The 1998 IEEE International Conference on*, 1998, pp. 69-73.

[128] J. Robinson and Y. Rahmat-Samii, "Particle swarm optimization in electromagnetics," *Antennas and Propagation, IEEE Transactions on,* vol. 52, pp. 397-407, 2004.

[129] F. Afshinmanesh, A. Marandi, and M. Shahabadi, "Design of a Single-Feed Dual-Band Dual-Polarized Printed Microstrip Antenna Using a Boolean Particle Swarm Optimization," *IEEE Trans. Antennas Propag.,* vol. 56, pp. 1845-1852, 2008.

[130] L. Lizzi, F. Viani, R. Azaro, and A. Massa, "A PSO-Driven Spline-Based Shaping Approach for Ultrawideband (UWB) Antenna Synthesis," *IEEE Trans, Antennas Propag.,* vol. 56, pp. 2613-2621, 2008.

[131] A. Nagliero, A. Lecci, R. A. Mastromauro, M. Liserre, and A. Dell'Aquila, "Particle Swarm Optimization of a universal inverter," in *IECON 2010 - 36th Annual Conference on IEEE Industrial Electronics Society*, 2010, pp. 199-204.

[132] W. Al-Saedi, S. W. Lachowicz, and D. Habibi, "An optimal current control strategy for a three-phase grid-connected photovoltaic system using Particle Swarm Optimization," in *Power Engineering and Automation Conference (PEAM), 2011 IEEE*, 2011, pp. 286-290.

[133] M. Miyatake, M. veerachary, F. Toriumi, N. Fujii, and H. Ko, "Maximum Power Point Tracking of Multiple Photovoltaic Arrays: A PSO Approach," *Aerospace and Electronic Systems, IEEE Transactions on,* vol. 47, pp. 367-380, 2011.

[134] C. Il-Yop, L. Wenxin, D. A. Cartes, and K. Schoder, "Control parameter optimization for a microgrid system using particle swarm optimization," in *Sustainable Energy Technologies, 2008. ICSET 2008. IEEE International Conference on*, 2008, pp. 837-842.

[135] D. Maiti, A. Acharya, M. Chakraborty, A. Konar, and R. Janarthanan, "Tuning PID Controllers using the Integral Time Absolute Error Criterion," in *Information and Automation for Sustainability, 2008. ICIAFS 2008. 4th International Conference on*, 2008, pp. 457-462.

[136] J. Chao, W. Jing, C. Liulin, and J. Qibing, "Parameters tuning of model free adaptive control based on minimum entropy," *Automatica Sinica, IEEE/CAA Journal of,* vol. 1, pp. 361-371, 2014.

[137] R. Kadri, J. P. Gaubert, and G. Champenois, "An Improved Maximum Power Point Tracking for Photovoltaic Grid-Connected Inverter Based on Voltage-Oriented Control," *IEEE Trans, Ind. Electronic.,* vol. 58, pp. 66-75, 2011.

[138] J. Holtz, "Pulsewidth modulation for electronic power conversion," *Proceedings of the IEEE,* vol. 82, pp. 1194-1214, 1994.

[139] J. Holtz, "Pulsewidth modulation-a survey," *IEEE Transactions on Industrial Electronics,* vol. 39, pp. 410-420, 1992.

[140] Z. Keliang and W. Danwei, "Relationship between space-vector modulation and three-phase carrier-based PWM: a comprehensive analysis [three-phase inverters]," *IEEE Transactions on Industrial Electronics,* vol. 49, pp. 186-196, 2002.

[141] D. G. Holmes and T. A. Lipo, "Pulse Width Modulation for Power Converters : Principles and Practice," 14 Oct 2003 ed: John Wiley & Sons Inc, 2003, p. 744.

[142] R. Zhang, "High Performance Power Converter System For Nonlinear and Unbalanced Load/Source," PhD, Electrical and Computer Engineering, Virginia Polytechnic Institute and State University, 1998.

[143] L. Hassaine, E. Olias, J. Quintero, and V. Salas, "Overview of power inverter topologies and control structures for grid connected photovoltaic systems," *Renewable and Sustainable Energy Reviews,* vol. 30, pp. 796-807, 2014.

[144] B. Bahrani, S. Kenzelmann, and A. Rufer, "Multivariable-PI-Based dq Current Control of Voltage Source Converters With Superior Axis Decoupling Capability," *Industrial Electronics, IEEE Transactions on,* vol. 58, pp. 3016-3026, 2011.

[145] J. Svensson, "Synchronisation methods for grid-connected voltage source converters," *Generation, Transmission and Distribution, IEE Proceedings-,* vol. 148, pp. 229-235, 2001.

[146] A. Reznik, M. G. Simões, A. Al-Durra, and S. M. Muyeen, "<formula formulatype="inline"><tex Notation="TeX">LCL</tex></formula> Filter Design and Performance Analysis for Grid-Interconnected Systems," *IEEE Transactions on Industry Applications,* vol. 50, pp. 1225-1232, 2014.

[147] K. H. Ahmed, S. J. Finney, and B. W. Williams, "Passive Filter Design for Three-Phase Inverter Interfacing in Distributed Generation," in *2007 Compatibility in Power Electronics*, 2007, pp. 1-9.

[148] M. Liserre, F. Blaabjerg, and S. Hansen, "Design and control of an LCL-filter based three-phase active rectifier," in *Conference Record of the 2001 IEEE Industry Applications Conference. 36th IAS Annual Meeting (Cat. No.01CH37248)*, 2001, pp. 299-307 vol.1.

[149] M. Liserre, F. Blaabjerg, and S. Hansen, "Design and control of an LCL-filter-based three-phase active rectifier," *IEEE Transactions on Industry Applications,* vol. 41, pp. 1281-1291, 2005.

[150] R. Teodorescu and F. Blaabjerg, "Flexible control of small wind turbines with grid failure detection operating in stand-alone and grid-connected mode," *Power Electronics, IEEE Transactions on,* vol. 19, pp. 1323-1332, 2004.

[151] A. Kiam Heong, G. Chong, and L. Yun, "PID control system analysis, design, and technology," *IEEE Transactions on Control Systems Technology,* vol. 13, pp. 559-576, 2005.

[152] R. C. Eberhart and Y. Shi, "Comparing inertia weights and constriction factors in particle swarm optimization," in *Evolutionary Computation, 2000. Proceedings of the 2000 Congress on*, 2000, pp. 84-88 vol.1.

[153] M. Clerc, "The swarm and the queen: towards a deterministic and adaptive particle swarm optimization," in *Evolutionary Computation, 1999. CEC 99. Proceedings of the 1999 Congress on*, 1999, p. 1957 Vol. 3.

Appendix A

A.1 Introduction

This appendix contains details descriptions of the equations used in the thesis. In a complex three-phase system, it is easier and useful to convert the three-phase components voltage and current into two-phase components. Clark's and Park's transformation employed to simplify the space vector. This appendix is also mention for the LCL-filter used. In addition, the principle of the current control of grid-connected inverter is also addressed.

A.2 Clark and Park Transformation

Clark transformation is converting the three-phase AC quantities v_{abc} and i_{abc} nature coordinates components to the stationary reference frame two-phase AC quantities $v_{\alpha\beta}$ and $i_{\alpha\beta}$ components. The following expression can be used to calculate $v_{\alpha\beta}$ and $i_{\alpha\beta}$ components:

$$\begin{bmatrix} v_\alpha \\ v_\beta \end{bmatrix} = \frac{2}{3}\begin{bmatrix} 1 & -\frac{1}{2} & -\frac{1}{2} \\ 0 & \frac{\sqrt{3}}{2} & -\frac{\sqrt{3}}{2} \end{bmatrix}\begin{bmatrix} v_a \\ v_b \\ v_c \end{bmatrix} \tag{A.1}$$

$$\begin{bmatrix} i_\alpha \\ i_\beta \end{bmatrix} = \frac{2}{3}\begin{bmatrix} 1 & -\frac{1}{2} & -\frac{1}{2} \\ 0 & \frac{\sqrt{3}}{2} & -\frac{\sqrt{3}}{2} \end{bmatrix}\begin{bmatrix} i_a \\ i_b \\ i_c \end{bmatrix} \tag{A.2}$$

where v_α and v_β are the stationary reference frame voltage; v_a, v_b and v_c are three-phase voltages; where i_α and i_β are the stationary reference frame current; i_a, i_b and i_c are three-phase currents.

Park Transformation

Park transformation is converting the two-phase $v_{\alpha\beta}$ and $i_{\alpha\beta}$ coordinates components to the synchronous reference frame two-phase v_{dq} and i_{dq} components. The d axes component describe the real part and q component describe the imaginary part. The following transformations in (A.3) and (A.4) can be used to calculate v_{dq} and i_{dq}components:

$$\begin{bmatrix} v_d \\ v_q \end{bmatrix} = \begin{bmatrix} \cos\theta & \sin\theta \\ -\sin\theta & \cos\theta \end{bmatrix} \begin{bmatrix} v_\alpha \\ v_\beta \end{bmatrix} \quad \text{(A.3)}$$

$$\begin{bmatrix} i_d \\ i_q \end{bmatrix} = \begin{bmatrix} \cos\theta & \sin\theta \\ -\sin\theta & \cos\theta \end{bmatrix} \begin{bmatrix} i_\alpha \\ i_\beta \end{bmatrix} \quad \text{(A.4)}$$

where v_d and v_q are the synchronous reference frame voltage v_α and v_β are the stationary reference frame voltage; i_d and i_q are the synchronous reference frame current, i_α and i_β are the stationary reference frame current, θ is the rotating angle. Figure A.1 shows the Clark and Park transformation reference frame.

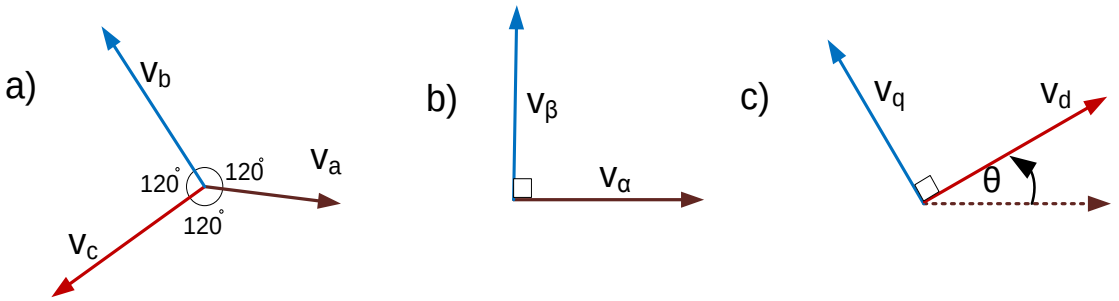

Figure A.1 Clark and Park transformation reference frame. a) three-phase reference frame b) stationary reference frame c) synchronous reference frame

Inverse Park transformation:

The voltage and current rotating synchronous reference frames are converted into orthogonal stationary reference frames using inverse Park transformation in the following expressions:

$$\begin{bmatrix} v_\alpha \\ v_\beta \end{bmatrix} = \begin{bmatrix} \cos\theta & -\sin\theta \\ \sin\theta & \cos\theta \end{bmatrix} \begin{bmatrix} v_d \\ v_q \end{bmatrix} \quad \text{(A.5)}$$

$$\begin{bmatrix} i_\alpha \\ i_\beta \end{bmatrix} = \begin{bmatrix} \cos\theta & -\sin\theta \\ \sin\theta & \cos\theta \end{bmatrix} \begin{bmatrix} i_d \\ i_q \end{bmatrix} \quad \text{(A.6)}$$

Inverse Clark transformation:

The voltage and current in the orthogonal stationary reference frames are transformed into three-phase reference frames using inverse Clark transformation in the following expressions:

$$\begin{bmatrix} v_a \\ v_b \\ v_c \end{bmatrix} = \begin{bmatrix} 1 & 0 \\ -\frac{1}{2} & \frac{\sqrt{3}}{2} \\ -\frac{1}{2} & -\frac{\sqrt{3}}{2} \end{bmatrix} \begin{bmatrix} v_\alpha \\ v_\beta \end{bmatrix} \quad \text{(A.7)}$$

$$\begin{bmatrix} i_a \\ i_b \\ i_c \end{bmatrix} = \begin{bmatrix} 1 & 0 \\ -\frac{1}{2} & \frac{\sqrt{3}}{2} \\ -\frac{1}{2} & -\frac{\sqrt{3}}{2} \end{bmatrix} \begin{bmatrix} i_\alpha \\ i_\beta \end{bmatrix} \quad \text{(A.8)}$$

The previous state expressions using Park's transformation can be used in the design of LCL filter.

A.3 LCL Filter Mathematical Model:

The LCL-filter in the Figure A.2 can be described in the following matrix expression based on rotating frames *d* axis and *q* axis at rotating speed *ω*

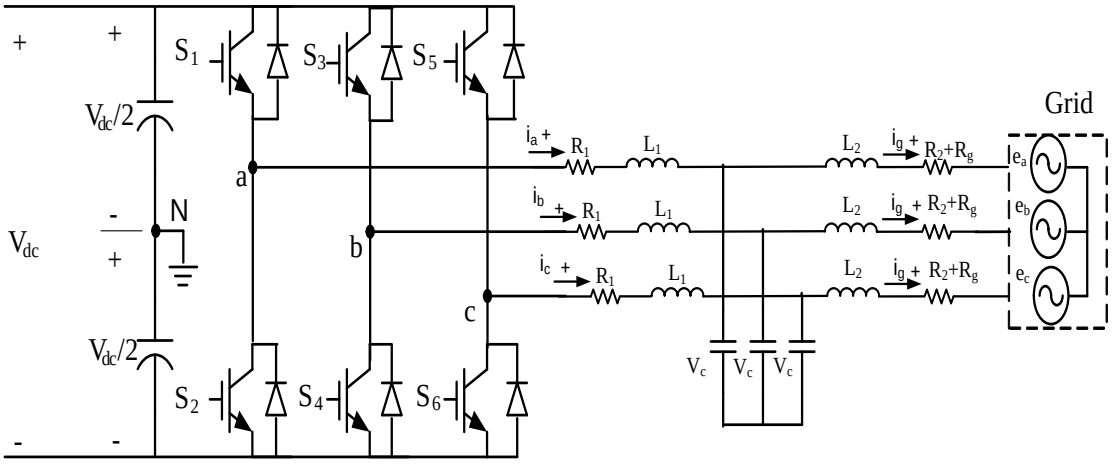

Figure A.2 Three-phase grid-connected inverter

$$\frac{d}{dt}\begin{bmatrix} i_d \\ i_q \\ v_{cd} \\ v_{cq} \\ i_{gd} \\ i_{gq} \end{bmatrix}$$

$$= \begin{bmatrix} -\frac{R_1}{L_1} & \omega & -\frac{1}{L_1} & 0 & 0 & 0 \\ -\omega & -\frac{R_1}{L_1} & 0 & -\frac{1}{L_1} & 0 & 0 \\ \frac{1}{c_f} & 0 & 0 & \omega & -\frac{1}{c_f} & 0 \\ 0 & \frac{1}{c_f} & -\omega & 0 & 0 & -\frac{1}{c_f} \\ 0 & 0 & \frac{1}{(L_2+L_g)} & 0 & -\frac{(R_2+R_g)}{(L_2+L_g)} & \omega \\ 0 & 0 & 0 & \frac{1}{(L_2+L_g)} & -\omega & -\frac{(R_2+R_g)}{(L_2+L_g)} \end{bmatrix} \begin{bmatrix} i_d \\ i_q \\ v_{cd} \\ v_{cq} \\ i_{gd} \\ i_{gq} \end{bmatrix} \quad \text{(A.9)}$$

$$+ \begin{bmatrix} 0 & 0 \\ 0 & 0 \\ 0 & 0 \\ 0 & 0 \\ -\frac{1}{L_1} & 0 \\ 0 & -\frac{1}{L_1} \end{bmatrix} \begin{bmatrix} e_d \\ e_q \end{bmatrix} + \begin{bmatrix} \frac{v_{dc}}{(L_2+L_g)} & 0 \\ 0 & \frac{v_{dc}}{(L_2+L_g)} \\ 0 & 0 \\ 0 & 0 \\ 0 & 0 \\ 0 & 0 \end{bmatrix} \begin{bmatrix} p_d \\ p_q \end{bmatrix}$$

where v_{dc} is the DC voltage, $v_{cd}$and v_{cq} is the capacitor in the synchronous reference frame; i_d and i_q are the synchronous reference frame current; i_{gd} and i_{gq} are the grid current in the synchronous reference frame; ω is the rotating angle where $\omega = 2\pi f$ and f is the fundamental frequency, R_1 and $R_2 + R_g$ are the filter resistors, L_1 and L_g are the filter inductors.

Note that, *d* axis and *q* axis rotating frames are decoupled together due to cross-couplings terms.

A.3 Current Control of Grid-connected Inverter

To understand the principle of current control three-phase grid-connected inverter, consider the single-phase equivalent circuit of a grid-connected inverter in Figure A.3. The inverter is connected to the grid through a simple L filter.

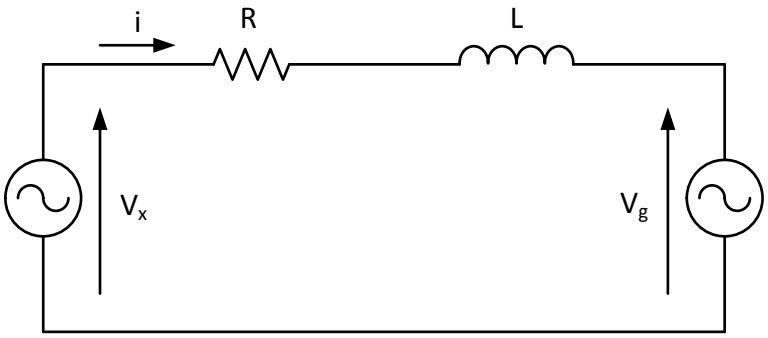

Figure A.3 Single-phase equivalent circuit of a grid-connected inverter

From the circuit in Figure A.3, we obtain the following equations.

$$\bar{V}_x = V_L + V_g \tag{A.10}$$

$$\bar{V}_x = I_L X_L + R\, I_L \tag{A.11}$$

$$\bar{V}_{dc} = V_g + IR + j\omega\, IL \tag{A.12}$$

where V_x is the inverter output voltage, V_g is the grid voltage, I is the current injected to the grid, R and L are the resistance and the inductance, respectively, of the filter, and ω is the angular frequency of the grid voltage.

The quantities in equation (A.12) can be represented in the phasor diagram of Figure A.4

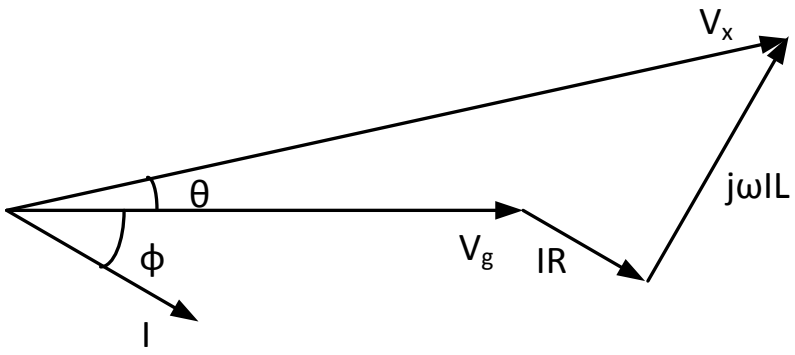

Figure A4 Phasor diagram of grid-connected inverter

The grid voltage is considered to be constant, while the inverter output voltage can be controlled by varying the modulation index of the inverter. It is desired to control the current being injected to the grid. This can be done by changing the inverter output voltage, through the modulation index of the inverter, assuming a constant DC link voltage. All current control techniques are

based on the fact that the current injected into the grid, or supplied to the load can be controlled by varying the modulation index of the inverter and hence the inverter output voltage.

The inverter output voltage is related to the DC link voltage by the equation below.

$$\bar{V}_x = m\,\frac{v_{dc}}{2} \tag{A.13}$$

where m is the modulation index of the inverter, and V_{dc} is the DC link voltage.

Appendix B

B.1 Introduction

This appendix contains a detail description of the hardware equipment used for the three-phase grid-connected inverter.

B.2 Isolation and Varic Transformers

Since the project concerns a three-phase grid-connected inverter, it has been connected to the grid via a 450 V mains supply in the experimental study. In this case, a supply variac transformer and isolation transformer are interfaced between the grid and the rig as shown in Figure B.1 and Figure B.2.

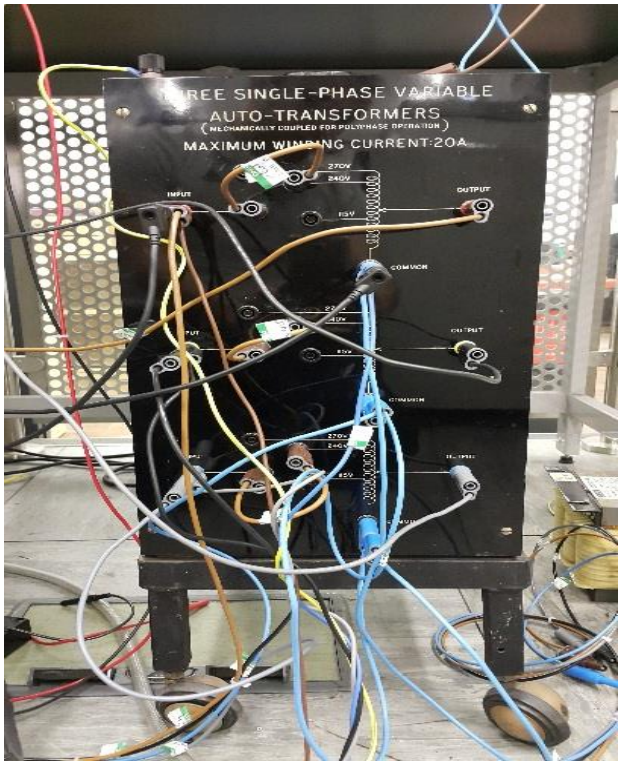

Figure B.1 Three phase variac transformer

Figure B.2 Three phase isolation transformer

The three-phase variac transformer is used in order to effectively regulate the voltage from the mains supply to the experimental grid-connected PV inverter system. In addition, it allows the DC link voltage to be used at low values instead of using the conversion ratio between DC/AC applications. However, the variac is a non-isolated transformer which has no protection from any feedback of the DC current into the mains supply. Thus, to overcome this issue, an isolation transformer is connected between the grid's mains supply and the variac transformer. The connection is Δ-Y as shown in

In addition, Figure B.3 shows the LCL filter connected the rig. An LCL filter has been used in the experiment to smoothe the output waveform from the AC side of the inverter and thus reduce the harmonic of the switching frequency.

Two three-phase inductances are tapped to five different readings in order to test the effect of various values of inductances. The L_1, tapped from 0.3mh to 0.8mh and L_2, tapped from 0.1mh to 0.3mh with a rating current of 15A. Different values of inductances and capacitances have been tested and the most suitable values chosen for a 10 KHz switching frequency.

Figure B.3 LCL filter experimental module connected to the rig

B.3 Three-phase Inverter

The module of the three-phase inverter is shown in Figure B.4. The module consists of two-input series DC source that provides DC link source from the DC power supply which is part of the experimental rig as shown in Figure B.5. The inverter has six transistor switches incorporated with freewheeling diodes. The first type of switches to be used the MOSFET IRFP140PBF which have low switching losses. However, this can only work in low voltage applications. Therefore, IGBT-IRG4PH50UDPBF was chosen for high-voltage DC purposes. 2700uF two capacitors are connected in parallel across the DC link. This type of capacitor allows the voltage to go as high as 250V. The output of the three-phase inverter is connected to the gate drive, as shown Figure B.1. The gate drive is employed to provide the link between the control board and the inverter board and apply PWM switching signal to the inverter switches.

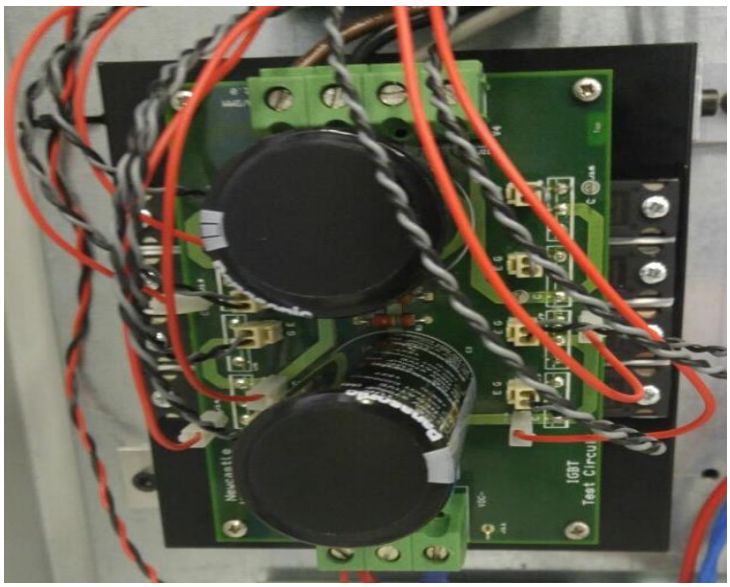

Figure B.4 Three-phase inverter experimental module

Figure B.5 The DC power supply

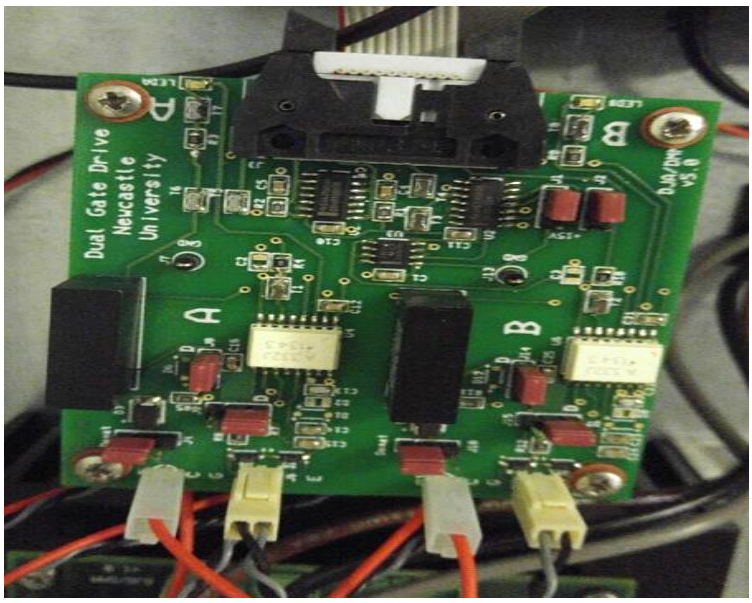

Figure B.6 Gate drive board

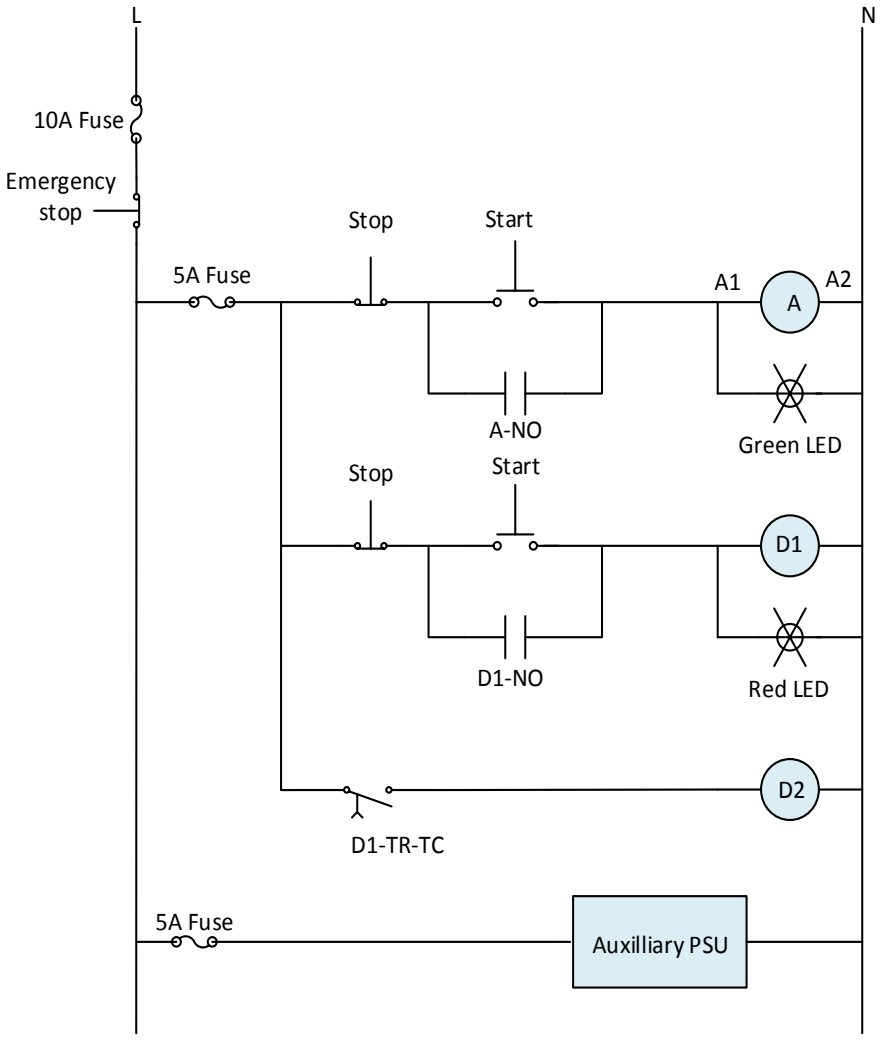

Figure B.7 Control ladder diagram

B.4 Digital Signal Processor

Digital signal processor (DSP) is a software card for TMS320F2833x series of floating-point. This eZdsp kit includes a 12-bit analogue digital converter (ADC) with 16 input channels to allow data transfer for communication. This card has 128Kx16 asynchronous SRAM, which is supported to the Code Composer Studio® Integrated Development.

B.5 Analog-to-Digital Converter

In power electronics, Analog-to-digital converter (ADC) is used to convert analogue signals such as the voltage signal into digital signal. ADC has employed 16 converting channels built-in which has 12-bit ADC core that sample-and-hold acquired.

B.6 Current Sensor

The current sensor is very important part of the three-phase grid-connected inverter in order to measure and control the current with the varying weak grid. Figure B.7 shows the schematics of the current sensor. It is important for the safety and protection of the power electronics rig from over current and any fault that occurs. In industry, there are many types of current sensors. One of these current sensors is CAS15-NP. This type of the current sensor has many features. It designed to work up to 50 A, and has a very low-temperature coefficient of offset. It has a galvanic isolation and it has high flexibility with reliability. It can work with different applications.

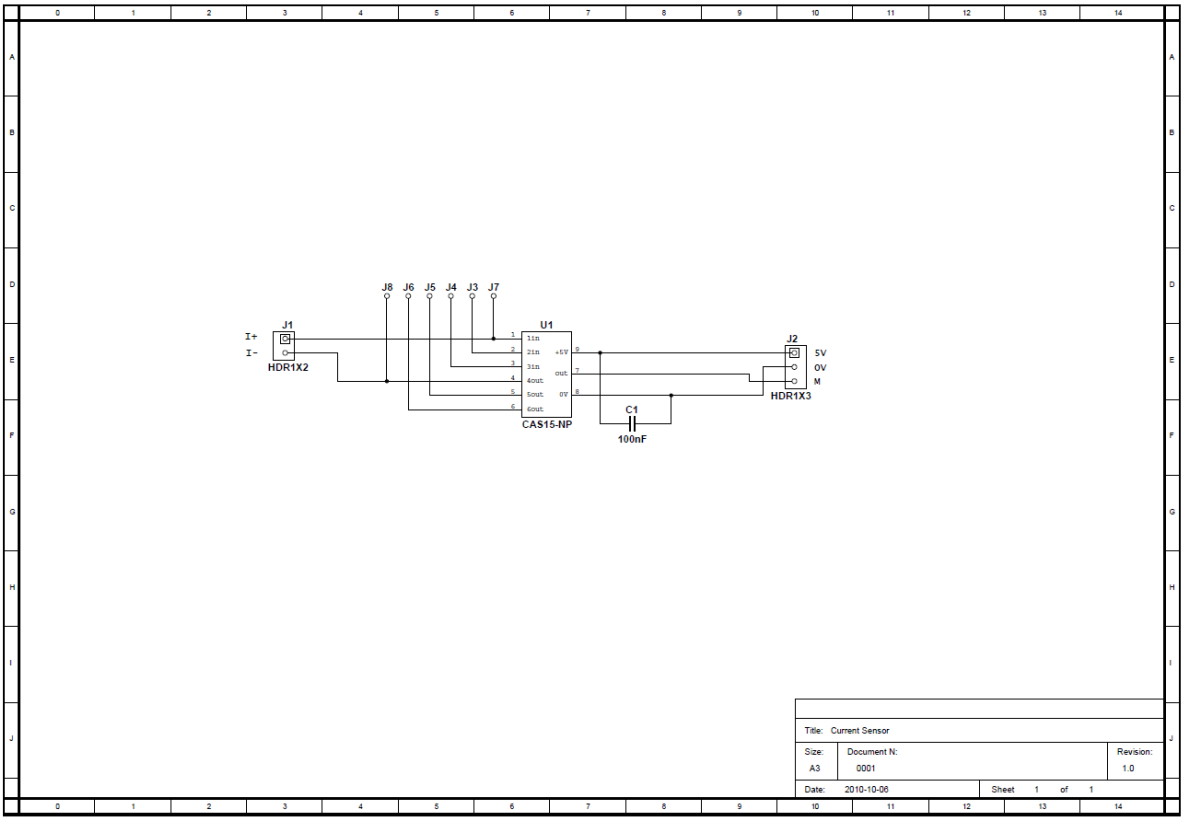

Figure B.7 Schematics of current sensor

B.8 Voltage Sensor

The grid voltage is measured using the AD215AY isolated voltage sensors which used to sense the output voltage and measure the voltage at the point of common coupling and the phase-locked loop angle. This type of voltage sensor has a galvanic isolation between output and input of the device and an auxiliary circuit. This type of the voltage sensor has high accuracy and is designed to work up to 750V *RMS*. It consists of rated power supply in a range of ± 15 VDC voltage.

B.9 LabVIEW

LabVIEW is powerful interface software program from National Instrument® company used for many purposes such as grid-connected applications. It is used here to monitor and control the real-time application. Figure B.8 shows the screenshot of LabVIEW used in this experimental. The LabVIEW program can interface to eZdsp via RS232 from the computer. It is used here to update the current demand and DC voltage as well as EX-time. LabVIEW divided the project into two interface panel, the front panel and block diagram panel.

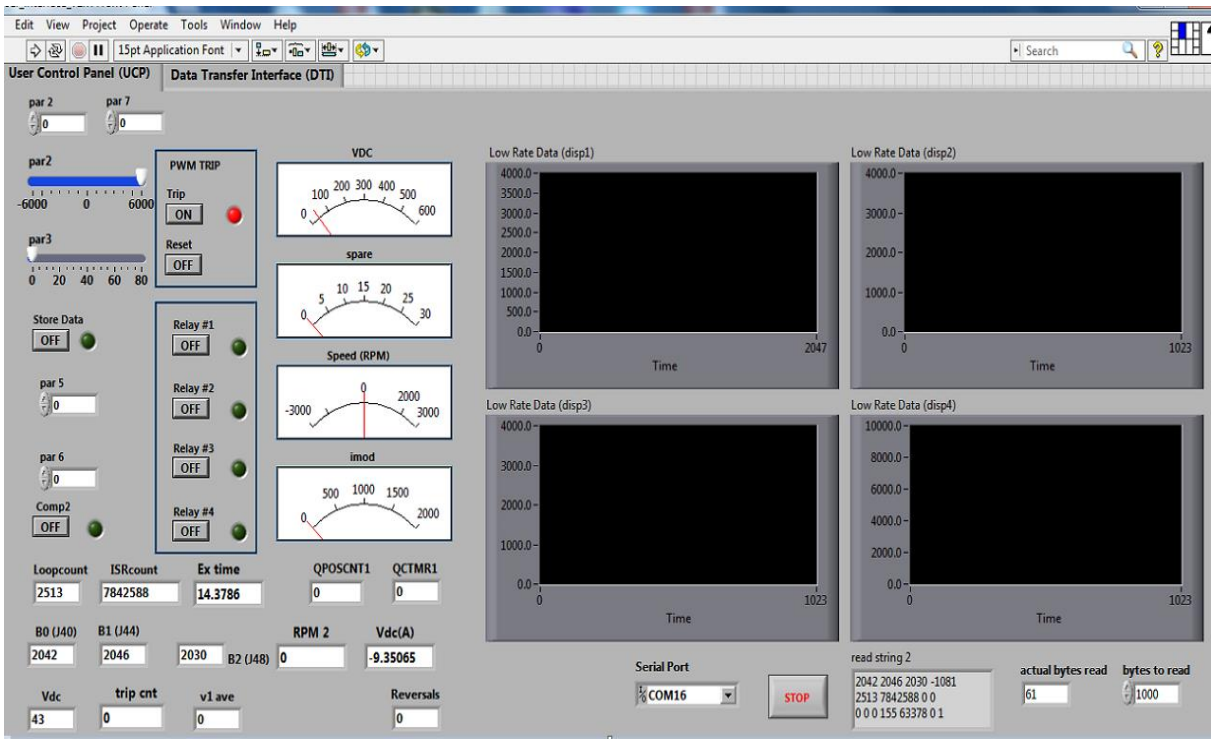

Figure B.8 Screenshot of LabVIEW

B.10 Experimental Result RL Load

The three-phase inverter has been verified experimentally with RL load. The experimental test rig was firstly tested with the open loop with different values of DC voltage. In this system, the DC-link voltage is kept constant using the DC power supply. In order to reduce the controller error in the three-phase inverter, a phasor diagram is essential.

To validate the control technique for the system in the laboratory, the system is scaled down and has been tested, using an RL load. The three-phases resistors R_a, R_b, R_c and the three-phases inductance L_a, L_b, L_c are varied in order to test them in balanced and unbalanced load. The values have been chosen as $R_a = 10\ \Omega$, $R_b = 10\ \Omega$ and $R_c = 10\ \Omega$ and the inductance values are $L_a = 0.881mH$, $L_b = 0.881mh$ and $L_c = 0.881mh$.

In the adaptive PR controllers, the current reference $i^*$is generated in the digital controller as a sine wave oscillating at a certain frequency. Thereafter, the signal is compared in an oscilloscope with the actual measured current value. The system has been tested first using stand-alone resistive and inductance (RL) load in different conditions, at steady-state and with sudden step responses. Different values of resistive load have been tested to check the control system's response. In the following, the resistive load is 1 Ω and the control technique work effectively.

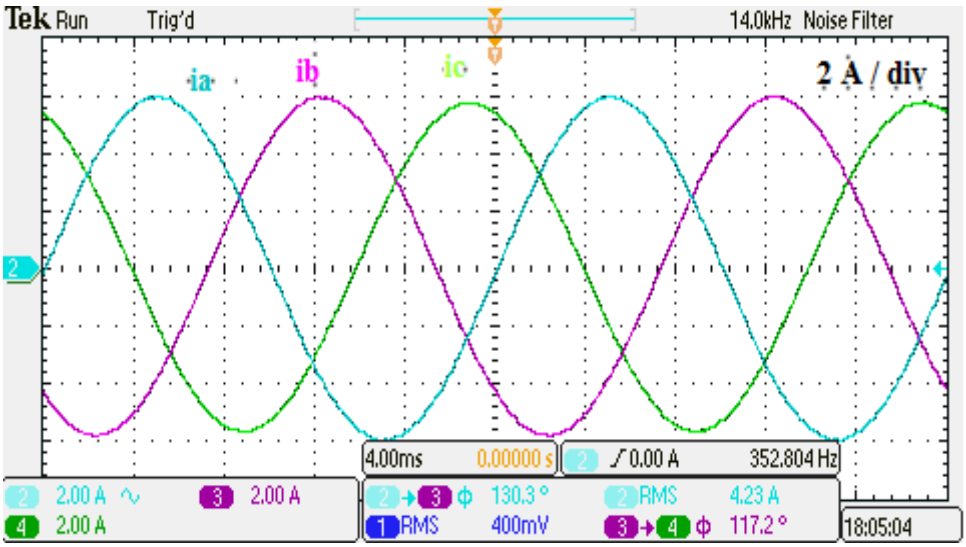

Figure B.10 The three-phase current waveform

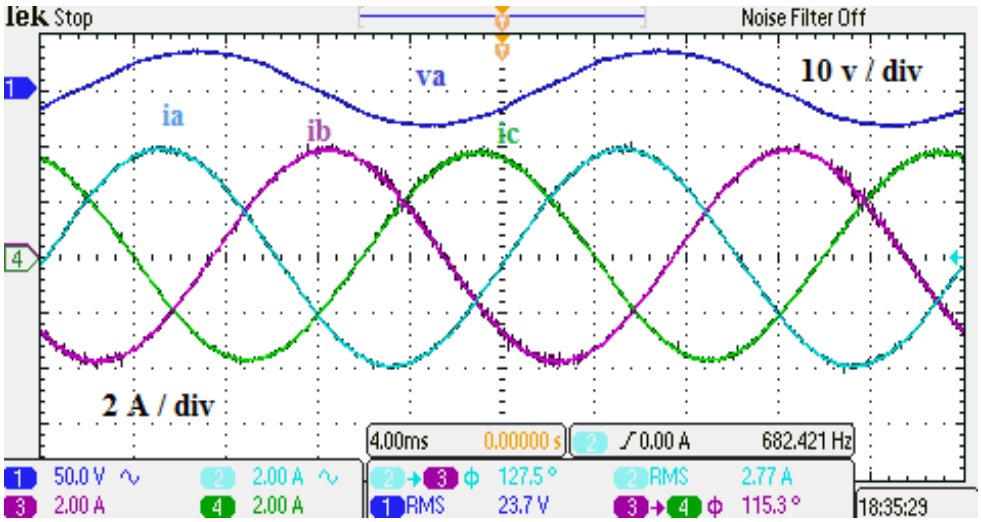

Figure B.11 The three-phase current with grid voltage waveform

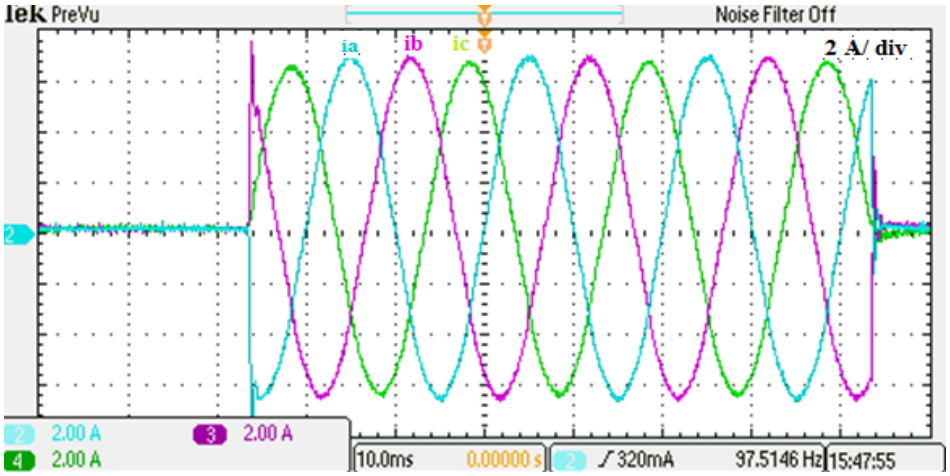

Figure B.12 The three-phase current waveform with step response stand alone

Appendix C

C.1 Introduction

This appendix explains the decomposition of the positive and negative sequence. To make the decomposition easier, the system is decomposed in the orthogonal two-phase α-β plane. In order to extract and separate the positive and negative sequence components with a phase shift of 90°. An adaptive low-pass filter based on the delay time cancellation method is used in order to detect and reduce any variation in the input frequency. The proposed technique detects an unbalanced voltage, comprising of positive and negative sequences and express these in the stationary reference frame.

C.2 The Method of Decomposition of the Voltage

The method of decomposition of the voltage sequence has been tested experimentally in the laboratory for different unbalanced conditions based on a line-to-ground fault or a line-to-line fault. Figure C.1 shows the three-phase voltage signals. There is a 120° phase shift between phases *a*, *b*, and *c*.

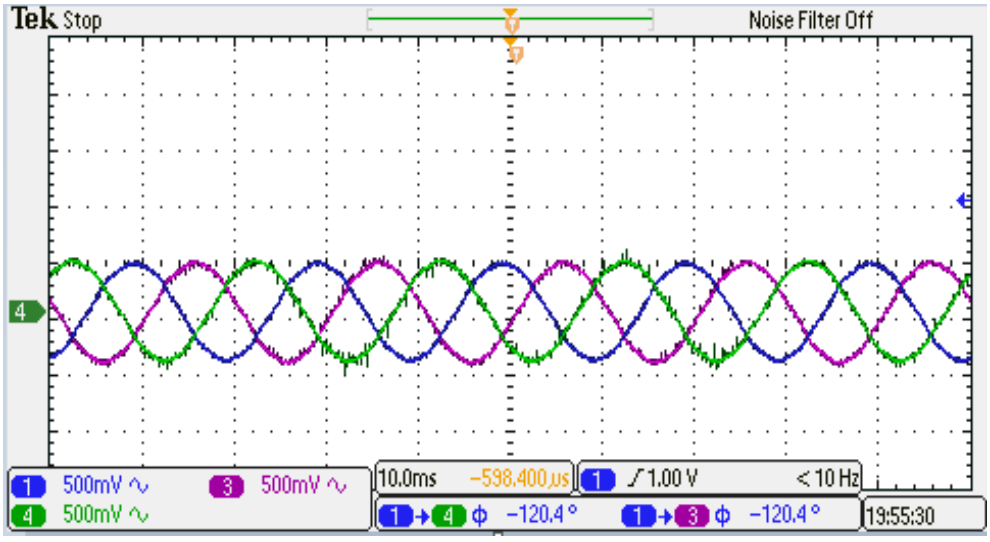

Figure C.1 The three-phase voltage waveform

Figure C.2 shows the positive and negative voltage sequence of the two-phase components. The positive voltage alpha (v_{α}^{+}) is shown in *(dark blue)* and the positive voltage beta (v_{β}^{+}) is shown in *(red)* whereas the negative sequence voltage alpha (v_{α}^{-}) is shown in *(light blue)* and the

negative voltage beta (v_{β}^{-}) is shown in *(green)*. Figure C.3 shows the unbalance happened in the voltage phase signal when the voltage has been dropped in phase a by 50%. Figure C.4 shows the decomposition of the positive and negative sequence when the voltage dropped by 25%. is shown the unbalance in the phases when the voltage dropped by 15%.

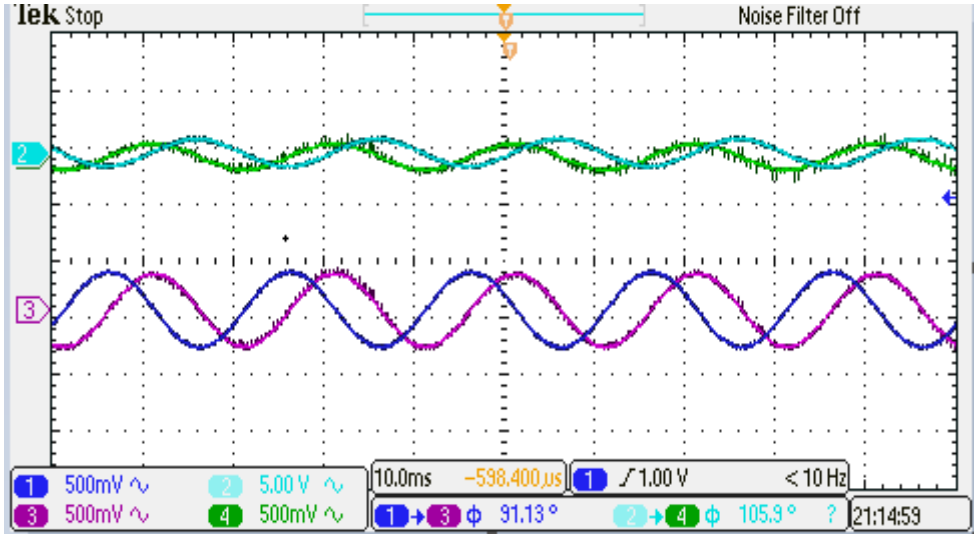

Figure C.2 The positive and the negative voltage sequences with voltage drop in phase a by 50%

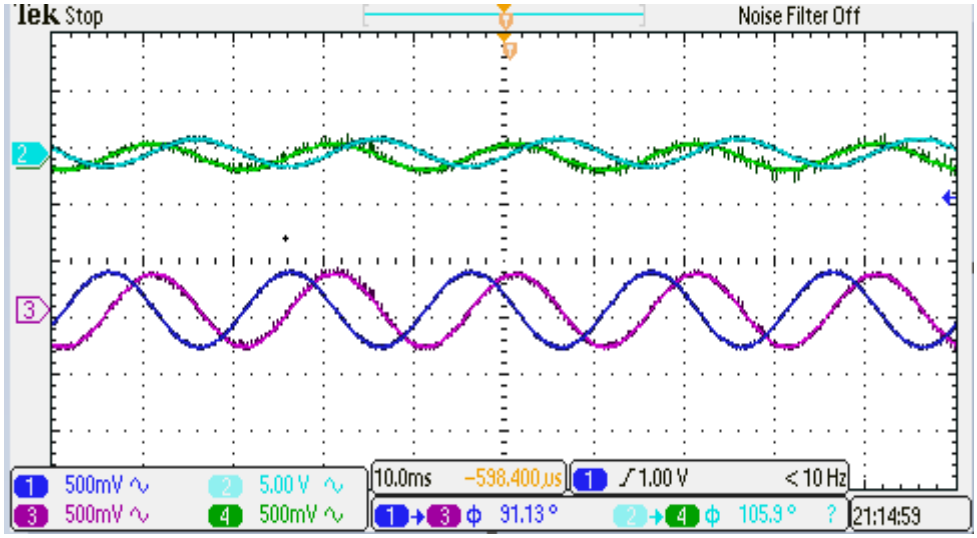

Figure C.3 The positive and the negative voltage sequences with voltage drop in phase a by 25%

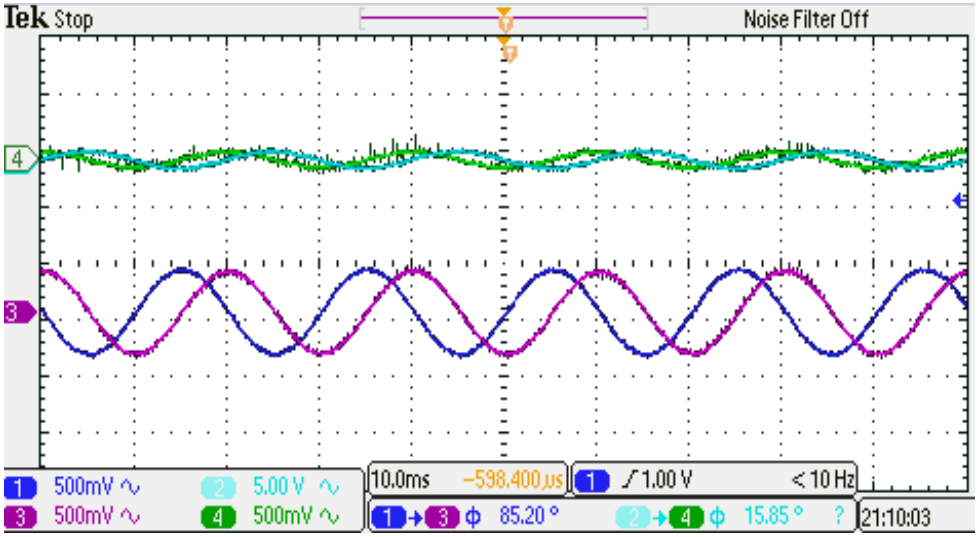

Figure C.4 The positive and the negative voltage sequences with voltage drop in phase a by 15%

Figure C.5 shows the positive voltage sequence angle *(in dark blue)* and negative voltage sequence angle *(in light blue)* for two-phase signals. Figure C.5 illustrate the angles when the voltage dropped by 50%. Figure C.6 shows the angles when unbalanced occurred by 25% of phase a voltage. Figure C.7 shows the result when the voltage reduced by 15% in phase a. It can be noticed that these results are achieved even if the negative sequence is small. However, when the voltage negative sequence becomes very small it is hard to find the negative angle and tuning the phase angle as can be seen in Figure C.8

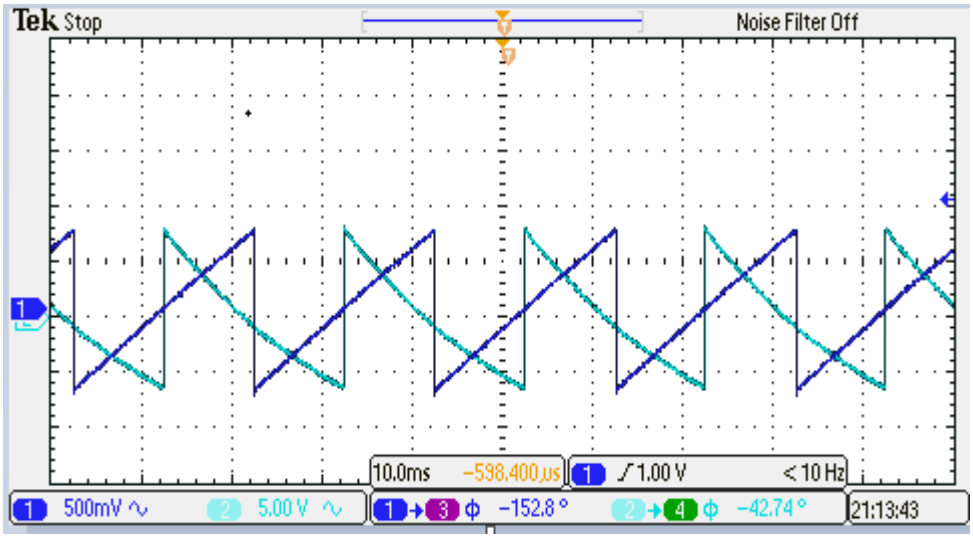

Figure C.5 The positive and the negative sequence angles detection when the voltage drop in phase a 50%

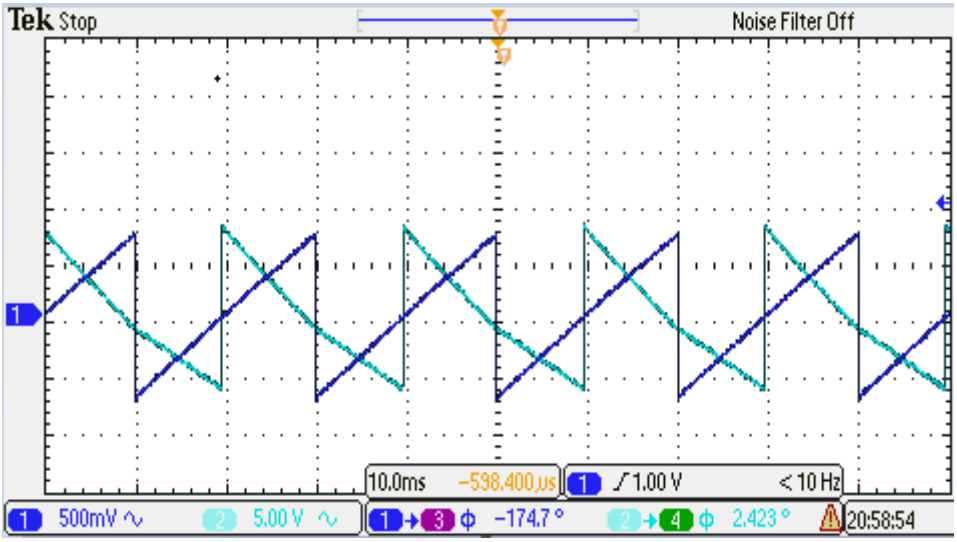

Figure C.6 The positive and the negative sequence angle detection when the voltage drop in phase a by 25%

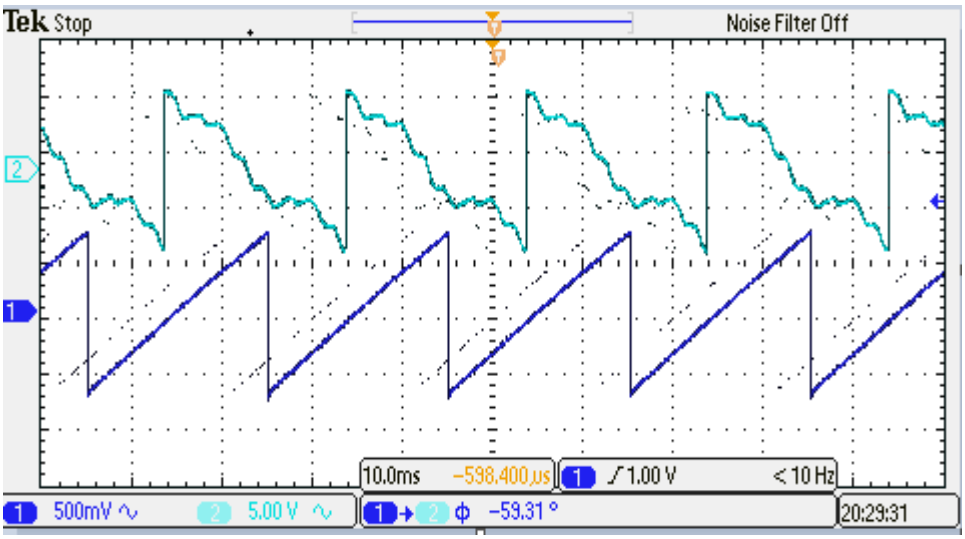

Figure C.7 The positive and the negative voltage sequences with voltage drop in phase a by 15%

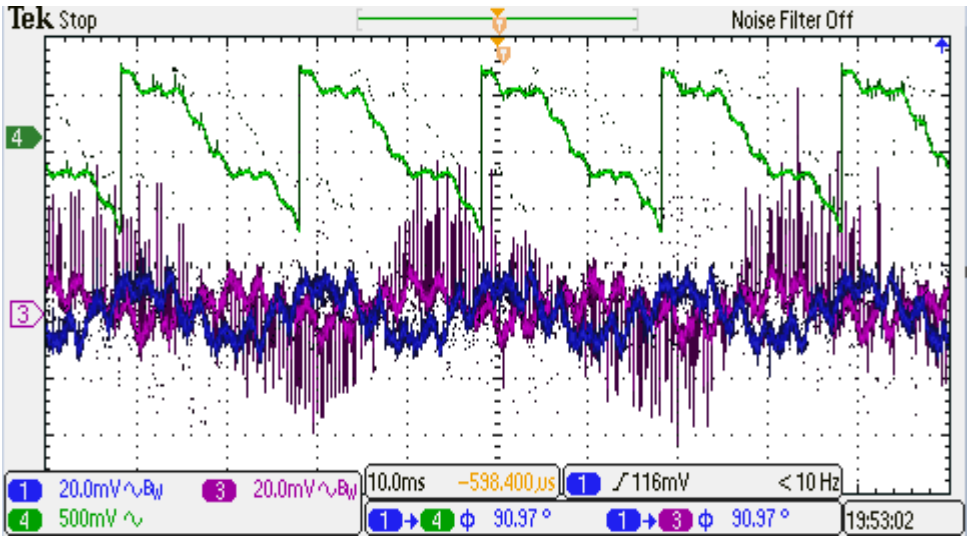

Figure C.8 The negative sequence voltage and the angle detection when the voltage drops in phase a by 10%